Downloaded from orbit.dtu.dk on: Apr 29, 2024

DTU Library

Stability of Tungsten Plates during High Temperatures

Ciucani, Umberto Maria

Publication date:
2021

Document Version
Publisher's PDF, also known as Version of record

Link back to DTU Orbit

Citation (APA):
Ciucani, U. M. (2021). *Stability of Tungsten Plates during High Temperatures*. Technical University of Denmark.

General rights
Copyright and moral rights for the publications made accessible in the public portal are retained by the authors and/or other copyright owners and it is a condition of accessing publications that users recognise and abide by the legal requirements associated with these rights.

- Users may download and print one copy of any publication from the public portal for the purpose of private study or research.
- You may not further distribute the material or use it for any profit-making activity or commercial gain
- You may freely distribute the URL identifying the publication in the public portal

If you believe that this document breaches copyright please contact us providing details, and we will remove access to the work immediately and investigate your claim.

DTU Mechanical Engineering
Department of Mechanical Engineering

Stability of Tungsten Plates during High Temperatures

Umberto Maria Ciucani

PhD Thesis

Stability of Tungsten Plates during High Temperatures

Umberto Maria Ciucani

Ph.D. Thesis

February 2021

Department of Mechanical Engineering

Technical University of Denmark

Author: **Umberto Maria Ciucani**

Title: **Stability of Tungsten Plates during High Temperatures**

Division: **Section of Materials and Surface Engineering, Department of Mechanical Engineering**

Submission date: **February 2021**

Main Supervisor: **Wolfgang Pantleon**

Co-supervisors: **Guangnan Luo**

Stability of Tungsten Plates during High Temperatures

Copyright ©2021 by Umberto Maria Ciucani. All rights reserved.

Ph.D. Thesis

DTU Mechanical Engineering
Section of Materials and Surface Engineering
Technical University of Denmark

Nils Koppels Allé
Building 425
2800, Kgs. Lyngby
Denmark
Tel (+45) 452 52205

ISBN: 978-87-7475-622-4

Abstract

A decade had passed since tungsten was promoted to the main candidate material for plasma facing armour material (PFM) in fusion reactors. Exposure to high operational temperatures and neutron bombardment in a fusion reactor imposes the risk of undesired recrystallization. This is a microstructural process that reinstates brittleness in the material which should be avoided for PFMs undergoing thermal stress fatigue. Since the last decade, experimental work to find thermally stable tungsten materials has been ongoing along two major routes. One approach to solve the problem has been to design tungsten as a composite. For instance, a composite tungsten material could consist in a stacking of heavily cold rolled plates, stacked one on the other, or in the form of fibre reinforced tungsten composites, where drawn tungsten fibres are covered by chemically vapour deposited (CVD) tungsten. Alternatively, obtaining an increased understanding of how microstructural rearrangement phenomena such as recovery and recrystallization evolve in pure deformed tungsten is pursued. In this case, recrystallization is investigated depending on the amount of deformation put into the material and a comprehensive understanding of the dependence of recrystallization from the amount of work-hardening is being attempted. Understanding the thermal stability of tungsten in the different designs is strictly needed. In this concern this thesis investigated recovery and recrystallization in different tungsten designs: plates work-hardened to different extents and tungsten fibre reinforced CVD coated tungsten composites. Understanding the mechanisms fostering or preventing recrystallization in tungsten are potentially the key towards design with higher recrystallization resistance design, ultimately allowing commercial feasibility of fusion energy for carbon-free future.

The annealing behavior of thin tungsten plates of four different thicknesses achieved by warm- and (in two cases) cold-rolling is investigated. Isothermal experiments at five different temperatures between 1300 °C to 1400 °C were performed. Hardness testing of annealed specimens allowed tracking the degradation of the mechanical properties and, indirectly, the microstructural evolution. Supplementary microscopical investigations of the microstructure in the as-received state as well as after annealing were performed to characterize the initial condition and to support the identification of the involved restoration processes. All four tungsten plates undergo microstructural restoration and a concise description of both isothermal and isochronal annealing treatments is achieved using well-established models for the kinetics of recovery and recrystallization. A systematic dependence of the recovery kinetics at different temperatures on the hardness loss during recovery at a particular temperature has been identified. For the recrystallization kinetics, an Avrami exponent of 2 is observed in general. On the other hand, the activation energies revealed for different characteristic times of the recrystallization process depend on the plate thickness (or more precisely, the defect density stored). These findings, in particular, an activation energy far below that of short circuit diffusion, indicate the possibility of persisting nucleation throughout annealing.

Moreover, the thermal response of a sintered, hot isostatically pressed tungsten plate warm-rolled to 80% thickness reduction is assessed in the temperature range between 1150 °C and 1300 °C. Isothermal annealing treatments were performed at six different temperatures. With increasing annealing time, the macro hardness decreased and different stages corresponding to different stages of the microstructural evolution and the progress of recrystallization could be identified and

confirmed by electron backscatter diffraction. For all six annealing temperatures a stagnation period in the evolution of the macro hardness was observed where the degradation of mechanical properties halted for a significant amount of time, before it resumed. Microstructural investigations revealed that the stagnation occurred when tungsten was still only partially recrystallized. For the time to half recrystallization, an activation energy of 548 kJ/mol comparable to the activation energy of bulk self-diffusion is inferred. The microstructural changes due to recrystallization in this heavily recovered, warm-rolled, tungsten plate are investigated in the temperature range from 1150 °C to 1200 °C by means of EBSD. The evolution of the major texture components of rolled bcc metals are examined together with the evolution of the stored energies, the boundary surface densities and relevant microstructural parameters of both the recovered and recrystallized regions. A homogeneous nucleation and growth of recrystallized grains is found up to a recrystallized fraction of about 60%. Stagnation of recrystallization is observed after achieving the stagnation period. Non-uniform impingement behaviour is inferred up to complete recrystallization. A heavily reduced stored energy density is observed in the recovered regions and it is suggested recrystallization stagnates due to the depleted defect content which in turn influences the nucleation of new grains in an ordered manner leading to non-uniform impingement.

Finally, cylindrical single fibre composites with a single potassium-doped drawn tungsten wire in a chemically vapor deposited tungsten matrix, with or without a rare-earth oxide interlayer, were investigated as model systems. Individual specimens were annealed at 1400 °C up to four weeks and changes in their microstructure tracked by electron backscatter diffraction. In the as-processed condition, the tungsten matrix showed large wedge-shaped grains stretching radially from either the interface between matrix and wire or the oxide interlayer to the outer surface with very small grains in the vicinity of the interface/interlayer. Upon heating, two zones with larger grains compared to the as-processed condition developed: in the wire regions close to its perimeter primary recrystallization led to formation of new grains with orientations deviating slightly in alignment of their crystallographic <110> directions with the wire axis compared to the drawn wire. In the matrix, abnormally grown grains consumed the as-deposited microstructure in the vicinity of the interface/interlayer. Without an interlayer, abnormally growing grains from the matrix invaded the recrystallizing wire progressively consuming the wire. Both erbia and yttria interlayers efficiently prevented abnormally growing grains from invading the wire (except at few occasions where the oxide interlayer presented imperfections). In this manner, the presence of an interlayer becomes crucial for retaining an interface essential for the pseudo-ductility of the composite.

Acknowledgements

The path through a Ph.D. can be plenty of enthusiasm, excitement, questioning on the matter of study (and on ourselves!), inspiration, personal growth, worry and ultimately, unexpected events.

For this, I would like to thank first of all my supervisor, Wolfgang Pantleon, for the teachings from his very inspiring method, his deep understanding, guidance and continuous support.

I would like to thank my co-supervisor, Prof. Guangnan Luo, for providing the contacts and knowledge at the producer AT&M for securing some of the materials object of this study, his cooperation and guidance, the possibilities offered during this doctorate and the support and hospitality during my external stay at the CASIPP.

I would also like to thank Prof. Xiang Zan and Ph.D student Kang Wang for the interesting discussions and work performed together on tungsten during my external stay in China and nevertheless for their great hospitality.

A thanks to Euratom research and training programme for funding my Ph.D. programme.

I wish to acknowledge the incredible support of all technicians and colleagues at the Materials and Surface Eng. Section of the Mechanical Engineering Dept. at DTU, Adam Fuller and Alice Bastos da Silva Fanta from DTU NanoLab for their support while performing electron microscopy and Thomas Willum Hansen for his support on computing.

A thank to all the master students I have worked with in this project, with which I shared parts of the experimental work while they were completing their master thesis projects, in particular to Maximillian Fuhr, which conducted extensive work on the preliminary grain boundary spacing analysis, reported in this thesis.

A huge thank you to all my office mates for their great company and support throughout the Ph.D.

Finally, I need to acknowledge the immense support of my family being my sister and my mother, two outstanding women to which I owe everything in my life.

Kongens Lyngby, Februrary 2021,
Umberto Maria Ciucani.

Preface

This thesis is submitted in partial fulfillment of the requirements for the Ph.D. degree at the Technical University of Denmark.

This research work was mainly done at DTU Mechanical Engineering Dept. (Section of Materials and Surface Engineering) during the period December 2016 – September 2020. This work was supervised by Prof. MSO Wolfgang Pantleon and co-supervised by Prof. Guang-Nan Luo.

This work has been carried out partially within the framework of the EUROfusion Consortium and has received funding from the Euratom research and training programme 2014-2018 and 2019-2020 under grant agreement No. 633053. The views and opinions expressed herein do not necessarily reflect those of the European Commission.

Kongens Lyngby, February 2021,

Umberto Maria Ciucani.

List of Publications

The following list of papers and manuscripts constitute part of this thesis:

Thin Plates:

(Subchapters 4.1 and 4.2)

U.M. Ciucani, A. Thum, C. Devos, W. Pantleon, Isothermal annealing of thin rolled tungsten plates in the temperature range from 1300 °C to 1400 °C, *Nucl. Mater. Energy*, **15** (2018), 128-34.

U.M. Ciucani, A. Thum, C. Devos, W. Pantleon, Recovery and recrystallization kinetics of differently rolled, thin tungsten plates in the temperature range from 1325 °C to 1400 °C, *Nucl. Mater. Energy*, **20** (2019), 100701.

W80 Plate:

(Subchapters 5.1 and 5.2)

U.M. Ciucani, W. Pantleon, Stagnant recrystallization in warm-rolled tungsten in the temperature range from 1150 °C to 1300 °C, *Fusion Eng. Des.*, **146** (2019) 814–817.

U.M. Ciucani, W. Pantleon, Microstructural path investigation into stagnation of recrystallization in warm-rolled tungsten**,** under finalisation ahead of submission, 2021.

Tungsten fibre-reinforced tungsten composites:

(Sections 6.1.2.2 and 6.2.1)

U.M. Ciucani, L. Haus, H. Gietl, J. Riesch, and W. Pantleon, Microstructural evolution in single tungsten fiber-reinforced tungsten composites during annealing: recrystallization and abnormal grain growth, *Journal of Nucl. Mat.*, **543** (2021), 152579.

U.M. Ciucani, L. Haus, H. Gietl, J. Riesch, and W. Pantleon, Cyclic ring fiber textures in single tungsten fiber-reinforced tungsten composites, *submitted and review to 2021 IOP Conf. Ser.: Mater. Sci. Eng.*, (2021).

The following papers and manuscripts have been co-authored during the course of the Ph.D. but do not constitute a part of this thesis (available for consultation in the Appendix):

K. Wang, H. Sun, X. Zan, U.M. Ciucani, W. Pantleon, L. Luo, Y. Wu, Evolution of microstructure and texture of moderately warm-rolled pure tungsten during annealing at 1300 °C, *J. Nucl. Mater.*, **540** (2020), 152412.

G.G.B. Zaffaroni, O.V. Mishin, U.M. Ciucani, C. Gundlach, J.H. Nordlien, and R. Ambat, Characterization of high frequency welded aluminium microfin tube for heat exchangers, *Mater. Charact.*, **173** (2021), 110939.

D. Tarras Madsen, U.M. Ciucani, A. Hoffmann, W. Pantleon, Strong rotated cube textures in thin cold-rolled potassium-doped tungsten sheets during annealing up to 1300 °C, *submitted and review to 2021 IOP Conf. Ser.: Mater. Sci. Eng.*, (2021).

Table of Contents

Abstract 6
Acknowledgements 10
Preface 12
List of Publications 14
Table of Contents 18
List of Figures and Illustrations 20
List of Abbreviations 30
Chapter 1. Introduction 34
Chapter 2. Background 38
  2.1 The historical background 38
  2.2 The physics 42
  2.3 Technology and demands 45
  2.4 Needs: the base material, Tungsten 47
    2.4.1 Production route 48
    2.4.2 Mechanical properties 49
  2.5 The ongoing effort on tungsten as PFM 53
  2.6 Designing solutions: Recent developments in tungsten R&D against recrystallization 55
  2.7 As-deformed condition: microstructure and texture 60
  2.8 Microstructure and annealing phenomena 63
    2.8.1 Recovery 64
    2.8.2 Modelling of recovery: Kuhlmann kinetics 66
    2.8.3 Recrystallization 68
  2.9 Scanning Electron Microscopy 84
  2.10 Tools, the texture 89
    2.10.1 Crystallography 89
    2.10.2 Representation of orientations and texture 92
Chapter 3. Materials, Methods and tools 104
  3.1 Materials 104
  3.2 Oxidation 106
  3.3 Methods 107
    3.3.1 Metallographic Preparation 107
    3.3.2 Annealing 108

3.3.3 Vickers Hardness Testing 109

3.3.4 Electron BackScatter Diffraction (EBSD) 109

3.3.5 Recrystallized Fraction Evaluation 111

3.3.6 Calculation of Stored Energies 112

Chapter 4. Thin Plates 114

4.1 Isothermal annealing of this rolled tungsten plates in the temperature range from 1300 °C to 1400 °C 114

4.2 Recovery and recrystallization kinetics of differently rolled, thin tungsten plates in the temperature range from 1325 °C to 1400 °C 124

Chapter 5. W80 Plate 136

5.1 Stagnant recrystallization in warm-rolled tungsten in the temperature range 1150 °C to 1300 °C 136

5.2 Microstructural path investigation into stagnation of recrystallization in warm-rolled tungsten 142

Chapter 6. Tungsten fiber-reinforced tungsten composite (W_fW) 188

6.1 As-received condition 188

6.1.1 Topography 188

6.1.2 Cyclic <100> ring fiber texture in CVD tungsten 191

6.1.3 Cyclic ring fiber texture in single tungsten fiber-reinforced tungsten composite 196

6.1.4 Twin boundaries in CVD tungsten 204

6.1.5 Cyclic <110> fiber texture in tungsten wires 207

6.2 Annealed Condition 211

6.2.1 Microstructural evolution in single tungsten fiber-reinforced tungsten composites during annealing: recrystallization and abnormal grain growth 212

6.2.2 Further analysis 225

Chapter 7. Conclusions and Outlook 231

Bibliography 236

List of Figures and Illustrations

Figure 1:Cover page of TIME, the weekly news magazine, November 1952............................. 38

Figure 2: Lyman Spitzer and his Model-A Stellarator at Princeton University (USA) in 1951... 39

Figure 3: ITER first ever logo: a radiating Sun surrounded by the flags of the first partners...... 41

Figure 4: The ITER Agreement is signed at the Elysée Palace in Paris on 21 November 2006.. 41

Figure 5: The energy equivalent of the mass defect of the elements plotted as a function of their atomic mass.The energy release in the fusion or fission processes is equal to the difference in mass of the reactants [2]. 42

Figure 6: The overall fusion reaction process in fusion reactors as ITER. The basic fuels are deuterium and lithium (breeding), the waste product is helium [2].. 43

Figure 7: A cut-away of the ITER fusion reactor [2].. 44

Figure 8: The two different designs for fusion reactors. On the left, a tokamak while on the right, a stellarator. [2] 45

Figure 9: ITER vacuum vessel with the main components indicated: the divertor in the bottom and the first wall of the blanket in the remaining surrounding surfaces of the chamber [2]. 46

Figure 10: The interior of the JET torus. In the bottom of the chamber the divertor can be seen. On the internal central side, the first wall [2]. 46

Figure 11: Stress/strain curves for high purity single crystal and polycrystalline annealed tungsten from [16]... 49

Figure 12: Results of charpy impact tests on notched samples of tungsten plates. A brittle fracture can be seen at the lowest temperature and brittle to delamination fractures can be seen at 400 °C and 500°C. No fracture but only delamination takes place at higher temperatures [23].. 50

Figure 13: Temperature operation ranges for tungsten in different conditions: conventional polycrystalline tungsten after sintering, having a minimum DBTT of 600 °C circa, severely cold rolled tungsten with aminimum DBTT of -65°Cand potassium doped severely cold rolled tungsten, whose DBTT have not been yet determined. For all these designs, the maximum operational temperature is limited by the occurrence of recrystallization, and is often referred to as the recrystallization temperature. [26]. 52

Figure 14: Fracture surface of a W_f/W based bulk sample tested in a 3-point bending test. In subfigure b) the ductile deformation of the tungsten reinforcement wire toughening the matrix which contrarily exhibits brittle fracture (subfigures c) and d)) [45] 54

Figure 15: The very first tungsten coated carbon bulb from 1905 [55]. 56

Figure 16: Modern coated tungsten coils in filament bulbs [55]. 56

Figure 17: WfW composite produced by deposition of subsequent layers. In (a) a photo of the full sample is shown. (b) shows a light microscopy picture of the cross-section. Large pores in between the fibres are clearly visible as well as regions with high density. In (c) and (d) scanning electron microscopy pictures show the microstructure in detail. In (c) the star like growing grain structure of the matrix is shown. (d) shows a close up of the wire centre and its very fine grain structure. (Note that pictures (b-d) are showing details of (a) but not the same cross-sections [45]. 58

Figure 18: SEM pictures of fracture surfaces of particle reinforced tungsten (W-2wt.%Y2O3) after 3 point bend test as a function of test temperature, (a) 200 °C, (b) 250 °C, (c) 400 °C and (d) 500 °C respectively. In a) and b) show brittle fracture behaviour while for c) and d) a ductile behaviour [61]. 59

Figure 19: Microstructural defects in a deformed metal, from the smallest scale (a) to the largest (d) [66]. 60

Figure 20: Features of a deformed microstructure: (a) Cell-structure in cold-rolled copper, (b) in detail, (c) deformation bands in 12% compressed 70:30 brass, (d) deformation bands in Al-1%Mg, (e) shear bands in cold rolled copper and (f) shear bands in Al-Zn-Mg cold rolled alloy [66]. 61

Figure 21: Orientation space ($\varphi 2$=45°) section showing the relevant preferred orientation features of rolled bcc materials: the γ-fiber in blue, the α-fiber in green and the θ-fiber in red together with other relevant single orientations such as e.g. rotated cube, cube or rotated Goss. 63

Figure 22: Different consecutive stages of recovery (b-e) starting from the deformed condition (a) [66]. 65

Figure 23: Development of recrystallization within deformed copper with increasing time of annealing. Distinct uniformly shaded regions can be seen in the image which are the recrystallizing grains nucleating and growing [66]. 69

Figure 24: Schematics of the Bailey-Hirsch mechanism [66]. 71

Figure 25: a) Evolution of the fraction recrystallized with time for two different starting grain sizes. A faster kinetics is found for a smaller starting grain size. b) JMAK plots to deduce the Avrami exponents for the process [66]. 77

Figure 26: The dependence of the microstructural path parameter, q, on time and impingement behaviour (uniform, linear or planar) as from [96]. 80

Figure 27: Comparison of approximate MP model behavior of the partial path function $f\lambda rxt - \tau(Xv)$ for recrystallization of cold and hot deformed aluminum as from [96] 83

Figure 28: Structure of a scanning electron microscope (SEM) after [100]. 85

Figure 29: FEI NOVA NanoSem 600 vacuum chamber. The cone in the top center of the figure is the bottom of the column from which the electron beam exits. On the right, the SE detector identifiable by its outer acceleration grid. The specimen sits on top of a pre-tilted sample holder screwed into the stage of the microscope (bottom left). Picture from the author. 86

Figure 30: Comparison between (left) a secondary electron (SE) image providing topographical information on the sample and (right) backscattered electron image providing compositional information [100]. 86

Figure 31: Generation of topographic contrast in an image obtain by SE in an SEM due to trajectory effects [100]. 86

Figure 32: Generation of topographic contrast due to electron-number effects. More secondary electrons can escape features such as edges as compared to a flat surface [100]. 87

Figure 33: Details of the vacuum chamber showing, on the left, the EBSD detector in its retracted condition. On the right, the bottom of the column where the electron beam is focused to create the desired probe with, on its right, the Everhart-Thornley detector in charge of collecting secondary electrons for imaging purposes. Picture from the author. 88

Figure 34: EBSD pattern from copper consisting of Kikuchi bands. On the right the same pattern is indexed and zone axis poles specified by Miller indices [101] 88

Figure 35: 2D crystal structure with translation vectors represented in the form of arrows connecting what can be seen as the basis or the points of the translation lattice [25]. 89

Figure 36: Description of all the possible 14 Bravais lattices [25]. 91

Figure 37: Illustration of the preferred orientation desired in power transformer technology related products, the Goss orientation, having the normal of the (110) planes parallel to the normal direction of the specimen (ND) and the [100] direction parallel to the rolling direction (RD) [102]. 92

Figure 38: Orientation of the basal plane of an hexagonal crystal where the position of the (0001) pole is defined by the two angles α and β, although an additional pole is required for a univocal definition of the orientation, considered the remaining degree of freedom due to the rotational symmetry around the (0001) pole [78]. 95

Figure 39: Different crystal poles ([100] left, [110] centre and [111] right) of a diffracting volume within a material. More than one point is visible for each pole figure since each family of planes have more than one plane present in the crystalline system. 96

Figure 40: Inverse pole figures displaying the crystal directions within the specimen parallel to each of the specimen reference system axes, X, Y and Z. Colors describe the intensity in multiples of random density, from the highest occurring (red) to the lowest occurring (white) as illustrated in the color bar on the side. In the bottom image, blue points indicate each single measured direction for each of the specimen directions , x=RD, y=ND and z=TD. 97

Figure 41: Description of the three rotations defining the Euler Angles [104]. 98

Figure 42: The entire Euler space (in sections) where the OD of a pure bcc transition metal is displayed. In the $\varphi 2$ = 45° section, the α-and γ-fibers can be seen 103

Figure 43: Section of the euler space indicating the lowest Miller indeces ideal orientations and fibers [104]. 103

Figure 44: Cutting plan for the W80 plate. 105

Figure 45: Encapsulated specimen ahead of ampoule enclosure. 107

Figure 46: The FEI - NOVA NanoSem 600 used to record all orientation data for this project. 110

Figure 47: Detail of an orientation map of a partially recrystallized sample (W80) showing, colored in dark red, the recrystallized grains, the recovered regions (rcloc regions) ahead of the recrystallized grains colored depending on their orientation - via the inverse pole figure in the inset - according to the ND of the plate, the boundaries between the recrystllized grains (rxrx boundaries) in light brown and all the boundaries (misorientation > 2°) belonging to the rcloc region, in black 111

Figure 48: Cross section of W_f/W: Secondary electron image of the wire region and the CVD region in its immediate vicinity possessing a fine microstructure. The artificial colors are created by the Argus technique that can be found in the BRUKER Esprit 2.1 software. 189

Figure 49: Cross section of W_f/W: lower magnification secondary electron image of the wire region and the CVD region in its immediate vicinity, showing the radially growing grains whose thickness increases with increasing distance from the interface with the wire. In the red circle, knife-like grains (later referred to as triangular grains) interrupting the growth of these radially growing grains. The artificial colors are created by the Argus technique that can be found in the BRUKER Esprit 2.1 software. 190

Figure 50: Secondary electron image showing in detail of the triangular grains within radially growing grains. 190

Figure 51: Orientation maps of the W_f/W as in Figure 51 are showing the crystallographic directions along the (a) the x-direction, (b) the y-direction and (c) the z-direction colored according to the inset of Figure 51b; the z-direction is normal to the surface mapped, the x- and y-direction correspond to the horizontal and vertical direction in the map 192

Figure 52: 100, 110 and 111 pole figures of the CVD region of the as-received condition in Figure 51, with the horizontal direction indicated by x the vertical direction by y and the transverse direction lying at the center of the pole figure. The pole densities are given in multiples of random distribution.. 192

Figure 53: Orientation map of the W_f/W showing the crystallographic directions along the radial direction colored according to the inset. A complete predominance of the [100] directions is visible together with small areas characterized by a light blue to blue color. 193

Figure 54: 100, 110 and 111 pole figures of the CVD region the W_f/W as-received condition in Figure 51, using the alternative cylindrical reference coordinate system with the radial direction indicated by r and the azimuthal direction indicated by φ. The pole densities are given in multiples of random distribution.. 193

Figure 55: Magnified region of the orientation map in Figure 53 showing a region filled with many light blue colored grains consisting in grains separated from the preferential [100] radially growing grains by twin boundaries shown in blue in b) boundary map of the same region of Figure 55a with points shown as numbers indicating the points of origin of the diffraction patterns in Figure 56. In black, any other boundary in the map. The colors indicate the crystallographic direction along the radial direction colored according to the inset. 204

Figure 56: EBSD patterns from the points indicated in Figure 55 as a) 1, 2, and b) 7, 8 and 9. The identical pattern found upon mirroring of the patterns implies a twin boundary is dividing the triangular grains from the [100] preferential direction radially growing grains.. 206

Figure 57: Orientation map of the W_f/W region of the wire only as from Figure 48, colored according to the z-direction, using the color scheme as in the inset... 207

Figure 58:100, 110 and 111 pole figures from the orientations of the wire region only (from the orientation map in Figure 57) onto the specimen reference coordinate system having the horizontal direction indicated by x and the vertical direction direction indicated by y. The pole densities are given in multiples of random distribution. 208

Figure 59: 100, 110 and 111 pole figures from the orientations in the wire region only (from the orientation map in Figure 57) onto the specimen reference coordinate system having the horizontal direction indicated by x and the vertical direction direction indicated by y. The pole densities are given in multiples of random distribution. The pole densities below 3.5 are highlighted 208

Figure 60: Orientation map of the W_f/W region of the wire and the closest regions of the CVD matrix surrounding the wire as from Figure 48, colored according to the radial direction as in Figure 53, using the color scheme as in the inset. 209

Figure 61: Pole figures for the wire region only in orientation map in Figure 60 using the alternative cylindrical reference coordinate system with the radial direction indicated by r and the azimuthal direction indicated by φ 210

Figure 62: Pole figures for the wire region only in orientation map in Figure 60 using the cylindrical reference coordinate system with the radial direction indicated by r and the azimuthal direction indicated by φ, highlighting densities between 1 and 3.5 random. The stars indicate the points in the pole figures where the higher pole densities for an ideal {110}<110> orientation should be. 210

Figure 63: Orientation map in the vicinity of the drawn wire of the single W_f/W without any interlayer after annealing at 1400 °C for seven days. The blue circle highlights the inner, inner LGZ radius, in cyan the outer, inner LGZ radius and in pink the outer, outer LGZ radius. The colors are showing the crystallographic directions along the z-direction colored according to the inset. 226

Figure 64: Dependence of the boundary spacing on the radius to determine the ranges of the inner and outer LGZs. 226

Figure 65: Positions and widths of the large grain zones for the single W_f/W upon annealing at 1400 °C from 6 hours to 28 days. 228

List of Abbreviations

LAB	Low Angle Boundaries
HAB	High angle Boundaries
PFM	Plasma Facing Material
W_f**W**	Tungsten fibre-reinforced tungsten composite material
TP(s)	Thin Plate(s)
W80	80% reduction warm-rolled pure tungsten plates
RT	Room Temperature
DBTT	Ductile to brittle transition temperature
PM	Powder Metallurgy
CVD	Chemical Vapour Deposition
MP	Microstructural Path Methodology
SEM	Scanning Electron Microscope
TEM	Transmission Electron Microscope
EBSD	Electron Backscatter Diffraction
LOM	Light Optical Microscope
EBSP	Electron Backscatter Diffraction Pattern
BSE	Backscattered Electrons
SE	Secondary Electrons
Z	Atomic number
RD	Rolling Direction
ND	Normal Direction
TD	Transverse Direction

OD	Orientation Distribution
ODF	Orientation Distribution Function
W_f/**W**	Tungsten fibre-reinforced tungsten composite material
$W_f/Er_2O_3/W$	Erbia interlayered tungsten fibre-reinforced tungsten composite material
$W_f/Y_2O_3/W$	Yttria interlayered tungsten fibre-reinforced tungsten composite material
s	Seconds
m	Minutes
h	Hours
d	Days
IB	Inner boundaries
rc regions	Recovered regions in the microstructure
rx regions	Recrystallized regions in the microstructure
rcloc regions	Recovered regions neighbouring recrystallized regions
rcrx boundaries	Boundaries between the recovered and the recrystallized regions
rcrc boundaries	Boundaries separating recovered regions only
rxrx boundaries	Boudnaries between recrystallized grains only
rcloc rcrc boundaries	Boundaries between the rcloc regions and the rc regions only

Chapter 1. Introduction

Tungsten is at the moment being considered as the best candidate for application within fusion reactors as plasma-facing material (PFM). In order to perform its job in such an environment, the smallest possible induced radioactivity together with resisting the enormous heat radiating from the plasma is demanded. Such high temperatures trigger microstructural rearrangement phenomena, recovery and recrystallization, deteriorating tungsten's mechanical properties and ultimately leading to structural failure.

Recovery and recrystallization are competing mechanisms driven by energy minimization acting on the microstructure of a deformed material. A metal undergoing recovery reorganizes its structure into an energetically more stable configuration via dislocation motion and annihilation resulting in a smaller average dislocation density within the material and a higher average misorientation across Low Angle Boundaries (LABs). Recrystallization instead, is the process of development of defect-free grains within the material, nucleating and then growing via migration of High Angle Boundary (HABs) driven by the higher energy content ahead of the migrating boundary, the deformed or recovered matrix.

While recovery has the effect of lowering the dislocation density of tungsten which is ultimately responsible for tungsten's strength properties, recrystallization instead is far more dangerous an lead to structural failure of tungsten when used as PFM in fusion reactors. Higher and higher operation temperatures in fusion reactors are sought to achieve commercial feasibility of the technology, yet recrystallization limits such an increase in temperatures, due to the fact the higher the temperature the most likely and faster the recrystallization will take place. As a result, a better understanding of the physics of recrystallization is of paramount importance to find a strategy to limit or prevent it and achieve commercial feasibility of such a technology, renewable, radioactive-risk free energy.

Recovery and recrystallization have so far been studied in depth for metals such as e.g. aluminum, copper or iron but not for tungsten. Only in the last 10 years efforts have been put in understanding recrystallization behavior in refractory metals, such as molybdenum or tungsten. These are the circumstances driving this work on the thermal stability of tungsten. The aim of this thesis is the quantification and characterization of the phenomena of recovery and recrystallization in tungsten on the long term via mechanical and microstructural characterization.

Mechanical characterization pivoted on hardness testing whose results were used to determine the extent of the processes and to be described by theoretical models to better understand their kinetics. Light optical and electron microscopy allowed a deepened look into the microstructure to verify (or counter) the findings from the mechanical characterization and to suggest new hypothesis or interpretations of the phenomena based on features such as, e.g. texture or defect densities.

Examined materials consisted in warm and mixed warm-cold rolled plates, together with newly designed tungsten fibres-reinforced tungsten composite materials (W_fW). The former afor-mentioned design of tungsten, in the form of plates, is a commercially widespread product for which the production route is well known. Though the thermal stability of rolled tungsten products is yet to be fully understood, and calls for additional research, which is mainly the topic of this work. The composite design of tungsten instead, that of the W_fW, is relatively modern and knowledge of the microstructural features of such a composite as a whole, are yet to be fully known. Thermally activated phenomena for this composite are even less known and in this work they will be assessed, at least to a preliminary level. The work reported in this thesis aims at further improving our understanding of the microstructure and its evolution of tungsten, in different designs, within a high temperature environment.

The historical background in which fusion based energy was born and research ramped up in years, the physics of the process of fusion, the choice, production route and mechanical properties of tungsten in its annealed or deformed state, the state of the art knowledge and research on the material, a detailed description of the afore-mentioned annealing processes and their theoretical interpretation and modeling, an introduction on scanning electron microscopy, the technique used to analyze the texture and texture representation methods are described in Chapter 2. Detailed information on the materials studied, the experimental practice, the instrumentation used and a description on the treatment of the microstructural features are outlined in Chapter 3. The results and the discussion of the present work of this thesis is reported in separate chapters - in the form of published papers and unpublished manuscripts - according to the materials studied: a study on 4 warm-cold rolled thin plates (TPs) is reported in Chapter 4, that on a warm-rolled 80% reduced in thickness tungsten plate (W80) is reported in Chapter 5, that on the W_fW in Chapter 6. A summary with the conclusions and an outlook is in Chapter 7.

Chapter 2. Background

2.1 The historical background

Realisation of energy through nuclear power is the founding core of the European Atomic Energy Community (Euratom) since the Rome Treaty (European Economic Community Treaty), 1957, the beginning of the European Union as we see it today. This inclination towards the development of nuclear fusion technology though, stems from wider sociological, economical and political circumstances.

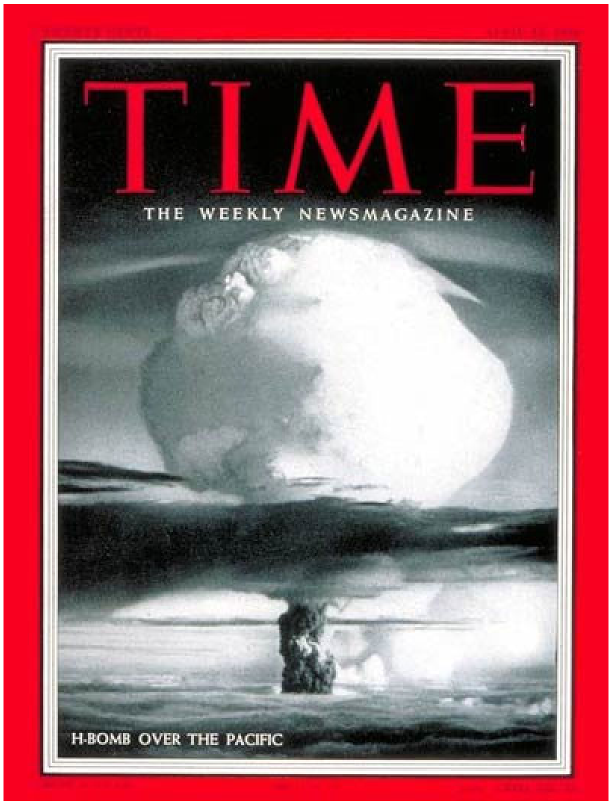

Figure 1:Cover page of TIME, the weekly news magazine, November 1952.

Only a few years have passed since the summer of 1945, the end of the second world war. In the mean time, the USSR balanced its strategic capabilities to allow for a new equilibrium with the “West”, advances in the field of nuclear physics and technology allowed to build and deploy technologically finer and more powerful bombs: H-bombs (Figure 1). Competition in improving those mass destruction weapons in the following years unavoidably brought together better understanding and handling of nuclear power. The wake of an after-war renaissance for the entire world together with a new balanced order set the way for an unwinding of the relationships between the East and the West. It was the beginning of a new era of fruitful collaboration between the two blocks: "the peaceful coexistence between states with differing political and social systems" [1].

In the following years visits from each of the two blocks were arranged to easen tensions, promote trade and regulate nuclear energy proliferation: an agreement on the latter was of utmost importance. As a result, in 1958, the "Second United Nations International Conference on the Peaceful Uses of Atomic Energy" marked the end of maintaining research in the field of nuclear physics classified between the major powers of the time: UK, US and USSR [2]. As years passed, nuclear weapon dismantlement progressed together with research in achieving nuclear power for peaceful purposes.

Research into fusion for energy started approximately at the end of the second world war. The idea of a reactor for fusion was first developed (and patented) by Sir George Paget Thomson and Moses Blackman, at the United Kingdom Atomic Energy Authority in 1946. The first fusion reactions were those related to weapons but, as history proves, advances in warfare bring along advances in science and experimental devices started to “sprout”, at first in the US. Declassified in 1958 at the “Atoms for Peace” Conference, the Sherwood Project was the first US programme in which several institutions converged this effort to promote a better understanding of fusion power; the device was a so-called Stellarator (as shown in Figure 2), invented by Lyman Spitzer in 1951 at Princeton University, one of the partners of the project. In the meanwhile, in the USSR at the Kurchatov Institute the First tokamak, T-1, was being built, beginning operations in 1958 [3].

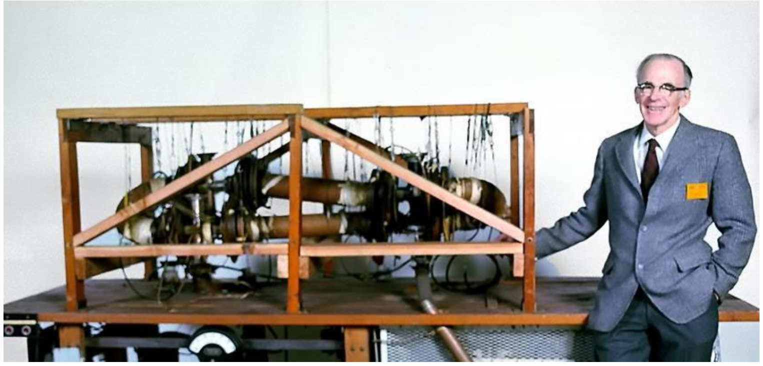

Figure 2: Lyman Spitzer and his Model-A Stellarator at Princeton University (USA) in 1951.

These two fusion reactor concepts using magnetic confinement were those on which all the following major research devices were built upon in the following years. Throughout the years, several different successful experiments were conducted on newer and newer reactors, just to name some of the most important ones, the Joint European Torus (JET) in Culham, UK, the ASDEX at the Max-Planck-Institute for Plasma Physics in Garching, and Wendelstein (7-A and 7-X, Stellarators) at the same institute in Greifswald, Germany, the DIII-D in San Diego, US, NSTX (National Spherical Torus Experiment) and the Japanese JT-60.

The tokamak, as reactor design, have been chosen over stellarators for future power devices, the reason being tokamaks are more promising, in terms of commercially viable energy production than stellarators which, albeit being capable of providing a much more constant plasma reaction, are far more complicated and more demanding to scale up to achieve the same energy outputs of tokamaks. The main purpose of stellarators is now focusing on research on specific aspects of fusion technology.

There are great expectations for the future years to produce free, radioactive-free, abundant energy, as the achievement of commercially viable on-grid electricity from fusion becomes closer and closer both thanks to advances in the technology and in the science of the process. Along this roadmap towards the achievement of fusion energy, now is the moment of ITER. Being built in France, to be completed in 2025, ITER is set to become the largest experimental tokamak in the world aiming at providing the international community the ultimate experimental facility for research purposes: demonstrating feasibility of fusion on a power-plant scale with 500 MW fusion power. What makes a difference with the past is its size: ITER had been designed to have the same scale as future fusion energy plants designed for energy production and delivery of electricity. ITER is in fact the last experimental step ahead of DEMO (and the Chinese CFETR): the fusion based DEMOnstration power plant in charge of demonstrating the readiness of commercialisation of the technology. ITER foundations are 30 years old; the actual idea of collaborating for such a project was first developed at the 1985 Geneva Summit, four years ahead of the end of the Cold War era. The two superpowers which in the former years have scientifically competed against each other then gradually increased collaboration on fusion, the USSR and US, and agreed on establishing this collaborative international programme. The following year the agreement was signed: EU, Japan, US and USSR committed on pursuing the project, conceptualised in 1988 and finalised in 2001 (the flags of these countries formed the first ever ITER logo as in Figure 3). In these years, other countries joined the project: e.g. China in 2003 and India in 2005. At this stage only a formality was missing, the institution of an entity in charge of coordinating the project: in 2007 the ITER Organisation was founded (with the agreement signed in Nov. 2006 in Figure 4) and in 2010 construction started. Now, over 30 countries are collaborating to this project.

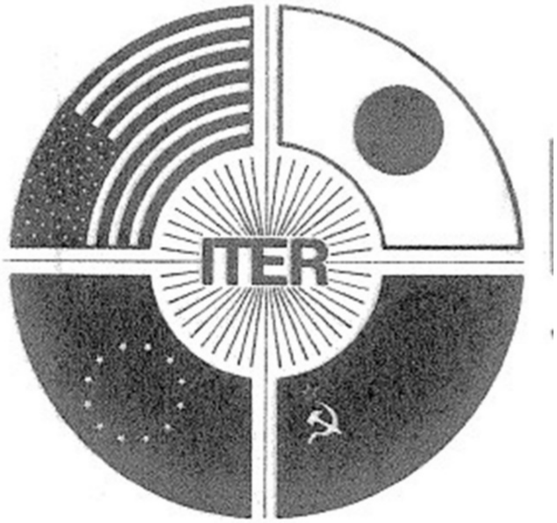

Figure 3: ITER first ever logo: a radiating Sun surrounded by the flags of the first partners.

Figure 4: The ITER Agreement is signed at the Elysée Palace in Paris on 21 November 2006.

During the years, around a hundred of tokamaks were built and operated around the world paving the way to ITER. The main challenge in recent years is in the reactor power handling. Efforts are converging to allow operation at energetically meaningful, progressively higher and higher temperatures to ensure high energy yields for times that are sufficiently long for the commercial feasibilities to be satisfied (in particular the reduction of the costs in exchanging the depleted PFMs after operation less frequently) [4].

2.2 The physics

What nuclear fusion aims at is to produce energy via controlled fusion of hydrogen isotopes, namely deuterium and tritium. The excess energy of the process is enormous (per atom, much larger than that of fission of uranium to iron, as shown in Figure 5) and arises from the difference in mass between the products and the reactants.

$$ {}^{2}_{1}H + {}^{3}_{1}H \rightarrow {}^{4}_{2}He\ (3{,}517\ MeV) + {}^{1}_{0}n\ (14{,}069\ MeV) \qquad (1) $$

The fundamental difference with respect to the traditional process of fission is in fuel availability. Fission fuels amount worldwide to 6.1 M tonnes (2018 estimate) which correspond to an availability of fission based nuclear energy for the next 130 years, if no commercially viable new technologies reducing the cost uranium production from alternative resources become available and consumption of uranium keeps steady, which is not the case, considering the constant annual increase in the nuclear reactors and energy demand worldwide [5].

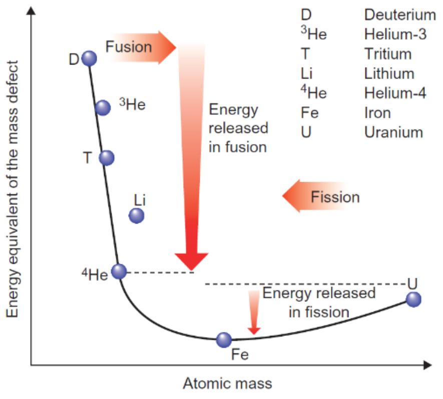
Energy equivalent of the mass defect
Atomic mass
Fusion
D
^{3}He
T
Li
^{4}He
Fe
U
Energy released in fusion
Fission
Energy released in fission
D Deuterium
^{3}He Helium-3
T Tritium
Li Lithium
^{4}He Helium-4
Fe Iron
U Uranium

Figure 5: The energy equivalent of the mass defect of the elements plotted as a function of their atomic mass.The energy release in the fusion or fission processes is equal to the difference in mass of the reactants [2].

Deuterium instead, is readily available in seawater and extraction technologies are already present. The need of tritium, present in a much lower concentration in nature, will be accommodated by reactions in the reactor via a so-called tritium-breeding process: free neutrons from the plasma react with lithium in salts in the blanket to form helium and tritium. The schematics of the fusion reaction process in DT-reactors is shown in Figure 6.

$$ {}^{6}_{3}Li + {}^{1}_{0}n \rightarrow {}^{4}_{2}He + {}^{3}_{1}H \tag{2} $$

$$ {}^{7}_{3}Li + {}^{1}_{0}n \rightarrow {}^{4}_{2}He + {}^{3}_{1}H + {}^{1}_{0}n \tag{3} $$

In order for the fusion reaction to take place, matter have to be in the plasma state, a condition in which, differently from the three other states, gaseous, liquid and solid, nuclei and electrons are bound to each other: nuclei and electrons are separated and coexist in the magnetically confined, reacting plasma mass at a temperature of the order of magnitude of millions °C.

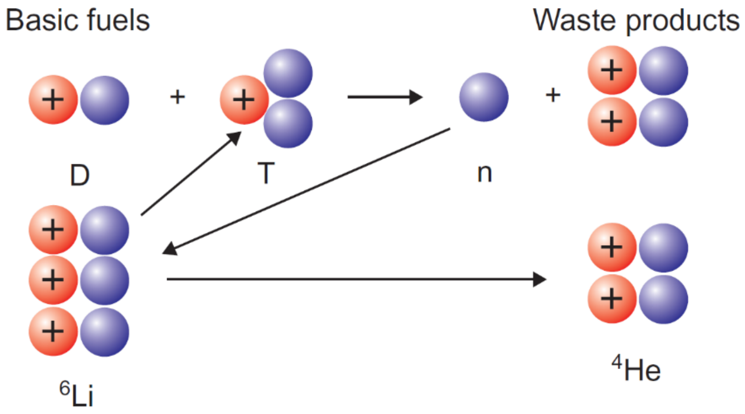

Figure 6: The overall fusion reaction process in fusion reactors as ITER. The basic fuels are deuterium and lithium (breeding), the waste product is helium [2].

Holding this temperature requires an enormous amount of energy. This is energy is at the start provided entirely by neutral beams (beams of high energy uncharged particles transferring energy to the plasma by collision) and high-frequency electromagnetic waves sources, and later, also by the fusion process itself. These two large amounts of energy, the energy put in to heat up or maintain the temperature of the plasma on the appropriate level and the output energy yield of the reaction, define a property of such a reactor, the fusion energy gain factor, Q, of such a reactor which is equal to the ratio between these two. While in the past years, research aimed at reaching breakeven, e.g. $Q = 1$, larger tokamaks as ITER, depicted in Figure 7, aim at $Q = 10$.

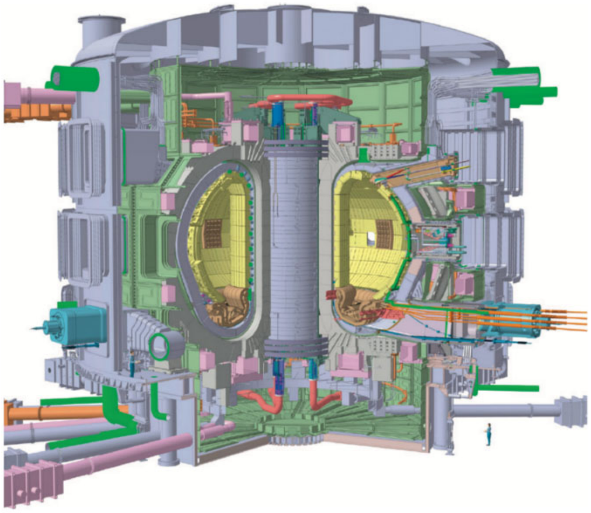

Figure 7: A cut-away of the ITER fusion reactor [2]

Clearly the larger Q the higher the economic viability of the process. ITER is aiming at producing 500 MW of power out of a maximum of 50 MW of power available to maintain the operating conditions and to compensate for process losses and initial heating of the plasma.

Fission based nuclear energy requires a very complex management of radioactivity of both the fuel and its products after fission. In this concern, fusion based nuclear energy is considered the activation-free alternative to fission. Though, activation is not completely avoided but rather reduced to much safer levels. As an example, irradiation of the PFMs of the reactor brings along activation of these materials. Still, radioactivity in the PFMs and the decay times of the activated materials are within relatively reasonable limits. This allows easier handling and potential reprocessing of these materials, after time windows that are in between 1 to 2 orders of magnitude smaller than those needed for conventional fission fuels to radioactively decay to safe levels.

2.3 Technology and demands

Main research activity in the field takes place using two different reactor designs: stellarators and tokamaks. Tokamaks have been preferred over stellarators because of the higher Q they are capable to achieve. A tokamak is a reactor in which the plasma is confined in a toroidal-like shape by three different magnetic field coils, of toroidal or poloidal kind (Figure 8).

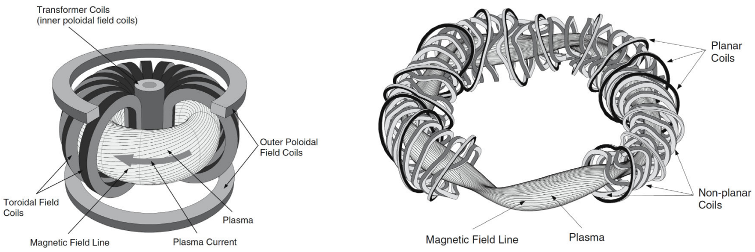
Transformer Coils
(inner poloidal field coils)
Outer Poloidal
Field Coils
Toroidal Field
Coils
Plasma
Magnetic Field Line
Plasma Current
Planar
Coils
Non-planar
Coils
Magnetic Field Line
Plasma

Figure 8: The two different designs for fusion reactors. On the left, a tokamak while on the right, a stellarator. [2]

Plasma operations require the chamber in which the plasma is confined, to be completely isolated and always free of impurities that can potentially alter or disrupt the fusion process. Hence, the entire process is run under vacuum conditions. The environment in the vacuum chamber is characterized by extremely harsh heat and particle bombardment condition. The walls enclosing it are efficiently designed to be in charge of extracting the heat of the reaction, take care of the particle fluxes and protecting the whole instrumentation and structure lying just behind them. Particles in play are of two different kind, charged and uncharged. The latter, mainly neutrons, are released from the plasma in every direction, therefore hitting every surface surrounding the torus. The charged ones are continuously kept in the torus unless they exit at the bottom (or top regions according to the reactor considered), - where flux lines are not closed and escape of charged particles from the plasma is possible – via the so-called divertor, the exhaust system of the reactor in charge of maintaining plasma purity [2].

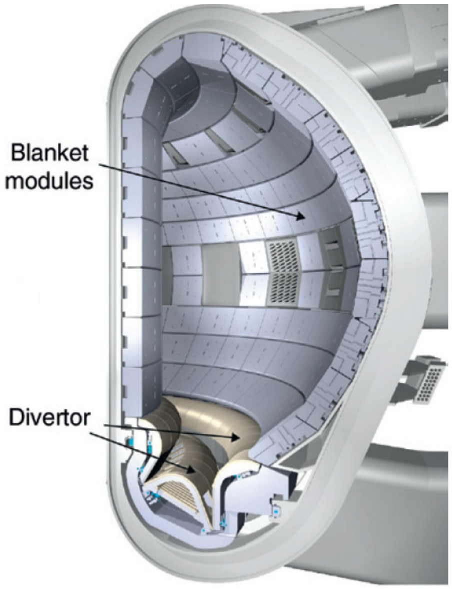

Figure 9: ITER vacuum vessel with the main components indicated: the divertor in the bottom and the first wall of the blanket in the remaining surrounding surfaces of the chamber [2].

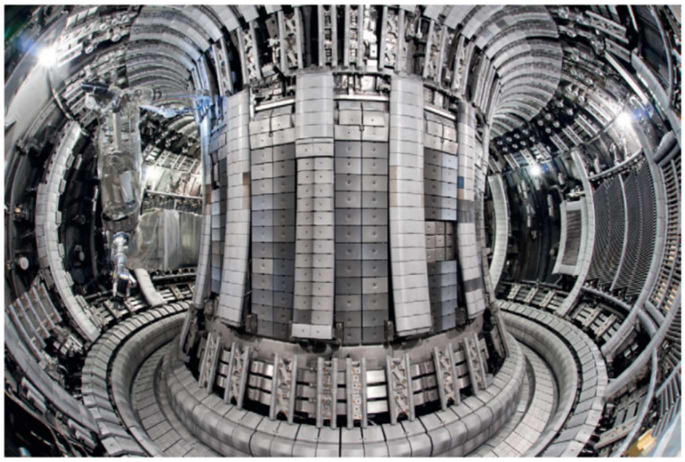

Figure 10: The interior of the JET torus. In the bottom of the chamber the divertor can be seen. On the internal central side, the first wall [2].

The surfaces of the vacuum chamber are of two kind: the divertor - consisting in a system of panels arranged in three parts, the central dome and the two lateral sides, located in the bottom (towards the ground surface) of the reactor (in DEMO there will also be one in the top) - and the first wall, consisting of all the remaining surface surrounding the torus (as depicted in Figure 9 and Figure 10). The first wall is mainly hit by neutrons and is exposed to less harsh thermomechanical conditions than the divertor. An important aspect of the extreme conditions on the armour is that of thermal radiation: ranging from 2 to 7 MW/m^2 to a maximum of 10 to 20 MW/m^2, for the first wall and the divertor respectively [6]. Second, a reacting plasma brings along mass interaction with the armour. Charged particles as the α-particles (exiting the plasma in the bottom region and hitting the divertor) or neutral atoms exit elsewhere and impact with the armour [7]. Together with neutrons, these particles are discharging large amounts of kinetic energy right into the material, leading to erosion (sputtering) and, if bombardment is substantial, subsequent pollution of the reacting plasma by species belonging to the armour material.

Nneutron bombardment lead to subsequent activation of the armour material and radiation damage. These extreme operating conditions imply outstanding demands.

2.4 Needs: the base material, Tungsten

So far, armour materials that been tested include tungsten-based, carbon-based and low atomic number materials such as berillium [8]. The choice for PFMs changed throughout years from SiC in the 1980s [9] to steel, tungsten-coated or not, to tungsten-based alloys or liquid flowing metals such as Li, Ga, Sn, Sn–Li [10], to bulk or particle-reinforced tungsten in the last decade [11]. Tungsten (W) is now the candidate base material for application both as divertor and first wall for future studies and implementation in DEMO, considering its capabilities, primarily due to cost reduction strategies [12], [13]. Tungsten is a very dense material (19.25 g/cm^3), with the lowest vapour pressure of all metals and is chemically inert at room temperature (RT). Its outstanding properties are related to its thermal and mechanical behaviour: the highest melting temperature of all metals (3695 K), a relatively low thermal expansion coefficient ($\alpha_l = 4.32 \cdot 10^{-6} \mathrm{K}^{-1}$), high yield strength, a high Young's modulus and a high thermal conductivity (164 W/m K at RT) even at high temperatures (98 W/m K at 2000 K) [14]. In a fusion reactor, its behaviour when exposed to neutron, hydrogen and helium bombardment must live up to the expectations of an uninterrupted service of at least 2 years: low erosion and retention make it a very good candidate in this concern [15]. Thanks to its thermal properties, tungsten has many applications: used as crucible material, as a high-temperature functional material as the filament in the light bulbs up until 2000, combined with lanthanum oxide as an ion source in scanning electron microscopes, in welding applications as a non-disposable welding electrode and last but not the least, in combination with carbon as WC, in tooling equipment.

2.4.1 Production route

The extremely high melting temperature of tungsten makes it impossible to obtain any part manufactured via the classic route of casting. The only process through which bulk tungsten parts can be manufactured is that of powder metallurgy. Tungsten occurs in nature in oxidized forms together with iron and manganese (Wolframite - $(Fe,Mn)WO_4$) or calcium (Scheelite – $CaWO_4$) [16]. Before entering the powder metallurgy route tungsten containing species need to be reduced to pure W powder: from its ore, e.g. Scheelite, it is reduced to the oxide via HCl according to the following reaction:

$$\mathrm{CaWO_4 + 2HCl \rightarrow WO_3 + CaCl_2 + H_2O} \tag{4}$$

and then further reduced to its pure form in a hydrogen atmosphere at temperatures of 550-800 °C:

$$\mathrm{WO_3 + 3H_2 \rightarrow W + 3H_2O} \tag{5}$$

Then it is compacted and finally sintered into ingot shapes (for further mechanical working) via Hot or Cold Isostatic Pressing (HIP/CIP). In such a process, pressure is applied isostatically to the compact the powder (approx. 200 MPa for HIP and 400 MPa for CIP). The green body formed in this manner is then heated up to temperatures as high as 2200 °C in a hydrogen atmosphere to sinter the powder [17]. The final product consist of a nearly completely dense material (usually approx. 98% density or more).

Powder metallurgy, as a process, is not free of consequences in terms of chemical impurities in the final product. In recent years, advances in powder metallurgy technologies made it possible to minimise this downside which is extremely important in the case of tungsten, having an extremely low solubility of impurities either as substitutionals or interstitials (C, N, H as interstitials hav a solubility of less than 100 ng / g [16]). Excess of impurities is considered an intergranular destabilising agent: segregation at grain boundaries weaken the latter from which the brittle nature of tungsten poly-crystals stems from [16]. As example, in Figure 11 the stress curves for tungsten as a poly-crystal and as a single crystal are shown, at RT and 400 °C. The fragile character of tungsten as a poly-crystal can be inferred by its stress curve at RT and by comparison with the stress curves for the single crystal, which show a region where necking takes place. Working of the material though increases the grain boundary area allowing for an increased surface in which these impurities can dissolve, reducing the effect. For tungsten bulk products, this is usually performed via warm rolling: the as sintered ingot undergoes progressive reductions along its shortest direction at a temperature high enough to allow a ductile regime.

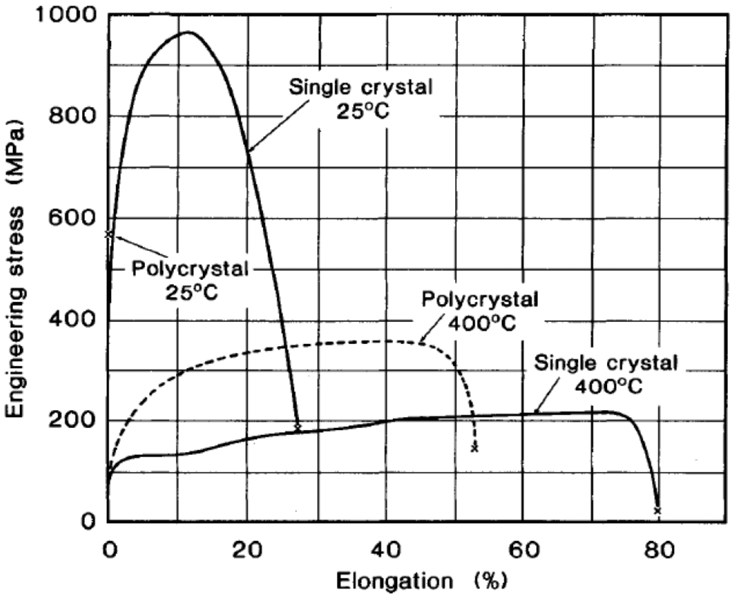

Figure 11: Stress/strain curves for high purity single crystal and polycrystalline annealed tungsten from [16].

2.4.2 Mechanical properties

When heat is provided to metallic materials, as tungsten, the deformed microstructure after cold or warm-working reorganises itself by lowering the internal stored energy (stored in the form of dislocations) via the two processes of recovery and recrystallization. While recovery does not turn tungsten's behaviour from ductile to brittle, recrystallization does, by reinstating fresh grain boundaries which get enriched with segregating impurities, acting as embrittlement agents [18]–[21]. The build up of stresses initiates a crack along HABs which then develops according to the condition of the microstructure ahead, intergranularly if recrystallized or also transgranularly if grains have grown reasonably large after grain growth [22]. An other mode of fracture have been so far identified in the transition stage between brittle and ductile. It is characterized by delamination (Figure 12), and occurs in the case of very elongated and pancake shaped grains such as in the microstructure of rolled metallic materials [23].

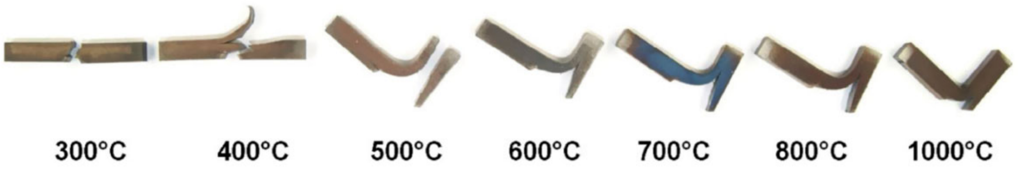

Figure 12: Results of charpy impact tests on notched samples of tungsten plates. A brittle fracture can be seen at the lowest temperature and brittle to delamination fractures can be seen at 400 °C and 500°C. No fracture but only delamination takes place at higher temperatures [23].

The mechanical properties of metals are ruled by their internal microstructure, which may on a first approximation be considered as made up by grains, their boundaries, all kind of defects and dislocations. Dislocations are responsible for plastic deformation the metal undergoes when worked: their motion (and creation) accommodate the change in shape. They can be in fact defined as “the border between the slipped and non slipped parts of the crystal” [24] undergoing deformation. Dislocations can be characterized by two parameters, the dislocation line vector and the Burgers vector, allowing to distinguish between the two types of dislocation, screw dislocations or edge dislocations. The dislocation line marks the actual location of the defect: the line in which the irregularity in the positioning of the atoms is largest. The Burgers vector is defined as the vector closing the closure failure of a path surrounding a dislocation. The Burgers vector of an edge dislocation is normal to the dislocation line while that of a screw dislocation is parallel to it. In general, dislocations have a mixed character, possessing a dislocation line and a Burgers vector neither parallel nor perpendicular, but lying at an arbitrary angle with each other.

Dislocations can move in two ways: by glide (slip) or by climb. Glide takes place when the dislocation line moves on a plane parallel to the Burgers vector, the latter when it moves perpendicularly to such a plane.

Deformation commonly take place via glide of dislocations, on crystal planes experiencing a resolved shear stress larger than a critical value. In bcc metals, such as tungsten, deformation preferentially occurs along $\langle 111 \rangle$ close-packed directions on mainly $\{110\}$ but also $\{112\}$ and

{123} (slip) planes. The combination of a slip direction and of a slip plane constitute a slip system so that e.g. tungsten deforms via glide of dislocation in the slip systems <111>{110}, <111>{112} and <111>{123}.

Deformation in bcc materials is controlled by the glide of screw dislocations. Slide of a screw dislocation requires large amounts of applied stresses, for which the most energetically favourable way of moving for a dislocation is to by the kink-pair mechanism[24]. When dislocations move they do not do it by displacement of the entire row of atoms in ahead of the dislocation. Vacancies diffuse up to the dislocation line so that only a small segment of the dislocation can progress to the next row of atoms. This segment is connect to the dislocation line in the former row of atoms by two segments called jogs. The dislocation hence moves along the slip plane thanks to these jogs which, when are both on the same slip plane are defined kinks. Nucleation of these jogs requires energy since the dislocation possessing kinks has a longer length, to which a higher energy is associated [24]. Still, the stress required to move a kink pair is much lower than the stress required to move the entire dislocation at once. The energetically most favourable movement of a dislocation is completed via the smallest possible lattice vector, which in bcc is the ½ <111>. These screw dislocations of such a Burgers vector are the ones controlling deformation in bcc metals[24]. At low or ambient temperatures, screw dislocations in bcc metals have a peculiar core structure; in order to minimise their energy, they dissociate into three partials, the 1/6 <111> : such a split core hinders their motion, energy is required to recombine them and allow motion. At higher temperatures more energy is available for the partials to recombine and this is why a (range of) temperature(s) exists above which the bcc metals start to behave in a brittle manner: the ductile to brittle transition temperature (DBTT) [25]. The origin of the brittle behavior of tungsten (even single crystals) at low temperatures, is rooted in its specific crystalline nature, namely, in the behavior of dislocations.

The DBTT of tungsten has been topic of renewed interest in research in the last 10 years given that it is one of the limiting factors for tungsten to be applied as structural material in fusion reactors. In a fusion reactor, the temperature at which these parts will be exposed is high enough to avoid brittle behaviour. On the other side, the temperature of the cooling agent might be too low for the material to behave in a ductile manner. Therefore either the cooling agent is kept at a temperature above the DBTT to prevent structural failure or a strategy to lower the DBTT shall be found. The cooler the coolant, the more heat is extracted, the more efficient the process is, the more economically viable will the technology be and hence decreasing the DBTT have become the strategy pursued. Moreover, having a temperature high enough to allow the material to be in its ductile regime might not be sufficient enough to ensure safe operation of tungsten as a structural material. In fact, if the temperature is too high, microstructural phenomena are triggered, one of which, recrystallization, sensibly alters the microstructural configuration reinstating brittleness. These circumstances define the operational window for tungsten in fusion reactors. In Figure 13 temperature ranges for tungsten-based material designs for application as PFM are reported.

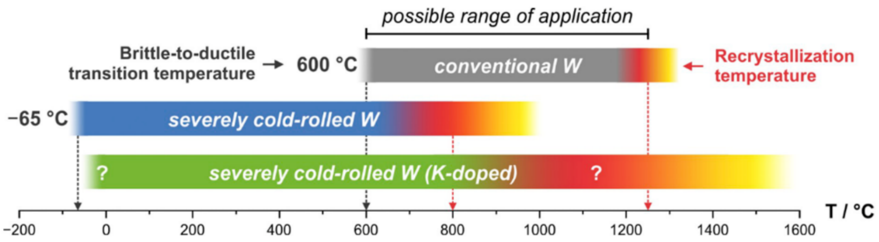

Figure 13: Temperature operation ranges for tungsten in different conditions: conventional polycrystalline tungsten after sintering, having a minimum DBTT of 600 °C circa, severely cold rolled tungsten with aminimum DBTT of -65°Cand potassium doped severely cold rolled tungsten, whose DBTT have not been yet determined. For all these designs, the maximum operational temperature is limited by the occurrence of recrystallization, and is often referred to as the recrystallization temperature. [26].

2.5 The ongoing effort on tungsten as PFM

Improving the properties of tungsten in terms of extending its operational temperature range without incurring into recrystallization or brittleness is therefore the objective of current research in the field of PFM for fusion applications. Conventional ways of doing such consist in - e.g. - additional work-hardening of the material, grain boundary refinement (against brittleness), precipitation of additional phases or solid solution strengthening, and are the conventional ways to influence the microstructure (against recrystallization), hence allowing for more severe operational conditions and enduring high temperatures while keeping the desired properties.

Pursue of solid solutions via alloying was based on the idea of altering the dislocation motion character, e.g. inhibiting partials formation or finding a way to let them move with a lower activation energy (and hence promoting the ductile behaviour at lower temperatures). Vanadium, molybdenum, titanium and tantalum alloys actually increased the DBTT or resulted in a rather brittle behaviour (see e.g. [27], [28]). Alloying demonstrated to be effective in lowering the DBTT and improving fracture toughness only for very few solutes (rhenium and iridium) that, unfortunately, are too costly to be produced in large amounts to a reasonable cost [29], [30] and suffer an increased radiation embrittlement [31]. When alloying tungsten with rhenium or iridium, an improved ductility is foreseen as the immobile property of dislocations is altered towards a mobile behaviour and ductility achieved at lower temperatures [32].

Particle reinforcement via lanthanum oxides demonstrated to be effective in increasing creep resistance and the recrystallization temperature, but did not turn into an effective solution: a fragile, brittle nature of the compound was still present [33] and the DBTT was found to be 150 K higher than that of pure tungsten [34].

Particle dispersion reinforcement using TiC or yttrium oxides demonstrated to be effective at reducing the grain sizes following the sintering process, but resulted in poor properties for application in a reactor, besides preventing the material from further deformation: thermal diffusivity and thermal conductivity decreased. Having different thermal expansion coefficients in the material [35] leads to a brittle condition of the material becoming incapable to withstand application into the fusion reactor chamber [36].

Vacuum melting and subsequent cold deforming resulted in a promising route due to reduction of detrimental alloying elements - such as carbon and oxygen - introduced in the material during processing but, again, economical unfeasibility of mass production promptly forced termination of research and development on this route since the normal powder metallurgy (PM) one is by far more convenient and potential for improvement of the materials produced in this way better sought [37]. Last but not the least, manufacturing composite materials has risen as an interesting alternative strategy to cope with tungsten's brittleness considering neither alloying nor nanostructuring by particles yield ground-breaking results so far. From the 2010s increasing attention have focused onto various new designs including W_fW [38]–[41] and laminate design [42], [43]. As an example, the rationale behind W_fW is to increase the material's resistance to failure by achieving pseudo-toughness via composite design (Figure 14) [41]. Pseudo toughness can be achieved by exploiting energy dissipation via controlled cracking and friction due to sliding of the wire itself (which is the load carrying element given its outstanding and much larger strength compared to bulk tungsten) with the surrounding matrix [44]. In order to have such an effect, the interface needs engineering: it must be strong enough to provide a congruous amount of load transfer and allow for dissipation, oppositely, it needs to be weak enough for debonding to take place [40]. To do so, a compliant coating needs to be developed.

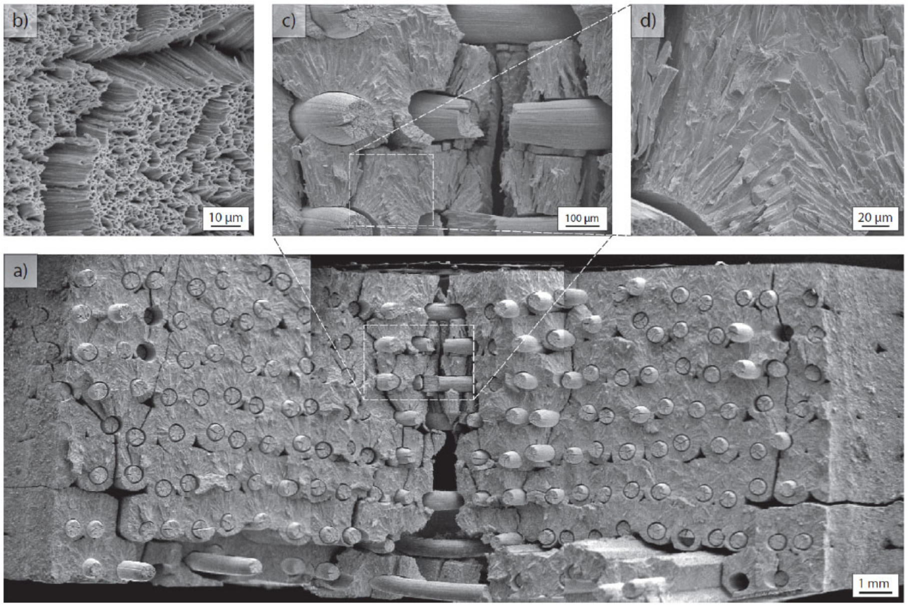

Figure 14: Fracture surface of a W_f/W based bulk sample tested in a 3-point bending test. In subfigure b) the ductile deformation of the tungsten reinforcement wire toughening the matrix which contrarily exhibits brittle fracture (subfigures c) and d)) [45]

In W_fW, the wires, are immersed in a tungsten matrix (for the case of the materials studied in this thesis, via a chemical infiltration method developed by both the Max-Planck-Institute for Plasma Physics and Jülich research centre [46]) providing the final part bulk properties allowing for use as PFMs. During operation though, recovery and recrystallization (the latter reinstating brittleness) will still take place, and such a heterogeneous microstructural arrangement – a fine largely deformed microstructure in the wire and a relatively coarsed grained microstructure in the matrix - will be affected, in manners that are yet not evaluated. This calls for further scientific exploration of these phenomena in such a composite. As a result, e.g. studies aiming at characterizing the evolution and the kinetics of such recrystallization and recovery were performed showing how different amounts of work put into tungsten plates determins a different life expectancy of pure tungsten plate products as PFMs [47], [48].

In this work, further experimental campaigns are reported involving experiments on thin plates as part of the laminate design of tungsten material [49], [50] (Subchapters 4.1 and 4.2), warm-rolled plates [51], [52] (Subchapters 5.1 and 5.2) and the very first campaigns to characterize the thermal stability of W_fW [53] (Section 6.2.1).

2.6 Designing solutions: Recent developments in tungsten R&D against recrystallization

The problem of achieving a ductile behaviour in tungsten throughout the entire application range required in fusion reactors can be solved via working as formerly stated, especially for temperatures in the lower side of the operation window. Increasing cold work put into the material extends the range for ductile behaviour of tungsten but impedes thermal stability. This widening of the temperature range in which tungsten behaves in a ductile manner is concurrent to a decrease in the recrystallization temperature or resistance to recrystallization in general. Still, the benefits of an extended application range for severely cold rolled tungsten are desirable and a strategy to retain thermal stability shall be found. Typical approaches for stabilising microstructures elucidated in the former subchapter involve, i) use of second phases as oxide or carbide particles, acting as impingement obstacles to dislocations and grain boundaries in general, ii) forming of a solid solution with other elements or iii) as it was discovered to be working for tungsten filaments in lamps (Figure 15 and Figure 16), potassium doping stabilising existing boundaries and prevents their long range motion occuring in recrystallization [54].

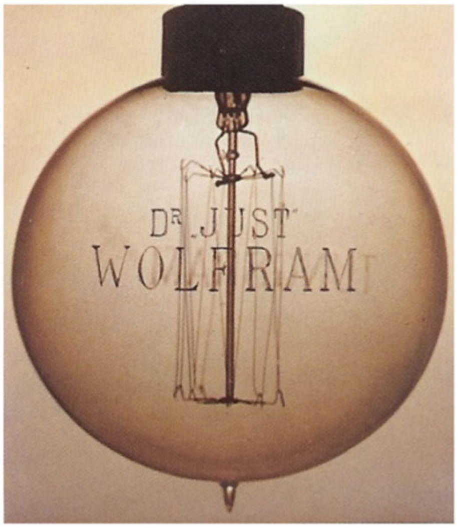

Figure 15: The very first tungsten coated carbon bulb from 1905 [55].

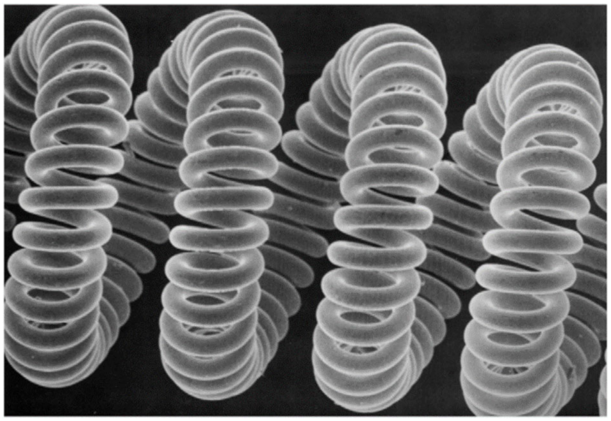

Figure 16: Modern coated tungsten coils in filament bulbs [55].

In fact, in the beginning of the 20th century, the microstructural stability and recrystallization resistance due to potassium doping were first observed and then further exploited for bulb mass production [55]. Filaments in such bulbs are potassium doped tungsten drawn wires, basically the same kind used in the W_fW.

When potassium is added to tungsten during sintering it subsequently arranges either in the form of bubbles or ellipsoids, the shape depending on the mechanical treatment altering the shape of the microstructure in its entirety. As a result, potassium acts as a pinning agent for dislocations and boundaries of the metallic phase [55]. In this view, attempts to exploit such a design for fusion applications or attempting to exploit the same properties but for plates as compared to drawn tungsten wires have been performed and tested recently [26]. Additionally, very recent work at KIT demonstrated that a DBTT temperature as low as -65 °C [56] can be achieved in tungsten via rolling to very large strains. Potassium particles act as a pinning agent for grain boundaries when moving, and therefore in an effective counter measure for grain growth: higher temperatures are needed to achieve comparable boundary velocities respect to an un-doped specimen. In the case of recrystallization, the effect achieved is that its evolution is slowed down, if not inhibited, but not prevented. Potassium has an active role in maintaining a smaller subgrain size during recovery if compared to an un-doped wire but fails to inhibit nucleation of recrystallizing grains. Locally, the stored energy might be enough to allow for nucleation of new grains; their motion will be impeeded by potassium [57]. Polygonisation of dislocations into (subgrain) boundaries in doped drawn wires takes place, but macroscopic movement of boundaries is prevented [58]. Yet, when drawn wires are used in a composite material, such as W_fW, as a strategy to form a bulk material for use as PFM (Figure 17), tungsten is deposited on top of the wire interfaced by an oxide substrate protecting it by Chemical Vapour Deposition, CVD. Such a microstructural arrangement is different from that of a rolled product: two very different microstructures are present. One is that of the wire, a highly deformed grain structure with elongated grains along the wire drawing direction, possessing a very high content of stored energy from the wire drawing process and high dislocation density. The other one is that of CVD tungsten, in which only a few dislocations are present and the dislocation density is negligibile. The surface area density of boundaries in the CVD region can be very high, especially close to the interface with the wire. The main difference between these two microstructures is that while in the wire there is potential for nucleation of recrystallization, in the CVD region is impossible that recrystallization will ever take place. In the CVD region, no dislocation content to generate recrystallizing grain nuclei is present nor a deformed microstructure providing driving force for recrystallized grain boundaries to bulge out and grow. The only possible microstructural phenomena the CVD region might undergo is that of grain growth, whose driving force is the energy of the existing grain boundaries. The microstructure of the CVD region is therefore rather stable, but is inherently brittle. Failure of the CVD region is in fact allowed by design, with the wires ensuring the structural integrity of the composite in its entirety. Recrystallization starts and progresses whenever a lowering of the internal stored energy due to the decrease of dislocation content is possible and hence, it is of interest to study how the microstructure of these two separate parts of the composite interact with each other at high temperatures.

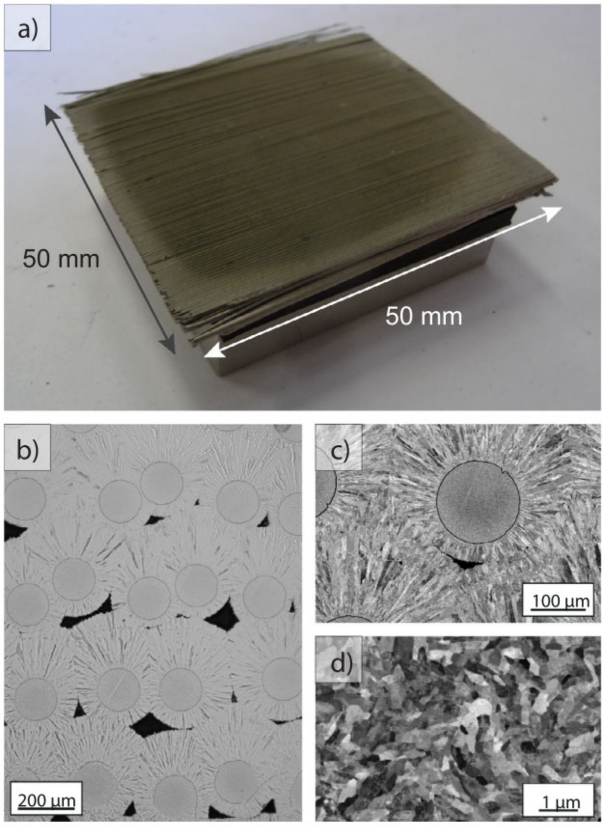

Figure 17: WfW composite produced by deposition of subsequent layers. In (a) a photo of the full sample is shown. (b) shows a light microscopy picture of the cross-section. Large pores in between the fibres are clearly visible as well as regions with high density. In (c) and (d) scanning electron microscopy pictures show the microstructure in detail. In (c) the star like growing grain structure of the matrix is shown. (d) shows a close up of the wire centre and its very fine grain structure. (Note that pictures (b-d) are showing details of (a) but not the same cross-sections [45].

Alternatively to potassium doping, particle reinforcement/dispersion strengthening was also attempted in the last 10 years as a strategy to inhibit recrystallization. The reasons for the use of particles in sintered products as tungsten are manifold. Aside from their interaction with defects and inhibition of grain growth and recrystallization processes, prevention of oxidation and stabilization of impurities at the grain boundaries are of tremendous relevance (since impurities act as a crack promoting factor at grain boundaries) as well [59], [60]. Besides lanthanum oxides or TiC particles, dispersion of yttrium oxides[61] or TaC [62] was attempted. Interesting results were obtained in terms of increased ductility (Figure 18) and/or improved thermal resistance but unfortunately any other phase in the material decreased the cohesion of grain boundary in tungsten. Additionally, development of oxides (from the elements of the reinforcing particles and oxygen as an impurity), having a lower safe service temperature than tungsten, reduced the erosion resistance, invalidating any possibility of their use for facing a reacting plasma [63]. Use of carbon as deoxidizing agent instead seems to succeed at preventing oxygen-impurities based second phases in the tungsten matrix when at least 5-9% of WC precursor is added in the sintering stage [64]. At the elevated temperatures of sintering processes like FAST (ca. 1900 °C), WC turns into W_2C. W_2C particles are located intergranularly, and provide thermal stability against grain growth [60], [64].

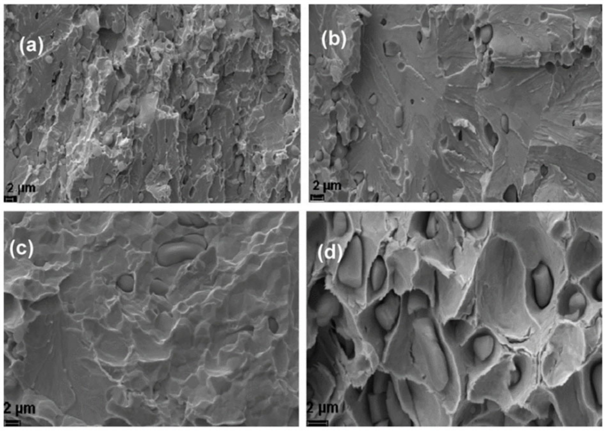

Figure 18: SEM pictures of fracture surfaces of particle reinforced tungsten (W-2wt.%Y2O3) after 3 point bend test as a function of test temperature, (a) 200 °C, (b) 250 °C, (c) 400 °C and (d) 500 °C respectively. In a) and b) show brittle fracture behaviour while for c) and d) a ductile behaviour [61].

Pure tungsten plates have been so far the most promising solution for implementation in fusion reactors as far as thermal stability is concerned. Pure tungsten plates rolled to an intermediate reduction have so far demonstrated the highest recrystallization temperature [48] for a commercially feasible designed operational time of 2 years [6], [65] of continuous energy production in the reactor.

2.7 As-deformed condition: microstructure and texture

Upon working of a metal, the work input by the mechanical processing in the material leads to the formation of defects, such as dislocations, although it only accounts for approximately 1% of the total work done [66]. Dislocation and boundaries are constituents of the microstructure and the actors of microstructural rearrangement. They are responsible for the progressive rearrangement and displacement of formerly perfectly crystalline volumes of the worked material, during plastic deformation [24]. We are used to the idea that when we desire a hardened metal we usually resort to working, e.g. rolling, for which the material undergoes work-hardening via dislocations. Increasing the dislocation content means the dislocations will find more other dislocations acting as obstacles against motion to achieve deformation, e.g. dislocations will not freely move to accommodate deformation but will be stopped by other dislocations along the way. To overcome these obstacles, larger forces are needed to continue deformation or new dislocations to accommodate the plastic deformation have to develop, increasing the dislocation content. A harder material has developed. The dislocations and boundaries arrange in the material in different manners (as in Figure 19) varying with the extent of deformation, type of deformation, temperature, etc.

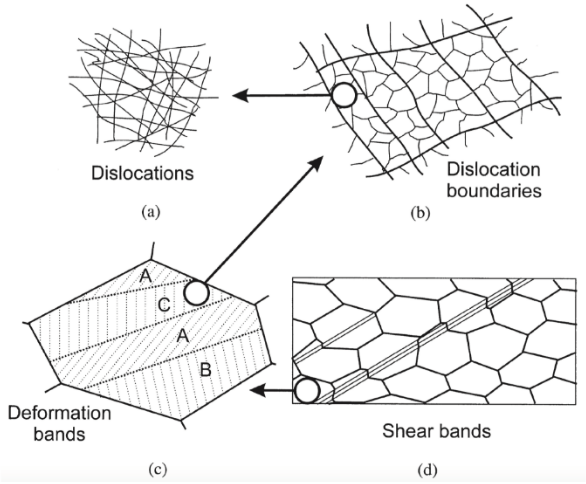

Figure 19: Microstructural defects in a deformed metal, from the smallest scale (a) to the largest (d) [66].

The grain boundaries are between regions of different orientation. When dealing orientation differences between grains, one considers misorientations. A misorientation is the rotation with the smallest rotation angle around an axis relating the former orientation A of a crystallite to the orientation ”B”. If the misorientation angle, is larger than 15°, the boundaries are termed HABs, if smaller, LABs.

As dislocations are generated and move, they can annihilate with each other if they possess an opposite nature (or sign). Dislocations rearrange within the deformed grains to form cells or subgrains (Figure 20a and b). The former (pre-deformed) grains have changed their shape from e.g. an equiaxed shape (after e.g.in tungsten, sintering) to, e.g., pancakes or needles, according to the geometry of the processing and the forces in play. The net result of creation of subgrains/cells (of a size of approximately 0.5 to 1 µm as in warm-rolled tungsten [67]) is that within each grain there are crystalline regions enclosed by a large amount of dislocations which are slightly rotated (rotated by a small angle, usually 1 degree) with respect to each other. Low angle (sub-grain) boundaries have formed, having a misorientation angle, usually defined to be below 15°.

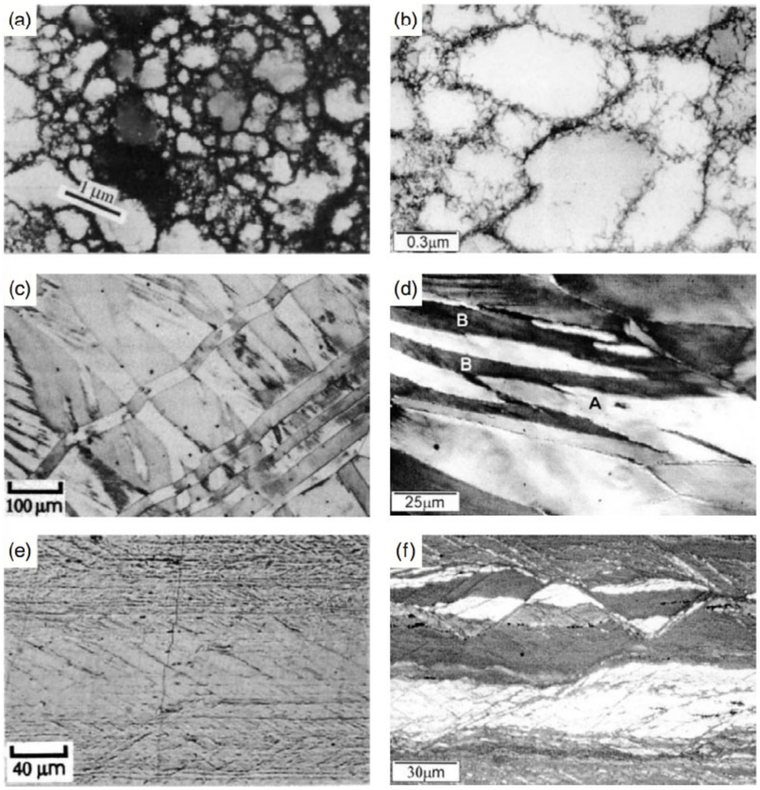

Figure 20: Features of a deformed microstructure: (a) Cell-structure in cold-rolled copper, (b) in detail, (c) deformation bands in 12% compressed 70:30 brass, (d) deformation bands in Al-1%Mg, (e) shear bands in cold rolled copper and (f) shear bands in Al-Zn-Mg cold rolled alloy [66].

These subgrains within the grains, taken as a whole set, can consist in microstructural features on a larger scale e.g. extending through the whole grain or through different grains. In the former case it is possible that an entire region within the same grain had been deformed in a way that all the belonging subgrains possess a misorientation that, if compared to neighbouring regions within the same grain, is much larger than that between the cells themselves: these regions are commonly defined as deformation bands; between them is a transition band consisting of a higher density of dislocations respect to that constituting the cells. Deformation and transition bands arise when instability within the grain or inhomogeneous stress on the grain itself upon deformation take place, implying deformation is performed in each of those regions via different slip systems ultimately instating large misorientations between them [66]. When these bundle of subgrains slightly misoriented to each other swipe across different grains rather than in the single grain only, we are talking about shear bands. They also are the result of plastic instability during the deformation process but are not crystallographic in their nature [66].

Wire drawing and rolling are two different deformation processes. With drawing it is possible to achieve a higher amount of deformation to the material respect to the first. Polycrystalline tungsten of high purity (electron beam melted tungsten) exhibits an average dislocation density as low as that in the order of 10^{6} m^{-2} as compared to rolled plates $10^{12} – 10^{14}$ m^{-2} and drawn wires 10^{14} – 10^{15} m^{-2} [16].

Imposed deformation produces displacements and rotation of volumes within the work-hardened piece and development of a complicated microstructure. According to the nature of the material and the mode of deformation, the final worked piece will present a preferred orientation; the material it is said to exhibit a texture. The modes of deformation, the preferred slip systems through which deformation takes place will give rise to specific, more frequent orientations. The texture becomes stronger the higher deformation is put into the materials via reduction. A typical rolling texture for a bcc metal consists in preferred orientations ranging along the α-fiber (from {100} <001> to {111} <110>), and along the γ-fiber (from {111} <110> to {111} <112>) as shown in Figure 21. This can be seen as having the <110> directions aligned with rolling direction (RD) and the <111> directions, aligned with the normal direction (ND) respectively. Upon recrystallization, orientations such as cube ({100} <001>) and rotated cube ({001} <110>) develop at the expense of the rolling texture components.

In the case of the wires instead, the axial symmetric configuration of the wire drawing process, e.g. the circular-shaped die wires are drawn through, leads to preferential orientations of the deformed microstructure, consisting in the <110> direction oriented along the drawing direction [68]. This specific kind of texture is referred as fiber texture [69]–[71].

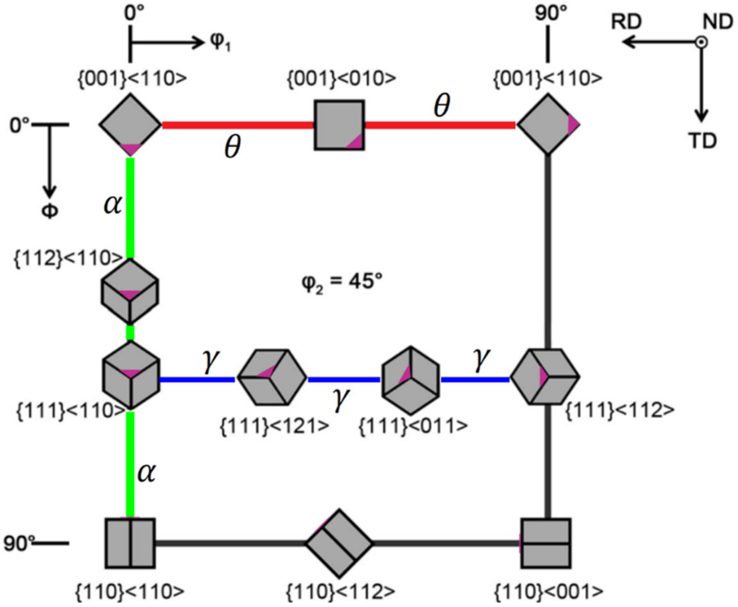

Figure 21: Orientation space (φ_2=45°) section showing the relevant preferred orientation features of rolled bcc materials: the γ-fiber in blue, the α-fiber in green and the θ-fiber in red together with other relevant single orientations such as e.g. rotated cube, cube or rotated Goss.

2.8 Microstructure and annealing phenomena

Any material, when worked, undergoes changes both macroscopically (shape changes) and microscopically (microstructural changes). The effect of deformation in a metal is to obtain the desired shape, designed for its foreseen application. Secondly but not least importantly, the microstructure changes, according to the processing, the forces and conditions in play. As a result the newly deformed material will possess a higher internal energy due to the stored dislocation content and possess a texture to which specific physical properties will be related. Application of a deformed product where heat is provided triggers rearrangements in the microstructure aiming at minimising the internal stored energy [66]. Those changes involve all the microstructural features introduced by processing, mainly, dislocations and grain boundaries [24]. In the following section an introduction on such microstructure will be given to best interpret the microstructural rearrangement phenomena of recovery, recrystallization and grain growth.

2.8.1 Recovery

Recovery is one of the thermally activated phenomena taking place in a material under the influence of temperature. Activation of such a process arises from provided heat, e.g. while the material is operating at high temperatures (even RT might be enough for recovery to take place, if annihilation of dislocations is considered to be part of it [72]) or when annealing. Recovery lowers the material's stored energy via dislocation annihilation and rearrangement to form subgrain structures such as the cells as compared to recrystallization, instead, in which the stored energy is lowered by depletion of the deformed structure (to which a certain energy is ascribed) within the deformed grains, to finally produce a defect-free grain microstructure [66]. The difference between the two is that while recovery starts as soon as the material is thermally activated; recrystallization needs nucleation of a new defect-free grain to take place and then spread throughout the deformed matrix, which is undergoing recovery. They are competing processes since at any time they both aim at lowering the internal stored energy of the material.

Since recovery takes place without any nucleation within a material, it is often referred to as an homogeneous and continuous phenomena, while in the case of recrystallization, the necessity of nucleation causes a discontinuous character. In recovery, dislocation annihilation takes place by the recombination of two dislocations of opposite sign of the Burgers vector via glide, climb (edge dislocations) or cross-slip (screw dislocations) [73]. Recovery usually does not remove all dislocations accumulated into the material: some dislocations may not annihilate finding their counterpart and re-arrange into LABs [74]. Dislocations in LABs possess a lower stored energy per dislocation line length, and rearrangement within recovery is referred to as polygonization. Recovery starts right after deformation and has no well defined finishing point.

Recovery can be framed into several consequent different stages (Figure 22): at first dislocations annihilate, via glide, climb or cross-slip, allowing them to rearrange and form cells, next comes dislocation annihilation within those cells and the cell walls, leading to the formation of sharp subgrain boundaries. Finally the subgrains grow as recovery proceeds. When recovery persists through time and recrystallization does not set in, subgrains continue growing; in this case, recovery is commonly termed extended recovery.

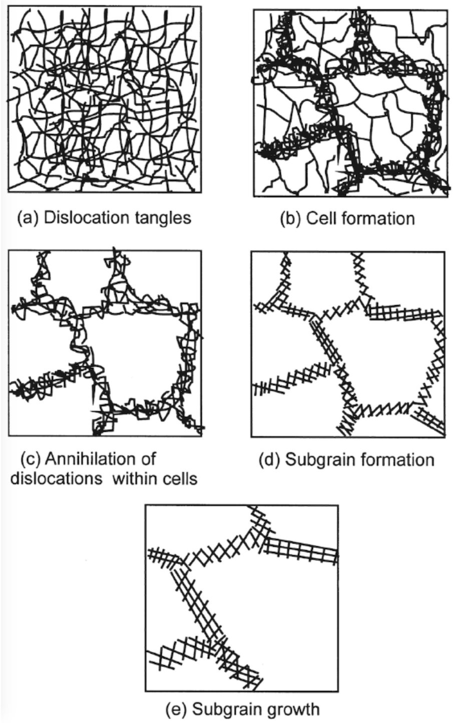

Figure 22: Different consecutive stages of recovery (b-e) starting from the deformed condition (a) [66].

When rolling a slab into a plate, for example, where several passes are needed in order to reduce the material to the desired thickness, dynamic recovery onsets in the first pass but continues also throughout the next rolling steps, with additional deformation put into the material. In each pass new dislocations are generated and the microstructure will rearrange continuously. The distribution of dislocations within the plat eis heterogeneous, meaning that different amounts of dislocations may be generated in different volumes of the processed material. This means that there will always be dislocation recovery taking place in the material.

So far the description of these re-arrangement processes did not consider the presence of solutes in the material, which is always the case, though to different extents. A dislocation is a linear defect consisting in a fault (discontinuity) in the arrangement of atoms. Such a defect create a surrounding stress and strain fields and solute atoms may find it energetically very favourable to sit on the dislocation line. Such a configuration interferes with the dislocation by hindering its motion. Solutes can hence potentially retard recovery favouring recrystallization all over the thermally activated volume in the competition lowering the internal stored energy content.

Work-hardening increases defect content which in turn determines a change in the mechanical properties of the material: increases its strength due to a higher concentration of dislocations. In this sense, recovery can be seen as the opposite: the decrease in defect content alters the readily obtained mechanical properties after work-hardening by softening the material. One can therefore track its evolution by measuring such changes via hardness testing although other methods are also possible, available and have been used before such as measuring changes in electrical resistivity or by calorimetry. In this work, it is assumed recovery is controlled by thermally activated glide and cross-slip of dislocations and its evolution modelled based on the assumption that the activation energy decreases with increasing dislocation content and increasing time spent at any temperature, as in the work from Kuhlmann [75], later confirmed by Cottrell and Aytekin [73] and Michalak and Paxton [76].

2.8.2 Modelling of recovery: Kuhlmann kinetics

Kuhlmann was the first to devise recovery as a phenomenon ruled by thermal activation rearrangement of dislocations aiming at lowering the dislocation density within the material when heat is provided. Specifically, dislocations thanks to thermal activation manage to move away from an obstacle initially locking them and swipe through a certain area before becoming trapped again and annihilate [75]. Since flow stress is directly related to the dislocation content [77]–[79], and recovery aims at reducing the stored energy content by lowering the amount of dislocations in the material, Kuhlmann described the evolution of flow stress σ within the material with time as follows:

$$\frac{d\sigma}{dt} = -c \exp\left(-\left(\frac{Q - \sigma\Delta V}{RT}\right)\right) \tag{6}$$

where ΔV is the activation volume $\Delta V = b \cdot \Delta A$ describing the area ΔA swept by a dislocation of Burgers vector b, when released from the obstacle by thermal activation, Q the activation energy needed for the dislocation to overcome the obstacle in the absence of any stress, R the universal gas constant, T the absolute temperature and c a rate constant.

The modelling above can be used with hardness, a much more readily obtainable property related to the dislocation content and related to the true stress since it relates to the flow stress[77] as:

$$HV = 3 \cdot \sigma \tag{7}$$

Integration in time of Eqn. 6 using hardness as the time dependent variable will yield:

$$HV = HV_0 - \frac{3RT}{\Delta V} \ln\left(1 + \frac{t}{t_0}\right) \tag{8}$$

which for times that are not too short can be written as:

$$HV = HV_0^* - \frac{3RT}{\Delta V} \ln t \tag{9}$$

For isochronal experiments the annealing time t_{isoch}, is constant and the evolution in hardness describes a linear decrease with increasing annealing temperature:

$$HV \approx HV_0^* - AT \tag{10}$$

with a slope:

$$A = \frac{3R}{\Delta V} \ln t_{isoch} \tag{11}$$

ultimately providing physical meaning via the microstructural parameters defining the activation volume. It shall be noted anyway that HV_0^* is slightly temperature dependent due to the integration constant being:

$$t_0 = \frac{RT}{c\Delta V} \exp\left[-\frac{(Q_0 - HV_0 \Delta V)}{3RT}\right] \tag{12}$$

2.8.3 Recrystallization

Contrarily to recovery, recrystallization is characterised by an heterogeneous nature. Recrystallization is a microstructural re-arrangement by which a deformed/recovered microstructure is replaced by defect-free grains, ultimately releasing all the energy stored in the form of dislocations. While recovery takes place homogeneously in the entire volume of the material, recrystallization is a process marked by the necessary development of an initial nucleus and its following growth throughout the deformed/recovered matrix (Figure 23). In this sense it has a discontinuous nature as it needs the development of a nucleus. Recovery and recrystallization take place simultaneously in the material. Recovery reduces the stored energy content in the form of dislocations, but does not remove all of them completely whilst recrystallization does. Recrystallization is a phenomenon, as well as recovery, pivoting on the amount of energy stored in the deformed material and its readiness to take place depends on both how the material rearranges with recovery to form nuclei for recrystallization but also on the stored energy ahead of the boundaries of the nucleus able to move. A recrystallizing grain will be more prone to move into regions possessing a higher stored energy content rather into those having a lower: dislocations and other defects are the driving force of a recrystallizing grains bulging out and leave crystallized region behind with no defects, e.g. stored energy.

Recrystallization is often referred to as primary recrystallization, to differentiate it from other microstructural phenomena carrying the same name, such as secondary recrystallization or continuous or dynamic recrystallization. When large strains are imposed on the worked material, the final microstructure may be characterized by a vast amount of HABs. Upon additional deformation or upon subsequent annealing, long range motion of boundaries may not be achieved and the microstructure may result of HABs surrounding very small crystalline regions. Since no nucleation and growth of recrystallizing grains is seen, this kind of recrystallization is often referred to as continuous recrystallization. When working materials at high temperatures, such as when hot rolling, this mechanism may take place as well and in this case is commonly referred to as dynamic recrystallization.

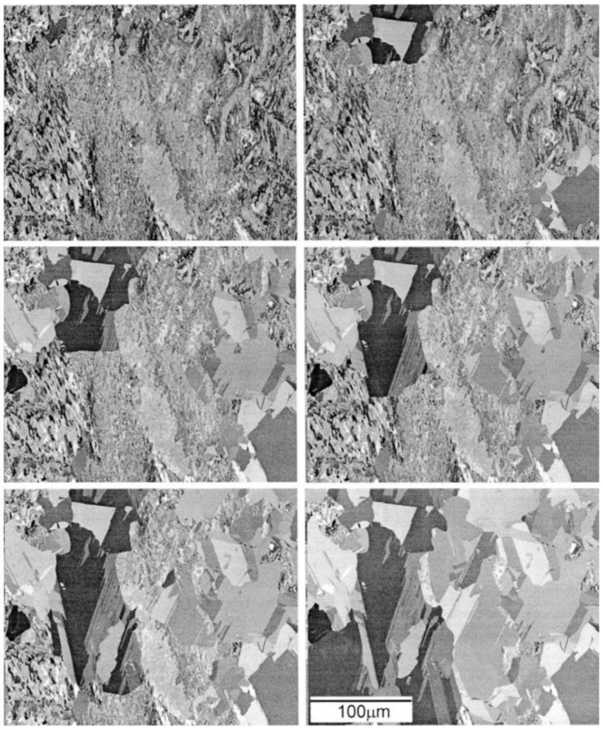

Figure 23: Development of recrystallization within deformed copper with increasing time of annealing. Distinct uniformly shaded regions can be seen in the image which are the recrystallizing grains nucleating and growing [66].

In materials science, nucleation is usually discerned for the process of solidification of a material from the liquid to a solid phase. In the case of recrystallization this is not the case. Taking as a reference a material that has partially recrystallized, there we have two volumes which have the same physical state, that of a solid. These two volumes though are completely different in terms of, e.g., stored energy in the form of dislocations in the deformed/recovered matrix (compared to the defect-free recrystallized grains), their microstructure is different. To explain the concept of nucleation the following example of phase transformation, which is different from recrystallization but needs nucleation as well, can be considered. Upon cooling of iron, ferrite nucleates and grows at the expense of austenite. The two phases are both solid but differ in crystal structure. There, the driving force instead of being the amount of dislocations in the material, consists in the difference between higher stored energy of the recrystallizing phase, austenite, and the lower stored energy of the product phase, ferrite, which at the lower temperatures achieved when cooling, becomes the stable crystal structure. Although this is not recrystallization, In the case of recrystallization of a material whose recrystallized phase is the same as that of the deformed, nucleation and growth of a grain means that a crystallite of very low internal energy nucleates and grows into a deformed or recovered material from which it is separated by a HAB[66].

HABs are in fact the only boundaries possessing a sufficient mobility for advancing recrystallization. Hence, while there is a depletion of energy by the creation of a defect free volume by the recrystallizing nuclei, there is an increase in energy due to the development of an HAB. The balance between these two determine the minimum size, R, of a nuclei. The size of a critical nucleus depends on the surface energy of the boundary γ_b and the curvature pressure P_b (which can be related to the stored energy to be removed ahead of the boundary Δu by creation of such a defect-free zone) by the Gibbs-Thomson relationship as follows:

$$R = \frac{2\gamma_b}{P_b} \tag{13}$$

Therefore, considering the regions with highest dislocation content to possess the highest possible stored energy, it comes straightforward that these should be the preferential sites for recrystallization nucleation: the size that the nucleus in such regions will have to reach before growing, and hence becoming a proper recrystallizing grain, is smaller compared to one in a region of lower stored energy. Since the energy of a nucleus increases with its free surface size, it will be easier for recrystallized grains to nucleate at grain boundaries or, e.g., triple junctions, shear or transition bands [66].

As the nuclei formed, its boundaries start to migrate under the balance of two pressures, that of the curvature of the surface, P_b, of the boundary dragging the recrystallizing grain backwards as in Eqn. 13 and that of the stored energy content ahead of the boundary, the driving force for recrystallization, P_d, (determined by the dislocation density ρ, the Burgers vector b and the shear modulus S of the material) pushing the boundary towards the deformed region (Figure 24) [66]:

$$P_d = \alpha\rho S b^2 \tag{14}$$

This pressure difference influences the motion of such a boundary, and hence its velocity being the growth rate $\dot{G}$ equal to [66]:

$$v = \dot{G} = MP = M(P_d - P_c) = M\left(\alpha\rho S b^2 - \frac{2\gamma_b}{R}\right) \tag{15}$$

where M is the mobility of such a boundary.

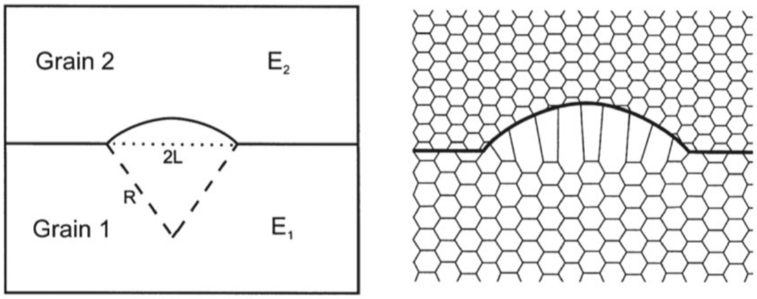

Figure 24: Schematics of the Bailey-Hirsch mechanism [66].

As it was formerly mentioned, recovery influences recrystallization; while recovery is needed for the nucleation of recrystallizing grains, it can be seen in Eqn. 15 that a lower dislocation content, as recovery progresses, corresponds to a lower driving force slowing down recrystallizing boundaries motion, retarding (if not inhibiting, if extensive recovery took place) recrystallization. It should be noted that the mobility M of a boundary depends on many factors, the most blatant in a pure metal, being the misorientation, i.e. the orientation difference with the deformed regions ahead of the recrystallizing boundary and should not be considered a constant. Although the reason for boundary migration is the difference between the two formerly mentioned pressures, grains might grow much faster and larger than others, due to favourable misorientations between them and the deformed matrix.

Mehl (1948), Burke and Turnbull (1952) after reviewing consistent experimental data, framed recrystallization as a thermally activated process generally obeying the following set of rules:

1. A certain amount of deformation is needed to trigger recrystallization
2. Increasing deformation in the material triggers recrystallization at lower temperatures

3. As the time spent at a specific temperature increases the temperature at which the material starts recrystallizing decreases
4. The recrystallized grain size in the fully recrystallized material decreases with increasing deformation (more nucleation sites)
5. Taken a specific amount of deformation put into the material the recrystallization temperature increases with increasing grain size (less favourable nucleation sites per volume) or increasing deformation temperature (dynamic recovery taking place in the material while being worked)

A larger amount of deformation in the material increases the rate and lowers the temperature at which recrystallization onsets, given that increasing deformation means a higher density of loci where nuclei could develop into recrystallizing grains. For strains below 0.03, recrystallization of single phase materials have never been seen to take place while for strains above 2 - 4 the rate of recrystallization does not increase any longer [66]. The deformation mode has also an influence; as an example, cross rolling was seen to promote recrystallization more than unidirectional rolling in both iron and copper [80], [81], as well as different strains path followed upon deformation promote recrystallization with respect to others [82]–[84].

Solutes also might influence recrystallization if in relative large quantities. Available literature indicate they have a role in limiting grain boundary motion and hence, can influence the growth rate of recrystallizing grains [66]. Since the microstructure and the stored energy of a deformed grain depend on the active slip systems upon deformation, the orientation of the grain before deformation will have an influence on the amount of stored energy. In turn, in a polycrystalline material, the existence of a specific preferred texture instead of, say, an other, will have an influence on recrystallization, e.g. in the distribution of nucleation sites [85], [86].

After nucleation and during growth, the misorientation across the recrystallizing grain boundary, with respect to the deformed region influences the motion of such a recrystallizing grain front. At a microscopical level, it shall be noted that, if a recrystallizing grain suddenly encounters a deformed region possessing a similar orientation, the misorientation across the boundary decreases eventually rendering the boundary a low angle one, reducing its mobility significantly. In other words, the surrounding of a recrystallizing grain plays an influence on its growth: it might advantage or disadvantage its growth.

In order to characterize quantitavely recrystallization some reference parameters are needed. One of the most important ones is the time it takes the material to recrystallize a volume fraction, X_v, of 50%, the time to half recrystallization, $t_{X_v=0.5}$. If the rate of recrystallization is characterised by this time to half recrystallization, an Arrhenius type relationship should be considered:

$$\frac{1}{t_{X_v=0.5}} = K \exp\left(\frac{-Q}{RT}\right) \tag{16}$$

where Q is the activation energy for both nucleation and growth processes for the time to half recrystallization in the material, R the universal gas constant and T the absolute temperature. This activation energy must reflect the underlying physics of the phenomenon and hence both nucleation and growth rates in recrystallization shall be formulated as:

$$\dot{G} = K_1 \exp\left(\frac{-Q_G}{RT}\right) \tag{17}$$

$$\dot{N} = K_2 \exp\left(\frac{-Q_N}{RT}\right) \tag{18}$$

two parameters of handful use in the description of recrystallization. Though, constant nucleation rates are not supposed to be found for recrystallization, considering the heterogeneous distribution of the energy content in the microstructure. Hence, an alternative approach to include this deviation from constant nucleation rates must be sought. Throughout the latest century, scientists and groups of researchers have developed models to better describe the evolution of recrystallization coping with a discontinuous nucleation rate, which will be reported and analysed in the following section.

2.8.3.1 JMAK kinetics

Around the middle of the twentieth century, nearly at the same time, but independently, four scientists developed a theoretical approach describing nucleation and growth phenomena that have been successfully applied to recrystallization [87]–[89].

It provides a sound description of the process in the light of the underlying evolving microstructure and the nature of recrystallization as a thermally activated phenomena. Those scientists were, in a time ordered fashion, Kolmogorov (1937), Avrami (1939), Johnson and Mehl (1939), whose initials became the acronym for the well known homogeneous nucleation model describing recrystallization kinetics: the JMAK model.

Onwards, we are assuming the nucleation and growth rates are constant in the recrystallizing material despite being unnecessary from a theoretical point of view. The nucleation rate of recrystallization, $\dot{N}$, consists in the amount of nuclei (nuclei density dN') developing during recrystallization in a given interval of time dt:

$$\dot{N} = \frac{dN'}{dt} \tag{19}$$

It is considered that nucleation takes place homogeneously everywhere in the material and that the hypothetical density of nuclei dN' appearing in the material in a time interval dt during recrystallization, consists of the density of nuclei forming only in the recovered volumes, dN, and the density of nuclei which would nucleate in volumes which already have a recrystallized, $dN'' = \dot{N} X_V dt$, although they are actually not in reality, so that:

$$dN' = dN + \dot{N} X_V dt \tag{20}$$

These recrystallizing nuclei can be visualised as the physically meaningful volume recrystallizing combined with a phantom one. At a specific time t during recrystallization, these volumes combined would occupy an extended recrystallized volume fraction:

$$X_{VEX} = \int_0^{t_{vex}} V \, dN' \tag{21}$$

where V is the volume of each recrystallizing grain.

The fraction of unrecrystallized material is $(1 - X_v)$ and since every dt the recrystallized fraction increases by dX_{VEX}, it follows that:

$$dX_V = (1 - X_V) dX_{VEX} \tag{22}$$

so that upon integration, the extended volume fraction recrystallized is found to be equal to:

$$X_{VEX} = \int_0^{X_V} dX_{VEX} = \int_0^{X_V} \frac{dX_V}{(1 - X_V)} = \ln \frac{1}{1 - X_V} \tag{23}$$

leading to:

$$X_V = 1 - \exp(-X_{VEX}) \tag{24}$$

If the incubation time of recrystallization, t_{inc}, is much shorter than the time to reach half recrystallization $t_{X_v=0.5}$, and if growth of spherical grains is assumed, then the recrystallizing grain possesses a volume equal to:

$$V = f\dot{G}^3 t^3 \tag{25}$$

where f is a shape factor determined by the shape of the recrystallizing grain which, for a sphere, is equal to $4\pi/3$.

If the nucleation rate is constant, upon integration the extended recrystallizing volume will be equal to:

$$X_{VEX} = f\dot{G}^3 \int_0^t \dot{N} t^3 dt = \frac{f N_0 \dot{G}^3 t^4}{4} \tag{26}$$

and finally:

$$X_V = 1 - \exp(-X_{VEX}) = 1 - \exp\left(-\frac{f N_0 \dot{G}^3 t^4}{4}\right) = 1 - \exp(-Bt^n) \tag{27}$$

From the assumptions, the exponent of time is supposed to be equal to 4 but this is actually never found in experimental practice: the exponent is nearly always lower. This is because the boundaries of a grain do not grow homogeneously in all directions and hence, the assumptions on the the spherical shape will not be valid any longer [90]. Authors have shown the Avrami exponent to drop from 4 to 1 at the end of recrystallization due to impingement, in the case of random nucleation at grain boundaries [91]. It is worth mentioning Kolmogorov did not require a constant nucleation rate. Avrami also considered a decreasing nucleation with time in his formulation, leading to an exponent lower than 4 but still in the range from 3 to 4. Two limiting case situation are useful to further understand the Avrami exponent. One is that of constant nucleation throughout the process for which, if grains grow as spheres, an Avrami exponent of 4 shall be expected, and an other one in which all nuclei develop at the beginning of nucleation implying the rate of nucleation immediately drops to zero: site saturated nucleation, to which corresponds an exponent of 3 since the fraction of extended recrystallized volume is equal to $fN_0\dot{G}^3t^3$. The different dimensionality of growth can be taken into account for both extreme cases in a way that if the growth of recrystallizing grains undertakes an n-dimensional growth, then the exponent will be equal to $n+1$ for constant nucleation rates and n for site saturated nucleation. Consequently in smaller exponents result, as a lower dimensionality comes in play as reported in Table 1.

Table 1: Different Avrami exponents according to growth dimensionality and nucleation behavior.

Growth Dimensionality	**Avrami Exponent**	
	Constant Nucleation Rate	*Site Saturated Nucleation*
3-D	4	3
2-D	3	2
1-D	2	1

Equation 28 can alternatively be modified to include an incubation time for recrystallization and written as:

$$X_V = 1 - \exp[-b^n(t - t_{inc})^n] \tag{28}$$

the coefficient b and the Avrami exponent n reflect the physics of both nucleation and growth of recrystallization. Rearrangement of Eqn. 28 into:

$$\ln[-\ln(1 - X_V)] = n \ln b + \ln(t - t_{inc}) \tag{29}$$

allows the determination of both by linear regression (such lines are usually plotted in so-called Avrami plots, as shown in Figure 25).

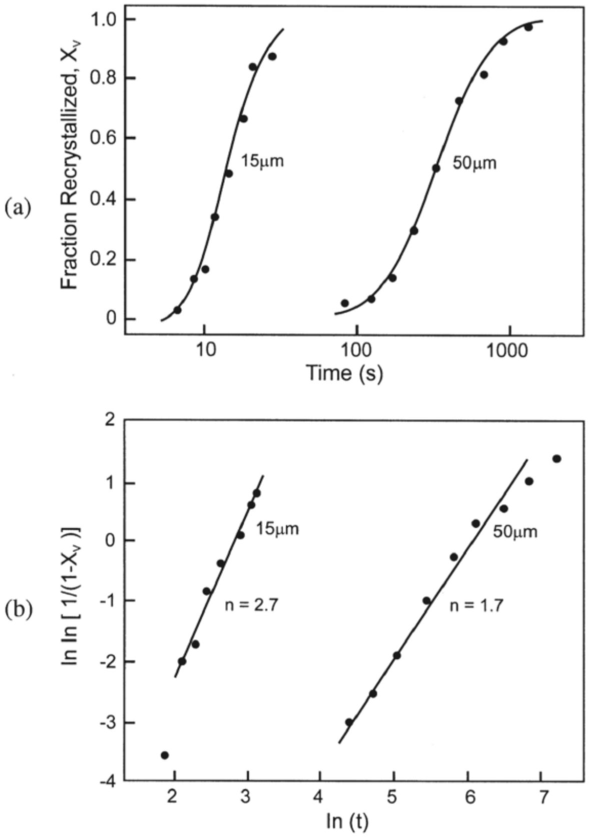

Figure 25: a) Evolution of the fraction recrystallized with time for two different starting grain sizes. A faster kinetics is found for a smaller starting grain size. b) JMAK plots to deduce the Avrami exponents for the process [66].

2.8.3.2 Microstructural Path Methodology

Fourty years later, Vandeermeer and Rath improved the JMAK recrystallization model by introducing the Microstructural Path (MP) approach/model with respect to recrystallization [92]–[94]. DeHoff first laid the foundations of such an approach [95] in 1985 by use of an analogy with thermodynamics: "The path of microstructural change is the sequence of states through which the system passes during a process. The microstructural state of a system may be thought of as a point in a space which has a number of dimensions equal to the number of variables quantified in identifying the state. The path is then the one dimensional curve in that space which connects the points in the sequence of states that characterize the process".

For a nucleation and growth process such as recrystallization, the nucleation and growth rates are assumed to be represented by power law functions as:

$$\dot{N}_{(t)} = \dot{N}_0 t^{\delta-1} \tag{30}$$

$$G_{(t)} = rPt^{r-1} \tag{31}$$

where δ, $\dot{N}_0$, P and r are coefficients.

The grains are assumed to grow in all three directions and their volume, $V_{(t-\tau)}$, and interfacial area density, $S_{(t-\tau)}$, are given by:

$$V_{(t-\tau)} = K_V \cdot a^3{}_{(t-\tau)} \tag{32}$$

$$S_{(t-\tau)} = K_S \cdot a^2{}_{(t-\tau)} \tag{33}$$

where K_V and K_S are shape factors depending on the shape of the recrystallizing grains which is tracked throughout the evolution of the process, by its semi-major axis $a_{(t-\tau)}$, which is given by:

$$a_{(t-\tau)} = \int_{\tau}^{t} G(t)\, dt \tag{34}$$

To account for impingement, the extended volume and surface idealised by JMAK are used, which, in terms of the afore-introduced variables, can be written as:

$$X_{VEX} = \int_{0}^{t} V_{(t-\tau)} \dot{N}(t) dt \tag{35}$$

$$S_{VEX} = \int_0^t S_{(t-\tau)} \dot{N}(t) dt \tag{36}$$

where $V_{(t-\tau)}$ and $S_{(t-\tau)}$ are the volume and the surface of a recrystallizing grain at a time t nucleated at a time τ, and $\dot{N}(t)$ is the nucleation rate of nuclei density at the time t.

In the hypothesis of random spatial distribution of nuclei, the extended space properties are assumed to be related to the real ones via Eqn. 27 and:

$$S_{VEX} = \frac{S_V}{1 - X_V} \tag{37}$$

The time dependence of the extended properties can be determined by substitution, integration by Laplace transformations and are:

$$X_{VEX} = U(K_V, \dot{N}_0, P^3)\ t^{3r+\delta} \tag{38}$$

$$S_{VEX} = V(K_S, \dot{N}_0, P^2)\ t^{2r+\delta} \tag{39}$$

indicating the path will depend on the value of the parameters r, δ, K_V, K_S, P and $\dot{N}_0$.

The value of δ provides insights on the nucleation type; while values of $\delta < 0$ are not possible since it would invalidate the use of Laplace transformations, $\delta = 0$ would indicate site saturated nucleation, $\delta = 1$ a constant nucleation rate. Values of $0 < \delta < 1$ or $\delta > 1$ indicate a nucleation rate decreasing or increasing in time respectively.

The value of r instead discloses information on the growth: $r < 0$ is not possible since the grains would shrink instead of grow, $r = 1$ indicate a constant growth rate whether $0 < r < 1$ a non constant growth as, e.g. the parabolic growth for $r = 1/2$.

By application of eqns. 38 and 39, the microstructural partial path function for the extended parameter S_{VEX} was determined to be of the type:

$$S_{VEX} = C\, {X_{VEX}}^q \tag{40}$$

where $q = 2r + \delta/3r + \delta$. Use of Eqns. 27 and 37 in Eqn. 40 allows for the determination of the path function based on the measurable parameters S_V and X_V:

$$S_{(t-\tau)}(t) = f_{S_{(t-\tau)}}(X_V) = S_V = C_0(1 - X_v)(-\ln(1 - X_V))^q \tag{41}$$

Such an equation, when conveniently plotted, allows for the determination of q which can be further used to infer the nucleation and growth characteristics in the material upon recrystallization. The exponent q is supposed to vary in time in a transition region, as shown in Figure 26.

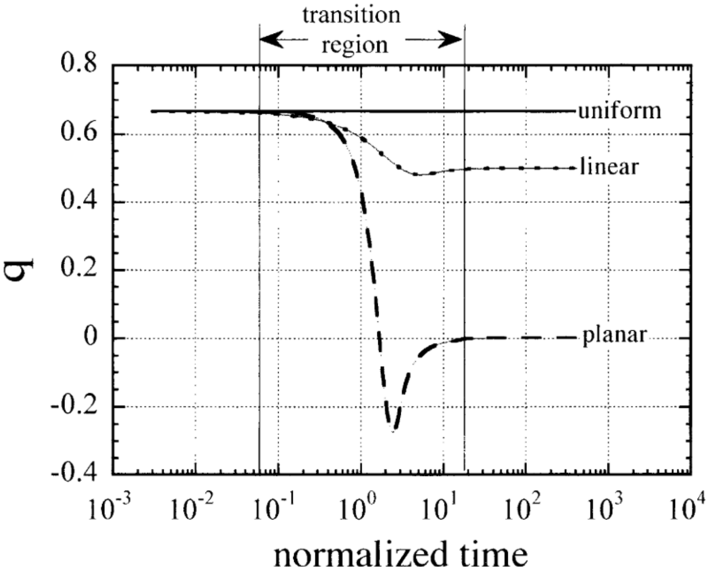

Figure 26: The dependence of the microstructural path parameter, q, on time and impingement behaviour (uniform, linear or planar) as from [96].

In three dimensions, an exponent q equal to or larger than 2/3 indicates uniform impingement, lower values indicate linear impingement and when $q \sim 0$ impingement is planar [96]. As shown above, introduction of additional microstructural parameters and use of more complex geometric models allow a more detailed and precise description of recrystallization in terms of nucleation and growth from experimental results, compared to the JMAK model. Although the assumption of spatially random nucleation still holds, an improvement in recrystallization description had been achieved.

2.8.3.3 Additional Microstructural Descriptors

Additional work from Vandermeer in 2005 integrated the MP model by adding other microstructural parameters such as the contiguity ratio, $C_{\alpha\alpha}$, the fraction of the total grain boundary area of recrystallizing grains shared with other recrystallizing grains or the mean chord length of recrystallizing grains $\langle\lambda_{rx}\rangle$. The mean chord length of a subset of grains is a measure of the grain size and is related to their interfacial area density, S_V, as:

$$\langle\lambda\rangle = \frac{1}{P_L} = \frac{2}{S_V} \tag{42}$$

where P_L is the number of intersection points between the boundaries of the grains for which the chord length is to be measured and test lines, per unit length.

So a new path function for describing the evolution of recrystallization is rationalised, made up by the two of the afore mentioned microstructural descriptors, X_V and S_V, the semi-axis variable, substituted by the mean chord length, and the contiguity ratio, yielding a four dimensional time dependent function:

$$F\left\{X_V, S_V, \langle\lambda_{rx}\rangle_{(t-\tau)}(t), C_{\alpha\alpha_{(t-\tau)}}(t)\right\} = 0 \tag{43}$$

from which partial path functions, can be used to interpret results:

$$S_{(t-\tau)}(t) = f_{S_{(t-\tau)}}(X_v) \tag{44}$$

$$\langle\lambda_{rx}\rangle_{(t-\tau)}(t) = f_{\langle\lambda_{rx}\rangle_{(t-\tau)}}(X_v) \tag{45}$$

$$C_{\alpha\alpha_{(t-\tau)}}(t) = f_{C_{\alpha\alpha_{(t-\tau)}}}(X_v) \tag{46}$$

The partial path function for the boundary surface density was introduced above and corresponds [94] to Eqn. 41. As for the boundary surface density, a partial path equation for the mean chord length of recrystallizing grains shall be determined.

By use of the afore introduced relationships relating the extended and the actual recrystallized volume, together with those relating the extended and actual mean chord lengths to the actual and extended density of nuclei [97], and the Fullman relationship between the sphere radius and the mean chord length [98], the following partial path function for the mean chord length in the case of uniform impingement can be found:

$$\langle \lambda_{rx} \rangle_{(t-\tau)}(t) = f_{\langle \lambda_{rx} \rangle_{(t-\tau)}}(X_v) = \langle \lambda_{rx} \rangle = \frac{1}{\alpha}\left(\frac{16}{9\pi N_0}\right)^{1/3} X_V^{1/3} \tag{47}$$

where α is a shape factor usually close to be equal to 1 and N_0, the nuclei density at zero time. In case of linear or planar impingement of grains the above equation needs alteration respectively into:

$$\langle \lambda_{rx} \rangle = \frac{1}{\alpha}\left(\frac{16}{9\pi L}\right)^{1/3} [-\ln(1 - X_V)]^{1/6} X_V^{1/3} \tag{48}$$

$$\langle \lambda_{rx} \rangle = \frac{1}{\alpha}\left(\frac{2}{3S}\right)^{1/3} [-\ln(1 - X_V)]^{2/3} X_V^{1/3} \tag{49}$$

These above are specific cases from which a general form of such a partial path function can be inferred as:

$$\langle \lambda_{rx} \rangle = K_\lambda X_V^{1/3} [-\ln(1 - X_V)]^p \tag{50}$$

where K_λ and p are constants depending on nucleation and impingement. As for the partial path function for the interfacial area density, plotting of Eqn. 50 - normalised by cubic root of the fraction recrystallized - against the extended recrystallized volume, as in Figure 27, allows evaluation of the parameter p. When $p = 0$, Eqn. 50 translates into Eqn. 47 and a uniform impingement is inferred. Likewise, for linear and planar impingement, p will result equal to 1/6 and 2/3 respectively.

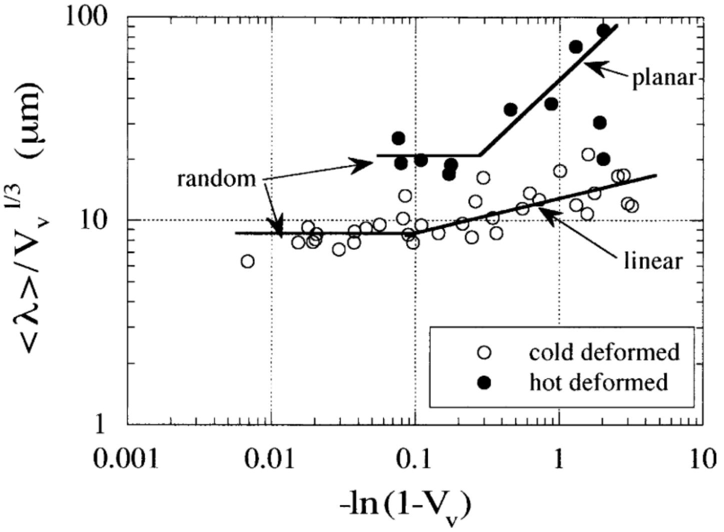

Figure 27: Comparison of approximate MP model behavior of the partial path function $f_{\langle\lambda_{rx}\rangle_{(t-\tau)}}(X_v)$ for recrystallization of cold and hot deformed aluminum as from [96].

The contiguity ratio instead, characterizes the spatial distribution of recrystallized nuclei[96] and can be expressed by the following equation:

$$C_{\alpha\alpha} = \frac{2S_{V\alpha\alpha}}{2S_{V\alpha\alpha} + S_{V\alpha\beta}} \tag{51}$$

where $S_{V\alpha\alpha}$ is the grain boundary area density between recrystallized volumes of the material and $S_{V\alpha\beta}$ that in between recrystallized and recovered volumes. The contiguity ratio increases monotonically from 0 at the beginning of recrystallization to 1 for a fully recrystallized sample. If nucleation of recrystallizing grains takes place homogeneously, $C_{\alpha\alpha} \sim X_V$ for all X_V according to the form derived analytically in Ref. [99]. Deviations from homogeneous distribution of nuclei in space lead to positive or negative deviations due to either clustering or ordering respectively.

2.9 Scanning Electron Microscopy

The scanning electron microscope (SEM) is by far the most used electron microscope due to the wealth of microstructural information that can be obtained considering its reduced costs when compared to Transmission Electron Microscopes (TEMs). SEMs can provide very insightful information of the specimens analysed without narrowing too much on the smallest possible scale of features present in the microstructure, as TEMs do (and hence losing the overall macroscopic character of the insight). The scale of the features from which the information provided comes is not as small as what TEMs can achieve (potentially sub-Angstrom scale for the TEMs when looking at dislocation cores or vacancies) but an SEM is still capable of picturing subgrains for example, or can be used to approximately determine dislocation density. Information can be obtained from comparably large areas: data can be collected in regions up to hundredths of micrometers in size, disclosing information on the chemical composition, the topology of the material studied and, via electron backscatter diffraction, EBSD, their crystalline lattice and orientation. Another main advantage of SEMs is its outstandingly large depth of field, when imaging, as compared to light optical microscopes (LOMs) (tens of micrometers at a 1000x magnification for an SEM as compared to 3-5 µm on a 5-10x magnification lens in a light optical microscope). For this reason, when an SEM is available and the information to be obtained economically viable, it is often preferred to a LOM. An SEM is able to provide a magnification from the same order of magnitude of a LOM down to 25000/50000 times. All of the above is thanks to the nature of the probe used, electrons, whose wave nature can be used to make them as fine probes (sub-Å for a 30kV beam vs 550 nm of light waves) allowing a resolving power much larger than LOMs (although it is not the minimum possible probe size limiting the resolution of a microscope but the machine itself and the specimen studied, since the interaction volume with the specimen will not allow such a resolution in the obtained maps).

An SEM consists of an electron gun (LaB6 (lower brightness) or W Field Emission Gun (higher brightness)) and a series of electromagnetic lenses and apertures below the gun as in Figure 28. Acceleration voltages in SEMs are one order of magnitude smaller than those of a TEM (30 kV vs. 300 kV). The lenses in an SEM only serve to form and direct the probe, not to form the image. In imaging, TEM images are instantaneous, coming from the incident beam itself at all points of the exposed area (and then re-focused to form an image), while in an SEM, the beam is scanned all over the area of interest and hence, its name: scanning electron microscope. Such a scanning is performed by a set of lenses called the scan coils. The interaction of the beam with the material will result in a signal that will be collected from a detector, which varies depending on the kind of information required to the study.

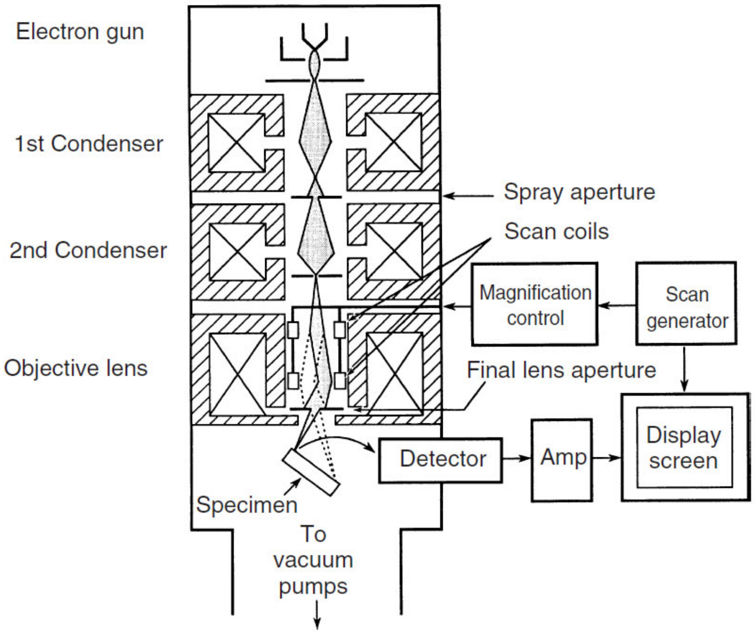
Electron gun
1st Condenser
2nd Condenser
Objective lens
Spray aperture
Scan coils
Magnification control
Scan generator
Final lens aperture
Detector
Amp
Display screen
Specimen
To vacuum pumps

Figure 28: Structure of a scanning electron microscope (SEM) after [100].

The response signal can be of many different kinds, and could consist of the same electrons which have interacted elastically or inelastically with the material, electrons or x-rays stemming from the probed material. Each signal is detected by a different detector located in the vacuum chamber (Figure 29). To image the topography of the material studied (as in Figure 30), secondary electrons, SE, (inelastic electrons) are used, whose yield depends by the shape of the probed volume (electron number effect) and the orientation of the probed surface with respect to the detector (trajectory effect), as shown in Figure 31 and Figure 32. The larger the volume of the specimen probed close to free surfaces, the higher the chance all those inelastic electrons can escape, the higher the amount of them detected, the brighter this region of the map is.

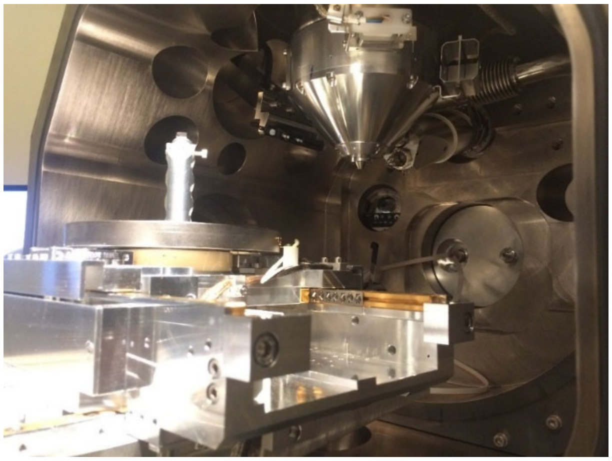

Figure 29: FEI NOVA NanoSem 600 vacuum chamber. The cone in the top center of the figure is the bottom of the column from which the electron beam exits. On the right, the SE detector identifiable by its outer acceleration grid. The specimen sits on top of a pre-tilted sample holder screwed into the stage of the microscope (bottom left). Picture from the author.

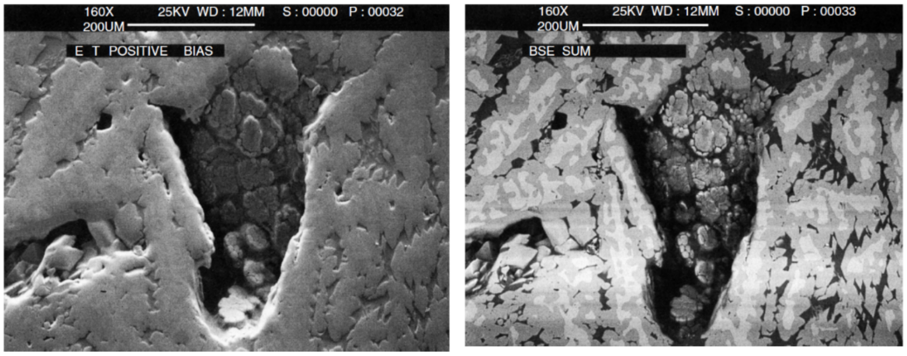
160X 25KV WD : 12MM S : 00000 P : 00032
200UM
E T POSITIVE BIAS
160X 25KV WD : 12MM S : 00000 P : 00033
200UM
BSE SUM

Figure 30: Comparison between (left) a secondary electron (SE) image providing topographical information on the sample and (right) backscattered electron image providing compositional information [100].

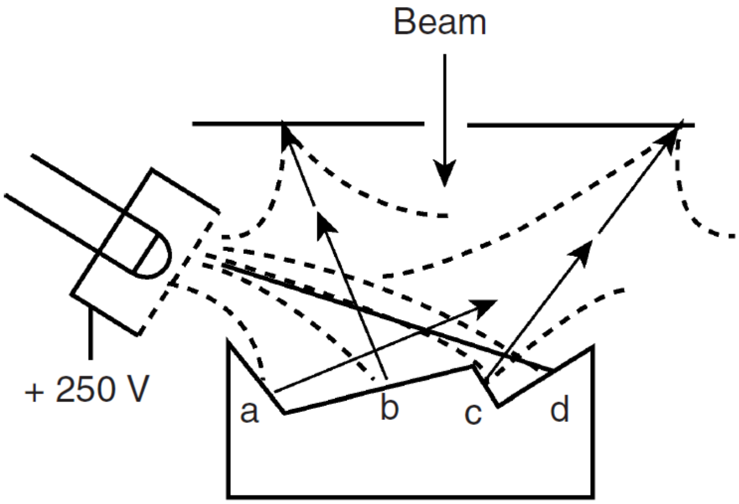
Beam
+ 250 V
a
b
c
d

Figure 31: Generation of topographic contrast in an image obtain by SE in an SEM due to trajectory effects [100].

This is why secondary electron topography imaging in SEMs is often referred to a pseudo-3D technique, since this feature of the response of the material to the beam provides an image that gives the impression of the 3-dimensionality of the specimen analysed.

The signal collected after interaction with the specimen can also be of an elastic nature, e.g. from the elastic interaction of electrons of the beam with the atoms of the material, and provides Z-contrast (contrast based on the atomic number of the species interacting with the beam) or the orientation of the crystallites. Those electrons are called backscattered electrons, BSE. For the purpose of collecting the backscattered electrons to image the compositional contrast in the specimen, the signal is collected by a detector which is placed just around the slit through which the incident beam passes, at the bottom of the acceleration column. The yield of backscattered electrons on the BSE detector depends on the ease with which those can elastically escape the material which in turn depends on the chemical species interacting with the beam. The higher the atomic number Z of the species from which they are diffracted back, the higher the interaction cross-section between the electron and the atom, the lower the yield; contrast arises: Z-contrast or compositional contrast. Interaction of the beam with the specimen can also yield lower energy electrons originating from the outer shells of the atoms involved, whose energy depends on the atomic species interacting. These electrons are called Auger electrons and provide chemical composition information on the material studied. Last but not least importantly, BSEs can also provide information on the crystallographic nature of the sampled region for which another detector in the chamber is in charge of collection, the EBSD detector (Figure 33). This kind of detector is used to acquire diffraction patterns originating from the back scattered diffraction of beam electrons with the specimen, from which orientation data can be obtained. Such information consists in the orientation of the crystalline domains with respect to the specimen coordinates.

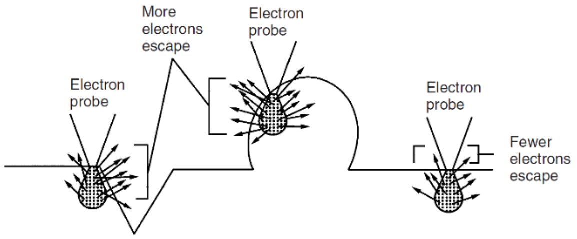

Figure 32: Generation of topographic contrast due to electron-number effects. More secondary electrons can escape features such as edges as compared to a flat surface [100].

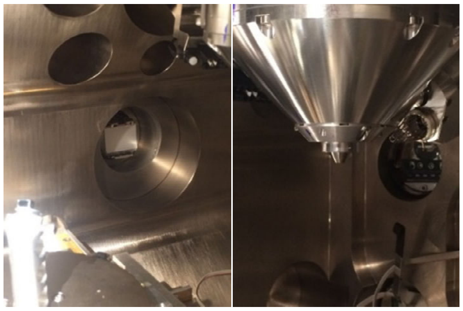

Figure 33: Details of the vacuum chamber showing, on the left, the EBSD detector in its retracted condition. On the right, the bottom of the column where the electron beam is focused to create the desired probe with, on its right, the Everhart-Thornley detector in charge of collecting secondary electrons for imaging purposes. Picture from the author.

The existence of crystallographic planes in polycrystalline materials makes it such that, for a specific family of planes (here to be intended as groups of parallel planes) being hit, a constructive interference of scattered electrons in specific directions will develop: crystallographic planes are diffracting electrons into specific directions at angles according the Bragg's Law:

$$n\lambda = 2d \sin\theta \tag{52}$$

where n is the diffraction order, λ is the wavelength of the electron and d is the interplanar distance between the parallel crystallographic planes. The diffracted signal on a detector consists of multiple, different bands of higher intensity of electrons (Kikuchi Bands as in Figure 34), each of which originating from a different family of parallel planes, and form a pattern. Microscope softwares take care of the automatic identification of such patterns revealing the orientation of the crystal structure of sampled volume with respect to the specimen reference system. Upon scanning of an area which is representative of the sample studied, the microstructure and the texture of the material studied can be determined.

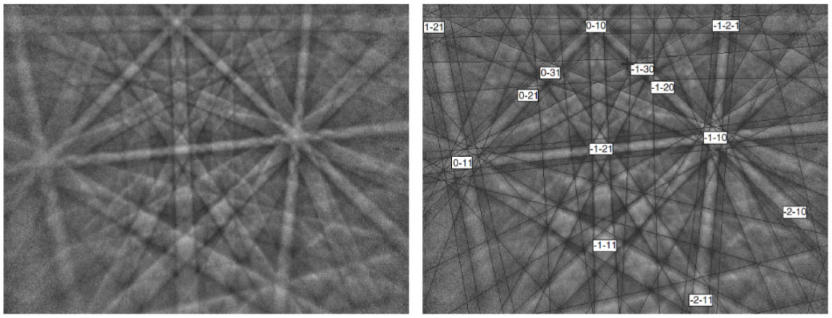

Figure 34: EBSD pattern from copper consisting of Kikuchi bands. On the right the same pattern is indexed and zone axis poles specified by Miller indices [101] .

2.10 Tools, the texture

2.10.1 Crystallography

Solid state materials are present in the universe in different shapes or forms, but all can be considered to possess a specific internal structure. They are termed to possess a crystalline or amorphous structure, depending on whether or not the atoms they are made of are arranged in an ordered manner, meaning atoms are organised in a regular, long range, periodic arrangement. Such a 3D arrangement can be summarized and reduced to single units constructing it. The unit cells are the elemental units the entire long range ordered arrangements of atoms considered can be entirely re-built from. Unit cells are described by use of three vectors, indicating the directions within them and distance from a chosen origin, the translation vectors, together with the three angles. If there is not a cell of smaller volume that can be used to rebuild the entire arrangement, the cell is termed primitive (unit cell). All the end points of translation vectors in space constitute the lattice of a specific crystalline structure and such a regularity denotes the so-called translation symmetry of the crystal structure. The material can consist of single atomic species, e.g. iron atoms, or could also be formed by several different ones, e.g. Cu and Zn atoms in brass. In each crystalline material, there will be a specific primitive unit cell and a specific translation lattice. The choice of which atom sits at each of those lattice points is represented by the motif. In this way a crystalline structure (Figure 35) is defined:

$$crystal\ structure = translation\ lattice + motif \tag{53}$$

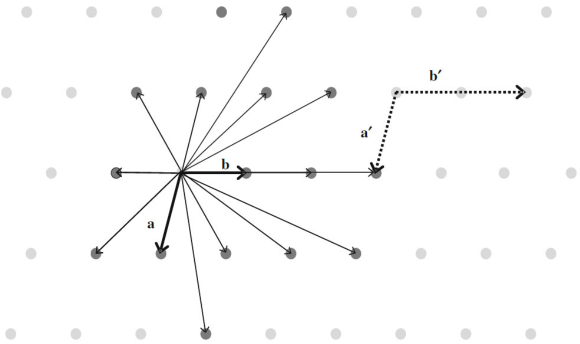

Figure 35: 2D crystal structure with translation vectors represented in the form of arrows connecting what can be seen as the basis or the points of the translation lattice [25].

Crystal structures are characterized by their symmetry or to a better statement, by all the symmetry operations, translational and rotational after which the original lattice remains unchanged.
In nature, every three dimensional crystal can be framed to belong to a specific crystal system. A crystal system is a group of crystalline structures that upon symmetry and translation operations retains their original structure, e.g. the operations leave the crystal structure unchanged. If one considers the translation vectors to be a, b and c, and angles in between them, α, β and γ, the crystal systems found in nature can be characterized into seven different kinds as follows:

1. Cubic $a = b = c$ and $\alpha = \beta = \gamma = 90°$
2. Tetragonal $a = b \neq c$ and $\alpha = \beta = \gamma = 90°$
3. Orthorombic $a \neq b \neq c$ and $\alpha = \beta = \gamma = 90°$
4. Hexagonal $a = b \neq c$ and $\gamma = 120°, \alpha = \beta = 90°$
5. Trigonal $a = b = c$ and $\alpha = \beta = \gamma$
6. Monoclinic $a \neq b \neq c$ and $\alpha = \gamma = 90°$
7. Triclinic $a \neq b \neq c$ and $\alpha \neq \beta \neq \gamma$

A more common and pragmatic categorization of those is that of the Bravais Lattices, describing the translational symmetry of crystal structures only. In total, there are 14 different Bravais lattices: 7 are those whose requirements on the translation lattice and angles coincide with those formerly defined for the crystal structures and other seven stem from four of these just mentioned seven, with the difference that special additional constrains for the parameters of the primitive cell must be taken into consideration. As an example, if one takes the rhombohedral primitive cell and adds the constrain of $\alpha = \beta = \gamma = 60°$, this new cell can also be described (e.g. the crystal structure can be defined with a different set of constrains) by a non-primitive cubic cell having constrains $a = b = c$ and $\alpha = \beta = \gamma = 90°$: the so called face centred cubic (fcc) lattice. Similarly, the body centred cubic (bcc) non primitive cell can be described by a rhombohedral primitive cell having the $\alpha = \beta = \gamma = 109.5°$ constrain. Below in Figure 36 a description of the possible 14 Bravais lattices is shown.

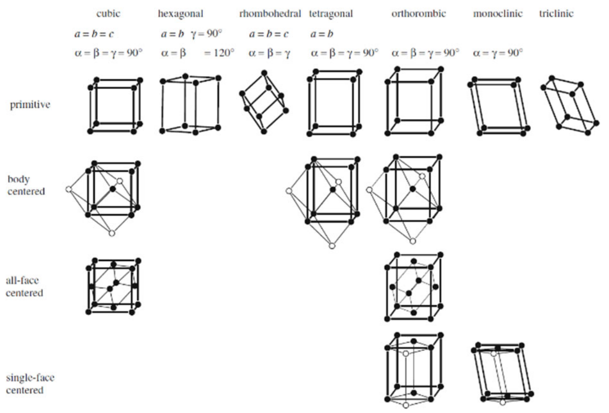
cubic
hexagonal
rhombohedral
tetragonal
orthorombic
monoclinic
triclinic
a = b = c
α = β = γ = 90°
a = b γ = 90°
α = β = 120°
a = b = c
α = β = γ
a = b
α = β = γ = 90°
α = β = γ = 90°
α = γ = 90°
primitive
body centered
all-face centered
single-face centered

Figure 36: Description of all the possible 14 Bravais lattices [25].

In order to usefully address the directions or planes for each lattice, the Miller (or Miller-Bravais for hexagonal crystals) indices have been developed. Briefly, a direction in the lattice can be provided by a linear combination of components along the axes defined by the translation vectors a, b and c, in a way that the total translation vector from the origin can be described as:

$$r = u\boldsymbol{a} + v\boldsymbol{b} + w\boldsymbol{c} \tag{54}$$

where u, v and w are integers and indicate the magnitude of the translation in the direction specified by the axes and indicate the lattice direction(s) (they indicate crystallographically equivalent families of directions as well as there are infinite parallel lattice direction to a one uvw). Each direction is indicated in Miller notation as $[uvw]$ while families of directions as $< uvw >$. Similarly, any set of points on the a, b and c axes in the form a/h, b/k and c/l can define a plane and hence any $na/h, mb/k$ and tc/l with an integer n, m, t defines a family of crystallographically equivalent planes. When one or two integers are equal to 0, it means the plane will never cross the axis to which the null integers belong, identifying planes parallel to that axis. To identify a plane, one has first to determine the points of intersection with the three axes then take their reciprocal value and finally multiply or divide them by the common factor rendering that set as one with the smallest integer numbers. In such a way the plane (or family of planes) is determined and identified by three integers as Miller indices and is written as (hkl), while families of planes with curly brackets as $\{hkl\}$.

The symmetry proper of the lattice can be such that some planes designated by the different integers, actually correspond to the same family of planes: a $\{111\}$ family is equivalent to the $\{\bar{1}11\}$. For cubic crystals for example, for every hkl combination, equivalent families are obtained for whatever arbitrary permutation of h, k and l but also for any change of those into their negative equivalent. This in turn means that, for cubic symmetries, a maximum of 48 equivalent planes families can be obtained although for some sets, part of the families are "degenerated", in a sense that only less than 48 are actually existing: e.g. 8 for the $\{111\}$ family and only 6 for the $\{110\}$ family.

2.10.2 Representation of orientations and texture

In order for an orientation to be specified, two orthogonal reference systems need to be defined, one proper to the specimen out of which the orientation is to be determined, the specimen coordinate system, and one related to the crystal structure, the crystal coordinate system. While the former is usually set to have some sort of reference to the relevant direction proper of the specimen, e.g. for the case of rolled products, the rolling, transverse and normal directions (respectively RD, TD and ND as in Figure 37), the latter is determined by the nature of the crystal (albeit the choice being completely arbitrary), e.g. the main directions proper of the crystal symmetry in play, e.g. for cubic crystals, the axes subtended by the $[100]$, $[010]$ and $[001]$ directions. Both systems are Cartesian.

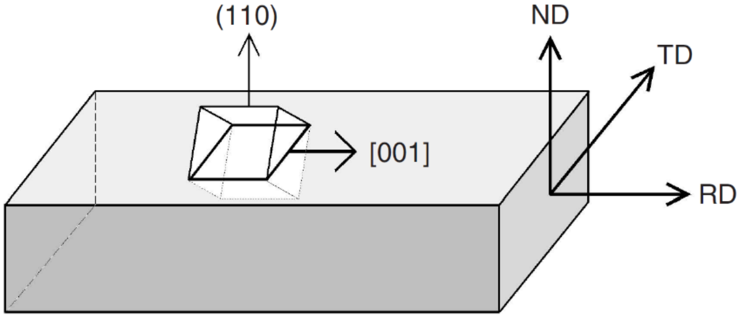

Figure 37: Illustration of the preferred orientation desired in power transformer technology related products, the Goss orientation, having the normal of the (110) planes parallel to the normal direction of the specimen (ND) and the [100] direction parallel to the rolling direction (RD) [102].

2.10.2.1 Rotation Matrix

Either of the two reference systems afore mentioned can be taken to coincide with the other, by means of a rotation that can be described by a rotation, or orientation matrix, g [102], [103] as follows:

$$C_c = \begin{pmatrix} x_c \\ y_c \\ z_c \end{pmatrix} = gC_s = g \begin{pmatrix} x_s \\ y_s \\ z_s \end{pmatrix} \tag{55}$$

where C_c and C_s are the coordinates with respect to the crystal and specimen reference coordinate systems respectively. The rotation matrix describes therefore a coordinate transformation between two different reference systems. All matrices are 3x3 matrices and g is obtained via the so called direction cosines of the angles in between the two different reference systems. Specifically, the first row of the orientation matrix is obtained by the cosines of the angles (α_1, β_1 and γ_1) in between one crystal axis, the $[100]$ and each of the three specimen coordinate system axis, X,Y and Z. The same holds for the remaining two axes (angles α_2, β_2 and γ_2 and α_3, β_3 and γ_3 for the axes [010] and [001]):

$$g = \begin{pmatrix} cos\alpha_1 & cos\beta_1 & cos\gamma_1 \\ cos\alpha_2 & cos\beta_2 & cos\gamma_2 \\ cos\alpha_3 & cos\beta_3 & cos\gamma_3 \end{pmatrix} = \begin{pmatrix} g_{11} & g_{12} & g_{13} \\ g_{12} & g_{22} & g_{23} \\ g_{13} & g_{23} & g_{33} \end{pmatrix} \tag{56}$$

It is critical to note that both rows and columns of the orientation matrix are vectors. The matrix is orthonormal, making the inverse of the matrix equal to its transpose.

Depending on the symmetry of the crystal system (and the specimen symmetry), there can be more than a single solution for a rotation operation. In the case of cubic symmetry there can be 24 different orientations that can suffice for the operation to be correct, hence, there are 24 possible solutions which are often termed, crystallographically related/equivalent. The cubic symmetry is the highest symmetry in between all crystal systems: e.g. hexagonal and orthorhombic crystals have 12 and 4 possible solutions respectively. Each of this 24 solutions is an orientation matrix valid for the operation performed and each can be considered the correct description of the orientation of each of the two systems with respect to the other.

2.10.2.2 Ideal Orientation (Miller or Miller-Bravais Indeces)

A very practical description of orientations, especially for laminated products as rolled plates, is that via Miller indices [102]. This is done by multiplying by a factor (N_1, N_2 or N_3 for the X, Y and Z directions respectively) the direction cosines of the first and last columns, respectively the X and Z directions of the specimen expresses in crystal coordinates, making all indices integer, and then dividing them by their lowest common denominator. In its final form, this orientation specification will be written in the form $(uvw)[hkl]$, where uvw, hkl, but also qrs factors (Miller indices) are specified in their orientation matrix g as follows:

$$g = \begin{pmatrix} \frac{u}{N_1} & \frac{q}{N_2} & \frac{h}{N_3} \\ \frac{v}{N_1} & \frac{r}{N_2} & \frac{k}{N_3} \\ \frac{w}{N_1} & \frac{s}{N_2} & \frac{l}{N_3} \end{pmatrix} \quad (57)$$

Use of only two directions is sufficient given the properties of such a matrix, as formerly mentioned, for which the Y direction can be determined by cross product between the other two: $[qrs] = (hkl) \times [uvw]$. The advantage of this kind of description is that specific orientation can be related to relevant specimen directions, a particularly handy method to denote textures of particular interest as in the case of the desired preferred orientation in power transformers as depicted in Figure 37. One should be careful though, since some orientations that might look identical (due to the presumed crystal symmetry) are actually not. As an example, for a cubic crystal, the $(123)[63\bar{4}]$ orientation is not equal (is not the an other solution of the orientation matrix) to $(123)[\bar{6}\bar{3}4]$.

2.10.2.3 Pole and Inverse Pole Figures

An alternative description of the orientation of any direction considered in the crystal can be expressed by the locus, the pole, where this vector hits a sphere surrounding the specimen. If this sphere is a specific reference system, the specimen system for example, then, it is possible to describe the single orientation with respect the reference frame of the sphere and hence determine the orientation matrix [104]. In order to visualize such a representation of orientations, the 3D sphere needs to be translated into a 2D figure and this is usually done using either the stereographic projection or the equal area projection.

The angle α describes the angle in between the pole and the azimuth, the north pole of the reference sphere (as in Figure 38) while β is the angle describing the rotation of the pole around the polar axis. It useful to set the sphere reference system parallel to the relevant specimen directions, which in the case of a rolled plate are the RD, TD and ND; with the north pole of the sphere, conventionally, taken as ND. In such a way the two reference systems are set and definition of the orientation(s) possible.

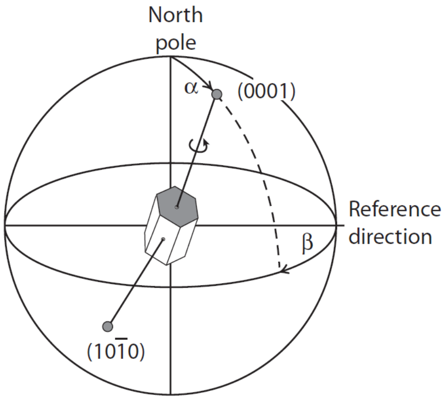

Figure 38: Orientation of the basal plane of an hexagonal crystal where the position of the (0001) pole is defined by the two angles α and β, although an additional pole is required for a univocal definition of the orientation, considered the remaining degree of freedom due to the rotational symmetry around the (0001) pole [78].

Parametrisation of the orientation using such a method can be set as follows: again we have a set of three axes per coordinate system (orthonormality conditions apply), $C_s = C_s(s_1, s_2, s_3)$ and $C_c = C_c(c_1, c_2, c_3)$. Any pole of interest can be defined as:

$$R = s_1 \sin(\alpha)\cos(\beta) + s_2 \sin(\alpha)\sin(\beta) + s_3 \cos(\alpha) = \frac{1}{N}(c_1 X + c_2 Y + c_3 Z) \qquad (58)$$

where s_1, s_2, s_3 are the unit vectors of the specimen reference system, c_1, c_2, c_3 are the unit vectors of the crystal reference system, X, Y, Z are the coordinates of the pole in crystal reference frame and $N = \sqrt{X^2 + Y^2 + Z^2}$ is the normalizing constant to turn R into unity. The above formulated definition formulated into matrices is as follows:

$$\begin{pmatrix} \sin(\alpha)\cos(\beta) \\ \sin(\alpha)\sin(\beta) \\ \cos(\alpha) \end{pmatrix} = \frac{1}{N} \begin{pmatrix} g_{11} & g_{12} & g_{13} \\ g_{12} & g_{22} & g_{23} \\ g_{13} & g_{23} & g_{33} \end{pmatrix} \begin{pmatrix} X \\ Y \\ Z \end{pmatrix} \tag{59}$$

One pole only is not sufficient to exactly define an orientation, considering the remaining degree of freedom due to the possible rotation around the pole axis and a second pole is therefore required. Usually, visualization of the orientation of a sample by pole figures is carried out by using three pole figures, most frequently using the [100], [110] and [111] directions, such as in Figure 39, unless a specific direction of interest is preferred over one of the others.

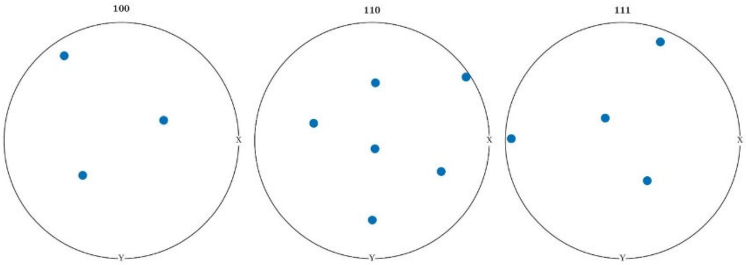

Figure 39: Different crystal poles ([100] left, [110] centre and [111] right) of a diffracting volume within a material. More than one point is visible for each pole figure since each family of planes have more than one plane present in the crystalline system.

Using pole figures to represent orientations means replying to the question: where are crystal directions pointing at? Conversely, one could ask the following: which crystal direction points (or to better say, is parallel) to a specific specimen direction? While in the first case, one would deal with the afore-mentioned visualization of orientations by pole figures, in the latter one, one uses inverse pole figures. Specifically, while in the case of pole figures the orientation of the crystal coordinate system is represented with respect to the specimen coordinate system, in inverse pole figures, it is the opposite: the orientations of the specimen system are projected onto the crystal reference system. Similar to pole figures, we define two angles ε and ϑ to track the positioning of a specimen axis with respect to the coordinate system of the crystal so that any vector s parallel to a specific specimen axis can be defined as:

$$s = c_1 \sin(\varepsilon)\cos(\vartheta) + c_2 \sin(\varepsilon)\sin(\vartheta) + c_3 \cos(\vartheta) \tag{60}$$

with scalar multiplication leading to:

$$\begin{pmatrix} X_c \\ Y_c \\ Z_c \end{pmatrix} = \begin{pmatrix} c_1 \sin(\varepsilon)\cos(\vartheta) \\ c_2 \sin(\varepsilon)\sin(\vartheta) \\ c_3 \cos(\vartheta) \end{pmatrix} = \begin{pmatrix} g_{11} & g_{12} & g_{13} \\ g_{12} & g_{22} & g_{23} \\ g_{13} & g_{23} & g_{33} \end{pmatrix} \cdot \begin{pmatrix} X_s \\ Y_s \\ Z_s \end{pmatrix} \tag{61}$$

with X_s, Y_s and Z_s being the unit vectors in the specimen reference frame. Such a representation is particularly useful in specimens possessing specific symmetries, like axial symmetric products as drawn wires, ans rolled products. Thanks to the symmetry some crystal systems have, it is sometimes not needed to display the entire inverse pole figure. For the case of cubic crystals for example, specifically the $m\bar{3}m$ space group, just the so-called unit triangle whose vertices are indicating the <100>, <110> and <111> families of directions will suffice to represent all the orientations (Figure 40).

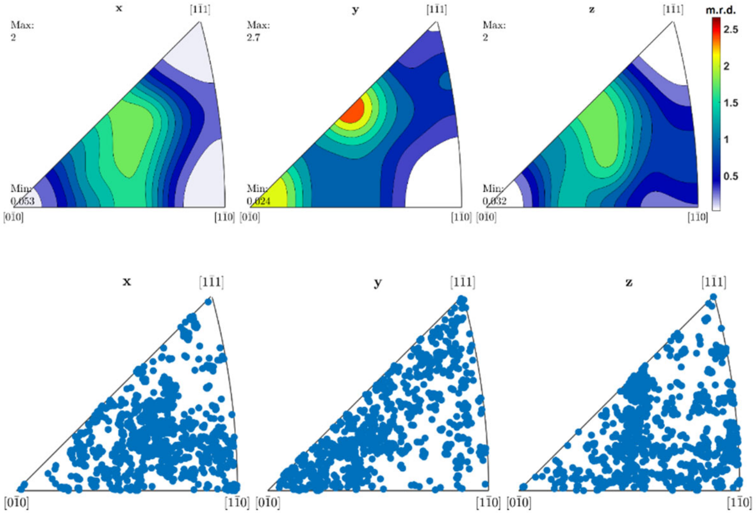

Figure 40: Inverse pole figures displaying the crystal directions within the specimen parallel to each of the specimen reference system axes, X, Y and Z. Colors describe the intensity in multiples of random density, from the highest occurring (red) to the lowest occurring (white) as illustrated in the color bar on the side. In the bottom image, blue points indicate each single measured direction for each of the specimen directions , x=RD, y=ND and z=TD.

2.10.2.4 Euler angles and Euler space

Given that three variables only are needed to define an orientation (together with the two systems of reference) a method using these three only was devised and rapidly became the most commonly used in microtexture practice: that of the Euler Angles [105]. The most common convention used to express these three angles is that formulated by Bunge [106] with the three angles being φ_1, Φ and φ_2 defined as the angle describing the rotation(s) of the crystal reference frame with respect to the specimen reference frame, making use of new provisional specimen reference frames (rotated) at each rotation, to describe the consecutive. If one takes two coincident reference systems of axes *X, Y, Z* and *X', Y'* and *Z'*, one can describe the Euler angles as follows: the first rotation (by φ_1) is performed around the Z' axis, having now the *X* and *X'* or *Y* and *Y'* axes not parallel any longer (Figure 41b), a second subsequent rotation (Φ) is that about the *X'* axis, changing the direction of the *Y'* and *Z'* axes (respect to the *XYZ* based coordinate system) again (Figure 41c), and then a third last rotation (φ_2) again about the *Z'*(Figure 41d).

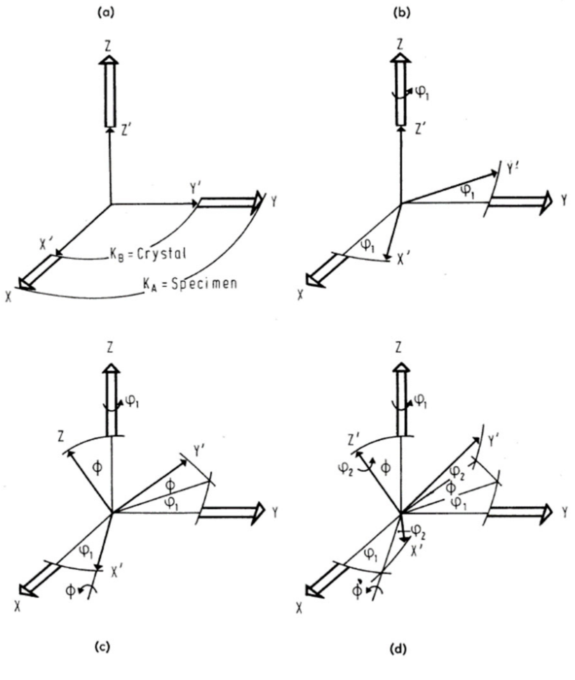

Figure 41: Description of the three rotations defining the Euler Angles [104].

These three rotations can be described as follows:

$$g_{\varphi_1} = \begin{pmatrix} \cos(\varphi_1) & \sin(\varphi_1) & 0 \\ -\sin(\varphi_1) & \cos(\varphi_1) & 0 \\ 0 & 0 & 1 \end{pmatrix} \qquad (62)$$

$$g_{\Phi} = \begin{pmatrix} 1 & 0 & 0 \\ 0 & \cos(\Phi) & \sin(\Phi) \\ 0 & -\sin(\Phi) & \cos(\Phi) \end{pmatrix} \tag{63}$$

$$g_{\varphi_2} = \begin{pmatrix} \cos(\varphi_2) & \sin(\varphi_2) & 0 \\ -\sin(\varphi_2) & \cos(\varphi_2) & 0 \\ 0 & 0 & 1 \end{pmatrix} \tag{64}$$

and thanks to their properties, the overall rotation can be expressed as the product of the three matrices: $g = g_{\varphi_1} g_{\Phi} g_{\varphi_2}$ so that the overall orientation matrix using Euler angles is:

$$\begin{aligned} g &= \begin{pmatrix} g_{11} & g_{12} & g_{13} \\ g_{12} & g_{22} & g_{23} \\ g_{13} & g_{23} & g_{33} \end{pmatrix} \\ &= \begin{pmatrix} \cos(\varphi_1)\cos(\varphi_2) - \sin(\varphi_1)\sin(\varphi_2)\cos(\Phi) & -\cos(\varphi_1)\sin(\varphi_2) - \sin(\varphi_1)\cos(\varphi_2)\cos(\Phi) & \sin(\varphi_1)\sin(\Phi) \\ \sin(\varphi_1)\cos(\varphi_2) + \cos(\varphi_1)\sin(\varphi_2)\cos(\Phi) & -\sin(\varphi_1)\sin(\varphi_2) + \cos(\varphi_1)\cos(\varphi_2)\cos(\Phi) & -\cos(\varphi_1)\sin(\Phi) \\ \sin(\varphi_2)\sin(\Phi) & \cos(\varphi_2)\sin(\Phi) & \cos(\Phi) \end{pmatrix} \end{aligned} \tag{65}$$

As an example, the ideal Goss orientation can be expressed by the three Euler angles $\varphi_1 = 0°, \Phi = 45°$ and $\varphi_2 = 0°$. Other relevant ideal orientations are listed in Table 2.

Table 2: Common relevant ideal orientations for cubic-orthorombic symmetries also expressed in Euler Angles. Only one set of Euler angles is given. The complete list of equivalent Euler angles defining each single ideal orientation amounts to 96 possibilities (24 x 4 = 96). After [104].

Component	**Miller Indices**	**Euler Angles (φ_1, Φ, φ_2) in degrees (°)**
cube	$\{001\} < 100 >$	(0°, 0°, 0°)
Brass	$\{011\} < 2\bar{1}1 >$	(35.264°, 45°, 0°)
Copper	$\{112\} < \bar{1}\bar{1}1 >$	(90°, 35.264°, 45°)
S	$\{213\} < \bar{3}\bar{6}4 >$	(58.98°, 36.699°, 63.435°)
Goss	$\{011\} < 100 >$	(0°, 45°, 0°)
Rotated cube	$\{001\} < 1\bar{1}0 >$	(0°, 0°, 45°)
Dillamore	$\{4\ 4\ 11\} < 11\ \overline{11}\ 8 >$ $\{111\} < \bar{1}\bar{1}2 >$ $\{112\} < 1\bar{1}0 >$ $\{113\} < 1\bar{1}0 >$	(90°, 27.215°, 45°) (90°, 54.736°, 45°) (0°, 35.264°, 45°) (0°, 25.239°, 45°)

Representation of an orientation defined by these three angles requires a 3D space, whose axes are orthogonal (Cartesian) and describe the magnitude of φ_1, Φ and φ_2. Hence, any orientation can find its specific place in this space, as if it was a point in space given *X, Y* and *Z* coordinates. The difference is that this space is clearly limited by the maximum possible value of a rotation due to the periodicity, 360°, but also by the symmetry of the crystal system. The lowest the symmetry, the maximum the size of the Euler space: e.g. for the triclinic symmetry $0° \leq \varphi_1, \Phi, \varphi_2 \leq 360°$ (constituting the so-called asymmetric Euler space unit) while for a bcc crystal symmetry, $0° \leq \varphi_1, \Phi, \varphi_2 \leq 90°$, a region only is sufficient (the asymmetric Euler space unit is subdivided into 4 x 4 x 4 = 64 equivalent subspaces for which there are 24 different possibilities to describe one and the same orientation, given an orthorhombic specimen symmetry). Misorientations can also be represented using the Euler space. In this case though, the crystal symmetry comes in play and further reduces the Euler space by 24 times. Additionally, since a misorientation is equal to its inverse (inverse misorientation) the Euler space is further reduced by 2. As a matter of fact, for cubic crystal symmetries there are 24x24x2=1152 possible ways of defining a misorientation, e.g. the asymmetric Euler space unit can be subdivided into 1152 equivalent subspaces.

2.10.2.5 Orientation Distribution Function (ODF)

The orientation distribution (OD) is a pivoting concept in texture analysis: such a distribution is used to describe the probability (normalized to have units of multiples of a random density) of finding a given orientation for a specific set of parameters defining the orientation itself [104]. Distribution functions can be defined in any continuous, periodic space describing rotations, for which three variables are needed and hence, for orientations, they can be defined via e.g. axis/angle pairs, Rodrigues vectors, unit quaternions or, Euler angles. Each point in the orientation distribution represents a single specific orientation. An orientation distribution can be described by a function, the orientation distribution function (ODF), sometimes also called orientation density function, which is a function in the orientation space that associates to each orientation g the volume percentage of crystals in a polycrystalline specimen that are in this specific orientation. The ODF has been historically associated to the series expansion method used to fit pole figure data to the generalized spherical harmonic functions – an OD based on this functions is of a continuous form of a kind, albeit a description of the OD can also be described in a discrete form. Harmonics functions and their coefficients constitute a mathematical entity to describe texture. If one aims at describing the orientation of each crystal region of a polycrystalline material, a function representing the orientation for each point in space (located at x,y,z coordinates) must be specified as:

$$g = g(x, y, z) \tag{66}$$

which written in Euler angles is:

$$\varphi_1 = \varphi_1(x, y, z) \tag{67}$$

$$\Phi = \Phi(x, y, z) \tag{68}$$

$$\varphi_2 = \varphi_2(x, y, z). \tag{69}$$

This means three functions are required, which are discontinuous, since grain boundaries divide crystalline regions from which orientation shall be described. This way of representing orientation can be mathematically quite complex and often impracticable so a simpler solution is preferred, which is to describe the orientation data of a sample neglecting the spatial coordinates so to avoid the discontinuity problem of those functions. If one denotes with dV all the regions of a sample possessing an orientation g with an elemental orientation dg and by V the total volume of the sample, then formally an orientation distribution function for that volume can be defined as:

$$f(g) = \frac{dV}{V\,dg} \tag{70}$$

Likewise, orientation differences of adjacent (sub)grains can be defined by a similar function if one takes the misorientations, instead of the orientations, and the boundaries between these different orientation regions dF, as the variable to be described:

$$f(\Delta g) = \frac{dF}{F\,d(\Delta g)} \tag{71}$$

where dF denotes the surface across which there is a misorientation (orientation difference) Δg, within the misorientation element dΔg. As formerly mentioned, ODFs have been historically developed by using series of generalized spherical harmonics so that a function $f(g)$ can be described using Euler angles as follows:

$$f(\varphi_1, \phi, \varphi_2) = \sum_{l=0}^{\infty} \sum_{m=-l}^{+l} \sum_{n=-l}^{+l} C_l^{mn} e^{im\varphi_2} P_l^{mn}(\Phi) e^{in\varphi_1} \tag{72}$$

Without getting into the mathematics of this description, such a function can represent orientation data and for its determination, fitting to data is necessary (determination of the coefficients in the spherical harmonics function). This can be done by exploiting the pole figures since they are projections of the orientation distribution. Data is available in a discrete form as e.g. EBSD. If one defines a cell on the surface of the sphere, where one can find poles sitting in, to be used to describe poles belonging to a specific orientation, then upon the summation of all intensities from all the cells and normalization, one can obtain the ODF (in bold) as:

$$1 = \frac{1}{8\pi^2} \sum_{\varphi_1} \sum_{\phi} \sum_{\varphi_2} \boldsymbol{f(\varphi_1, \phi_i, \varphi_2)}\, \Delta\varphi_1 \Delta\varphi_2 \left(cos\left(\phi_i - \frac{\Delta\phi}{2}\right) - cos\left(\phi_i + \frac{\Delta\phi}{2}\right) \right) \tag{73}$$

Such a function is very useful when one wants to determine the volume fraction of orientations $V_f(g)$ from the analyzed texture:

$$V_f(g) = \frac{\Delta V(g)}{V} = \frac{\int_{d\Omega} f(g) dg}{\int_{\Omega} f(g) dg} \tag{74}$$

where Ω indicates the entire orientation space and dΩ the region (volume) around the texture component of interest. Representation of such a function is conventionally done in the Euler space, via sections of such a space as in Figure 42: these planes indicate the variation of the OD intensity (as contour maps), having a third angle value fixed (defining the plane). The Euler space is shown on paper or screens by cuts of the Euler space either along the $\varphi_1$or φ_2 direction (e.g. $\varphi_2 =$

5°/10°/15° etc.). For specific cases, along those cuts, features belonging to the texture of materials possessing specific crystal systems and processed in a specific way (e.g. rolling of bcc materials) can be seen (Figure 43): e.g. the α-fiber and γ-fiber.

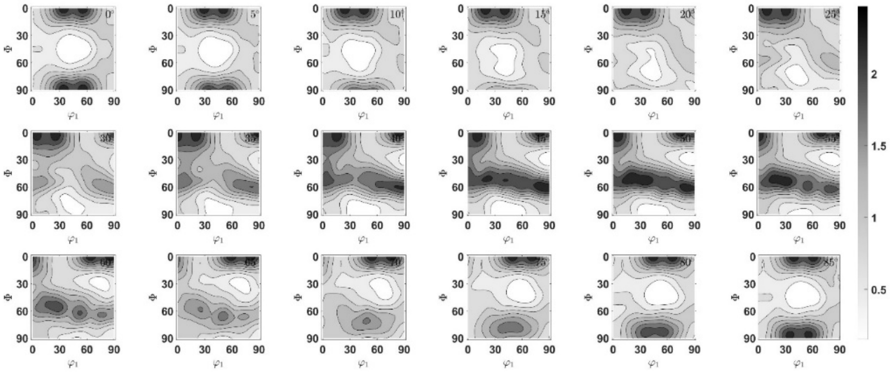

Figure 42: The entire Euler space (in sections) where the OD of a pure bcc transition metal is displayed. In the φ_2 = 45° section, the α-and γ-fibers can be seen

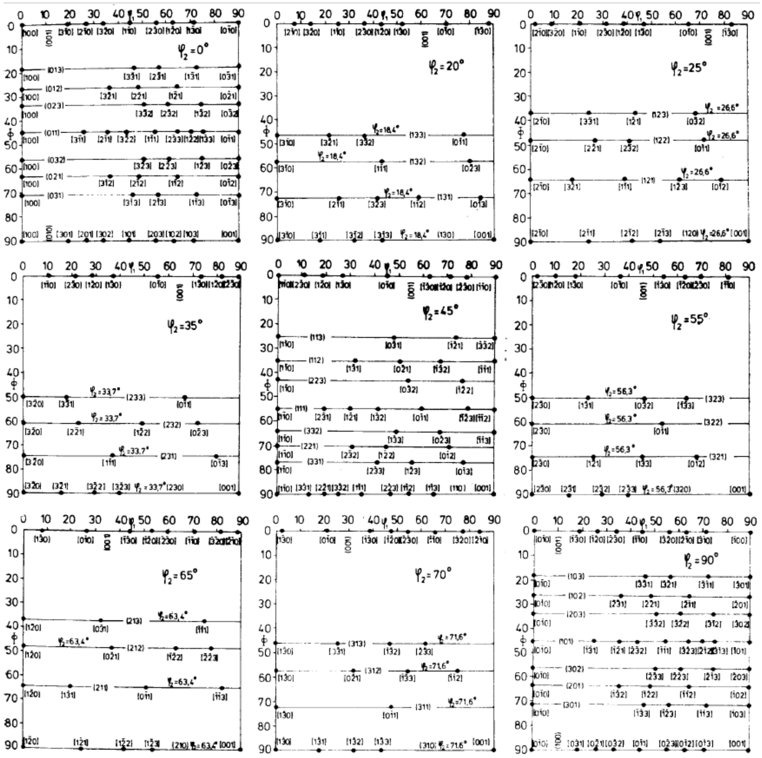

φ2 = 0°
φ2 = 20°
φ2 = 25°
φ2 = 35°
φ2 = 45°
φ2 = 55°
φ2 = 65°
φ2 = 70°
φ2 = 90°
φ1
Φ
0
10
20
30
40
50
60
70
80
90

Figure 43: Section of the euler space indicating the lowest Miller indeces ideal orientations and fibers [104].

Chapter 3. Materials, Methods and tools

3.1 Materials

The materials studied in this project were of two different kinds. Tungsten was studied in the form of plates, rolled to different reductions and in the form of W_fW consisting in drawn wires, surrounded by a CVD matrix of pure tungsten.
The different plates analysed consisted in two different batches. The first one was a batch of four rolled thin plates (TPs) of technical purity (higher than 99.97% wt.%), warm- and subsequently cold-rolled, rolled to different thickness reductions, manufactured at Plansee SE in Reutte, Austria. Their thicknesses is of 2 mm (TP2), 1 mm (TP1), 0.5 mm (TP0.5) and 0.2 mm (TP0.2). The RD and TD dimensions of all plates were 250 mm and 100 mm respectively for each TP but the TP2, which had the opposite (e.g. 100 mm RD and 250 mm TD) The two thicker ones were warm rolled only, while the two thinner ones, underwent additional final processing stages of cold-rolling. Each of the TPs was cut into smaller samples of dimensions equal to 5 mm x 4 mm x thickness of the plate respectively, with the longest direction belonging to the longest direction of each plate which, for the TP2, was TD while for all the remaining plates RD.

The second batch of plates consisted of a single plate, warm rolled to a reduction of 80 % (W80). The thickness of this plate (W80) was 8.3 mm with sizes along RD and TD of 200.8 mm and 100.3 mm respectively. The W80 (higher than 99.95% wt. % pure W) was produced at Advanced Technology & Materials (AT&M) Co. Ltd. in Beijing, China as follows: tungsten powder was cold-isostatically pressed and sintered under a hydrogen atmosphere at 2300 °C for 6 h. The ingot was subsequently pre-annealed at 1100 °C for 15 minutes prior to rolling to relieve stresses. After that, the ingot was warm-rolled by reverse rolling from a starting temperature of 1550 °C to a final temperature of 1100 °C in 10 passes, for a reduction of 80 %. The W80 plate was cut into smaller samples of dimensions 6 mm x 5 mm x 4 mm, along the RD, TD and ND respectively (Figure 44).

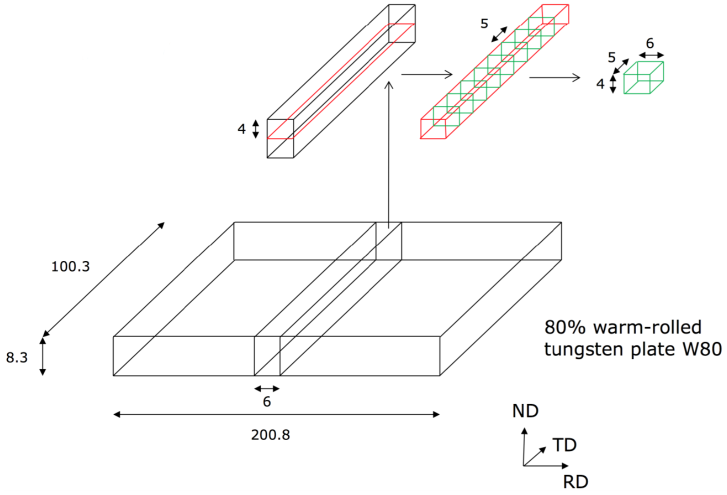

Figure 44: Cutting plan for the W80 plate.

W_fW examined in this thesis consists of three different kinds, differing by the kind of interface between the drawn wire and the CVD tungsten region. The wires belonging to the W_fW were produced by OSRAM Gmbh and are of commercial purity, doped with 60 ppm of potassium and possess a diameter of 150 µm. Only one kind did not have any rare earth oxide surrounding the wire as is thereafter termed as non-interlayered (W_f/W). Surrounding the wire, for the case of the case of interlayered W_fW, an interface of 1 µm of either yttria ($W_f/Y_2O_3/W$) or erbia ($W_f/Er_2O_3/W$) was magnetron sputtered according to the procedure as in Ref. [107]. Pure tungsten is further deposited by chemical vapor deposition (CVD) directly on the wire or the interface surrounding it at temperatures between 580 °C and 620 °C through the chemical reaction

$$\mathrm{WF_6} + 3\ \mathrm{H_2} \rightarrow \mathrm{W} + 6\ \mathrm{HF} \qquad (75)$$

to a final width of the W_fW of 3.0±0.1 mm for the W_f/W, 1.5±0.1 mm for the $W_f/Er_2O_3/W$ and 2.1±0.1 mm for the $W_f/Y_2O_3/W$. After cutting, each sample of the afore-mentioned three different kinds possessed a thickness (height) of 1.35±0.05 mm. The dimensions of all as-received materials and specimens cut for annealing campaigns object of study are reported in Table 3.

Table 3: As-received materials sizes

Material	Original Size	Specimen Sizes
Plates	(RD x TD x ND)	(RD x TD x ND)
TP2	100 mm x 200 mm x 2 mm (±0.05 mm)	4 mm x 5 mm x 2.0 mm (±0.05 mm)
TP1	200 mm x 100 mm x 1 mm (±0.05 mm)	5 mm x 4 mm x 1.0 mm (±0.05 mm)
TP0.5	200 mm x 100 mm x 0.5 mm (±0.05 mm)	5 mm x 4 mm x 0.5 mm (±0.05 mm)
TP0.2	200 mm x 100 mm x 0.2 mm (±0.05 mm)	5 mm x 4 mm x 0.2 mm (±0.05 mm)
W80	200.8 mm x 100.3 mm x 8.3 mm (±0.05 mm)	6 mm x 5 mm x 4.1 mm (±0.05 mm)
Composites	*(Longitudinal length x diameter)*	*(Diameter x thickness)*
W_f/W	350 mm x 3.0 mm (±0.1 mm)	3.0±0.05 mm x 1.35±0.05 mm
W_f/Er_2O_3/W	350 mm x 1.5 mm (±0.1 mm)	1.5±0.05 mm x 1.35±0.05 mm
W_f/Y_2O_3/W	350 mm x 2.1 mm (±0.1 mm)	2.1±0.05 mm x 1.35±0.05 mm

3.2 Oxidation

For protection of the specimens against oxidation and formation of volatile WO_3 during annealing treatments, specimens were encapsulated in quartz glass ampoules (either individually, as for the W80 (Figure 45), or together, as in the case of W_f/W, with other specimens having different interlayers and in the case of the TPs, with 4 different thicknesses all in the same ampoule). The procedure consists of evacuating the ampoules, flushing them with Argon (with purity higher than 99.99%), evacuating again and finally sealing them with a blowtorch.

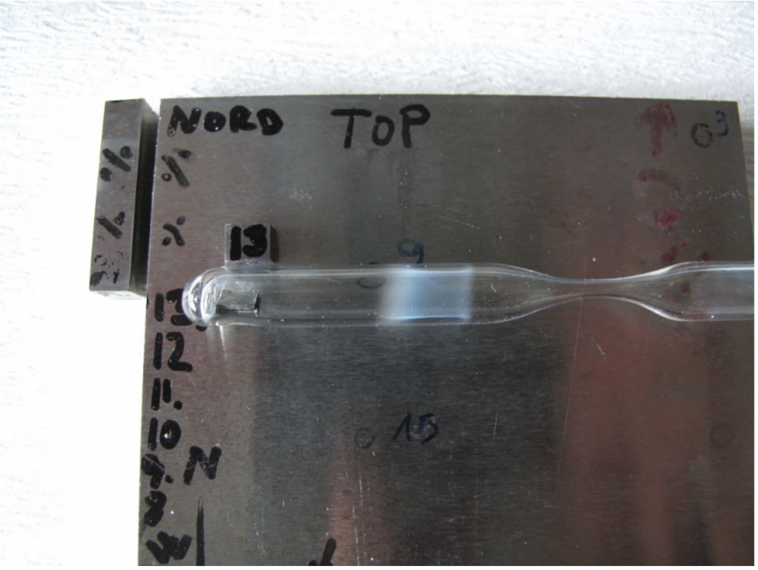

Figure 45: Encapsulated specimen ahead of ampoule enclosure.

3.3 Methods

3.3.1 Metallographic Preparation

Metallographic preparation of the surfaces to be inspected depended on the purpose. For hardness testing solely, only two steps of mechanical grinding were performed: grinding with 2000 and 4000 grit size. Each grinding step lasted 3 minutes and the force applied never exceeded 20 N. Considering the vast amount of specimens to be analysed via EBSD, the author decided not to embed any specimen into resin. Instead, all the metallographic preparation steps - besides electropolishing - were performed by conveniently and optimally enclosing each sample in a custom made support that have allowed plane parallel preparation of the surface of interest, preventing subsequent un-embedding and eventual unwanted spoiling of the prepared surfaces. For electron backscatter diffraction, the surfaces need to be free of any leftover deformation from the preparation and additional steps are required. A 3 μm size diamond paste was used for mechanical polishing solely (10 minutes long), followed by electropolishing at a voltage of 12 V, a current of 2 A and different times according to the geometry and amount of deformation expected in the specimens. Electropolishing was performed in an aqueous solution of NaOH wt. 3 %, for times ranging from 40 to 100 s for W80, from 20 s to 40 s for TPs, and from 3 to 15 s for W_f/W. In preparation for LOM, etching was performed by use of Murakami reagent, consisting in an aqueous solution of 10 g of $K_3Fe(CN)_6$ and 10 g of NaOH as recommended from [108].

3.3.2 Annealing

In order to assess the thermal stability of the studied materials, isochronal as well as isothermal experiments were performed on the different batches. Isochronal experiments were performed for twofold reasons: to assess the evolution of the kinetics of recovery and to determine the optimal temperature range for performing isothermal experiments. The reason for the latter was time efficiency: if the temperature is too high, recrystallization might take place so quickly that thorough analysis is inhibited (e.g. the heating time of the specimen in the furnace could be comparable to the incubation time for recrystallization or the time to half or full recrystallization itself). Conversely, a too low temperature would result in a kinetics that is too slow for reasonable experimental campaign times to be arranged within the time span of a doctorate or the time span allowed for completion of the task given by the funding agency. Such an isochronal experiment allows inferring of an effective temperature range for 4 or 5 isothermal experiments to fully characterise the thermal stability of the material with respect to recovery and recrystallization. Isochronal experiments were performed for the plates solely (TPs and W80) and consisted of 2 h long heat treatments in a range of temperatures going from 900 °C to 1500 °C. Isothermal experiments for all studied materials are summarised in Table 4.

Table 4: Annealing times for the different isothermal experiments performed on each of the studied materials

Material	**Temperature / °C**	**Annealing Time**
TPs	1325 / 1375 / 1400	1 h to 48 h
W80	1150 / 1175 / 1200 / 1225 / 1250 / 1300 / 1350 / 1400	1 h to 1872 h
W_fW	1350 / 1375 / 1400	6 h to 28 d

3.3.3 Vickers Hardness Testing

Hardness testing is a very efficient method of relatively low invasiveness to determine the mechanical properties of a metallic sample. The materials' resistance to deformation in compression is related to the defect content stored in the material and can be determined by the size of each indentation (the quantity measured when hardness testing) left on the indented surface [78]. For vickers hardness testing pyramidal diamond indents were used. The pyramidal groove which the surface presents at the end of the indentation time period (10 s) is characterized by the size of the diagonals of the square (base of the pyramidal void) left on the surface after indenting. The two diagonals are averaged and the hardness is determined according to the following formula:

$$HV = 2P \sin\left(\frac{136°}{2}\right) \cdot \frac{1}{L^2} = 1.854 \frac{P}{L^2} \left[\frac{kgf}{mm^2}\right] \tag{76}$$

where L is the average of the two diagonals and P is the applied load (in kgf). Loads from 10 kgf (W80) to 0.2 kgf (TPs) were used.

3.3.4 Electron BackScatter Diffraction (EBSD)

To record the orientation of crystallites and determine the evolution of texture alongside that of recrystallization via the parameters ,as in Section 2.8.3, in this work, EBSD was used. Orientations are determined by the automatic indexing of diffraction patterns on a CCD detector by the microscope software (BRUKER Esprit 2). For this work, all EBSD data was recorded using an FEI NOVA NanoSem 600 SEM (Figure 46) with applied voltages of 20 kV, apertures from 40 to 60 µm and currents ranging from 1.1 to 6.3 nA. The microscope was equipped with a Bruker e–FlashHD EBSD detector. Step sizes ranged from 2 µm for the large maps of W80 to 100 nm for the highest resolution maps of both the W_f/W and W80.

Figure 46: The FEI - NOVA NanoSem 600 used to record all orientation data for this project.

In this work, instead of analysing data via the microscope software, orientation data in the form of text files was exported and analysed in MATLAB with the MTEX Toolbox.

3.3.4.1 EBSD Data Analysis - MTEX Toolbox

The MTEX Toolbox for MATLAB© provides the possibility to visualise, analyse and interpret orientation data based on integral – pole figures – or discrete (EBSD) measurement [109]. After importing of such datasets, the texture of specimens can be visualised and analysed, orientation densities functions in terms of model functions can be calculated and scripts to evaluate other relevant microstructural information can be written. As an example, in depth analysis of all grain boundaries can be performed (misorientation distributions, curvatures, CSLs), visualisation of orientation data can be performed via more than one method (e.g. Axis/Angle, RF-space, ODFs in the Euler space), Schmid and Taylor factors evaluated, triple junction analysed, dislocations arrangement and their charachter analysed. A detailed description of the functioning of such a toolbox can be found at [109]. The tools available in such a toolbox have been key for the author to develop a customised procedure allowing a fine and comprehensive analysis of the grain boundaries separating the recovered from the recrystallized regions (Figure 47). A detailed explanation of all the microstructural features studied, their parametrisation into the coding of

MTEX and their use is reported in the manuscript titled "Microstructural path investigation into stagnation of recrystallization in warm-rolled tungsten" in Subchapter 5.2.

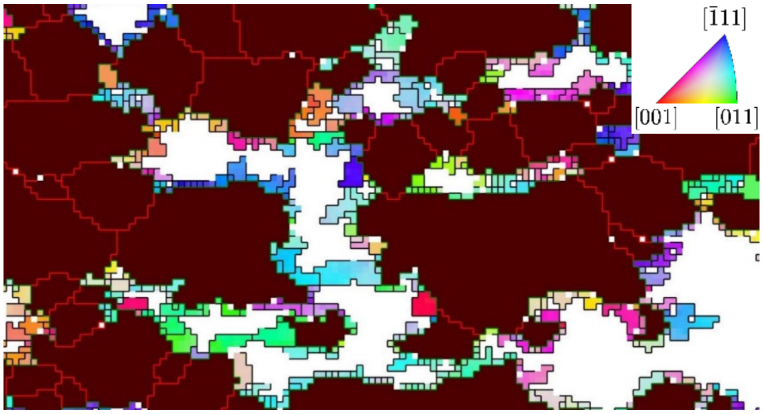

Figure 47: Detail of an orientation map of a partially recrystallized sample (W80) showing, colored in dark red, the recrystallized grains, the recovered regions (rcloc regions) ahead of the recrystallized grains colored depending on their orientation - via the inverse pole figure in the inset - according to the ND of the plate, the boundaries between the recrystllized grains (rxrx boundaries) in light brown and all the boundaries (misorientation > 2°) belonging to the rcloc region, in black.

3.3.5 Recrystallized Fraction Evaluation

The recrystallized fraction of each sample studied in this work has been evaluated in two ways: via Vickers hardness measures and via analysis of orientation maps obtained by EBSD.

In hardness testing, the size of the indentation left into the material is representative of the average flow stress needed to induce strain from deformation [77]. Both recovery and recrystallization cause a decrease in the amount of defects which can be traced by a decrease in hardness. If the hardness of a fully recrystallized sample (HV_{rex}) is measured, together with that of a heavily recovered specimen (HV_{rec}) - which is about to initiate recrystallization – those two values can be used as the extremes in between which the hardness changes during recrystallization. In the case of W80, given the absence of good recovery data the author used the hardness of the as-received condition as HV_{rec}, considering the plate underwent consistent restoration. The actual hardness, during recrystallization evolution, as a function of the fraction recrystallized X_V can be described by the rule of mixtures as follows:

$$HV = X_V\, HV_{rex} + (1 - X_V)\, HV_{rec} \tag{77}$$

and hence, by rearrangement of Eqn. 77, the fraction recrystallized can be determined via the hardness HV of the tested specimen as:

$$X_V = \frac{HV_{rec} - HV}{HV_{rec} - HV_{rex}} \tag{78}$$

Evaluation of the recrystallized fraction from the EBSD datasets is not as immediate. It requires the identification of recrystallized grains, evaluation of their area and their fraction in the map, under the assumption such a fraction is representative of the whole sample. One cannot evaluate such a fraction visually unless merely aiming at approximately estimating it. An automatic analysis of the data was hence performed using MATLAB and MTEX to determine these fractions whose procedure is reported in the manuscript titled “Microstructural path investigation into stagnation of recrystallization in warm-rolled tungsten” in Subchapter 5.2.

3.3.6 Calculation of Stored Energies

In the present work, stored energies are calculated from the defects and boundaries present in each orientation mapping. The microstructure in fact, consists of grain and subgrains separated by low or high angle boundaries as well boundaries within the deformed regions. The stored energy depends on the amount of such defects and on the boundaries as well, which ultimately depends on the misorientation across them. The surface energy of boundaries depends on the misorientation angle θ, across them according to the Read Shockley equation [110]:

$$\gamma(\theta) = \begin{cases} \gamma_b (\theta/\theta_m)[1 - \ln(\theta/\theta_m)] & if\ \theta < \theta_m \\ \gamma_b & if\ \theta \geq \theta_m \end{cases} \tag{79}$$

where $\gamma_b = 0.869 J/m^2$ is the surface boundary energy of HABs in tungsten [111] and θ_m is the misorientation angle above which the surface boundary energy is independent from the misorientation angle, and is equal to 15°. The stored energies densities for LABs (u_{LAB}) and HABs (u_{HAB}) are evaluated as follows:

$$u = S_V \gamma_b = \left\{ \sum_{all\ segments} \gamma(\theta) \right\} \frac{\Delta x}{A} \tag{80}$$

where S_V is the boundary surface densitiy, Δx the step size of the orientation mapping and A the area of the region considered.

Chapter 4. Thin Plates

4.1 Isothermal annealing of this rolled tungsten plates in the temperature range from 1300 °C to 1400 °C

This work was performed on the TPs. The first one [49] concerned the analysis of the as-received condition and the qualitative evolution of recovery and recrystallization. The second published work [50] concerned the analysis of kinetics of both processes, recovery and recrystallization, in terms of Kuhlmann's recovery model [75] and the JMAK model [87]–[89] respectively. In [49] it is demonstrated how the different recovery and recrystallization behaviour of different plates depend on the defect content within the microstructure accumulated during working. In [50] fitting of the afore-mentioned models demonstrated can accurately describe the kinetics of both recovery and recrystallization. Also, a linear decrease of the recovery coefficient A with the hardness loss during recovery was proved for all plates getting them in a systematic order not by their thickness achievable. An Avrami exponent n, of 2 fitted the evolution of recrystallization but systematic correlations between both the hardness loss due to recovery and the recovery coefficient A with the nucleation/growth coefficient for recrystallization b, were found indicating the paramount role of the microstructure and the therein defect content in ruling the annealing. In general, the higher the work-hardening of the tungsten plates, the lower the thermal stability, as it was inferred by the time to half recrystallization.

Nuclear Materials and Energy 15 (2018) 128–134

Contents lists available at ScienceDirect

Nuclear Materials and Energy

journal homepage: www.elsevier.com/locate/nme

Isothermal annealing of thin rolled tungsten plates in the temperature range from 1300 °C to 1400 °C

Umberto M. Ciucani*, Angela Thum, Chloé Devos, Wolfgang Pantleon

Section of Materials and Surface Engineering, Department of Mechanical Engineering, Technical University of Denmark, 2800 Kongens Lyngby, Denmark

ARTICLE INFO

Keywords:
Tungsten
Annealing
Recrystallization
Thermal stability
Hardness testing
EBSD

ABSTRACT

The annealing behavior of thin tungsten plates of four different thicknesses achieved by warm- and (in two cases) cold-rolling is investigated. Isothermal experiments at five different temperatures between 1300 °C to 1400 °C were performed. Hardness testing of annealed specimens allowed tracking the degradation of the mechanical properties and, indirectly, the microstructural evolution. Supplementary microscopical investigations of the microstructure in the as-received state as well as after annealing were performed to characterize the initial condition and to support the identification of the involved restoration processes. All four tungsten plates undergo microstructural restoration by recovery and recrystallization. The observed differences in their behavior were rationalized in terms of the identified differences in the microstructure in the as-received state, rather than their different initial thickness.

1. Introduction

One of the most critical components of future fusion reactors are the plasma-facing components of the blanket and the divertor. They will be exposed to high particle and high heat fluxes, requiring superior performance in terms of thermal stability and mechanical resistance. Tungsten meets many of the requirements for plasma-facing components [1]: a high thermal conductivity (164 W/mK), high strength, high yield point and creep resistance at high temperatures, highest melting point of all metals (3422 °C), and a low sputtering yield due to a high sputtering threshold energy [2,3]. In an annealed state, tungsten shows an intrinsic brittleness at room temperature [4–7] and a rather high ductile-to-brittle transition temperature [8–10]. After plastic deformation, tungsten behaves ductile even at room temperature. Operation of plastically deformed tungsten parts at higher temperatures is nevertheless limited by the occurrence of recrystallization replacing the ductile, deformed microstructure by an intrinsically brittle one. Following earlier studies on rolled foils [11–13] and plates [14–16], the annealing behavior of thin tungsten plates is characterized with focus on recrystallization; the main interest being whether a reduced thickness can lead to an improved performance in view of the thermal activated processes occurring during annealing.

2. Materials and methods

Four plates with four different thicknesses (2 mm, 1 mm, 0.5 mm and 0.2 mm) of 99.97% technically pure tungsten [17], produced via conventional powder metallurgical route were acquired from Plansee SE (Reutte, Austria). The interstitial impurity content of the plates is below 5 ppm for Hydrogen and Nitrogen, below 20 ppm for Oxygen and below 30 ppm for Carbon, as guaranteed by the manufacturer. The thin plates (TP) with sizes 100 mm × 250 mm × *thickness* were cut from larger pieces not specified in any more detail by the manufacturer. According to the specifications of the manufacturer, the two plates with larger thicknesses (2 mm (TP2) and 1 mm (TP1)) were obtained by warm-rolling, whereas the two plates with smaller thicknesses (0.5 mm (TP0.5) and 0.2 mm (TP0.2)) were achieved by final cold-rolling steps. From the thin plates, rectangular samples of 3 mm × 4 mm × plate *thickness* were cut for annealing, with their long side corresponding to the long direction of the as-received plates, so that the different directions can be identified later. To prevent high temperature oxidation during annealing, the specimens were encapsulated in glass ampoules. Each ampoule contained four different specimens, one from each of the TPs, in an argon atmosphere.

Isothermal annealing of the small specimens was performed in a general-purpose tube furnace NaberTherm RHTC 80-230/15 between 1300 °C and 1400 °C at five specific temperatures for times up to 67 h. Although rolling reduces porosity and homogenises the microstructure within the plates compared to the as-sintered condition, heterogeneities within the rolled plates are expected. Therefore, a large number of isothermal annealings for different time periods are performed for each annealing temperature to ensure the validity of the results.

---

* Corresponding author.
E-mail address: umciuc@mek.dtu.dk (U.M. Ciucani).

https://doi.org/10.1016/j.nme.2018.03.009
Received 14 December 2017; Received in revised form 2 March 2018; Accepted 17 March 2018
Available online 28 March 2018
2352-1791/ © 2018 Elsevier Ltd. This is an open access article under the CC BY-NC-ND license (http://creativecommons.org/licenses/BY-NC-ND/4.0/).

The microstructure of the material was assessed by Light Optical Microscopy (LOM), Electron Back-Scatter Diffraction (EBSD) and Vickers hardness testing. For light optical microscopy, conventional metallographic preparation by mechanical grinding and polishing was performed. In a final step, the specimens were etched with Murakami's etchant (10 g NaOH, 10 g $K_3Fe(CN)_6$ in 100 ml distilled water). Rolling direction (RD) and transverse direction (TD) of each plate were identified through LOM on different sections: while three of the rectangular plates were cut by the manufacturer with their long direction along RD, TP2 was cut with the long side along TD. This difference between the cuts was taken into account when investigating the microstructure in specific individual sections.

After conventional metallographic preparation, cross sections containing RD and the normal direction (ND) were prepared for EBSD by electropolishing using an aqueous solution containing 3 wt% NaOH at RT with an applied voltage of 12 V and a current of approximately 2 A for times ranging from 15 s to 75 s for the thinnest and the thickest plates, respectively. EBSD investigations were performed with a Bruker NOVA NanoSEM with an applied voltage of 20 kV and a step size of 100 nm. For each plate orientation maps of 100.8 µm × 86.9 µm (100.8 µm × 86.5 µm in case of TP0.2) were acquired.

Hardness testing was performed with a Vickers indenter and a load of 0.5 kg on the outer surface of the plates parallel to the rolling plane, i.e. containing RD and TD, in the as-received as well as the annealed condition to track the changes of the mechanical properties during annealing. For each condition, at least 10 indents were analyzed, the smallest and the largest of which were discarded and the average hardness values obtained from the remaining are reported together with the standard deviation of the average.

3. Results

3.1. Thin plates in as-received

The hardness values of the as-received plates are summarized in Table 1. In general, the thin plates showed an increased hardness with reduced thickness, from 550 ± 3 HV0.5 for TP2 to 642 ± 2 HV0.5 for TP0.2, as expected from an increased thickness reduction by rolling. The plate TP1, however, did not follow this trend and showed an exceptionally low hardness of 541 ± 2 HV0.5 which must have been caused by a difference in manufacturing of the plate (cf. Section 4).

Large orientation maps were obtained by EBSD on the longitudinal section (containing RD and ND) and shown in Fig. 1. The maps reveal the typical microstructural features after thickness reduction by rolling. The grains are elongated along the rolling direction with an aspect ratio increasing, in general, with decreasing plate thickness. Where the aspect ratio of the grains in the two thicker plates, TP2 and TP1, appear quite similar, a much higher aspect ratio is observed in TP0.5 and TP0.2 due to the (additional) cold-rolling. As a measure of the grain size, the average chord length between high angle boundaries (with disorientation angles above 15°) was determined along ND by the line intercept method. As obvious from Table 2, a smaller average chord length is observed in general for the plates with smaller thicknesses. The cold-rolled plates TP0.5 and TP0.2 show a much smaller chord length compared to the values of the thicker plates TP2 and TP1 which have been warm-rolled only. The slightly larger chord length of TP1 (564 ± 12 nm) compared to TP2 (538 ± 17 nm) supports the suspicion that TP1 has a different manufacturing history.

From the orientation data collected by EBSD, the 100 pole figure is derived for each TP and shown in Fig. 1(e)–(h). The pole figures reveal the existence of a single, preferential texture component, the rotated cube component {100}⟨011⟩, for all four plates. As summarized in Table 2, the strength of the texture as quantified by either the maximum 100 pole density or the volume fraction of the {100}⟨011⟩ component (allowing a deviation of 15° from the ideal orientation) increases with decreasing plate thickness from 35% to 57%, with exception of TP1 showing not only a much weaker texture (with maximum pole density of 4.2), but also a much lower volume fraction (13%) of the {100}⟨011⟩ component than all other plates.

Table 1
Vickers hardness values (HV0.5) for four thin tungsten plates in the as-received, severely recovered and fully recrystallized condition after isothermal annealing at 1325 °C. The hardness values obtained with 0.5 kgf are reported as average values with the standard deviation of the average value.

	HV_{def}	HV_{rec}	HV_{rex}	HV_{def} - HV_{rec}
TP2	550 ± 3	492 ± 2	449 ± 2	58
TP1	541 ± 2	507 ± 2	449 ± 1	38
TP0.5	595 ± 3	475 ± 2	414 ± 1	120
TP0.2	642 ± 2	479 ± 2	415 ± 3	163

3.2. Thin plates after isothermal annealing

Isothermal annealing was performed at five temperatures (1300 °C, 1325 °C, 1350 °C, 1375 °C, and 1400 °C) for times up to 67 h. The hardness values determined on the rolling planes are summarized in Fig. 2 for all four thin plates.

In general, the hardness decreases with the progress of annealing in a characteristic manner involving two different stages. These are indicated in Fig. 3 on the example of the behavior of all four plates during annealing at 1325 °C. Both stages are characterized by an initial hardness drop followed by a stagnation period leading to an apparently constant hardness value. The first, rapid initial drop in hardness from the as-received state is related to recovery processes in the deformed microstructure reducing its stored energy. Caused by this reduction in the driving force for recovery, the progress of recovery slows down leading to an apparent stagnation period, corresponding to a very late phase of recovery. The second hardness reduction occurring in a slightly milder manner is caused by recrystallization and leads to a second stagnation stage of constant hardness, attributed to complete recrystallization. Table 1 compares the hardness values of both stagnation stages obtained after annealing at 1325 °C, i.e. in the late phase of recovery and after complete recrystallization. The hardness values for the first apparent stagnation stage (attributed to severe recovery) are slightly lower for the two cold-rolled, thinner plates than for the two warm-rolled, thicker plates. In general, the average hardness loss due to recovery ($HV_{def} - HV_{rec}$) increases with decreasing plate thickness, except for TP1 which shows the smallest hardness loss due to recovery of all plates (see Table 1). Similar trends are observed for the hardness values of the second stagnation stage corresponding to complete recrystallization.

Comparing the hardness evolution at all different temperatures in Fig. 2, the stagnation values for the hardness after severe recovery seem not to be largely different, while rather different hardness values for the fully recrystallized states are observed for the different annealing temperatures. Peculiar behaviors at both, the lowest and highest annealing temperature are observed: for isothermal annealing at 1300 °C, only a single restoration stage is clearly identified; after 2 h the hardness has already dropped to a low value due to recovery and stays rather unaltered up to the largest annealing time of 67 h indicating contuation of recovery. For all four thin plates,the occurrence of recrystallization may still be questioned. On the other, for isothermal annealing at 1400 °C, a further decrease in hardness is observed after 16 h. This third stage of hardness reduction is attributed to grain growth occurring after completion of recrystallization.

Such an assignment of the dominant microstructural processes to the different annealing stages in the hardness evolution is confirmed by metallographical observations. Fig. 4 presents light optical micrographs from TP2 after different periods of annealing at 1325 °C. Fig. 4(a) shows the elongated grain structure after warm-rolling and resembles closely the orientation map of the same condition in Fig. 1(a). With increasing

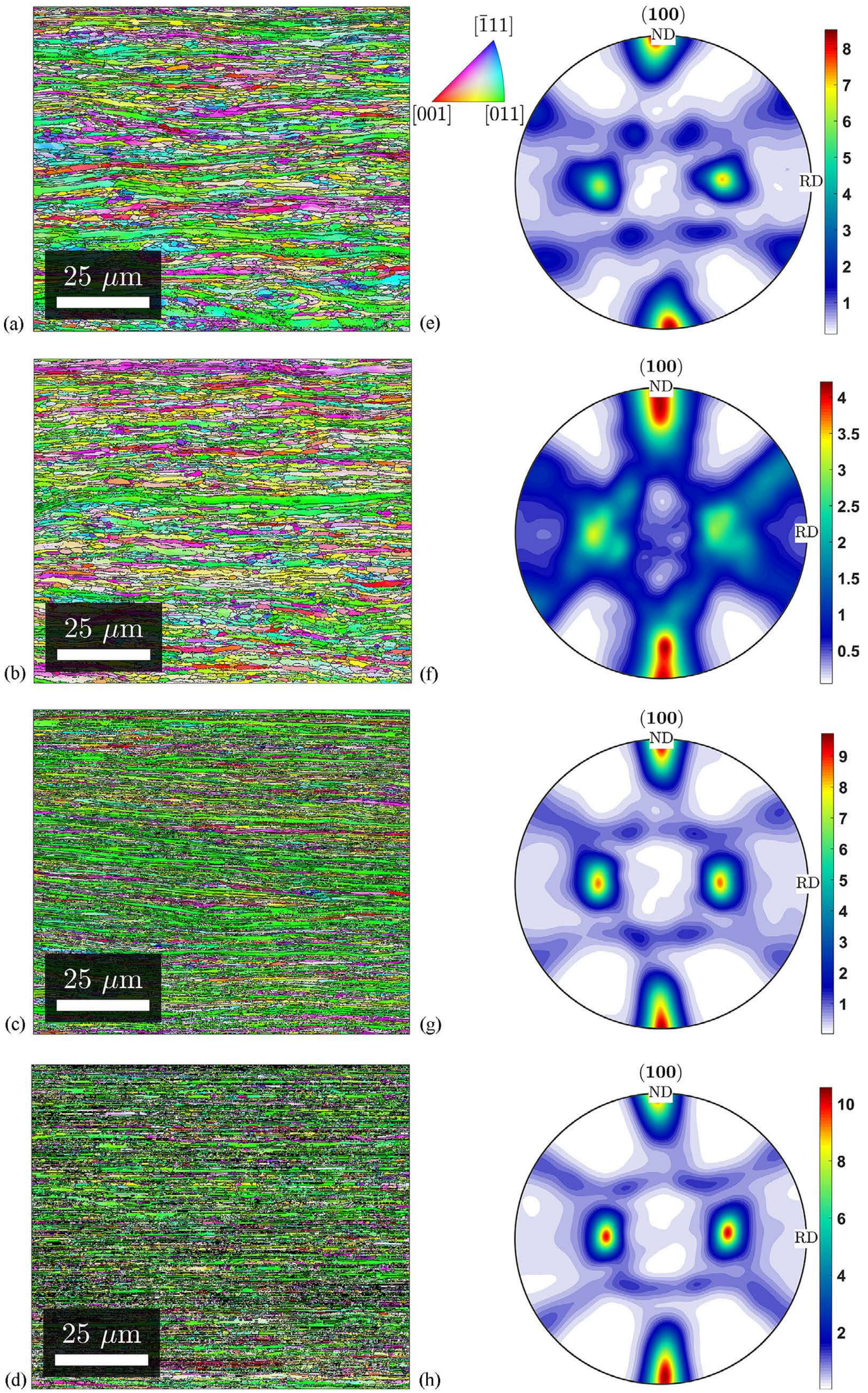
(a)
(b)
(c)
(d)
(e)
(f)
(g)
(h)
25 μm
[$\bar{1}$11]
[001]
[011]
(100)
ND
RD
8
7
6
5
4
3
2
1
4
3.5
3
2.5
2
1.5
1
0.5
9
8
7
6
5
4
3
2
1
10
8
6
4
2

Fig. 1. Orientation maps of the as-received condition obtained by EBSD on the RD/ND section (with RD being horizontally) in the center of the specimen (a) TP2, (b) TP1, (c) TP0.5 and (d) TP0.2. The colors represent the crystallographic direction along RD according to the inverse pole figure in the insert. (e), (f), (g) and (h) show the corresponding 100 pole figures with the pole density given in terms of multiple random.

Table 2
Quantitative characterisation of the microstructure in the as-received thin plates as obtained by EBSD. The volume fraction of the rotated cube component is determined allowing a maximal deviation of 15° from the ideal orientation.

	Average chord length along ND (nm)	Maximal (100) pole density (times multiple random)	Volume fraction of rotated cube {100}⟨011⟩ component
TP2	538 ± 17	8.5	35%
TP1	564 ± 12	4.2	13%
TP0.5	327 ± 3	9.7	48%
TP0.2	229 ± 4	11.0	57%

annealing time, the elongated grain structure is progressively replaced by an equiaxed grain structure due to recrystallization. Fig. 4(b) and (c) represent partially recrystallized conditions after 4 h and 16 h, respectively, whereas Fig. 4(d) represents the fully recrystallized state achieved after 24 h.

Additionally, a microstructural heterogeneity throughout the plate is revealed by LOM in Fig. 4. The lower part of the images, corresponding to the region close to the open surface which during rolling has been in contact with the rolls, shows a different stage of the microstructural evolution where recrystallization has been retarded. For instance, the outer layer in Fig. 4(b) resembles more the as-received condition and elongated grains can still be traced after 4 h of annealing. This explains why the observed hardness values after 4 h of annealing at 1325 °C as measured by indenting the rolling surface, did not show evidence for recrystallization, but rather indicate a late stage of recovery (cf. Fig. 3). The central part of the plate recrystallizes earlier than the outer parts. From Fig. 4(d), on the other hand, complete recrystallization of the entire plate can be concluded. This is confirmed by Fig. 5(a) revealing the microstructure of TP2 after annealing at 1325 °C for 24 h with larger magnification.

Comparing the fully recrystallized microstructure with a hardness of 449 ± 2 HV0.5 in Fig. 5(a) with the microstructure of TP2 after annealing at 1400 °C for 48 h having a hardness of 428 ± 1 HV0.5 shown in Fig. 5(b), a larger grain size can be recognized in the latter. The difference of about 30 HV0.5 is attributed to grain growth lastly occurring in the outer layer after complete recrystallization.

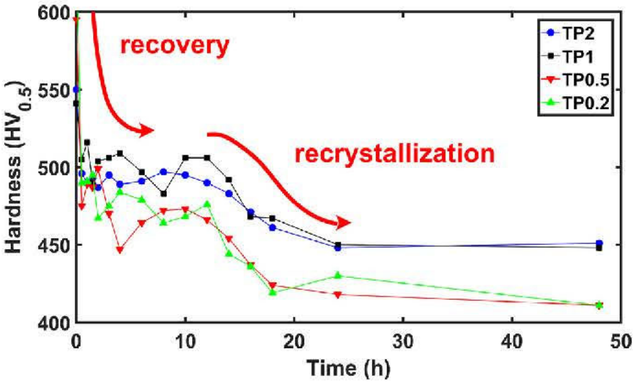

Fig. 3. Hardness evolution of all four thin plates during isothermal annealing at 1325 °C indicating the different stages of recovery and recrystallization. (The standard deviations of the average values are in all cases smaller than the markers.).

The microstructural heterogeneity imposed by the rolling conditions and inherited to the annealed microstructures was assessed for TP2 by hardness profiles along ND. The microhardness profiles shown in Fig. 6 were obtained by indenting with a Vickers indenter and a small load of 50 gf on the RD/ND section at different distances from the open surface which have been in contact with the rolls. Care was taken to displace the different indents more than 2.5 times their diagonal from each other. The obtained profiles after annealing (Fig. 6(a) and (b)) reveal an exponential decrease in hardness with increasing distance from the outer rolling surface:

$$HV\,(x) = HV_{center} + (HV_{surface} - HV_{center})\exp(-x/\lambda).$$

The hardness is significantly higher (up to 60 HV0.05) in a surface layer of about 150 nm than in the recrystallized center of the plate (cf. Table 3). With increasing annealing time, the size of the outer layer is reduced due to the progress of recrystallization there.

As seen from the microhardness profile through the entire plate TP2

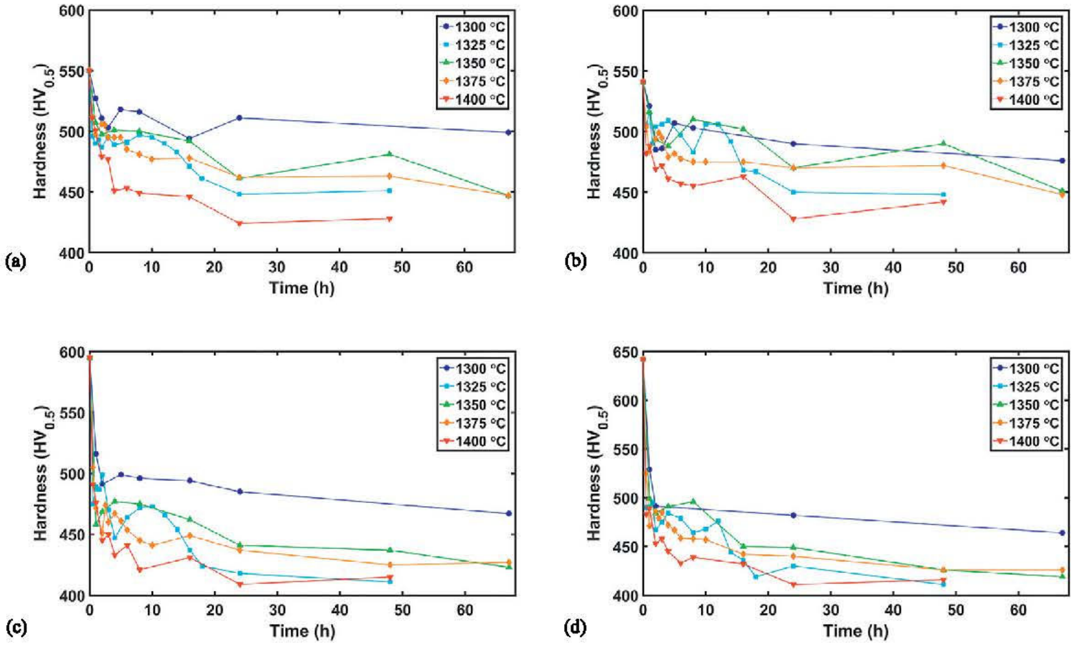

Fig. 2. Hardness evolution of the thin plates after isothermal annealing up to 67 h at five different temperatures between 1300 °C and 1400 °C as obtained on the rolling plane. (a) TP2, (b) TP1, (c) TP0.5 and (d) TP0.2. (The standard deviations of the average values are in all cases smaller than the markers.).

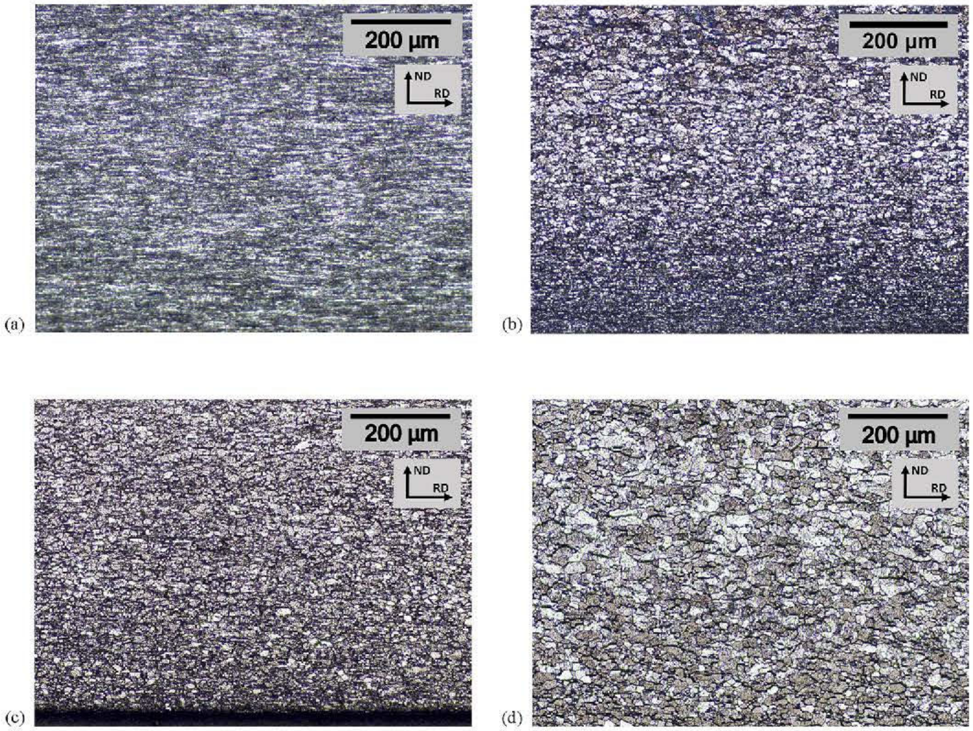

Fig. 4. Light optical micrographs of warm-rolled TP2 in the as-received condition (a) and after isothermal annealing at 1325 °C for (b) 4 h, (c) 16 h and (d) 24 h. Rolling and normal direction are indicated; the lower part of the images is close to the outer rolling surface of the plate.

in the as-received condition shown in Fig. 6(c), the initial variation in hardness across the plate is less pronounced (40 HV0.05) with a slightly asymmetrical distribution. Despite the higher hardness in the outer layers of the plate in the as-received condition and hence a higher stored energy there, recrystallization of the outer layers occurs last.

4. Discussion

The hardness of the thin plates in their as-received condition should reflect the plastic work put into the material during rolling with a larger thickness reduction (and hence,presuming the same initial height, a smaller thickness) corresponding to a higher hardness value. This expectation is satisfied in general, disrupted though by the too low hardness of TP1 only. The deviating behavior of TP1 is further substantiated by inspecting the microstructure of the as-received state using EBSD. For TP1, the average chord length along ND, is slightly larger than that of TP2 (instead of smaller as expected from presumed further rolling). The strength of the deformation texture and the volume fraction of the characteristic rotated cube texture component {100}⟨011⟩ are both lower than for all other plates. Finally, the hardness loss during recovery is smaller for TP1 than for all the other plates indicating that the driving force for recovery has been lower for this plate as confirmed by the lower initial hardness. All findings can be rationalized by presuming that TP1 may have been manufactured in a deviating manner than the other plates. Unfortunately, details of the processing of the plates were not revealed by the manufacturer and the received cuts might originate from different batches. Even if the same rolling sequence was applied on material from the same batch, TP1 may have recrystallized either dynamically during one of the passes of warm-rolling or statically during an intermediate annealing between some of the warm-rolling passes. Nevertheless, TP1 in its as-received state shows a typical deformed microstructure after warm-rolling without any indication for partial recrystallization; no evidence for any recrystallized volume fraction is gained from the orientation data in

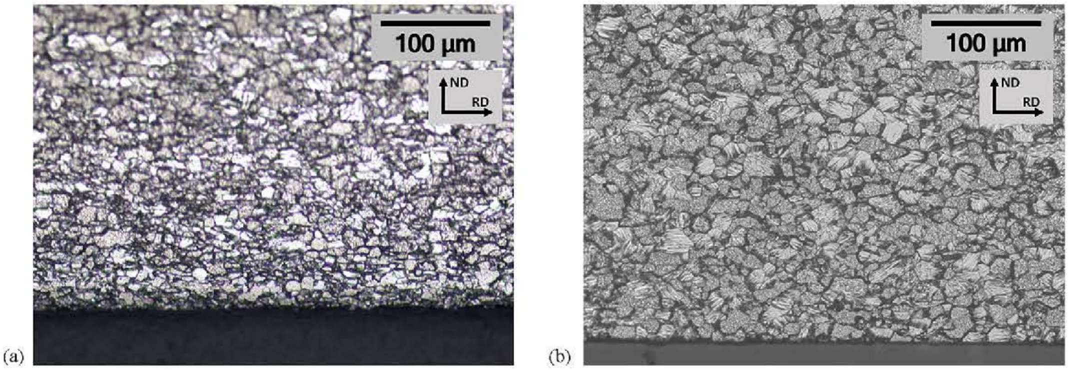

Fig. 5. Light optical micrographs of warm-rolled TP2 after isothermal annealing (a) at 1325 °C for 24 h and (b) at 1400 °C for 48 h. Rolling and normal direction are indicated; the lower part of the images is close to the outer rolling surface of the plate.

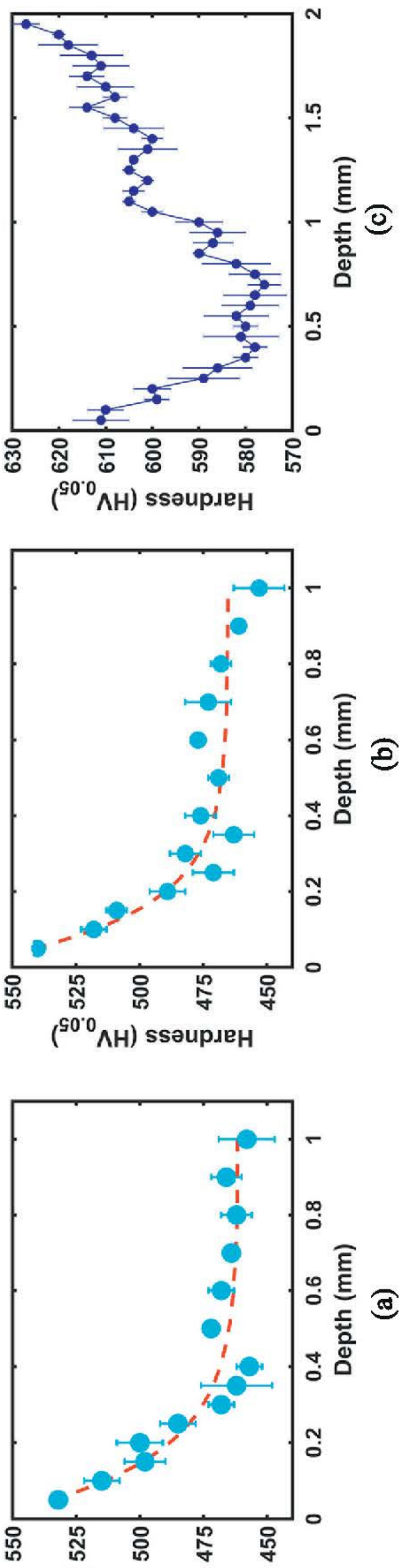

Fig. 6. Microhardness profiles along ND obtained by Vickers indentation with 50 gf on an RD/ND section for TP2 after annealing at 1325 °C for (a) 4 h and (b) 8 h and (c) in the as-received condition.

Table 3
Fitting parameters for the exponential decrease describing the hardness profile along ND in TP2 after annealing at 1325 °C .

Annealing time (h)	HV_{center}	$HV_{surface}$	Decay length λ (nm)
4	461	563	150
8	465	576	132

Fig. 1(b) ruling out that recrystallization has happened during the last rolling pass. Consequently, the thickness of the plates is not decisive for their annealing behavior. Yet, if the plates are ordered with respect to their initial hardness (as indicator of the stored energy in the deformation structure) instead of the plate thickness, all observations follow a common trend between the four plates revealing a systematic dependence on the initial hardness.

5. Conclusions

The annealing behavior of four rolled plates of pure tungsten with different thicknesses has been characterized in terms of their combined microstructural and hardness evolution. Different stages in the hardness evolution have been attributed to different microstructural restoration processes and confirmed by microstructural investigations. A systematic dependence of the annealing behavior on the initial hardness, but not on the initial plate thickness has been identified and discussed. The comprehensive data set for isothermal annealing at five different temperatures can form an indispensible basis for a quantitive analysis of the restoration kinetics of these thin tungsten plates, in particular for quantification of the recrystallization kinetics.

Acknowledgments

This work has been carried out partially within the framework of the EUROfusion Consortium. The views and opinions expressed herein do not necessarily reflect those of the European Commission.

References

[1] J. Davis, V. Barabash, A. Makhankov, L. Plöchl, K. Slattery, Assessment of tungsten for use in the ITER plasma facing components, J. Nucl. Mater 258–263 (1998) 308–312, http://dx.doi.org/10.1016/S0022-3115(98)00285-2.
[2] E. Lassner, W.-D. Schubert, The *element tungsten*, Tungsten, (1999), pp. 1–59, http://dx.doi.org/10.1007/978-1-4615-4907-9_1.
[3] R.G. Abernethy, Predicting the performance of tungsten in a fusion environment: a literature review, Mater. Sci. Technol. 836 (2016) 1–12, http://dx.doi.org/10.1080/02670836.2016.1185260.
[4] B. Gludovatz, S. Wurster, A. Hoffmann, R. Pippan, Fracture toughness of polycrystalline tungsten alloys, Int. J. Refract. Met. Hard Mater 28 (2010) 674–678, http://dx.doi.org/10.1016/j.ijrmhm.2010.04.007.
[5] D. Rupp, R. Mönig, P. Gruber, S.M. Weygand, Fracture toughness and microstructural characterization of polycrystalline rolled tungsten, Int. J. Refract. Met. Hard Mater. 28 (2010) 669–673, http://dx.doi.org/10.1016/j.ijrmhm.2010.05.006.
[6] D. Rupp, S.M. Weygand, Experimental investigation of the fracture toughness of polycrystalline tungsten in the brittle and semi-brittle regime, J. Nucl. Mater 386–388 (2009) 591–593, http://dx.doi.org/10.1016/j.jnucmat.2008.12.184.
[7] B. Gludovatz, S. Wurster, T. Weingärtner, a. Hoffmann, R. Pippan, Influence of impurities on the fracture behaviour of tungsten, Philos. Mag. 91 (2011) 3006–3020, http://dx.doi.org/10.1080/14786435.2011.558861.
[8] M. Rieth, B. Dafferner, Limitations of W and W-1%La2O3 for use as structural materials, J. Nucl. Mater 342 (2005) 20–25, http://dx.doi.org/10.1016/j.jnucmat.2005.03.013.
[9] M. Rieth, A. Hoffmann, Influence of microstructure and notch fabrication on impact bending properties of tungsten materials, Int. J. Refract. Met. Hard Mater. 28 (2010) 679–686, http://dx.doi.org/10.1016/j.ijrmhm.2010.04.010.
[10] M. Rieth, A. Hoffmann, Impact bending tests on selected refractory materials, Adv. Mater. Res. 59 (2009) 101–104, http://dx.doi.org/10.4028/www.scientific.net/AMR.59.101.
[11] J. Reiser, M. Rieth, B. Dafferner, Tungsten foil laminate for structural divertor applications – basics and outlook, J. Nucl. Mater 423 (2012) 1–8, http://dx.doi.org/10.1016/j.jnucmat.2012.01.010.
[12] J. Reiser, M. Rieth, B. Dafferner, A. Hoffmann, X. Yi, D.E.J. Armstrong, Tungsten foil laminate for structural divertor applications - Analyses and characterisation of

tungsten foil, J. Nucl. Mater. 424 (2012) 197–203, http://dx.doi.org/10.1016/j.jnucmat.2013.01.295.

[13] T. Palacios, J. Reiser, J. Hoffmann, M. Rieth, A. Hoffmann, J.Y. Pastor, Microstructural and mechanical characterization of annealed tungsten (W) and potassium-doped tungsten foils, Int. J. Refract. Met. Hard Mater. 48 (2015) 145–149, http://dx.doi.org/10.1016/j.ijrmhm.2014.09.005.

[14] A. Alfonso, D. Juul Jensen, G.N. Luo, W. Pantleon, Recrystallization kinetics of warm-rolled tungsten in the temperature range 1150–1350 °C, J. Nucl. Mater. 455 (2014) 591–594, http://dx.doi.org/10.1016/j.jnucmat.2014.08.037.

[15] A. Alfonso, D. Juul Jensen, G.N. Luo, W. Pantleon, Thermal stability of a highly-deformed warm-rolled tungsten plate in the temperature range 1100–1250 °C, Fusion Eng. Des. 98–99 (2015) 1924–1928, http://dx.doi.org/10.1016/j.fusengdes.2015.05.043.

[16] S. Bonk, J. Reiser, J. Hoffmann, A. Hoffmann, Cold rolled tungsten (W) plates and foils: evolution of the microstructure, Int. J. Refract. Met. Hard Mater. 60 (2016) 92–98, http://dx.doi.org/10.1016/j.ijrmhm.2016.06.020.

[17] PLANSEE SE, Pure-W Specifications, (2017). https://www.plansee.com/en/materials/tungsten.html.

4.2 Recovery and recrystallization kinetics of differently rolled, thin tungsten plates in the temperature range from 1325 °C to 1400 °C

Nuclear Materials and Energy 20 (2019) 100701

Contents lists available at ScienceDirect

Nuclear Materials and Energy

journal homepage: www.elsevier.com/locate/nme

Recovery and recrystallization kinetics of differently rolled, thin tungsten plates in the temperature range from 1325 °C to 1400 °C

Umberto M. Ciucani*, Angela Thum, Chloé Devos, Wolfgang Pantleon

Section for Materials and Surface Engineering, Department of Mechanical Engineering, Technical University of Denmark, 2800 Kongens Lyngby, Denmark

A R T I C L E I N F O

Keywords:
Tungsten
Annealing
Recovery
Recrystallization
Thermal stability
Hardness testing

A B S T R A C T

The thermal stability of thin tungsten plates of four different thicknesses achieved by warm- and (in two cases) cold-rolling is investigated in the temperature range between 1325 °C to 1400 °C. Hardness testing of annealed specimens allows tracking the degradation of the mechanical properties and, indirectly, the involved restoration processes during the microstructural evolution. For all four tungsten plates, a concise description of both, isothermal and isochronal annealing treatments is achieved using well-established models for the kinetics of recovery and recrystallization. A systematic dependence of the recovery kinetics at different temperatures on the hardness loss during recovery at a particular temperature has been identified. For the recrystallization kinetics, an Avrami exponent of 2 is observed in general. On the other hand, the activation energies revealed for different characteristic times of the recrystallization process depend on the plate thickness (or more precisely, the defect density stored). These findings, in particular, an activation energy far below that of short circuit diffusion, indicate the possibility of persisting nucleation throughout annealing.

1. Introduction

On the path to utilize fusion energy in future power plants, one of the toughest hurdles yet to be overcome is the development of armor materials for the plasma facing components of the first wall and the divertor. For the latter, operational requirements call for improvements in thermal stability [1] such that a desired lifetime of at least two years can be achieved [2]. The armor materials face persistent high heat and particles fluxes, demanding extraordinary material properties to resist heat and mechanical stresses. This resistance has to combine with exceptional thermal conductivity, particularly at the designed high operation temperatures, in order to fulfil the purpose of fast heat transport. Accounting for the requirement for low-activation materials [3], tungsten is considered the most promising choice for plasma facing components in terms of high thermal conductivity, strength, creep resistance and low sputtering yield [4–6]. On the contrary, tungsten is in general brittle at room temperature [5,7–10], although severe plastic deformation considerably reduces the ductile-to-brittle transition temperature [5,11].

Improving the mechanical behaviour of tungsten by plastic deformation though is not free of complications. When kept at high temperatures as in operating fusion reactors, plastically deformed tungsten will undergo restauration processes: recovery, recrystallization and grain growth will occur and alter the microstructure. These phenomena, in particular recrystallization, restore the intrinsic brittleness of annealed tungsten by replacing the beneficial deformation structure with an equiaxed, almost defect-free new grain structure. Different amounts of plastic work done to the material lead to a different stored energy in the material in the form of defects and correspondingly to a different tendency of the material to recrystallize. Considering that a certain ductility (introduced by plastic deformation) and a sufficient thermal stability (to maintain the deformation structure) both are required for tungsten to be applied as plasma facing material, a thorough understanding of their mutual interrelation and their dependence on the plastic deformation is of paramount importance. In extension of earlier investigations on plates [12–14] and foils [15,16], the thermal stability of rolled, thin tungsten plates (TPs) is characterised with focus on recovery and primary recrystallization. Following their microstructural assessment in the as-received state as well as after isothermal annealing [17], new data on isochronal annealing are presented. Based on the obtained isochronal data the temperature range between 1300 °C and 1400 °C is determined as a decent compromise between the desired operational temperatures and the feasibility of performing annealing experiments (with reasonably short annealing times to observe the above-mentioned phenomena). A quantitative description of all annealing treatments is provided in terms

---

* Corresponding author.
E-mail address: umciuc@mek.dtu.dk (U.M. Ciucani).

https://doi.org/10.1016/j.nme.2019.100701
Received 19 April 2019; Received in revised form 12 August 2019; Accepted 25 August 2019
Available online 26 August 2019
2352-1791/ © 2019 The Authors. Published by Elsevier Ltd. This is an open access article under the CC BY-NC-ND license
(http://creativecommons.org/licenses/BY-NC-ND/4.0/).

Table 1

Vickers hardness values (HV0.5) for the four thin tungsten plates in the as-received, recovered and recrystallized condition after isothermal annealing at three different temperatures (data taken from [17]), together with the hardness losses between the different conditions. (* Values marked with an asterisk are estimated from the isochronal annealing behaviour by extrapolation of the recovery behaviour according to Eq. (4)). Note, that the loss during recovery ΔHV_{rec} is an average between all three temperatures. Therefore, the individual losses during recovery and recrystallization (ΔHV_{rec} and ΔHV_{rex} respectively) do not add exactly to the total loss ΔHV_{tot}).

Plate	As-received condition hardness	Hardness at first stagnation (late recovery)			Hardness at second stagnation (full recrystallization)			Average loss during recovery	Average loss during recrystallization			Average total loss		
	HV_{rolled}	HV_{rec}			HV_{rex}			ΔHV_{rec}	ΔHV_{rex}			ΔHV_{total}		
		1325 °C	1375 °C	1400 °C	1325 °C	1375 °C	1400 °C	all	1325 °C	1375 °C	1400 °C	1325 °C	1375 °C	1400 °C
TP2	550 ± 3	492 ± 2	500 ± 9	504*	449 ± 2	479 ± 1	450 ± 1	51 ± 4	43 ± 4	21 ± 10	54 ± 1	101 ± 7	71 ± 6	101 ± 6
TP1	541 ± 2	507 ± 2	496 ± 4	498*	449 ± 2	475 ± 1	456 ± 1	44 ± 3	58 ± 3	21 ± 4	42 ± 1	96 ± 9	70 ± 7	89 ± 8
TP0.5	595 ± 3	475 ± 2	473 ± 6	481*	414 ± 4	445 ± 2	426 ± 5	119 ± 2	61 ± 3	27 ± 8	55 ± 5	181 ± 9	150 ± 7	170 ± 10
TP0.2	642 ± 2	479 ± 2	477 ± 8	468*	415 ± 4	441 ± 1	432 ± 2	166 ± 2	64 ± 5	36 ± 9	36 ± 2	227 ± 7	201 ± 4	212 ± 5

of sound and well-established models for the evolution of recovery and recrystallization.

2. Materials and Methods

Four plates (100 mm × 250 mm cut from larger pieces) of four different thicknesses of 99.97% technically pure tungsten [18] were acquired from Plansee SE (Reutte, Austria). The two thicker plates (2 mm (TP2) and 1 mm (TP1)) were manufactured solely by warm-rolling, whereas the two plates with smaller thicknesses (0.5 mm (TP0.5) and 0.2 mm (TP0.2)) experienced final cold-rolling steps.

The as-received condition of the thin plates had been investigated previously [17] as summarized in Table 1. The microhardness of the as-received condition reveals an increasing hardness with decreasing thickness of the plates with exception of TP1 showing the lowest hardness of the batch. Microstructurally, with exemption of TP1, the TPs show the typical characteristics of rolled metals: increasing grain elongation along the rolling direction and decreasing chord length along the normal direction (from 538 nm (TP2) to 327 nm (TP0.5) and 229 nm (TP0.2) with exceptional 564 nm for TP1), but also an increasing volume fraction of the rotated cube texture component {100}[011] with increasing thickness reduction. The details of the more elaborate microstructural analysis including an assessment of the heterogeneity of the plates is reported in [17]. Smaller specimens were cut from the plates, encapsulated in quartz glass ampoules in an argon atmosphere and annealed in a general-purpose tube furnace NaberTherm RHTC 80-230/15. Details on the production route, sample sizes and cutting, protective atmosphere encapsulation, direction identification and impurity content are reported in [17].

Different series of annealing experiments were performed on the TPs: The new isochronal series with a constant annealing time of 2 h at temperatures ranging from 800 °C to 1450 °C allowed to assess their recovery behaviour and to confirm the interesting temperature range for isothermal annealing. Isothermal experiments were formerly performed at five different temperatures between 1300 °C and 1400 °C and reported in [17]. Out of these five isothermal experiments, three series performed with annealing times up to 67 h at the temperatures of 1325 °C, 1375 °C and 1400 °C are taken into account forevaluation of the recrystallization kinetics.

Vickers hardness measurements with load 0.5 kg and dwell time 10 s were performed on the surface parallel to the rolling plane, i.e. containing the rolling and the transversal direction. Due to the small thickness of the thin plates, only this surface allowed performing a sufficient number of hardness indents (at least 10) for performing a statistically sound analysis.

3. Results

3.1. Isochronal annealing and model description of recovery kinetics

To assess the relevant temperature range for isothermal experiments, isochronal annealing experiments for 2 h were performed at temperatures from 800 °C to 1450 °C. With increasing annealing temperature more pronounced hardness reductions are observed (as seen in Fig. 1). In general, two different regimes can be distinguished: the (almost) linear decrease of the hardness with temperature observed at lower temperatures is attributed to recovery, whereas the more pronounced hardness decrease at higher temperatures indicates onset of recrystallization.

In modelling the recovery behaviour, Kuhlmann's recovery model [19,20] based on thermal-activated dislocation motion was employed. According to this interpretation, recovery kinetics is governed by an Arrhenius-like relationship for the evolution of the resistance σ against dislocation motion (for not too low σ)

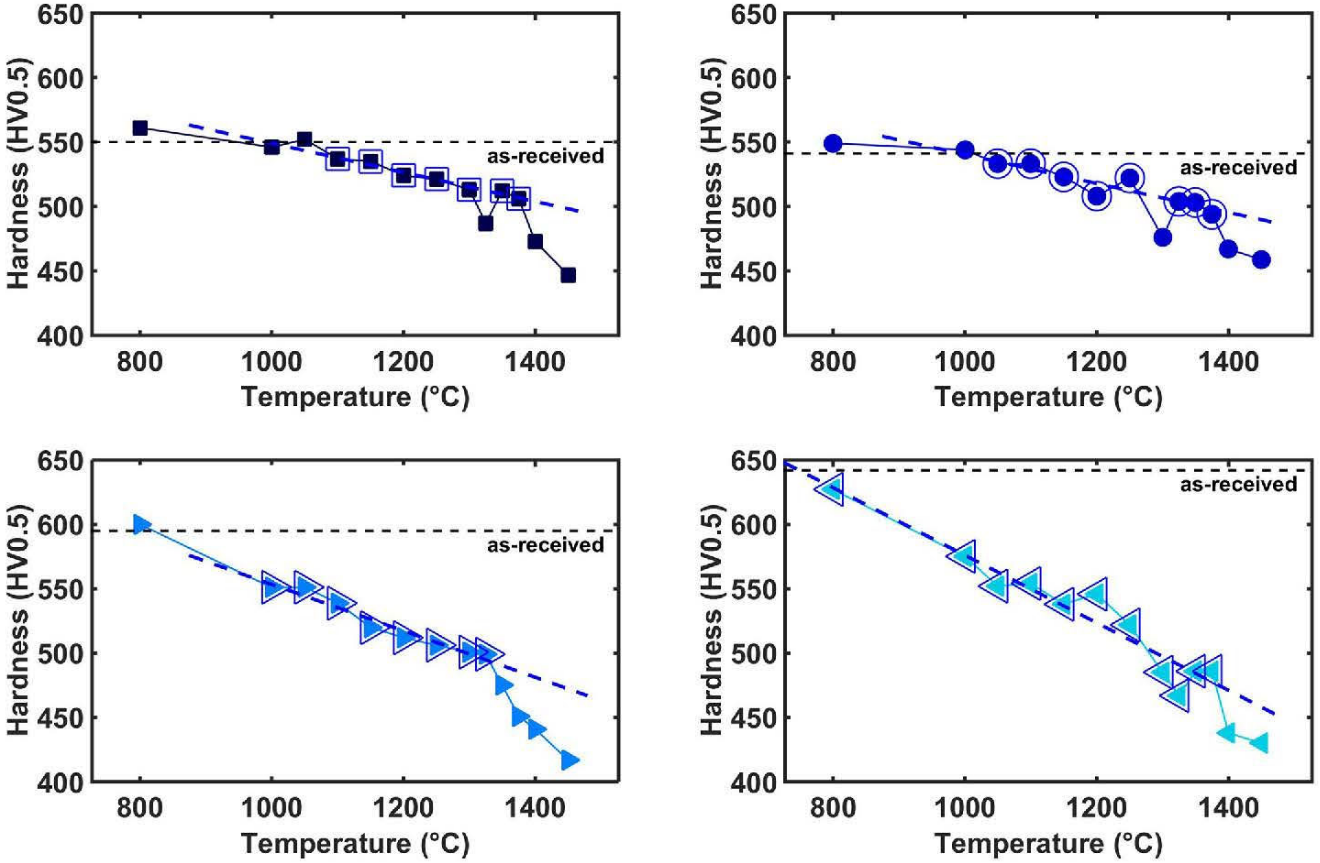

Fig. 1. Hardness changes with temperature during isothermal annealing for 2 h for tungsten plates of different thicknesses: (a) 2 mm (TP2), (b) 1 mm (TP1), (c) 0.5 mm (TP0.5), and (d) 0.2 mm (TP0.2).

$$\frac{d\sigma}{dt} = -c\exp\left(-\frac{Q_0 - \boldsymbol{\sigma}\boldsymbol{\Delta}V}{RT}\right) \tag{1}$$

with an effective activation energy $Q_0 - \boldsymbol{\sigma}\boldsymbol{\Delta}V$ lowered from the intrinsic activation energy Q_0 of recovery by the resistance σ through an activation volume ΔV. The activation volume $\Delta V = b_{\mathrm{Burgers}}\ \Delta A_{\mathrm{act}}$ quantifies the area ΔA_{act} swept by a dislocation with Burgers vector b_{Burgers}, if released from an obstacle by thermal activation. Due to the proportionality $HV = C\sigma$ between Vickers hardness and flow stress (with $C \approx 3$) [21], an equivalent behaviour of the hardness is expected. Kuhlmann's evolution Eq. (1) can be integrated in time,

$$HV = HV_0 - \frac{CRT}{\boldsymbol{\Delta}V}\ln\left(1 + \frac{t}{t_0}\right) \tag{2}$$

leading for not too short times t to a logarithmic dependence of the hardness

$$HV = HV_0^* - \frac{CRT}{\boldsymbol{\Delta}V}\ln(t) \tag{3}$$

on the annealing time t. For a constant annealing time $t = t_{isochr}$ as in the isochronal experiments, Eq. (3) describes an almost linear decrease in hardness with annealing temperature T

$$HV \approx HV_0^* - AT \tag{4}$$

with a slope

$$A = \frac{CR}{\boldsymbol{\Delta}V}\ln(t_{isochr}). \tag{5}$$

Note, that the integration constant $t_0 = (RT/c\boldsymbol{\Delta}V)\exp(-(Q_0 - \boldsymbol{\sigma}_0\boldsymbol{\Delta}V)/RT)$ in the exact Eq. (2) causes a weak additional temperature dependence of the effective initial hardness value HV_0^* and slight deviations from linearity for large temperature variations.

The lowest temperature for which a significant loss of hardness (with respect to the as-received condition) due to recovery can be noticed differs strongly between the thin plates, ranging from 1100 °C for the TP2 to 800 °C for TP0.2. For fitting of the linear temperature dependence according to Eq. (4) to the obtained hardness values after annealing for 2 h, hardness values from lower annealing temperatures which were within a standard deviation of the as-received material hardness were excluded. Also,measurements belonging to a condition where recrystallization already set in are not considered in the analysis, such as that of TP2 for 2 h at 1325 °C in Fig. 1a, clearly belonging to the regime of more pronounced hardness decrease. For all four thin plates a good fit of the linear temperature dependence of Eq. (4) is obtained in specific temperature intervals as seen from Fig. 1. For example, for TP2 the model description fits the data in the temperature interval from 1100 °C to 1350 °C very well ($R^2 = 0.95$). The obtained values for the back-extrapolated initial hardness HV_0^* and the recovery coefficient A are summarized in Table 2. Both, the back-extrapolated initial hardness and the recovery coefficient, increase with decreasing thickness but for TP1, showing the lowest values for both the parameters. From the results of these isochronal experiments, it appeared most appropriate to perform isothermal annealing treatments in the temperature range between 1300 °C and 1400 °C for longer periods of time.

3.2. *Isothermal annealing and model description of recrystallization kinetics*

Three isothermal annealing experiments performed at 1325 °C,

Table 2
Kinetics parameters obtained by fitting of Eq. (4) to the hardness evolution during isochronal annealing of the thin plates for 2 h.

Plate	A / K^{-1}	HV_0* (HV0.5)
TP2	0.117 ± 8%	700 ± 14
TP1	0.109 ± 15%	679 ± 23
TP0.5	0.179 ± 7%	779 ± 17
TP0.2	0.250 ± 6%	894 ± 21

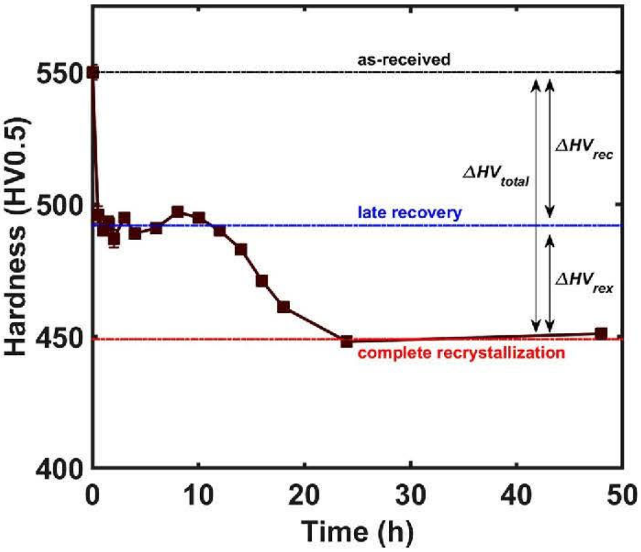

Fig. 2. Hardness evolution of TP2 during isothermal annealing at 1325 °C (reproduced from Fig. 2 in [17]). The dashed lines represent the hardness level of the as-received condition and the two stagnation stages of late recovery and complete recrystallization. Different hardness losses discussed are also illustrated. The slight re-increase in hardness level towards the end of the annealing is within experimental variation.

1375 °C and 1400 °C for annealing times up to 67 h are analysed in detail. In all three cases, and for all the plates, the resolved hardness evolution with time consisted of two stages (besides the additional grain growth stage for the thinner plates TP0.5 and TP0.2) each with an initial hardness drop followed by a stagnation leading to an apparently constant hardness value. This is illustrated in Fig. 2 for the case of TP2. After the initial sharp drop in hardness from the as-received state related to ongoing recovery processes, a first stagnation stage takes place. This stagnation of hardness evolution at an apparently constant hardness value corresponds to a very late phase of recovery where further changes in hardness with annealing time lessen as the driving force dwindles and the logarithmic dependence does not hold any longer (cf. [20]). The second, milder hardness loss due to recrystallization follows a characteristic sigmoidal shape evolution and leads to a second stage of constant hardness attributed to complete recrystallization. This designation of the dominant annealing processes to the different stages is confirmed by metallographical observations [17] which also revealed that recrystallization last took place in the outer parts of the plate (those in contact with the rolls in the rolling stage) whereas the center of the parts recrystallized earlier.

Table 1 compares the hardness values obtained for the different annealing temperatures in both stagnation stages, i. e. in the late phase of recovery and after complete recrystallization. The hardness losses $\Delta HV_{total} = HV_{rolled} - HV_{rex}$ suffered during the entire annealing process i.e. from the as-received to the fully recrystallized state are also tabulated, as well as the hardness losses during the individual stages of recovery ($\Delta HV_{rec} = HV_{rolled} - HV_{rec}$)and recrystallization ($\Delta HV_{rex} = HV_{rec} - HV_{rex}$) only (cf. Fig. 2). The hardness values HV_{rec} of each plate for the first stagnation stage attributed to a late phase of recovery are approximately equal, irrespective of the annealing temperature. They are lower for the cold-worked, thinner plates and slightly larger for the two warm-rolled, thicker ones. In general, the average hardness loss due to recovery ΔHV_{rec} increases with decreasing plate thickness, except for TP1 which shows the smallest hardness loss due to recovery of all plates (44 ± 3 HV0.5) (see Table 1).

While the stagnation values for the hardness after severe recovery seem not to be largely different between the three different temperatures, rather different hardness values of the fully recrystallized states are revealed for the different annealing temperatures. A harder recrystallized state was found for all thin plates after annealing at 1375 °C, while those annealed at 1325 °C and 1400 °C have very similar hardness values (see Table 1).

Recrystallization kinetics can be described quantitatively in terms of the Johnson-Mehl-Avrami-Kolmogorov model [22]. The recrystallized volume fraction increases through time according to the modified JMAK equation

$$X_V = 1 - \exp(-b^n (t - t_{inc})^n) \tag{6}$$

allowing for a possible incubation time t_{inc} before the onset of recrystallization (e.g. [12,13]). Both, the effective rate coefficient b and the Avrami exponent n [23], reflect the combined effects of nucleation and growth of recrystallized grains.

The modified JMAK Eq. (6) can be rearranged into the form:

$$\ln(-\ln(1 - X_V)) = n \ln b + n \ln(t - t_{inc}) \tag{7}$$

enabling to determine the two kinetic parameters (the Avrami exponent n and rate coefficient b) by linear regression (from so-called JMAK plots) for different assumptions concerning the incubation time t_{inc}. The iterative procedure to extract all three parameters is outlined below.

In order to assess the kinetics quantitatively, the recrystallized volume fraction X_V was determined according to the rule of mixtures

$$HV = X_V HV_{rex} + (1 - X_V) HV_{rec} \tag{8}$$

from the actual measured hardness value HV and the hardness values of the recovered and the recrystallized regions, i.e. HV_{rec} and HV_{rex}, respectively.

The evolution of the recrystallized volume fraction X_V obtained in this manner from the hardness data is illustrated in Fig. 3 for annealing of the four thin plates at different temperatures.

The evolution of the obtained recrystallized fraction provides evidence for the need of taking an incubation time into account as shown in Fig. 3a for the example of annealing TP2 at 1325 °C. Approximately, 10 hours are required before the recrystallization process starts and the recrystallized fraction evolves following the afore-mentioned sigmoidal shape throughout time. Without any incubation no proper description of the evolution can be achieved, whereas considering an incubation time allows a satisfying description of the kinetics (see the obtained fits for different conditions in Fig. 3). Taking into account approximate incubation times (heuristically determined as the time just before any indication of an onset of recrystallization can be recognized in the hardness evolution and different for each plate and annealing temperature), preliminary Avrami exponents close to 2 are found in all cases. i.e. for all temperatures and all four thin plates, from JMAK plots as the ones in Fig. 4 for annealing of all four plates at the lowest temperature of 1325 °C. Therefore, the exponent was fixed to be exactly 2 in order to further evaluate the incubation times t_{inc} and coefficients b for all plates at all isothermal annealing temperatures.

The obtained values for the incubation times t_{inc} and the coefficients b summarized in Table 3 reveal certain interrelations: the higher the annealing temperature and the thicker the plate (except TP1 reflecting its deviating behaviour), the larger the rate coefficient b. Similar trends have been reported earlier on thicker plates in dependence on temperature [24] and thickness reduction [25].

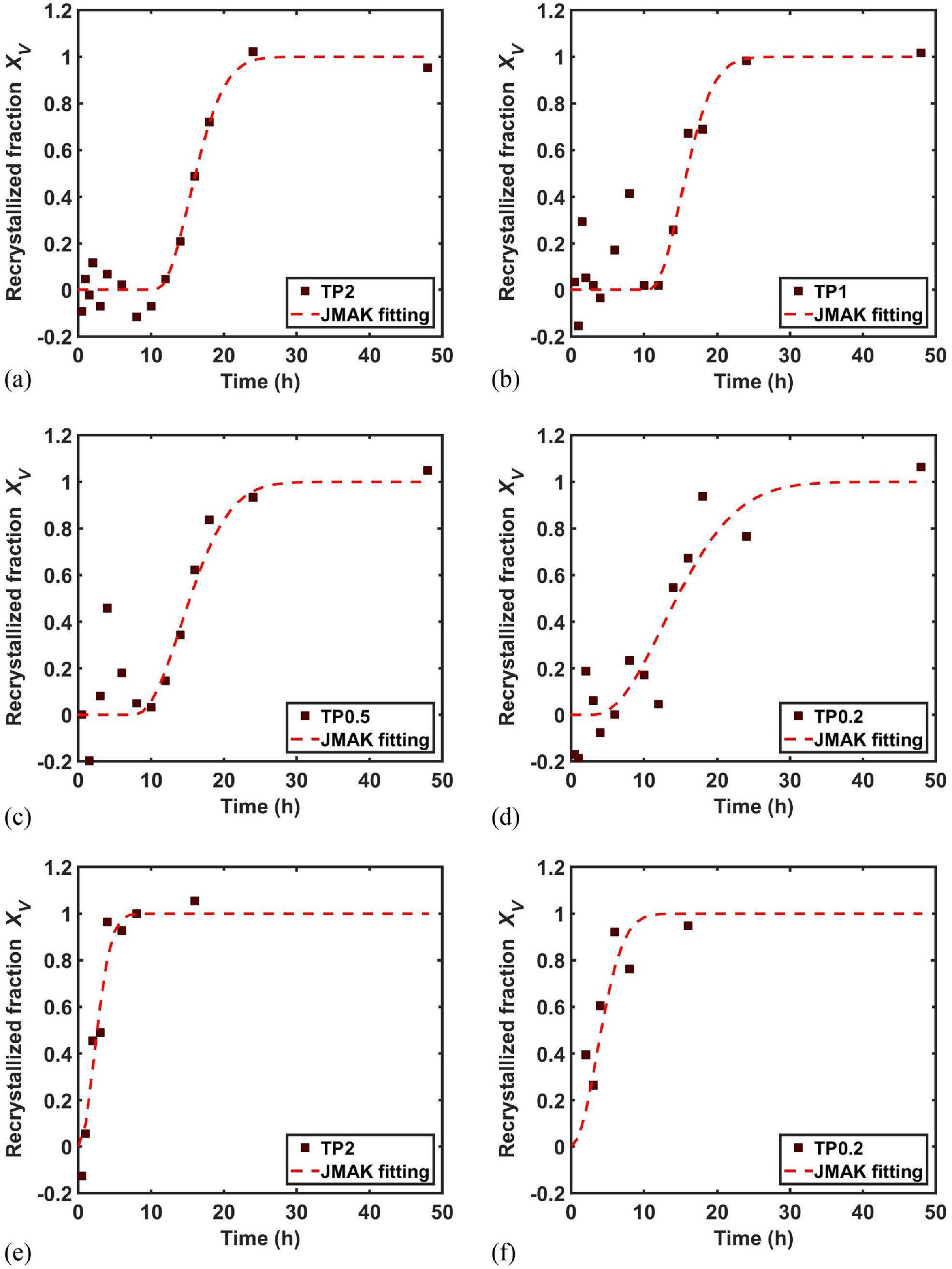

Fig. 3. Evolution of the recrystallized fraction in thin tungsten plates during isothermal annealing at different temperatures: (a) TP2 at 1325 °C, (b) TP1 at 1325 °C, (c) TP0.5 at 1325 °C, (d) TP0.2 at 1325 °C, (e) TP2 at 1400 °C, and (f) TP0.2 at 1400 °C. The dashed line represents a fit of the modified JMAK model according to Eq. (6) with fixed Avrami exponent n of 2. The obtained fitting parameters are listed in Table 3.

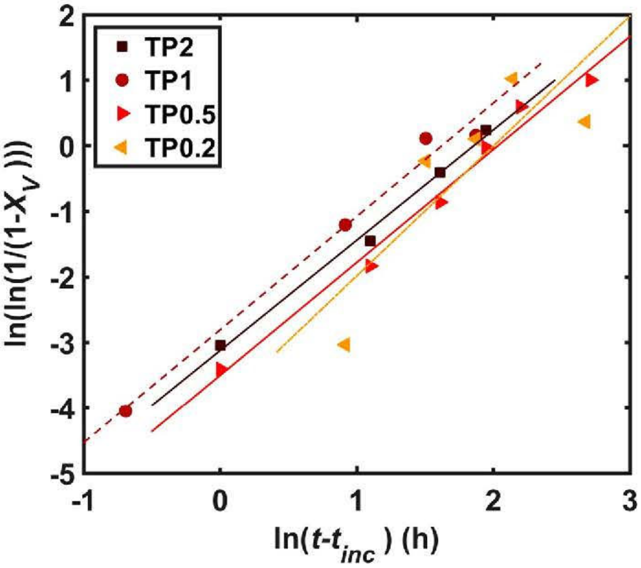

Fig. 4. JMAK plot (according to Eq. (7)) for isothermal annealing of all four thin plates at 1325 °C with incubation times considered from initial guesses.

In the cases where there is a recognizable incubation period in the hardness evolution, the incubation times follow the same trend as the rate coefficients b (and show a deviating behaviour for TP1 as well). For annealing of TP0.5 for 1375 °C and the entire isothermal annealing at 1400 °C, no evidence for an incubation time necessary to describe the kinetics was found (as recrystallization onsets immediately, cf. Figs. 3e and f, for TP2 and TP0.2, respectively) and a vanishing incubation period was assumed.

As seen in Fig. 3 for quite different starting and annealing conditions, application of the listed parameters in Table 3 resulted in a rather good description of the datasets. From the governing evolution Eq. (6), the times to achieve half-recrystallization (i.e. $X_V = 0.5$) are inferred finally:

$$t_{X_V=0.5} = \frac{1}{b}\sqrt{-\ln(1-X_V)} + t_{inc} = \frac{1}{b}\sqrt{\ln 2} + t_{inc}. \tag{9}$$

In this manner, three characteristic times describing the duration of thermally activated processes are obtained: the time to half recrystallization $t_{X_V=0.5}$, the incubation time t_{inc} and the inverse of the rate coefficient b^{-1}, describing the combined effect of nucleation and growth of recrystallizing grains. For all three characteristic times, a temperature dependence according to an Arrhenius law

$$t = t^{*}\exp\left(\frac{Q}{RT}\right) \tag{10}$$

is assumed allowing determination of their corresponding activation energies Q.

As shown in Fig. 5 and summarized in Table 3, the Arrhenius plots (semi-logarithmic plots of the time to half recrystallization or b^{-1} vs. the inverse of the absolute annealing temperature) resulted in two different ranges for the activation energies: in the case of the times to half recrystallization ranging from 363 ± 47 kJ/mol for TP0.2 to 569 ± 27 kJ/mol for TP1, while in the case of the coefficients b from 235 ± 75 kJ/mol for TP2 to 285 ± 142 kJ/mol for TP0.5.

4. Discussion

4.1. Recovery behaviour

Probing the as-received state by hardness testing should reflect the increasing plastic deformation of the material with decreasing thickness through an increased dislocation density stored in the material, causing an increased Vickers hardness of the thinner plates. This expectation is satisfied in general, disrupted though by the too low hardness of TP1 only. The deviating behaviour of TP1 has been further substantiated by inspecting the microstructure of the as-received state using EBSD [17] and attributed to eventual recrystallization during or between the warm-rolling passes rationalizing the similar grain size of TP1 and TP2 along ND (564 nm and 538 nm, respectively [17]). Peculiar differences in the behaviour of TP1 are also revealed in the recovery kinetics analysed here: the recovery coefficient A of TP1 is the smallest between all the investigated thin plates (see Table 2).

According to Kuhlmann's model, changes in hardness during recovery are not simply proportional to the hardness after plastic deformation. The present hardness value rather determines the further hardness loss by a reduction in activation energy for recovery from the materials intrinsic value Q_0 through an activation volume ΔV (cf. Eq. (1)). The recovery coefficient A (defined in Eq. (5)) is related to the microstructure present in the material in the as-received state through the activation volume ΔV due to the presence of a dislocation structure as a result of plastic deformation. An increased dislocation content in the material implies a smaller spacing between dislocations. Dislocations with Burgers vector b_{Burgers} released in a thermal-activated event will travel only a shorter distance, pass through a smaller area ΔA_{act} and hence have a smaller activation volume $\Delta V = b_{\mathrm{Burgers}}\Delta A_{\mathrm{act}}$. The smaller activation volume will in turn lead to a faster recovery kinetics and a higher recovery coefficient A. Consequently, larger plastic deformation should indirectly lead to a larger recovery coefficient A. As discussed earlier, the final plate thickness cannot be used as a measure for the plastic deformation as the resulting hardness does not depend systematically on the plate thickness (due to the observed deviations for TP1). Instead the recoverable increase in hardness due to deformation, corresponding to the hardness loss ΔHV_{rec} during recovery up to the first stagnation value, is used as a measure for the induced plastic deformation and, indirectly, the stored dislocation density. Relating the recovery coefficient A and the hardness loss during recovery for all four plates, as in Fig. 6, for an annealing temperature of 1325 °C, reveals a systematic linear dependence. (A similar linear dependence is observed when relating the coefficient A to the average hardness loss during recovery between all three investigated temperatures as the values differ only slightly as seen in Table 1.) This non-trivial relationship

Table 3
Recrystallization of thin tungsten plates at different temperatures: summary of the fitting parameters obtained by fitting the modified JMAK model of Eq. (6) with a fixed Avrami coefficient to the evolution of the recrystallized volume fraction similar to Fig. 3.

Plate	Incubation time t_{inc}			Rate coefficient b			$Q_{X_V=0.5}$	Q_b	Maximum possible temperature for 2 fpy
	1325 °C	1375 °C	1400 °C	1325 °C	1375 °C	1400 °C	kJ/mol	kJ/mol	
TP2	10.7 ± 0.1	3.0 ± 0.7	0	0.153 ± 0.005	0.319 ± 0.097	0.322	529 ± 61	235 ± 75	1088 ± 17 °C
TP1	10.8 ± 0.4	1.6 ± 1.5	0	0.168 ± 0.037	0.347 ± 0.173	0.353	569 ± 27	236 ± 73	1099 ± 8 °C
TP0.5	7.8 ± 0.3	2.5 ± 0.2	0	0.111 ± 0.013	0.306 ± 0.024	0.262	468 ± 3	285 ± 142	1059 ± 1 °C
TP0.2	3.2 ± 3.7	0.2 ± 4.9	0	0.074 ± 0.050	0.120 ± 0.011	0.202	363 ± 47	284 ± 66	996 ± 14 °C

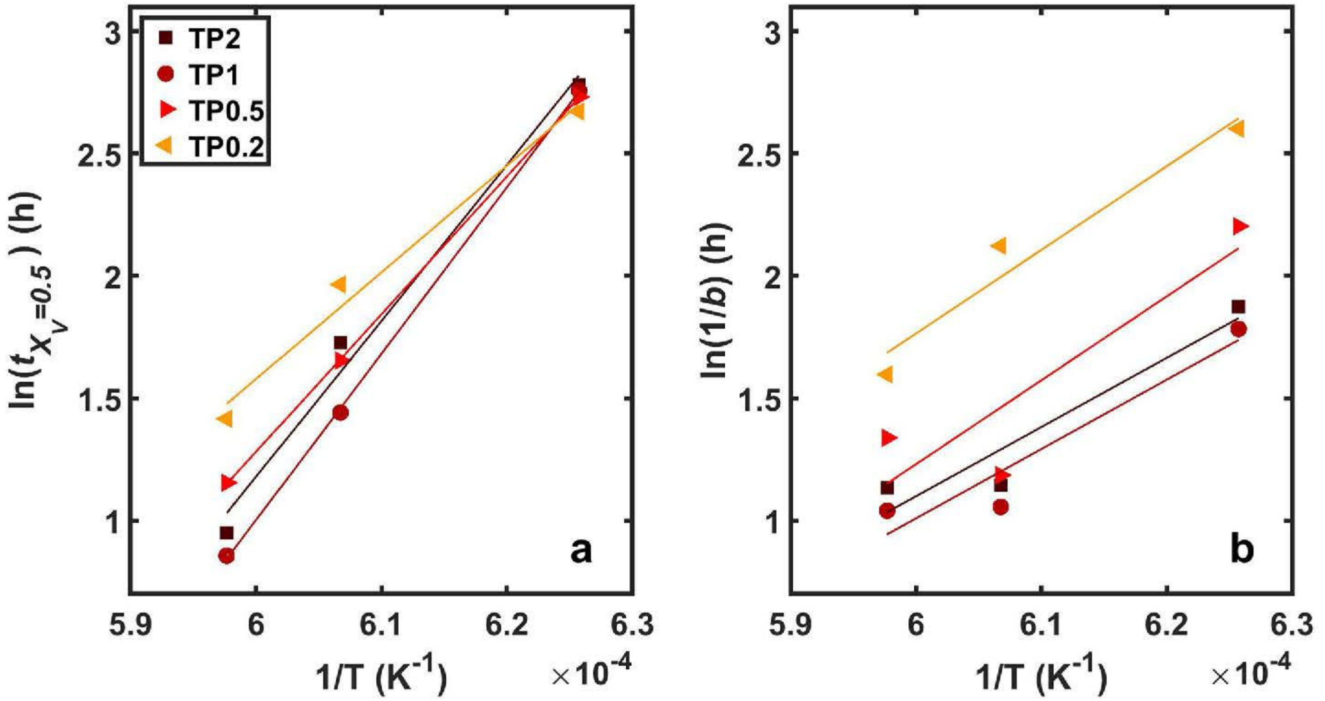

Fig. 5. Arrhenius plots for a) the time to half recrystallization b) the inverse of the rate coefficient b allowing the evaluation of activation energies for different characteristic times of the recrystallization process.

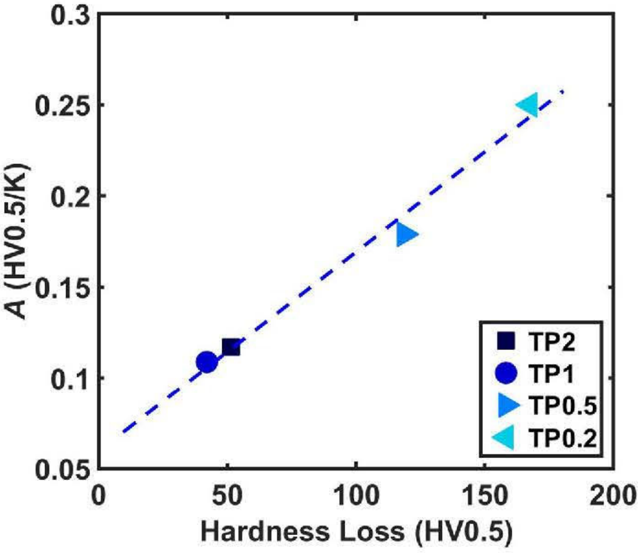

Fig. 6. Recovery of thin plates during isochronal annealing: recovery coefficient A vs. hardness loss during recovery ΔHV_{rec} at 1325 °C (i.e. difference between hardness of as-received condition and hardness of severely recovered condition seen as the first stagnation in hardness evolution).

roots in the reduction of the activation volume due to an increased defect content (dislocation density). Remarkably, even the data from TP1 follow the same linear relationship, indicating that it is indeed the microstructure of the as-received state, rather than the thickness reduction, which is governing the annealing behaviour.

In view of this correspondence between the hardness loss during recovery and the recovery kinetics, all other findings concerning the hardness in the as-received condition and even all microstructural information appear consistent: the higher the induced defect density by rolling, the higher the initial hardness, the higher the hardness loss achievable during recovery, the lower the activation volume for recovery and the faster the recovery kinetics. This general trend follows the reduction in plate thickness except for the deviating behaviour of TP1, manifested in a less deformed microstructure, a lower initial hardness after rolling and a relatively higher activation volume for recovery compared to TP2. This is very likely caused by a lower work-hardening experienced by TP1 which could be possibly a consequence of dynamic recrystallization of TP1 occurring during one of the warm-rolling passes or static recrystallization at the elevated temperatures between the passes.

4.2. *Recrystallization behaviour*

The observed recrystallization kinetics is concisely described by the JMAK model with an Avrami exponent of 2 and different activation energies for the different characteristic times governing the recrystallization process. It should be noted that the two solely warm-rolled plates, TP2 and TP1, as well as the two plates with final cold-rolling, TP0.5 and TP0.2, show pairwise quite similar activation energies. In the case of the time to half recrystallization, TP2 and TP1 showed activation energies $Q_{X_V=0.5}$ comparable to the activation energy of self-diffusion in tungsten (502-586 kJ/mol) [5], while the activation energies $Q_{X_V=0.5}$of TP0.5 and TP0.2 are similar to that of short-circuit diffusion (377-460 kJ/mol) [5].

For the growth/nucleation coefficient b^{-1}, on the other hand, all activation energies were found to be even below the reported range for self-diffusion. This rather surprising observation of a too low activation energy might originate from the fact that the coefficient b is actually describing the combined effect of nucleation and growth of recrystallizing grains and not a single thermal-activated process. If both processes follow individual thermal-activated events with different activation energies for nucleation and growth, Q_N and Q_G, respectively, and correspondingly different Avrami exponents n_N and n_G, their combined effect can be assessed (based on rate theory and [22]) in the following manner

$$\begin{aligned} b^{n} &= b_{G}^{n_G} b_{N}^{n_N} = \left[b_{G,0} \exp\left(-\frac{Q_G}{RT}\right)\right]^{n_G} \left[b_{N,0} \exp\left(-\frac{Q_N}{RT}\right)\right]^{n_N} \\ &= b_{G,0}^{n_G} b_{N,0}^{n_N} \exp\left(-\frac{n_G Q_G + n_N Q_N}{RT}\right) = \left[b_0 \exp\left(-\frac{n_G Q_G + n_N Q_N}{(n_G + n_N)RT}\right)\right]^{n_G + n_N} \end{aligned} \tag{11}$$

The effective activation energy for the combined rate coefficient b

$$Q_b = \frac{n_G Q_G + n_N Q_N}{n_G + n_N} \tag{12}$$

is, hence, a weighted sum of the activation energies of both, nucleation and growth. An effective Avrami coefficient $n = n_G + n_N$ of 2 can be rationalized in two different idealized manners [22]: either two dimensional growth ($n_G = 2$) with site-satured nucleation ($n_N = 0$) or quasi-one dimensional growth ($n_G = 1$) with continuous nucleation with constant nucleation rate ($n_N = 1$), the corresponding activation energies being $Q_b = Q_G$ and$Q_b = (Q_G + Q_N)/2$, respectively. In the latter case, a nucleation process with comparably low and almost vanishing activation energy ($Q_N \approx 0$, a fair assumption at least for the heavily cold-rolled plates TP0.5 and TP0.2), would lead to $Q_b \approx Q_G/2$ and, hence, allow to explain values for the activation energy lower than that of self-diffusion governing the growth process. Values of the activation energy for the rate coefficient b close to half of the activation energy of self-diffusion suggest such an interpretation in terms of sustained nucleation (with negligible activation energy) and quasi-one dimensional growth.

The value for activation energy for the time to half recrystallization obtained for TP0.5 is slightly above the reported values [5] for short circuit diffusion, the one of TP0.2 slightly below. This might be a consequence of the time to half recrystallization being actually the sum of two different times describing different thermal-activated processes, the time to incubation of recrystallization and the time for the progress of recrystallization (cf. Eq. (9)). A physical interpretation of the activation energy to half recrystallization has rather to be based on the individual processes.

Analogous to the activation energy, pairwise similar hardness values for the warm- (TP2 and TP1) and cold-rolled (TP0.5 and TP0.2) thin plates were obtained in the fully recrystallized state (second stagnation in Table 1) for all three annealing temperatures. This indicates the presence of pairwise similar deformation structures before annealing with larger differences between the deformation structures after warm- and cold-working (leading also to pairwise similar hardness values in the later stages of recovery).

In general, the recrystallization behaviour of the thin plates follows the same trend as seen for the recovery behaviour: the onset of recrystallization occurs earlier (as seen from a shorter incubation time t_{inc}) and the kinetics (as seen from the higher rate coefficient b) becomes faster with higher thickness reduction and hence larger plastic deformation. The deviating behaviour of TP1 is attributed again to its initial structure with lowest hardness and largest chord length.

An interesting systematic dependence between the hardness loss during recovery and the rate coefficient b for recrystallization of the different plates is revealed from Fig. 7: the higher the rate coefficient b of a plate, the lower its hardness loss during recovery. (The same trend is observed for the total hardness loss, whereas the hardness loss during recrystallization is almost the same for all plates.) Considering that the nucleation/growth coefficient b reflects the rate at which recrystallization takes place due to the energy stored in the deformation structure and that the hardness loss during recovery quantifies the loss of driving force for the recrystallization process due to recovery, the linear dependence $\Delta HV = \Delta HV^{*} - kb$ between both parameters is rationalized. The relation reflects the competition of both processes about the same driving force, i. e. the stored energy in the as-received state: A large hardness loss during recovery eliminates part of the driving force for recrystallization and causes slower recrystallization kinetics. On the other hand, a large hardness loss during recovery will cause a fast recovery kinetics as discussed above in connection with Fig. 6. Remarkable, in both cases the extraordinary behaviour of TP1 concerning its plastic deformation and related defect density as expected from the achieved thickness reduction becomes nicely rationalized when considering its lower hardness loss during recovery instead of the thickness reduction.

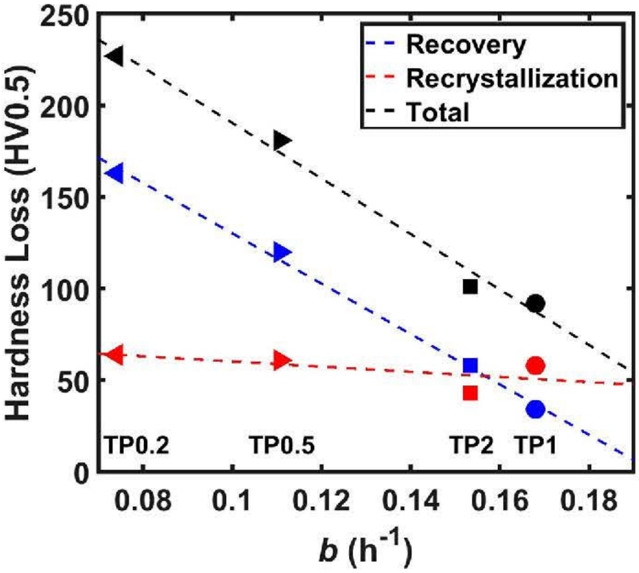

Fig. 7. Hardness loss during recovery ΔHV_{rec} vs. coefficient b describing nucleation/growth rate during recrystallization. (The values for the total hardness loss and the hardness loss during recrystallization are for a temperature of 1325 °C.).

Finally, the concise description of the recrystallization kinetics achieved in the investigated temperature range (cf. Fig. 3) and the obtained activation energies can be used to extrapolate the recrystallization kinetics to the service temperature at which the materials are expected to operate in a fusion reactor (tacitly assuming that the same process will held at these temperatures as well). For instance, the maximal service temperatures for which the recrystallized volume fraction in the materials will not exceed 50% during two years of service can be assessed. These temperatures (cf. Table 3) range between 996 °C for TP0.2 and 1099 °C for TP1. These extrapolated temperatures will enable the use of these thins plates as plasma-facing armor for the first wall (at an expected service temperature of 800 °C) for 2 years, but are far below the temperature expected for the plasma-facing divertor components experiencing high heat fluxes [26].

5. Conclusions

The thermal stability of four plates of pure tungsten with different thicknesses was investigated to assess the effect of progressive thickness reduction through rolling. Isothermal annealing at three different temperatures was performed up to complete primary recrystallization. The microstructural evolution during annealing was tracked by Vickers hardness testing. Well-established kinetic models for recovery and recrystallization allowed a concise description of the observed hardness evolution. The obtained kinetic parameters for the different phenomena are consistent with the expectations of an increased amount of plastic deformation and hence an increased dislocation density with increasing rolling reduction for all plates but TP1: the latter is attributed to the lower as-received hardness of TP1 caused probably by dynamic recrystallization through one of the warm-rolling passes or static recrystallization between them.

Describing the recovery kinetics by Kuhlmann's model revealed a linear dependence of the recovery coefficient A on the hardness loss during recovery for all plates (instead of the plate thickness or thickness reduction). Description of primary recrystallization through the JMAK model yielded Avrami exponents equal to 2, incubation times and nucleation/growth coefficients *b*, all reflecting the work-hardening due to the rolling experienced by the plates and featuring a lower activation energy for recrystallization for plates which underwent a larger work-hardening. The small values for the activation energy of the nucleation and growth coefficient *b*, less than the activation energy for short-circuit diffusion, indicate a sustained nucleation with rather low activation energy. Systematic correlations between the hardness loss due to recovery, the recovery coefficient *A* or the nucleation/growth coefficient *b* for recrystallization were found, indicating the paramount role of the microstructure and the therein stored energy in ruling the annealing behaviour.

In general, an increased work-hardening in the tungsten plates results in a reduced thermal stability as characterized by the time to achieve recrystallization in half of the material. For an envisaged time in service of 2 years for plasma-facing components before half of the volume of the materials recrystallizes, the investigated plates are expected, from extrapolation based on the obtained kinetic parameters and activation energies, to endure service temperatures between 1000 °C and 1100 °C. These temperatures are well above those foreseen for the armor material of the first wall (800 °C), but too low compared to those simulated for the divertor implying possible application in the former case only.

Data availability

The raw/processed data required to reproduce these findings cannot be shared at this time as the data also forms part of an ongoing study.

Declaration of Competing Interest

The authors declare that they have no known competing financial interests or personal relationships that could have appeared to influence the work reported in this paper.

Acknowledgements

This work has been carried out partially within the framework of the EUROfusion Consortium and has received funding from the Euratom research and training programme 2014-2018 and 2019-2020 under grant agreement No. 633053. The views and opinions expressed herein do not necessarily reflect those of the European Commission.

Supplementary materials

Supplementary material associated with this article can be found, in the online version, at doi:10.1016/j.nme.2019.100701.

References

[1] F. Romanelli, Efda, Fusion Electricity: A Roadmap to the Realisation of Fusion Energy, (2012), pp. 1–75 doi:ISBN 978-3-00-040720-8.

[2] J.H. You, E. Visca, C. Bachmann, T. Barrett, F. Crescenzi, M. Fursdon, H. Greuner, D. Guilhem, P. Languille, M. Li, S. McIntosh, A.V. Müller, J. Reiser, M. Richou, M. Rieth, European DEMO divertor target: Operational requirements and material-design interface, Nucl. Mater. Energy 9 (2015) 171–176, https://doi.org/10.1016/j.nme.2016.02.005.

[3] E.E. Bloom, R.W. Conn, J.W. Davis, R.E. Gold, R. Little, K.R. Schultz, D.L. Smith, F.W. Wiffen, Low activation materials for fusion applications, J. Nucl. Mater. 122 (1984) 17–26, https://doi.org/10.1016/0022-3115(84)90570-1.

[4] J.. Davis, V.. Barabash, A. Makhankov, L. Plöchl, K.. Slattery, Assessment of tungsten for use in the ITER plasma facing components, J. Nucl. Mater. 258–263 (1998) 308–312, https://doi.org/10.1016/S0022-3115(98)00285-2.

[5] E. Lassner, W.-D. Schubert, Tungsten: Properties, Chemistry, Technology of the Element, Alloys, and Chemical Compounds, 1st ed., Springer, Boston, MA, 1999, https://doi.org/10.1007/978-1-4615-4907-9.

[6] R.G. Abernethy, Predicting the performance of tungsten in a fusion environment: a literature review, Mater. Sci. Technol 0836 (2016) 1–12, https://doi.org/10.1080/02670836.2016.1185260.

[7] B. Gludovatz, S. Wurster, A. Hoffmann, R. Pippan, Fracture toughness of polycrystalline tungsten alloys, Int. J. Refract. Met. Hard Mater 28 (2010) 674–678, https://doi.org/10.1016/j.ijrmhm.2010.04.007.

[8] D. Rupp, R. Mönig, P. Gruber, S.M. Weygand, Fracture toughness and microstructural characterization of polycrystalline rolled tungsten, Int. J. Refract. Met. Hard Mater. 28 (2010) 669–673, https://doi.org/10.1016/j.ijrmhm.2010.05.006.

[9] D. Rupp, S.M. Weygand, Experimental investigation of the fracture toughness of polycrystalline tungsten in the brittle and semi-brittle regime, J. Nucl. Mater. 386–388 (2009) 591–593, https://doi.org/10.1016/j.jnucmat.2008.12.184.

[10] B. Gludovatz, S. Wurster, T. Weingärtner, a. Hoffmann, R. Pippan, Influence of impurities on the fracture behaviour of tungsten, Philos. Mag. 91 (2011) 3006–3020, https://doi.org/10.1080/14786435.2011.558861.

[11] M. Rieth, B. Dafferner, Limitations of W and W-1%La2O3 for use as structural materials, J. Nucl. Mater. 342 (2005) 20–25, https://doi.org/10.1016/j.jnucmat.2005.03.013.

[12] A. Alfonso, D. Juul Jensen, G.N. Luo, W. Pantleon, Recrystallization kinetics of warm-rolled tungsten in the temperature range 1150-1350 °C, J. Nucl. Mater. 455 (2014) 591–594, https://doi.org/10.1016/j.jnucmat.2014.08.037.

[13] A. Alfonso, D. Juul Jensen, G.N. Luo, W. Pantleon, Thermal stability of a highly-deformed warm-rolled tungsten plate in the temperature range 1100-1250 °C, Fusion Eng. Des. (2015) 1924–1928, https://doi.org/10.1016/j.fusengdes.2015.05.043 98–99.

[14] S. Bonk, J. Reiser, J. Hoffmann, A. Hoffmann, Cold rolled tungsten (W) plates and foils: Evolution of the microstructure, Int. J. Refract. Met. Hard Mater. 60 (2016) 92–98, https://doi.org/10.1016/j.ijrmhm.2016.06.020.

[15] T. Palacios, J. Reiser, J. Hoffmann, M. Rieth, A. Hoffmann, J.Y. Pastor, Microstructural and mechanical characterization of annealed tungsten (W) and potassium-doped tungsten foils, Int. J. Refract. Met. Hard Mater 48 (2015) 145–149, https://doi.org/10.1016/j.ijrmhm.2014.09.005.

[16] J. Reiser, M. Rieth, B. Dafferner, A. Hoffmann, X. Yi, D.E.J. Armstrong, Tungsten foil laminate for structural divertor applications - Analyses and characterisation of tungsten foil, J. Nucl. Mater. 424 (2012) 197–203, https://doi.org/10.1016/j.jnucmat.2013.01.295.

[17] U.M. Ciucani, A. Thum, C. Devos, W. Pantleon, Isothermal annealing of thin rolled tungsten plates in the temperature range from 1300 °C to 1400 °C, Nucl. Mater. Energy (2018), https://doi.org/10.1016/J.NME.2018.03.009.

[18] PLANSEE SE, Pure-W Specifications, (2017). https://www.plansee.com/en/materials/tungsten.html.

[19] D. Kuhlmann, G. Masing, J. Raffelsieper, Zur Theorie der Erholung, Zeitschrift Für Met. 40 (1949) 241–246.

[20] D. Kuhlmann, Zur Theorie der Nachwirkungserscheinungen, Zeitschrift Für Phys. 124 (1948) 468–481.

[21] D. Tabor, The hardness and strength of metals, J. Inst. Met. 79 (1951) 1–18.

[22] A.N. Kolmogorov, A statistical theory for the recrystallisation of metals, Izv. Akad. Nauk. SSSR (1937) 3.

[23] M. Avrami, Kinetics of phase change. I General Theory, J. Chem. Phys. 7 (1939) 1103–1112, https://doi.org/10.1063/1.1750380.

[24] M. Yu, K. Wang, X. Zan, W. Pantleon, L. Luo, X. Zhu, Y. Wu, Hardness loss and microstructure evolution of 90% hot-rolled pure tungsten at 1200–1350 °C, Fusion Eng. Des. 125 (2017) 531–536, https://doi.org/10.1016/j.fusengdes.2017.05.072.

[25] K. Wang, X. Zan, M. Yu, W. Pantleon, L. Luo, X. Zhu, P. Li, Y. Wu, Effects of thickness reduction on recrystallization process of warm-rolled pure tungsten plates at 1350 °C, Fusion Eng. Des. 125 (2016) 521–525, https://doi.org/10.1016/j.fusengdes.2017.03.140.

[26] T. Hirai, S. Panayotis, V. Barabash, C. Amzallag, F. Escourbiac, A. Durocher, M. Merola, J. Linke, T. Loewenhoff, G. Pintsuk, M. Wirtz, I. Uytdenhouwen, Use of tungsten material for the ITER divertor, Nucl. Mater. Energy 9 (2016) 616–622, https://doi.org/10.1016/j.nme.2016.07.003.

Chapter 5. W80 Plate

5.1 Stagnant recrystallization in warm-rolled tungsten in the temperature range 1150 °C to 1300 °C

Fusion Engineering and Design 146 (2019) 814–817

Contents lists available at ScienceDirect

Fusion Engineering and Design

journal homepage: www.elsevier.com/locate/fusengdes

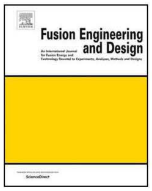

Stagnant recrystallization in warm-rolled tungsten in the temperature range from 1150 °C to 1300 °C

Umberto Maria Ciucani*, Wolfgang Pantleon

Section for Materials and Surface Engineering, Department of Mechanical Engineering, Technical University of Denmark, 2800 Kongens Lyngby, Denmark

ARTICLE INFO

Keywords:
Tungsten
Rolling
Annealing
Recrystallization
Thermal stability
Hardness testing

ABSTRACT

Pure tungsten is the prime candidate for armor material of fusion reactors; its application at the expected operation temperatures for longer times will result in changes in the microstructure, in particular due to recrystallization, undermining the otherwise outstanding properties of tungsten. Investigating the thermal stability of tungsten depending on the manufacturing technology is therefore crucial. The thermal response of a sintered, hot isostatically pressed tungsten plate warm-rolled to 80% thickness reduction is assessed in the temperature range between 1150 °C and 1300 °C. Isothermal annealing treatments were performed at six different temperatures. With increasing annealing time, the macro hardness decreased and different stages corresponding to different stages of the microstructural evolution and the progress of recrystallization could be identified and confirmed by electron backscatter diffraction. For all six annealing temperatures a stagnation period in the evolution of the macro hardness was observed where the degradation of mechanical properties halted for a significant amount of time, before it resumed. Microstructural investigations revealed that the stagnation occurred when tungsten was still only partially recrystallized. For the time to half recrystallization, an activation energy of 548 kJ/mol comparable to the activation energy of bulk self-diffusion is inferred.

1. Introduction

Tungsten is considered the prime candidate for the armour material of plasma-facing components of future fusion reactors as it combines high thermal conductivity, high yield stress, strength, and creep resistance even at high temperatures [1,2]. In particular, its high melting temperature enables tungsten to withstand the high heat loads, high temperatures and temperature gradients arising at the first wall and the divertor [3]. For a safe operation, non-brittle behaviour of the material between room and operation temperature is desired. This can be achieved by severe plastic deformation, as tungsten in a deformed state behaves rather ductile [1,4]. At the high stationary operation temperatures (up to 1200 °C [3] at the divertor), the microstructure of the material will be altered by recovery and recrystallization, degrading eventually the mechanical properties. During recrystallization the undeformed, polycrystalline state is reinstated. The dislocation-free, almost equiaxed grain structure is characterized by lower strength than the deformed state and a brittle behaviour caused by incompatible plastic deformation at grain boundaries [1,5,6]. By selecting proper manufacturing conditions, the microstructure of tungsten can be tailored and its thermal stability ought to be improved. Several studies on thermal stability and recrystallization of pure tungsten plates and foils rolled to different reductions have been reported [7–15].

The work presented here investigated the thermal stability of tungsten warm-rolled to an intermediate rolling reduction (80%) in comparison with two earlier investigations on lower (67%) [7] and higher (90%) [8] rolling reductions which showed a significant difference in their recrystallization kinetics. The most important finding is the discovery of an incomplete recrystallization even upon annealing at high temperatures for long periods of time. Such a stagnation in the recrystallization process may provide guidance towards materials with an improved thermal stability.

2. Materials and methods

The thermal stability of warm-rolled 99.95% pure tungsten was investigated on a plate with dimensions 200.8 × 100.3 × 8.3 mm^3 along rolling direction (RD), transversal direction (TD) and normal direction (ND), respectively. The plate (termed W80) has been manufactured by Advanced Technology & Materials Co. Ltd. in Beijing using a powder metallurgical route (sintering and hot isostatic pressing) followed by warm-rolling to a thickness reduction of 80% to be compared with two earlier investigated plates warm-rolled to 67% (W67 [7]) and 90% thickness reduction (W90 [8]). From the plate, small specimens

---

* Corresponding author.
E-mail address: umciuc@mek.dtu.dk (U.M. Ciucani).

https://doi.org/10.1016/j.fusengdes.2019.01.088
Received 5 October 2018; Received in revised form 16 January 2019; Accepted 16 January 2019
Available online 24 January 2019
0920-3796/ © 2019 Elsevier B.V. All rights reserved.

(6×5 x 4 mm^3 along RD, TD and ND, respectively) were cut for annealing. They were encapsulated in sealed quartz glass tubes flushed by Argon to prevent oxidation of tungsten and the formation of volatile oxides. Isothermal annealing treatments were performed in a general-purpose tube furnace NaberTherm RHTC 80–230/15 at six different temperatures ranging from 1150 °C to 1300 °C for different time spans as long as 1872 h (i.e. 78 days) to assess the thermal stability and the recrystallization behaviour of W80. Additionally, two samples were annealed at even higher temperatures (1350 °C and 1400 °C) to ensure full recrystallization.

The progress of the microstructural evolution was traced by Vickers hardness testing of the annealed specimens in comparison to the as-received condition. The macro hardness of the as-received plate was tested on both open rolling surfaces with a load of 10 kgf. After cutting the plate into bars with a size of 6 mm along RD, micro hardness mapping of several TD/ND sections was performed using a smaller load of 0.5 kgf, additional to macro hardness testing (HV10). For the annealed specimens, macro hardness tests with a load of 10 kgf were performed solely on TD/ND sections. For each condition, 24 macro indents were analysed (with the exception of 1250 °C and 1300 °C where a lower number, but at least 10 macro indents, were performed for each condition). Discarding the smallest and the largest hardness value measured, the resulting average hardness are reported together with the standard deviation of the average.

For a concise characterization of the microstructure, orientation mapping is employed using electron backscatter diffraction. EBSD investigations were performed with Bruker Esprit software on a FEI NOVA NanoSEM 600 using an applied voltage of 20 kV and a step size of 500 nm for the as-received condition and 2 µm for the annealed ones. For each annealed condition, two orientation maps of 792 µm × 660 µm on the RD/ND section adjacent to each other along ND were acquired and combined into a single map slightly smaller than 792 µm x 1320 µm due to the required overlap for stitching. Both, macro hardness testing and orientation mapping were performed as close as possible to the centre of the plate with respect to ND, i.e. in the region furthest away from contact with the rolls.

3. Results

3.1. As-received condition

Macro hardness testing of the as-received plate on both rolling surfaces revealed a substantial heterogeneity in the hardness distribution. This was further substantiated by micro hardness mapping of TD/ND sections after cutting into bars along RD. By mapping several TD/ND sections, reasonably large regions in the plate of homogeneous hardness could be identified. The relatively constant hardness value of these regions of 437 ± 2 HV10 is taken as hardness of the as-received condition; it is quite similar to the hardness of the earlier investigated plates, i.e. 423 ± 4 HV10 for W67 [7] and 434 ± 2 HV10 for W90 [8]. In order to minimize the effect of the heterogeneous hardness in the plate, specimens for the annealing experiments were cut solely from regions where a constant hardness is expected from the micro hardness mapping of neighboring regions.

Orientation maps on RD/ND sections of the regions with homogeneous hardness in the as-received condition (not shown here) revealed the presence of a partially recrystallized structure after warm-rolling. Even before any annealing, almost equiaxed, recrystallized grains accounting for a recrystallized volume fraction X_V of (18 ± 2)% were observed alongside with elongated and fragmented grains representing the deformed structure.

3.2. Hardness evolution during isothermal annealing

The hardness evolution during isothermal annealing between 1150 °C and 1300 °C is summarized in Fig. 1. During annealing, the macro hardness decreases gradually from the value 437 ± 2 HV10 of the as-received condition (the black point in Fig. 1) to the much lower hardness of the recrystallized condition. The hardness value of 357 ± 2 HV10 considered representative for the fully recrystallized condition was obtained as an average of several conditions at different annealing temperatures (illustrated by the bottom grey band of Fig. 1) for which complete recrystallization could be presumed and confirmed by EBSD investigations (see e.g. Fig. 2a). The occasionally observed intermittent increase in hardness is considered to be unphysical and ignored; it is attributed to the use of individual samples for each data point and the heterogeneity of the initial condition in the plate which was not be completely eliminated by selecting samples from proper regions.

The overall evolution (even ignoring any non-monotonous behaviour) does not follow the commonly observed trend with an initial, slight decrease slowing down with annealing time due to recovery, continued by a more severe decrease following a sigmoidal curve characteristic for recrystallization (see for instance [7,8]). Instead the decrease in hardness seems to come to a temporary halt. The most obvious halting period occurs at a macro hardness level of about 390 ± 10 HV10 (marked as the middle one of the grey bands in Fig. 1), a similar halting period may be seen at 417 ± 7 HV10 at least for the three lowest temperatures (top grey band in Fig. 1). After the initial decrease to 417 ± 7 HV10 and halt, the hardness decreases relatively suddenly to the lower halting value of 390 ± 10 HV10. At this hardness value, the hardness evolution stagnates for a considerable amount of time without any further reduction (at least for the four annealing experiments at the lowest temperatures between 1150 °C and 1225 °C; at 1250 °C stagnation occurs at slightly lower hardness). For all except the two lowest annealing temperatures, the hardness finally decreases to the value 357 ± 2 HV10 of the fully recrystallized condition (for 1200 °C after 200 h, for 1250 °C after 50 h and at 1300 °C from 24 h).

3.3. Microstructure evolution during annealing

The peculiarities in the hardness evolution during annealing relate to the underlying microstructure evolution. Fig. 2a shows the microstructure of a sample annealed for 192 h at 1250 °C as obtained by EBSD; the orientation map reveals an abundance of defect-free, almost equiaxed grains. Only in small regions, remains of the deformation structure can be traced; the structure is (almost) fully recrystallized. From the EBSD data, a recrystallized volume fraction X_V of (99 ± 1)% is determined, which is confirmed by the low hardness value 358 ± 1 HV10. Fig. 2b, on the other hand, shows the microstructure after annealing for 1872 h at 1150 °C. Despite the rather long annealing time (the longest in the entire study, about 2.5 months), the sample has not fully recrystallized and the recrystallized volume fraction X_V is only (65 ± 2)%. After the stagnation value of about 390 HV10 is attained after 286 h at this temperature, the hardness almost does not change during the following 1500 h (two months) (see insert in Fig. 1). Several samples annealed for different times at different temperatures with a hardness value corresponding to this stagnation value (390 ± 10 HV) have been investigated and their microstructure analysed by EBSD. The vast majority of them resulted in a recrystallized volume fraction between 60% and 80% as determined from the orientation maps. In a similar manner, samples with a hardness value of 417 ± 7 HV10 corresponding to the first apparent period of stagnation showed a recrystallized volume fraction about 40% proving that also the initial hardness drop is caused by progress in recrystallization from the partially recrystallized, as-received condition.

3.4. Annealing kinetics

The hardness of a partially recrystallized structure follows from the rule of mixtures

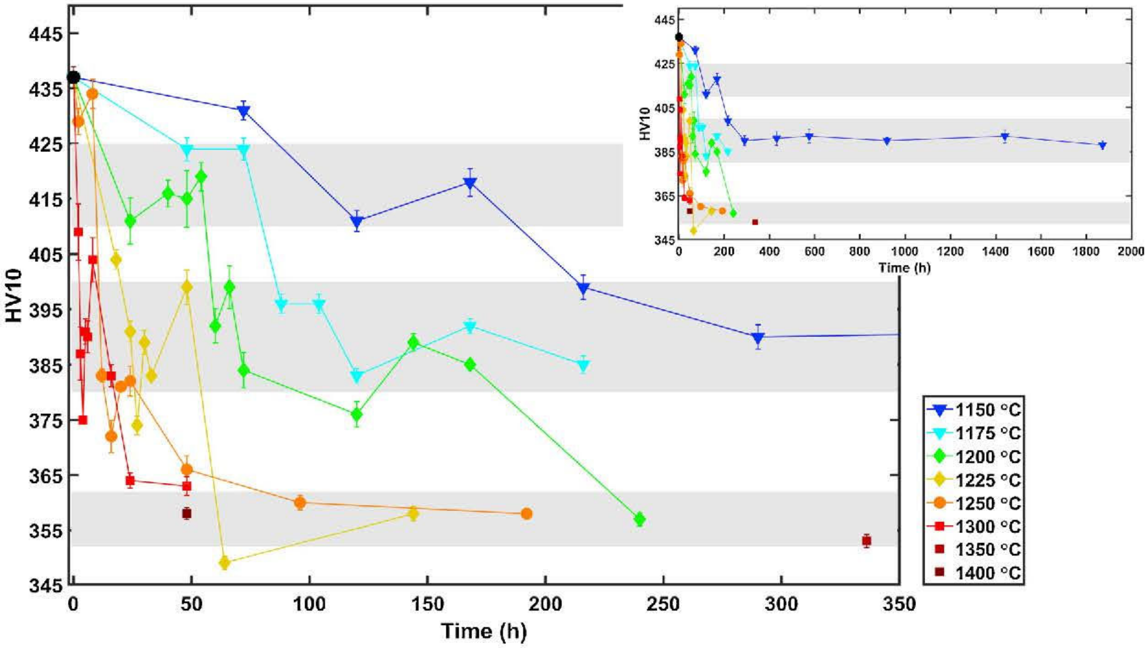

Fig. 1. Hardness evolution during annealing of tungsten warm-rolled to 80% thickness reduction (W80). Symbols and error bars mark average hardness value and their standard deviations. The three grey bands highlight the intermediate halting periods (For interpretation of the references to colour in this figure legend, the reader is referred to the web version of this article).

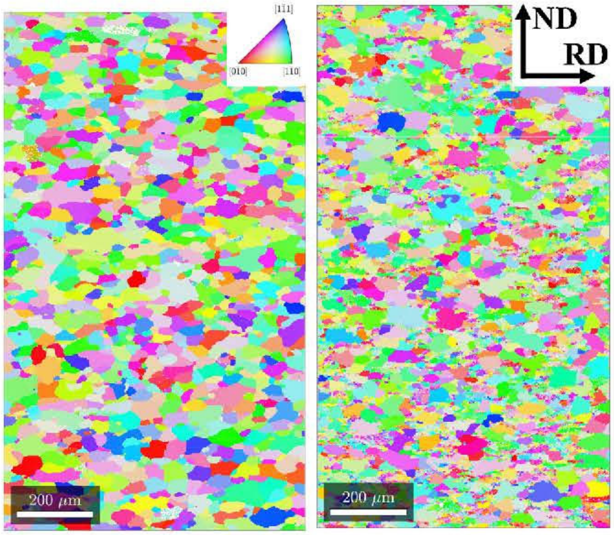

Fig. 2. Orientation maps obtained by EBSD on RD/ND sections of tungsten warm-rolled to 80% thickness reduction (W80) annealed for (a) 192 h at 1250 °C (fully recrystallized) and (b) 1872 h at 1150 °C (partially recrystallized with a recrystallized volume fraction of (65 ± 2)%). The colors indicate the crystallographic direction along RD according to the insert. The rolling direction is horizontal; the top parts are closest to the center of the warm-rolled plate.

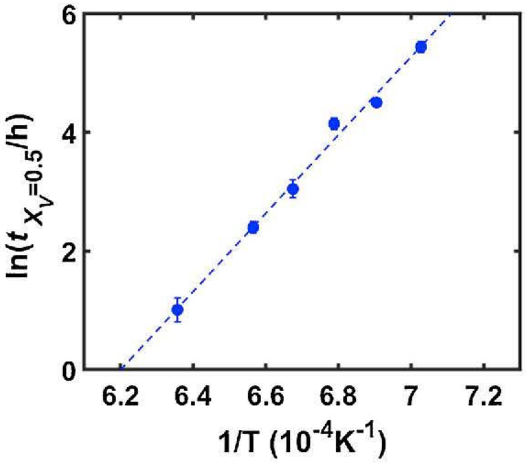

Fig. 3. Time to half recrystallization of tungsten warm-rolled to 80% thickness reduction as determined from the hardness evolution in dependence on annealing temperature (Arrhenius plot).

$$HV_c = X_V HV_{rex} + (1 - X_V) HV_{def} \tag{1}$$

from the hardness of the deformed structure (HV_{def}) and that of the fully recrystallized structure (HV_{rex}). If the partial recrystallization ($X_V = 18\%$) of the as-received condition is taken into account, the recrystallized volume fraction corresponding to the hardness value of 390 HV10 during stagnation is estimated to 66%, in good agreement with the values determined by EBSD e.g. (65 ± 2)% after annealing for 1872 h at 1150 °C (Fig. 2b).

In a similar manner, the time to half recrystallization can be estimated from the hardness evolution. The hardness value of half recrystallized material ($X_V = 0.5$) is estimated to 406 HV10 from the hardness of the as-received and recrystallized condition taking into account the partial recrystallization in the as-received state. In the hardness evolution during isothermal annealing, this value occurs always between the two halting levels at 417 ± 7 HV10 and 390 ± 10 HV10. For each isothermal series, the time to half recrystallization is hence inferred by interpolation between the measured hardness values just before and after the sudden drop (for example, in case of 1150 °C, the hardness values at 168 h and 216 h). As illustrated in Fig. 3, these estimated times to half recrystallization $t_{X_V=0.5}$ decrease with increasing temperature as expected for a thermal activated process. The consistency between the determined times to half recrystallization for different temperatures confirm that effects caused by the heterogeneity of the plate have been successfully confined to some extent.

4. Discussion

Assessment of the thermal stability of the tungsten plate warm-rolled to 80% thickness reduction is partially hindered by the macroscopic heterogeneity and the partial recrystallization of the as-received condition. An attempt has been made to limit the influence of the heterogeneity, but as seen from the non-monotonous behaviour in the hardness evolution, this was not always successful. Analysis of the recrystallization kinetics is hence limited to an analysis of the time to half recrystallization $t_{X_V=0.5}$. As seen from Fig. 3, the dependence on temperature T follows accurately an Arrhenius relation

$$t_{X_V=0.5} = t^*_{X_V=0.5}\exp\left(\frac{Q}{RT}\right) \tag{2}$$

with a prefactor $t^*_{X_V=0.5}$ and the ideal gas constant R. The activation energy Q of 548 kJ/mol obtained by fitting compares well with the one (579 ± 7% kJ/mol) reported for the slightly less warm-rolled plate W67 [7] and the activation energy of bulk self-diffusion in polycrystalline tungsten (506–586 kJ/mol) [1], but it is significantly higher than the observed activation energy (352 ± 4% kJ/mol) for the more severely warm-rolled plate W90 [8] or that of short-circuit diffusion in tungsten (377–460 kJ/mol) [1]. The behaviour of W80 warm-rolled to 80% thickness reduction resembles more that of the plate warm-rolled to 67% thickness reduction than the one warm-rolled to 90% thickness reduction. The transition in activation energy for the time to half recrystallization from the one of bulk diffusion at low rolling reductions to the one of short-circuit diffusion at higher rolling reductions observed earlier occurs obviously not before 80% thickness reduction.

For all investigated temperatures, the time to half recrystallization reported here for W80 is shorter than the one of W67. This is mainly due to the larger driving force given by the larger stored energy density in the deformation structure as reflected also in the higher hardness of the as-received condition of W80, despite the apparent partial recrystallization. Due to the partial recrystallization of the as-received condition, the time to half recrystallization reported here must be considered only to be an estimate and would have to be corrected for the time span to reach the recrystallized volume fraction of $X_V = 18\%$ of the as-received state. This time span would be governed also by thermal activated processes and depend on the annealing temperature; neglecting it, does not alter the apparent activation energy presuming the same governing processes through the late and early stages of recrystallization. Despite all mentioned problems with the heterogeneity of the plate, the occurrence of a period of time in which the hardness decrease halted and the process of recrystallization stagnated was clearly revealed. The time span, during which the processes halted, increases with decreasing temperature and lasted for the lowest temperature of 1150 °C for more than two months without leading to complete recrystallization as evidenced by Fig. 2b. The reason for such stagnation in the process of recrystallization is not obvious and one might speculate that particular texture components in the deformation structure might be harder to be invaded by moving grain boundaries carrying recrystallization (e.g. [16]). This might be either caused by a low mobility of the moving boundaries due to orientation pining or a low driving force for boundary motion due to significantly lower stored energy density (either as a result of plastic deformation during warm-rolling or caused by recovery during annealing).

Conclusions and outlook

During annealing of tungsten warm-rolled to 80% thickness reduction, the hardness does not decrease continuously and intervals of stagnation were identified. During these periods of time the hardness evolution and the progress of recrystallization halted. These halting periods turn even more relevant for assessing the suitability of the warm-rolled tungsten plates for future fusion applications. Neither complete recrystallization, nor full degradation of the mechanical properties occurs before recrystallization commences after the end of the halting period, deeming the W80 plate more suitable for application as armor material than expected solely from the time to half recrystallization and the inferred activation energy of 548 kJ/mol. It is envisaged, that the phenomenon of halted recrystallization discovered here could enable the design of deformed tungsten material which even not being unaffected by recrystallization, survive at the high operation temperatures in a partially recrystallized state not undergoing complete recrystallization for extended periods of time.

Acknowledgements

This work has been carried out partially within the framework of the EUROfusion Consortium and has received funding from the Euratom research and training program 2014-2018 under grant agreement No 633053. The views and opinions expressed herein do not necessarily reflect those of the European Commission.

References

[1] E. Lassner, W.-D. Schubert, The Element Tungsten, Tungsten (1999) 1–59, https://doi.org/10.1007/978-1-4615-4907-9_1.
[2] R.G. Abernethy, Mater. Sci. Technol. 0836 (2016) 1–12.
[3] J. Davis, V. Barabash, A. Makhankov, L. Plöchl, K. Slattery, J. Nucl. Mater. 258–263 (1998) 308–312.
[4] J. Reiser, J. Hoffmann, U. Jäntsch, M. Klimenkov, S. Bonk, C. Bonnekoh, M. Rieth, A. Hoffmann, T. Mrotzek, Int. J. Refract. Met. Hard Mater. 54 (2016) 351–369.
[5] B. Gludovatz, S. Wurster, A. Hoffmann, R. Pippan, Int. J. Refract. Met. Hard Mater. 28 (2010) 674–678.
[6] D. Rupp, S.M. Weygand, J. Nucl. Mater. 386–388 (2009) 591–593.
[7] A. Alfonso, D. Juul Jensen, G.N. Luo, W. Pantleon, J. Nucl. Mater. 455 (2014) 591–594.
[8] A. Alfonso, D. Juul Jensen, G.N. Luo, W. Pantleon, Fusion Eng. Des. 98–99 (2015) 1924–1928.
[9] K. Wang, X. Zan, M. Yu, W. Pantleon, L. Luo, X. Zhu, P. Li, Y. Wu, Fusion Eng. Des. 125 (2017) 521–525.
[10] M. Yu, K. Wang, X. Zan, W. Pantleon, L. Luo, X. Zhu, Y. Wu, Fusion Eng. Des. 125 (2017) 531–536.
[11] K. Tsuchida, T. Miyazawa, A. Hasegawa, S. Nogami, M. Fukuda, Nucl. Mater. Energy. 15 (2018) 158–163.
[12] U.M. Ciucani, A. Thum, C. Devos, W. Pantleon, Nucl. Mater. Energy. 15 (2018) 128–134.
[13] T. Palacios, J. Reiser, J. Hoffmann, M. Rieth, A. Hoffmann, J.Y. Pastor, Int. J. Refract. Met. Hard Mater. 48 (2015) 145–149.
[14] S. Bonk, J. Reiser, J. Hoffmann, A. Hoffmann, Int. J. Refract. Met. Hard Mater. 60 (2016) 92–98.
[15] J. Reiser, M. Rieth, B. Dafferner, A. Hoffmann, J. Nucl. Mater. 423 (2012) 1–8.
[16] Z. Zhang, Y. Zhang, O.V. Mishin, N. Tao, W. Pantleon, D. Juul Jensen, Metall. Mater. Trans. A 47 (2016) 4682–4693.

5.2 Microstructural path investigation into stagnation of recrystallization in warm-rolled tungsten

Microstructural path investigation into stagnation of recrystallization in warm-rolled tungsten

Umberto M. Ciucani*, Wolfgang Pantleon

Section for Materials and Surface Engineering, Department of Mechanical Engineering, Technical University of Denmark, 2800 Kongens Lyngby, Denmark;

Corresponding Author: Umberto M. Ciucani, Section for Materials and Surface Engineering, Department of Mechanical Engineering, Technical University of Denmark, 2800 Kongens Lyngby, Denmark, umciuc@mek.dtu.dk, +45 45254883.

Corresponding Author ORCID: orcid.org/0000-0003-3881-4811

Microstructural path investigation into stagnation of recrystallization in warm-rolled tungsten

Tungsten is the main candidate material for application in fusion reactors as plasma-facing structural material. Cold working renders tungsten ductile so that application as armor material in a reactor can be envisioned. Exposure to high operational temperatures subjects the material to the risk of embrittlement by recrystallization, ultimately jeopardizing its performance. The microstructural changes due to recrystallization in a heavily recovered tungsten plate warm-rolled to 80 % thickness reduction are investigated in the temperature range from 1150 °C to 1200 °C by means of electron backscatter diffraction. The microstructural evolution during annealing is examined quantitatively in terms of major texture components as well as other microstructural parameters as stored energy or boundary surface densities of both the recovered and recrystallized regions in order to map the microstructural path. During recrystallization, a rather homogeneous nucleation and growth of recrystallized grains is revealed up to a recrystallized fraction of about 60 %. Afterwards, an unexpected stagnation of the progress of recrystallization is observed. The microstructural reasons for the change in recrystallization behavior are investigated: after the stagnation period, impingement occurs non-uniformly up to complete recrystallization. Additionally, a strongly reduced stored energy density is observed in the recovered regions. It is suggested that recrystallization stagnates due to a combination of defect content depletion caused by static recovery with non-uniform impingement due to ordered formation of nuclei, e.g. along deformation bands, together with recrystallization progressing along bands of high remaining stored energy.

Keywords: tungsten; annealing; recrystallization; impingement; thermal stability; EBSD, microstructural path method.

1. Introduction

Tungsten is the main candidate material for armor of plasma-facing components in fusion reactors[1–4]. Exposure to high operational temperatures, high heat and neutron fluxes in a fusion reactor chamber imposes the risk of undesired microstructural changes: recrystallization of tungsten reinstates brittleness in the material and must be avoided for components experiencing thermal stress fatigue. Over the last decade, materials development towards identifying thermally stable tungsten materials has been pursued along two major routes. One approach has been to design tungsten composites[5], for instance, tungsten fiber-reinforced tungsten composites where drawn tungsten fibers were embedded in a chemically vapor deposited tungsten matrix[6,7]. Alternatively, particle reinforcement of tungsten by dispersing rare earth oxides[8] or tungsten (semi)carbide[9] is considered. In both cases, Zener pining of boundaries by dispersed particles is supposed to arrest recrystallization fronts. In a similar way, potassium bubbles formed by doping tungsten with small amounts of insoluble potassium are able to inhibit boundary motion; a methodology developed to technological readiness in drawn wires for light bulbs[10] and, more recently attempted, in thin rolled plates[11].

A fundamentally different approach is based on gaining a deeper understanding of recrystallization in pure deformed tungsten (mainly after rolling) and exploit this knowledge to identify particular manufacturing conditions that allow production of material with improved thermal stability. For tungsten rolled in different manners, e.g. to different thickness reductions corresponding to different amounts of strain[12–16], the recrystallization kinetics has been investigated with the aim to understand the dependence of recrystallization on the deformation history and the thermal stability of differently deformed tungsten. Within this framework, investigation on the recrystallization behavior of a particular warm-rolled tungsten plate has led to the discovery of stagnation in the recrystallization process[17]. During isothermal annealing at temperatures between 1150 °C and 1200 °C, a pure tungsten plate warm-rolled to 80 % thickness reduction shows conventional progress of recrystallization up to a recrystallized volume fraction of about 60 %, whereupon the progress stagnates, and further recrystallization halts for long times, before recrystallization resumes and reaches completeness. Understanding the mechanisms preventing the progress of recrystallization in such a plate is potentially key to the design of materials possessing higher recrystallization resistance. In order to exploit the finding, the microstructure is investigated aiming towards revealing the microstructural reason behind the temporary halt in recrystallization progress.

2. Materials and Methods

2.1. Materials and hardness evolution

A 99.95 wt.% pure tungsten plate of size 200.8 x 100.3 x 8.3 mm^3 along the rolling direction (RD), transverse direction (TD) and normal direction (ND), respectively, was acquired from Advanced Technology & Materials Co. Ltd. in Beijing. The plate is produced via a powder metallurgical route. The original ingot is cold-isostatic pressed and sintered under hydrogen atmosphere at 2300 °C for 6 h and pre-annealed at 1100 °C for 15 minutes to relieve stresses prior to rolling. Finally, the ingot is warm-rolled – by reverse rolling – in 10 passes to a thickness reduction of 80 % (hence termed W80), from a starting temperature of 1550 °C to a final temperature of 1100 °C.

For the purpose of annealing, the plate is cut into smaller specimens of sizes 6 x 5 x 4 mm^3 along RD, TD and ND, respectively. Each specimen is individually encapsulated in a quartz ampoule upon flushing with an inert gas 99.99% pure Argon and evacuating for the sake of preventing oxidation. Isothermal annealing is performed in a general-purpose tube furnace

NaberTherm RHTC 80-230/15 at different temperatures between 1150 °C and 1400 °C for times up to 1872 h.

The progress of recrystallization was tracked previously[17] by means of Vickers hardness testing. At the highest temperatures of 1225 °C and above, complete recrystallization is observed after periods shorter than 3 days (see Fig. 1). For the three lower temperatures (1150 °C, 1175 °C and 1200 °C), a step-wise evolution of recrystallization occurred as seen from the hardness evolution; full recrystallization was never achieved for the two lowest temperatures (1150 °C and 1175 °C) – even after 2.5 months (at 1150 °C). Upon annealing, a loss in hardness occurred the faster, the higher the annealing temperature. After the hardness loss amounts to a recrystallized fraction of about 60 % to 75 %, a stagnation period is observed during which no further loss in hardness takes place, before recrystallization commences. The lower the temperature, the longer the stagnation period. A fully recrystallized condition is achieved for temperatures of 1200 °C and above only.

In its as-received condition, the plate was already partially recrystallized having a recrystallized volume fraction of 15% and possessing a hardness of 437 HV10, while the hardness for the fully recrystallized condition is 355 HV10 as shown in Fig. 1. Based on this, the time to achieve a recrystallized volume fraction of 50 % has been analyzed[17], but further analysis of the recrystallization kinetics was prevented by the occurrence of the stagnation period.

In order to achieve a proper description of the recrystallization behavior including the stagnation period, a thorough microstructural investigation of the partially recrystallized conditions is performed. Information on texture and microstructural evolution during recrystallization is obtained by orientation mapping and analyzed based on the microstructural path method[18,19]. Tracing the microstructural path in this manner aims towards revealing the characteristic changes occurring in the process causing the temporary halt of recrystallization.

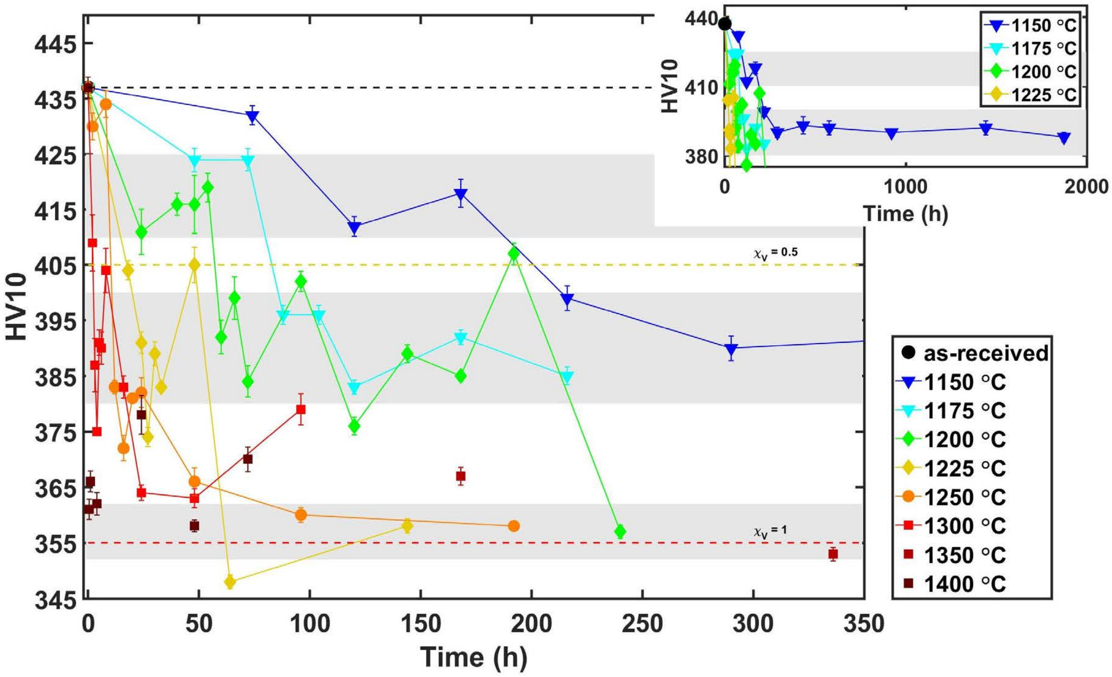

Figure 1: Hardness evolution during annealing of tungsten warm-rolled to 80% thickness reduction (W80). Symbols and error bars mark average hardness value and their standard deviations. The three grey bands highlight halting periods in the evolution. Different recrystallized fractions (X_V=0, 0.5 and 1) are indicated by dashed lines (data from [13]).

2.2. Modelling recrystallization

Analysis of the recrystallization behavior in W80 by means of hardness only allowed the determination of an activation energy for the time for half recrystallization[17], whilst the stagnation of recrystallization impeded the understanding of the kinetics by means of conventional modelling. The classical Johnson–Mehl–Avrami–Kolmogorov (JMAK) model, proposed theoretically for crystallization by Kolmogorov[20] and (independently) deduced empirically by Johnson and

Mehl[21] and Avrami [22], describes the evolution of recrystallization through the increase of the fraction recrystallized X_v with time t according to the following equation (modified[12] to account for an incubation time t_{inc}):

$$X_V = 1 - \exp[-b^n(t - t_{inc})^n] \tag{1}$$

with a coefficient b describing the combined effect of nucleation and growth rates. The Avrami exponent n depends on the dimensionality of the growing grains[20]. Additionally it characterizes, whether nucleation occurs continuously or is of a site-saturated character. The model assumes homogeneous nucleation, i.e. a random distribution of recrystallization nuclei in the volume, which is very often not taking place.

By use of additional parameters, characterization of recrystallization has been improved by Vandermeer and Rath[18,19,23]. Their method accounts for microstructural effects on the recrystallization evolution by providing a framework for quantification the average nucleation and growth conditions of recrystallizing grains following stereological principles – albeit it fails to reveal information on the physical mechanisms. In their method, the path of microstructural evolution during recrystallization is expressed in general as mathematical function

$$f\left[X_V(t), S_{V_{rxrc}}(t), \langle\lambda_{rx}\rangle(t), C_{rxrx}(t)\right] = 0 \tag{2}$$

of several microstructural parameters[24] such as the fraction recrystallized X_V, the interfacial boundary density $S_{v_{rxrc}}$ between recrystallized (rx) and recovered (rc) regions, the average chord length $\langle\lambda_{rx}\rangle$ or the contiguity ratio C_{rxrx} of the recrystallized grains. The time-independent partial path functions (e.g. $S_{V_{rxrc}}(X_V)$ or $\langle\lambda_{rx}\rangle(X_V)$) of these parameters provide information on the nucleation and growth of recrystallized grain in the material. These microstructural parameters can be inferred from prepared sections of the microstructure in annealed specimens by light optical microscopy or orientation mapping:

1. The interfacial boundary density $S_{V_{rxrc}}$, i.e. the boundary surface density of boundaries separating recrystallized regions from recovered ones, has been used by Cahn and Hagel[25] to describe average growth rates. Assuming a power law dependence of both, nucleation and growth rate, an analytic expression for the partial path function $S_{V_{rxrc}}(X_V)$ is developed[19,26]

$$S_{V_{rxrc}} = C_0(1 - X_V)[-\ln(1 - X_V)]^q \tag{3}$$

which provides insight on nucleation and growth through the coefficients C_0 and q and allows an assessment of the appropriateness of the JMAK model.

2. The contiguity ratio C_{rxrx}, which is a stereological parameter characterizing the spatial distribution of the recrystallized grains[24],

$$C_{rxrx} = \frac{2S_{V_{rxrx}}}{2S_{V_{rxrx}} + S_{V_{rxrc}}} \tag{4}$$

is the fraction of the total grain boundary area of recrystallizing grains shared by other recrystallized grains and is defined in terms of the boundary surface densities between recrystallized grains $S_{V_{rxrx}}$ and the interface boundary density $S_{V_{rxrc}}$ between recrystallizing grains and recovered matrix defined above. The contiguity ratio increases monotonically with fraction recrystallized. For randomly dispersed nuclei, the dependence has been derived analytically[27]; deviations from that master curve can be attributed to a heterogeneous distribution of nuclei, either due to clustering or ordering;

3. The average chord length $\langle\lambda_{rx}\rangle$ of recrystallized grains, which is in particular useful to characterize grain impingement[24], follows a suggested partial path function[24]:

$$\langle\lambda_{rx}\rangle = K_\lambda(X_V)^{1/3}[-\ln(1 - X_V)]^p \tag{5}$$

with coefficients K_λ and p depending on the nucleation and impingement behavior of recrystallized grains. Uniform impingement corresponding to random nucleation and isotropic growth leads to

$p = 0$; smaller values of $p = 1/6$ or $p = 2/3$ suggest linear and planar impingement[24], respectively.

2.3 Electron backscatter diffraction

An analysis of the microstructural paths as outlined in the previous section is undertaken to improve the understanding of nucleation and growth of recrystallization of an 80% reduced warm-rolled pure tungsten plate and to obtain additional insights into the nature of the temporary stagnation observed in the course of recrystallization.

In order to access microstructural descriptors to describe recrystallization, orientation maps are gathered from as-received and annealed specimens (see table 1) by electron backscatter diffraction (EBSD) in a FEI Nova Nano SEM 600, with applied voltages of 20 kV and currents ranging from 1.1 nA to 6.3 nA, equipped with a Bruker e–FlashHD EBSD detector. The step sizes used were 500 nm and 100 nm for the as-received condition, and 2 μm for partially and fully recrystallized specimens. High-resolution scans of the as-received condition with the small step size of 100 nm were performed to assess the underestimation of the stored energy density in maps of larger step size. Orientation maps of an area 791.4 x 682.6 μm^2 were gathered on square grids with a step size of 2 μm and 0.5 μm at a magnification of 191x, while maps obtained on square grids with step size of 0.1 μm and magnification 800x covered a smaller area of 186.5 x 163.5 μm^2. Datasets exported from the microscope software BRUKER Esprit 2.1 were analyzed by use of MTEX toolbox version 5.2.3[28,29].

For determination and analysis of the microstructural descriptors introduced above, such as boundary surface densities or average chord lengths of recrystallized grains, specific routines were purposely developed based on proper definitions of recrystallized grains and grains in general. The main aspects are outlined in the following.

2.3.1 Classification of boundaries and grains

1) In orientation maps gathered on square grids, the misorientation between neighboring pixels is determined as the orientation difference with lowest misorientation angle with respect to cubic crystalline symmetry.
2) The presence of a boundary between neighboring pixels is inferred whenever a misorientation angle of at least 2° is found between adjacent pixels. (This chosen minimum threshold angle of 2° is obviously too low to allow proper definition of grains in deformed or recovered regions. There, the identified entities should rather be addressed as subgrains. For simplicity, the term grain will be retained throughout the text.)
3) Boundaries possessing a misorientation angle smaller than 15° are classified as low angle boundaries (LABs), whilst high angle boundaries (HABs) have misorientation angles of at least 15°.
4) Grains are defined as regions completely enclosed by boundaries (irrespective of the misorientation angle). This does not exclude the existence of inner boundaries (IBs) within a grain, neither LABs nor HABs. In general, no lower limit is required for the size of a grain and grain areas are determined from the number of indexed points assigned to the grain.

2.3.2 Recrystallized vs. recovered grains

In order to identify recrystallized regions, recrystallized grains need to be distinguished from the entire set of grains. For this sake, recrystallized grains are identified in the following manner:

5) Only grains with apparent areas larger or equal to 32 μm^2 (i.e. consisting of 8 pixels at least) are considered as potentially recrystallized grains; grains below this size are

discarded as recrystallized grains. Including such small grains would cause an excessive amount of the deformed matrix to be mistakenly considered as recrystallized (such a choice also prevents any artefacts smaller than 8 pixels to affect the analysis).

6) In order to consider a grain as recrystallized, at least 25% of its outer boundary length (shared with other grains) must consist of HABs, as only boundary with misorientations angles of at least 15° are regarded as mobile and capable of moving into the deformed matrix during recrystallization.
7) For ruling out grains with remaining deformation structures to be considered as recrystallized grains, the total length of inner boundaries must be below 10% of its outer boundary length.

In this manner, two different subsets of grains are distinguished: recrystallized grains (rx) and non-recrystallized grains. The latter will be addressed as recovered grains (rc) as they still contain a deformation structure albeit after some recovery. Similarly, recrystallized and recovered regions are defined as regions consisting of solely recrystallized or recovered grains, respectively. For the recrystallized grains, their average chord length $<\lambda_{\mathrm{rx}}>$ in an orientation map is obtained by averaging all available chord length of recrystallized grains in horizontal and vertical direction of the map.

The recrystallized volume fraction X_V is determined as area fraction of the recrystallized region formed by all recrystallized grains (assuming equivalence between area and volume fraction). The accuracy of identifying recrystallized grains in this manner throughout the different orientation maps is estimated by visual comparison; in terms of the volume fraction a underestimation of less than 2% is achieved.

Fig. 2 illustrates the results of the procedure on the example of W80 annealed at 1150 °C for 1872 h. An orientation map of the partially recrystallized is shown in Fig. 2a where the individual orientations are colored according to the crystallographic direction along ND, according to the inverse pole figure color scheme in the inset where red, green and blue correspond to the <100>, <110> and <111> directions respectively. Non-indexed points are presented in white. The same orientation map is shown in Fig. 2b with the recrystallized grains presented in dark brown while the coloring is retained for all other grains. These non-recrystallized grains constitute deformed grains after recovery due to annealing and represent the remainder of the deformation structure. In Fig. 2c these recovered grains are presented in dark brown, while the colors of recrystallized grains reflect their crystallographic direction along ND.

2.3.3 Boundaries and boundary densities

Having identified two subsets of grains, recrystallized (rx) grains and recovered (rc) grains, and distinguished between inner boundaries (IBs) and grain boundaries (outer boundaries) of grains, different subsets of grain boundaries can be defined: (i) rxrx boundaries separating recrystallized grains, (ii) rxrc boundaries between recrystallized grains and the recovered matrix and (iii) rcrc boundaries being those between recovered grains solely. The rxrc boundaries are the boundaries able to carry on recrystallization by further moving into the recovered region. They can be utilized to define a subset of recovered grains in the recovered matrix in direct contact with the recrystallized grains and hence identify the potential region invaded next by the recrystallization front. As a result, grains classified as recovered (rc grains) are further subdivided into two subsets: rcrc grains belonging to the recovered matrix and in contact with other recovered grains only and rcloc grains, the subset of recovered grains bordering recrystallized grains.

In turn, each subset of grains possesses different sets of boundaries: rcloc grains have rcrc boundaries and rxrc boundaries, rcrc grains possess only rcrc boundaries, while rx grains possess both rxrc and rxrx boundaries. Additional to the grain boundaries, which are the outer boundaries of grains, inner boundaries may exist in the grains.

Grain boundaries of all grain subsets are further distinguished by their misorientation angle: they are either LABs or HABs. In Fig. 2d, boundaries from the entire recovered region (from the rc grains) are shown. For rcrc boundaries, LABs are colored in red and HABs in black; all rxrc boundaries are highlighted as thick green lines. Fig. 2e shows only the rcloc region formed by rcloc grains colored according to their crystallographic direction along TD; rxrc boundaries are in brown with thick lines, LABs and IBs in red and HABs in black. A boundary map for rcrc grains is shown in Fig. 2f with IBs colored in cyan, LABs in red and HABs as thick black lines.

Fig. 3 depicts a magnified orientation map displaying only rcloc grains (colored according to the crystallographic direction parallel to TD) and rx grains in dark brown. All boundaries (HABs, LABs, and IBs) of the rcloc region are marked in black, the rxrc boundaries in dark green and the rxrx boundaries in red.

When boundary surface densities are reported, global boundary surface densities S_V and local (specific) boundary surface densities S_V^* must be distinguished. Where the former represent densities with respect to the entire map, the latter are local densities with respect to specific regions only. The two measures are connected by the volume fraction of the corresponding region, for instance, for boundaries of the recrystallized region

$$S_V = X_V S_V^* \tag{6}$$

and that of the recovered region

$$S_V = (1 - X_V) S_V^* \tag{7}$$

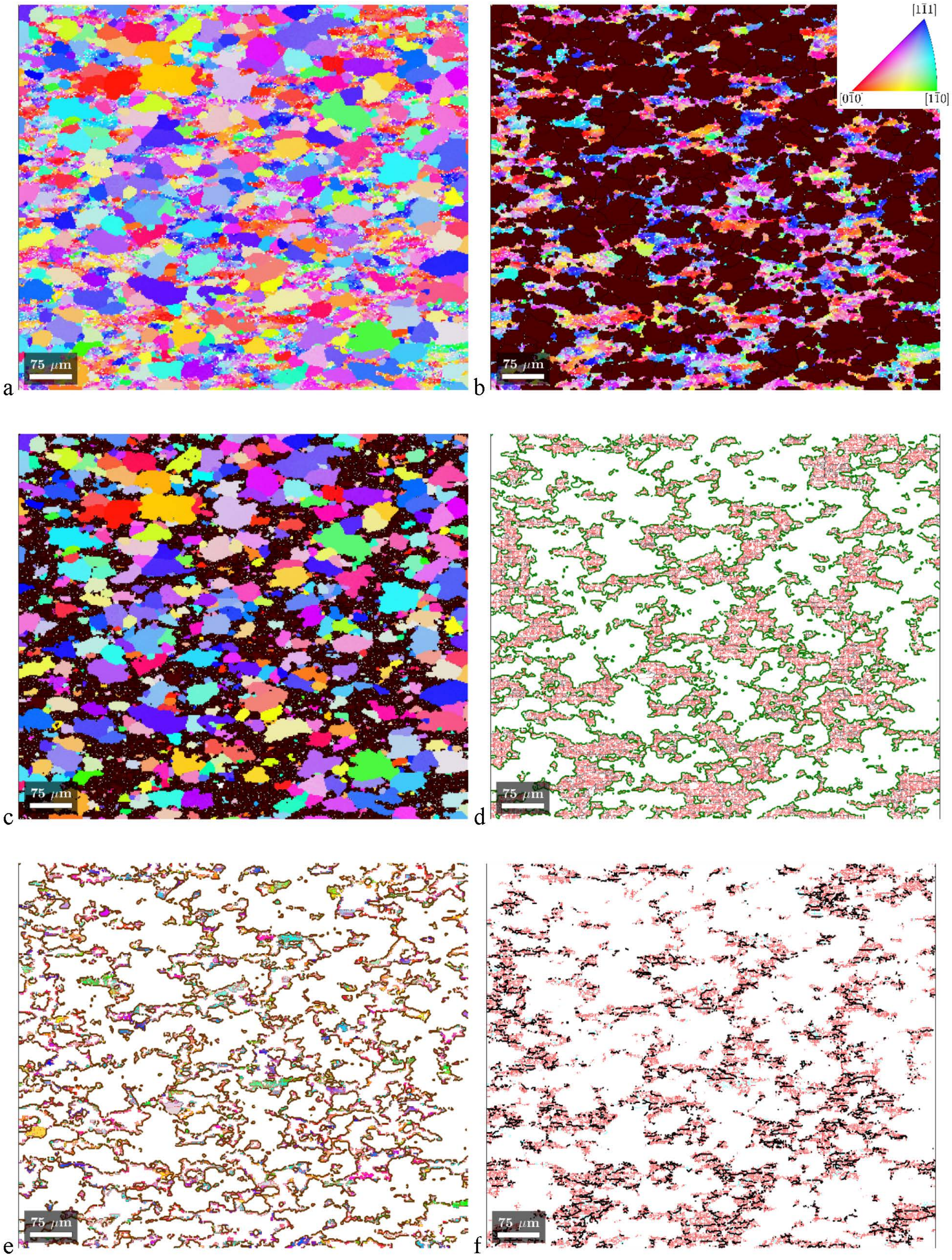
a
b
c
d
e
f
75 μm
75 μm
75 μm
75 μm
75 μm
75 μm
[1$\bar{1}$1]
[0$\bar{1}$0]
[1$\bar{1}$0]

Figure 2: Orientation and boundary maps of tungsten warm-rolled to 80% thickness reduction (W80) and annealed at 1150 °C for 1872 h showing the different features of the microstructure under investigation. a) Orientation map with all orientations colored according to the crystallographic direction parallel to ND with respect to the IPF shown in the insert of Fig. 2b, b) map with recrystallized grains in dark brown and recovered grains colored as in (a), c) map with recovered grains in dark brown and recrysallized grains colored as in (a), d) boundary map highlighting rxrc boundaries (green), LABs and IBs (both in red), and HABs (black) e) orientation map highlighting the rcloc grains colored according to TD with rxrc boundaries in brown, LABs and IBs (both in red), and HABs (black), f) boundary map of the rcrc grains highlighting IBs in cyan, LABs in red and HABs in black.

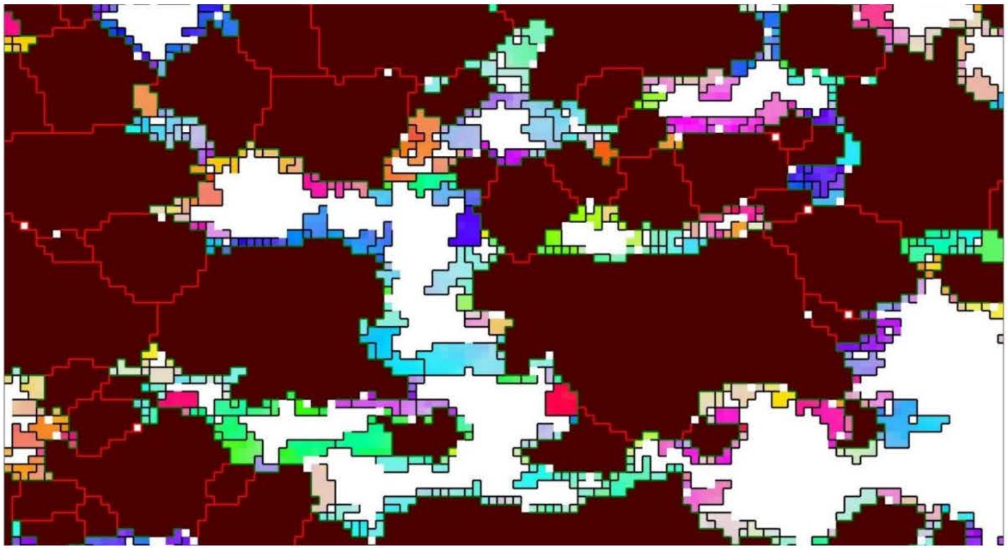

Figure 3: Detail of an orientation map of tungsten warm-rolled to 80% thickness reduction (W80) and annealed at 1150 °C for 1872 h showing recrystallized grains in dark brown, rxrx boundaries in red and rxrc boundaries in dark green. The orientation of the rcloc grains are colored according to the crystallographic direction parallel to TD with respect to the insert in Fig. 2b. All the boundaries in the rcloc grain region are colored in black and rcrc grains appear white.

2.3.4 Stored energy density

All boundary segments in the microstructure have a surface energy γ depending on their misorientation angle θ according to the Read-Shockley equation[30]:

$$\gamma = \begin{cases} \gamma_m(\theta/\theta_m)[1 - \ln(\theta/\theta_m)] & if\ \theta < \theta_m \\ \gamma_m & if\ \theta \geq \theta_m \end{cases} \tag{8}$$

with the boundary energy γ_m = 0.869 kJ/mol of HABs in tungsten[31] and the threshold misorientations angle θ_m above which γ is independent of the misorientation angle taken to be 15°. The energy density

$$u = \gamma S_V = \sum_{all\ segments} \gamma(\theta) \frac{\Delta x}{A} \tag{9}$$

stored in form of boundaries in the microstructure is calculated as sum of the boundary energy of each individual boundary segment, their segment length corresponding to the step size Δx and the area A of the considered region.

2.3.5 Texture components

Based on the gathered individual orientations, the texture evolution during annealing was tracked for the major fiber texture components of rolled bcc metals being the α-, γ-, and θ-fiber as well as for specific single texture components derived from individual ideal orientations belonging to those fibers: The cube component with ideal orientation {001}<100>, the ND rotated cube component {001}<110>, two components ({111}<110> and {111}<112>) along the γ-fiber, the TD rotated cube component {110}<110> and two more components ({112}<110> and {113}<110>) along the α-fiber. In Fig. 5b the position of the different fibers and individual orientation are illustrated in the $\varphi_2 = 45°$ section of Euler space where, for instance, the α-fiber is found along the line $\varphi_1 = 0°$, the γ- and θ-fibers along Φ=54.7° and Φ=0°, respectively. The volume fractions f of the different texture components are determined based on the individual orientation of each pixel. A pixel possessing an orientation deviating maximal 15° from either an ideal orientation of a single texture component or from one of the orientations describing the particular fiber is considered belonging to the single texture component or the fiber texture component, respectively. An individual orientation may belong to a single texture component and several fiber texture components, which has to be considered when the combined volume fraction of all fiber texture components is determined; instead of simply adding the volume fractions of the α-, γ-, and θ-fiber, the volume fractions of the two shared components {001}<110> and {111}<110> must subtracted.

2.3.6 Orientation maps

A list of all recorded maps used to determine the afore-mentioned microstructural descriptors and texture components is given in Table 1, while the orientation maps of the as-received condition and eight selected annealed conditions (besides the annealing at 1150 °C for 1872 h shown in Fig. 2) taken as an example for further microstructural investigation are reported in Fig. 4.

Table 1: List of recorded and analyzed orientation maps for the as-received specimen and annealed specimens.

Condition	Range of fraction recrystallized	Annealing time in hours	Step size
As-received	15 %	0	0.5 / 0.1 µm
1150 °C	31 %-74 %	288/920/1440/1872	2 µm
1175 °C	27 %-74 %	48/72/88/104/120/168/216	
1200 °C	29 %-97 %	48/54/60/66/72/96/120/144/168/240	
1250 °C	49 %-96 %	8/192	
1350 °C	98 %	336	
1400 °C	95 %	0.5	

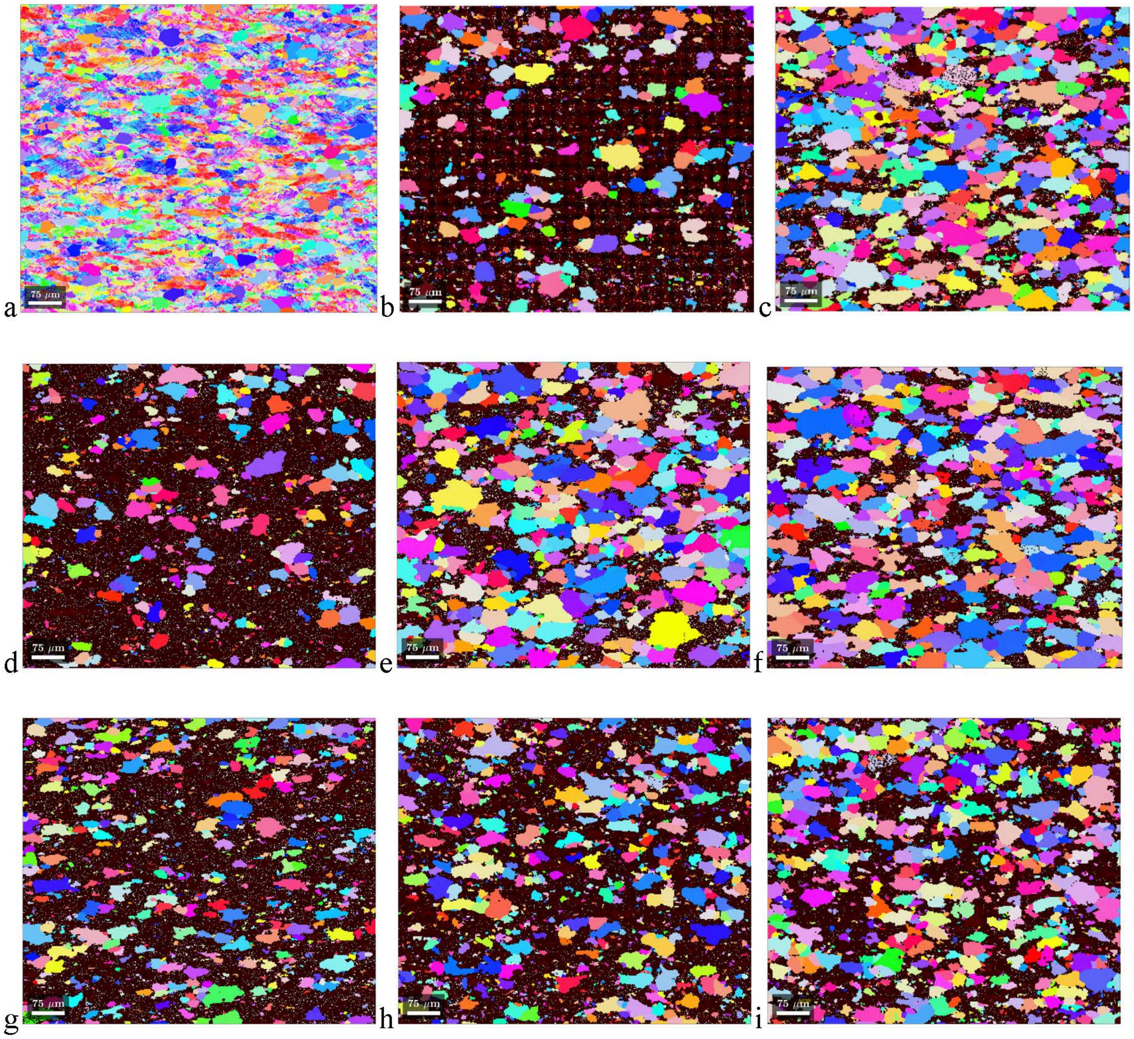

Figure 4: Orientation maps on the RD/ND section of tungsten warm-rolled to 80% thickness reduction (W80) for a) the as-received condition and after different annealing treatments. b) 1150 ℃ for 288 h, c) 1150 ℃ for 920 h, d) 1175 ℃ for 72 h, e) 1175 ℃ for 120 h, f) 1175 ℃ for 216 h, g) 1200 ℃ for 48 h, h) 1200 ℃ for 96 h, and i) 1200 ℃ for 144 h. The colors represent the crystallographic direction parallel to ND (vertical direction) with respect to the insert of Fig. 2b. Only recrystallized regions are highlighted in (b-i), while recovered regions are marked dark brown.

3 Results

3.1 As-received condition

The orientation map of the as-received condition is shown in Fig.4a. Based on all orientations in the map, the orientation distribution function (ODF) is calculated using a de la Vallee Poussin kernel with a half width of 7.5°. Fig. 5 presents the φ_2 = 45° section of Euler space.

The texture of the as-received materials is illustrated in Fig. 5a; the typical texture components for rolled bcc metals are marked in Fig. 5b. From the ODF of the as-received condition the presence of α- and γ-fiber components can be noticed, whereas the θ-fiber is hardly recognizable. Only low orientation densities below 2 are revealed even for the characteristic fibers (α-, γ-, θ-finer) expected to be present after rolling of a bcc metal.

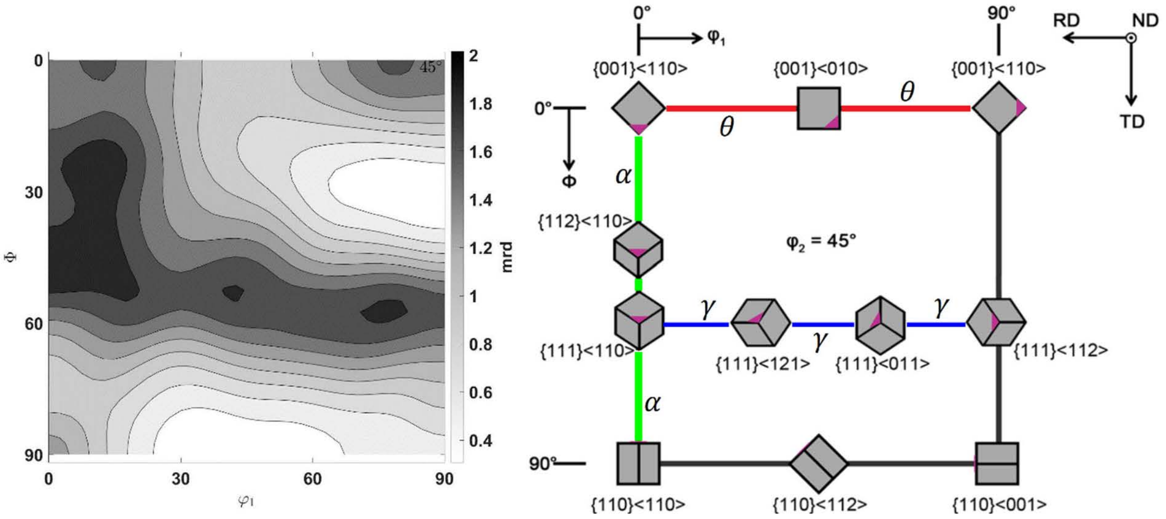

Figure 5: Section of Euler space with φ2=45°. (a) orientation distribution function obtained for the as-received condition of tungsten warm-rolled to 80% thickness reduction (W80) and (b) schematic representation marking the positions of the ideal orientations of the texture components and fiber textures tracked. The orientation densities are given in multiples of that of a random orientation distribution (mrd); the maximum orientation density being 1.9.

In the orientation map of the as-received condition in Fig. 4a, a number of recrystallized grains are noticeable. Using the approach outlined above, a recrystallized volume fraction of 15 % is detected. For quantifying the stored energy in the deformed structure, these recrystallized grains are excluded. By analyzing the non-recrystallized regions in the orientation map obtained with a step size of 0.5 µm, the stored energy density due to all boundaries of the deformed (and potentially slightly recovered) matrix reported in Table 2 are obtained for the different fiber textures components (α-, γ-, and θ-fiber) and single texture components belonging to those fibers. In general, the γ-fiber has a higher stored energy density (577 kJ/m^3) than the other two fibers, the θ-fiber (545 kJ/m^3) and the α-fiber (534 kJ/m^3) with an average stored energy density in the deformed regions of the as-received condition of 575 kJ/m^3. The highest values of stored energy density (above 600 kJ/mol) are found for the TD rotated cube {110}<110>, the ideal cube {001}<100>, and the {111}<110> component shared between α- and γ-fiber. The other components along the α-fiber, i.e. the ones not belonging to the γ-fiber or the TD rotated cube component; show rather low values (about 500 kJ/mol and less).

Table 2: Stored energy densities in the non-recrystallized regions of the as-received condition of tungsten warm-rolled to 80 % thickness reduction (W80) as obtained from the orientation map with 0.5 µm step size ignoring recrystallized regions.

Fiber texture component	Stored energy density
α-fiber	534 kJ/m^3
γ-fiber	577 kJ/m^3
θ-fiber	545 kJ/m^3
Entire map	575 kJ/m^3

Texture component with ideal orientation	Stored energy density
{001}<110>	485 kJ/m^3
{001}<100>	631 kJ/m^3
{113}<110>	478 kJ/m^3
{112}<110>	502 kJ/m^3
{111}<110>	611 kJ/m^3
{111}<112>	537 kJ/m^3
{110}<110>	689 kJ/m^3

For the recrystallization behavior, the boundaries between the recrystallized and the recovered regions are of particular importance, as their motion brings about the progress or recrystallization. The orientation differences across these rxrc boundaries are analyzed and the distributions of misorientation angles and axes shown in Fig. 6. The misorientation angle distribution in Fig. 6a shows two different maxima, one for LABs at a misorientation angle of about 5° and a second for HABs at about 45°. Additionally, two sharp peaks are seen at angles of

30° and 60°. These particular misorientation angles are found widely to arise from single pixel grains (recovered grains) with apparently misindexed patterns and were therefore ruled out as artifacts of indexing EBSD patterns. Careful pixel-by-pixel analysis of such misorientation angles showed that the indexing of the incremented patterns of single pixel grains based on the proper indexing of a zone axis, but an erroneous assignment of bands (wrongly indexed by 30° and 60° rotations with respect to the actual bands). To decrease the effect of such artifacts, single pixel grains in the maps were spared from further misorientation analyses. Unfortunately, peaks at those two misorientation angles persist to a lower extent in the distributions due to grains consisting of two pixels which could not be removed from the analysis automatically without largely affecting the correctly indexed points of the dataset otherwise.

The misorientation axes distribution are shown in Fig. 6b for all boundaries (with misorientations angles above 2°) and in Fig. 6c for HABs only. The latter allows comparison with the axes distributions of annealed specimens for which HABs are analyzed only (in Fig. 9). Removing LABs from the subset of boundaries analyzed leads expectedly to an increase in the frequency of misorientation axes along the [110]-[111] line from 1.15 to 1.6-1.8 times random density. The low densities below 1.8 in Fig. 6 shows the misorientation axes distribution for the as-received condition to be rather random without clear preference for any misorientation axes.

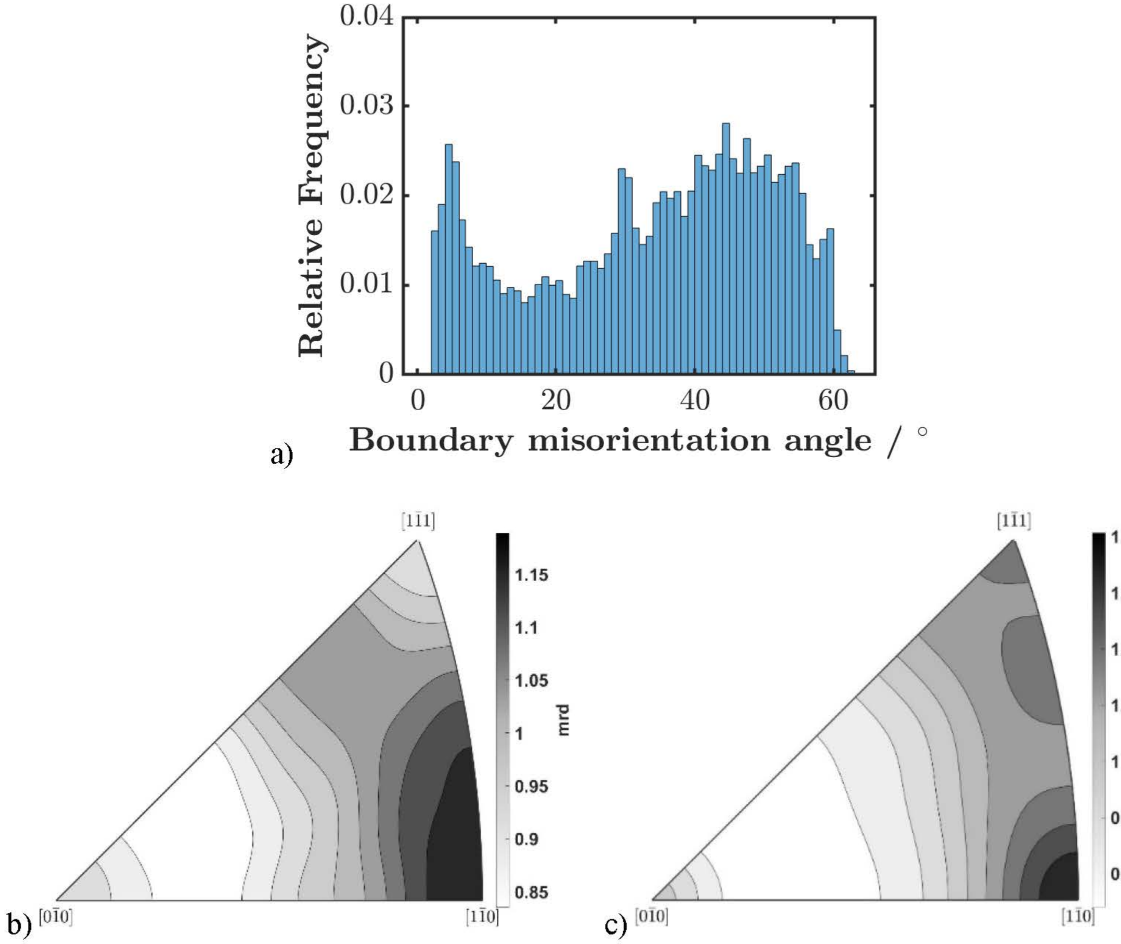

Figure 6: Misorientations across rxrc boundaries (i.e. boundaries between recrystallized and recovered regions) in the as-received condition of tungsten warm-rolled to 80 % thickness reduction (W80). a) misorientations angle distribution for boundaries having misorientations angles of at least 2°; misorientation axes distribution for b) all boundaries having misorientations angles of at least 2° and c) high angle boundaries with misorientations of at least 15° only. Densities are given in multiples of that of a random orientation distribution (mrd).

3.2 Texture Evolution

The texture evolution of W80 with the progress of recrystallization is illustrated in Fig. 8 in terms of the volume fractions f of the different resolved texture components. Thereby, the global volume fractions f_{global} in the entire maps are distinguished from volume fractions $f_{rc}^{*} = f_{global}/(1 - X_V)$ and $f_{rx}^{*} = f_{global}/X_V$ within the recovered and recrystallized regions, respectively.

3.2.1 Evolution in the recovered regions

The global volume fractions f_{global} of the different fiber texture components in the recovered region are shown in Fig. 8a as a function of the recrystallized fraction X_V. The black symbols denoted α+γ+θ represent the volume fraction contained in all three fibers where the sum of the volume fractions of the three fibers is corrected for the single texture components shared between two fibers as, for instance, the rotated cube orientation shared between α- and θ- fiber and {110}<110> shared between α- and γ-fiber. As obvious from of Fig. 8a, the global volume fractions of the fiber texture components formed by recovered grains decrease with increasing volume fraction recrystallized as expected due to the removal of recovered grains. Notably, the γ-fiber decreases its volume fraction much faster and reaches a volume fraction smaller than the θ-fiber at a fraction recrystallized of about 60%. This decrease is mainly caused by the decreasing volume fraction of the recovered regions in the entire map.

Therefore, in Fig. 8b, the recovered volume fraction, i.e. the volume fraction of the different texture components solely in the recovered region with respect to the recovered volume fraction, is traced. The recovered volume fraction of all fibers combined (α+γ+θ) as well as that of the α-fiber remains constant throughout the evolution of recrystallization. The recovered volume fraction of the γ-fiber decreases with increasing recrystallized fraction indicating a preferential depletion of the γ-fiber in the recovered region while the recovered volume fraction of the θ-fiber is slightly increasing possibly indicating that θ-fiber components are retained due to a slower depletion of these texture components in the course of recrystallization. Again, the recovered volume fractions of γ- and θ-fiber cross at a recrystallized volume fraction of 60%.

3.2.2 Evolution in the recrystallized regions

In Figs. 8c and 8d, the evolution of the global and the recrystallized volume fraction of the fiber texture components in the recrystallized regions is shown against *Xv*. In Fig. 8c, an increase in global volume fraction for fibers proportional to the recrystallized volume fraction is seen, but no signs for a larger increase of any fiber respect to any other is resolved. Fig. 8d confirms this: the recrystallized volume fraction of each fiber texture component remains constant throughout recrystallization and no change in the texture takes place in the recrystallized regions during the course of recrystallization. From Fig. 8d, two exceptional conditions can be recognized where the global volume fraction of the γ-fiber texture component in recrystallize regions exceeds 50%. Both data points originate from two smaller maps of the as-received condition gathered with a finer step size in an arbitrarily regions which contained a very large amount of orientations belonging to the γ-fiber. These non-representative maps shall be excluded from further analysis of texture evolution.

Finally, the global volume fractions of the fiber texture components without distinction between recovered and recrystallized regions are presented in Fig. 8e as a function of the fraction recrystallized. Again, no systematic change is seen for the individual fiber texture components in the course of recrystallization, although a small decrease in the combined fraction of all fibers tracked can be asserted.

The horizontal, colored lines added to Figs. 8b, d and e indicate the theoretical volume fractions of each fiber texture component in the absence of any texture. Obviously, these values for random orientation distributions are less than the observed volume fractions of fiber texture components typical after rolling of bcc metals confirming the existing of a rolling texture that is retained during recrystallization.

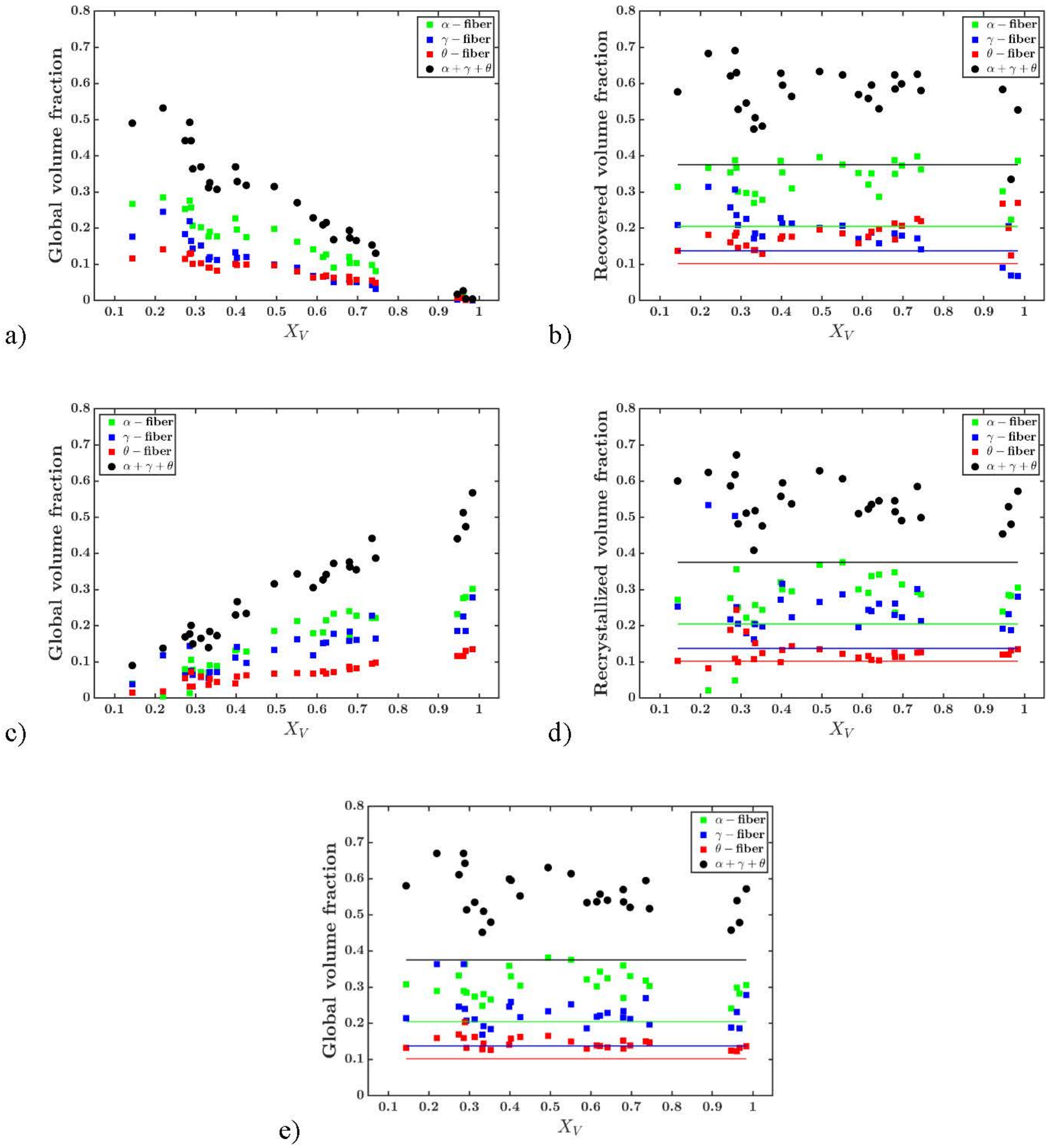

Figure 8: Volume fractions (separated into recovered and recrystallized regions) of typical fiber texture components of rolled bcc materials of tungsten warm-rolled to 80% thickness reduction (W80) and annealed at different conditions. Volume fraction for α-, γ-, and θ-fiber of (a) recovered grains globally in the entire map, (b)recovered grains locally in the recovered regions, (c) recrystallized grains globally in the entire map, (d) recrystallized grains locally in the recrystallized regions and (e) all grains in the entire map. Horizontal, colored lines represent the expected volume fractions for a random orientation distribution.

3.3 Misorientations at the interface between recovered and recrystallized regions

Misorientation axis and angle distributions of boundaries between recovered and recrystallized regions (rcrx boundaries) are shown in Fig. 9 for three specimens annealed at 1175 °C for different times. All distributions are restricted to HABs, as only HABs have sufficient mobility to carry recrystallization. These samples are selected as an example for the entire range of annealing treatments; other samples did not differ in an essential manner from the ones shown.

Independent of the fraction recrystallized, all misorientation angle distributions in Fig. 9a-c are a combination of three contributions. (i) an uncorrelated misorientation distribution due to all orientations present in the map[32,33] (which due to the weak texture resembles almost a Mackenzie distribution[34] for random orientation considering cubic symmetry), (ii) the aforementioned peaks at 30° and 60° that could not completely be removed from the distributions (by excluding single misindexed pixels due to misindexed point pairs), and (iii) a still pronounced contribution with misorientation angles in the range 15° to 25° compared to the expectation from the uncorrelated misorientation distribution similar to a Mackenzie distribution. This latter contribution is a consequence of the abundance of deformation-induced boundaries with low misorientation angles in the deformed and recovered regions or more precisely[32,33], the tail of such a contribution at angles above 15° (as obvious, for instance, in the as-received condition shown Fig. 6a in section 3.1).

The enhanced frequency of HABs at the rcrx interface with moderate misorientation angles between 15° and 25° in comparison with the uncorrelated misorientation distribution, originates from local orientation correlations causing a recrystallization nucleus forming in the deformation structure being at least partially neighbored by regions with similar, but not identical orientations. The same reasoning applies for the misorientation angle distribution at angles below 15° (not shown here for the annealed states). Such small misorientations angles stem mainly from rxrc boundaries between recrystallized grains and the deformed and recovered grains they originally nucleated in. Alternatively, they may have formed by coincidence due to a similar orientation of a recrystallizing grain and the recovered matrix to be invaded, leading to orientation pinning[35] and arresting of the recrystallization front.

Information about the misorientation axes is needed to characterize the rxrc boundaries fully. The distributions in Fig. 9d-f for the three samples annealed at 1175 °C show a lack of misorientation axes around the [100] direction as expected due to the restriction to HABs (as demonstrated for the as-received condition in Figs. 6b and c). The low observed densities below 1.4 reveal that the observed misorientations axis distributions are similar to those of a random orientation distribution.

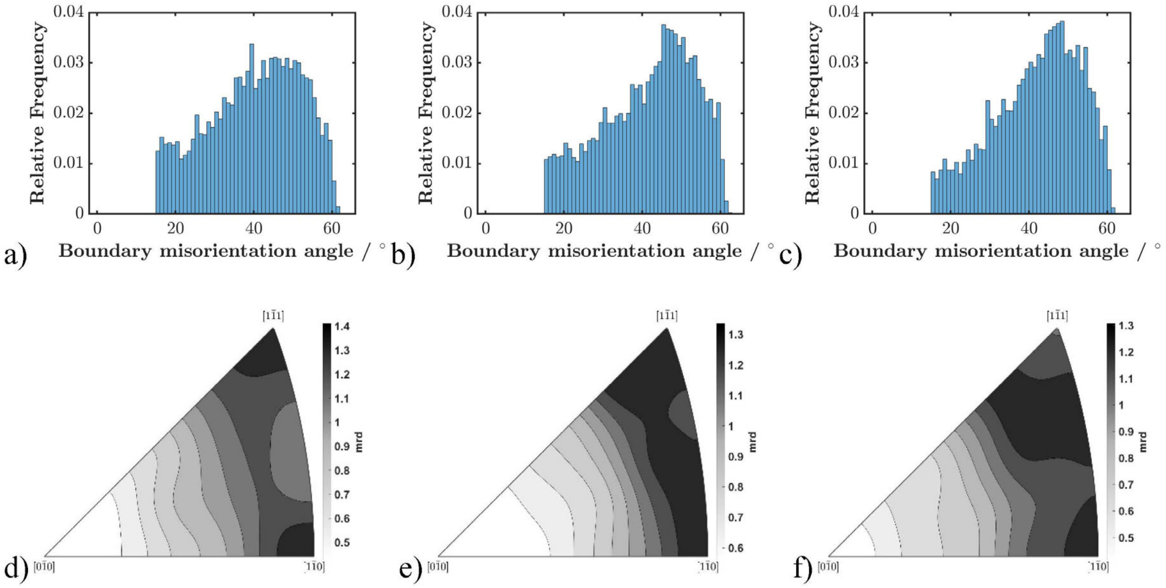

Figure 9: Misorientation angle distributions (a-c) and misorientations axis distributions (d-f) for high angle boundaries of recrystallizing grain facing the recovered matrix (rxrc boundaries) in tungsten warm-rolled to 80 % thickness reduction (W80) and annealed at 1175 °C for 72 h (a,d), 120 h (b,e) or 216 h (c,f). Densities are given in multiples of that of a random orientation distribution (mrd).

3.4 Microstructural path

Additional understanding on the nature of the recrystallization process at the recrystallization front, i.e. the interface between the recovered and the recrystallized region, is gained by analyzing different microstructural path functions:

In Fig. 10, the evolution of the boundary surface density $S_{V_{rxrc}}$ is shown as a function of the fraction recrystallized (cf. Eq. (3)). $S_{V_{rxrc}}$ is the boundary surface density of boundaries of recrystallized grains that are not impinged already against any other recrystallized grain. Only such boundaries are potentially able to move into the recovered matrix. The boundary surface density $S_{V_{rxrc}}$ assumes its maximum at a recrystallized fraction of about 50%. Such a behavior is found in case of homogeneous random nucleation and shape-preserving growth of recrystallizing grains[25]. Interestingly, this maximum value is attained well before the temporal stagnation of recrystallization occurs (at about 60%) indicating that the progress of recrystallization initially occurs in a conventional manner.

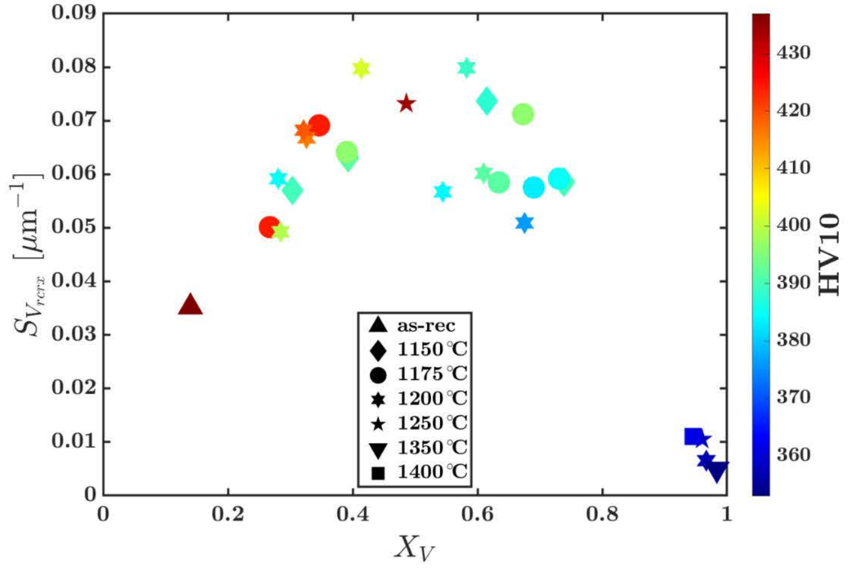

Figure 10: Microstructural path $S_{V_{rxrc}}(X_V)$: Boundary surface density of rxrc grain boundaries in dependence on fraction recrystallized X_V for tungsten warm-rolled to 80 % thickness reduction (W80) and annealed at different conditions. The colors of the symbols reflect the Vickers hardness according to the color bar.

Fig. 11 presents the total boundary surface density $S_{V_{total}}$ for all boundaries in the map as a function of the fraction recrystallized. While replacing deformed and recovered regions of high boundary density with recrystallized regions of low boundary density, the evolution follows a continuous, (almost) linear decrease with increasing recrystallized fraction, if the largest surface boundary density of 0.93 µm^{-1} is not considered. This particular boundary surface density is determined from the map of the as-received condition obtained with highest magnification, highest resolution and smallest step size of 0.1 µm. The corresponding value from the orientation map for the as-received condition gathered with 0.5 µm step size becomes 0.75 µm^{-1}. Consequently, when evaluating maps of the as-deformed state gathered with larger step size, the boundary surface density is underestimated by approximately 20%.

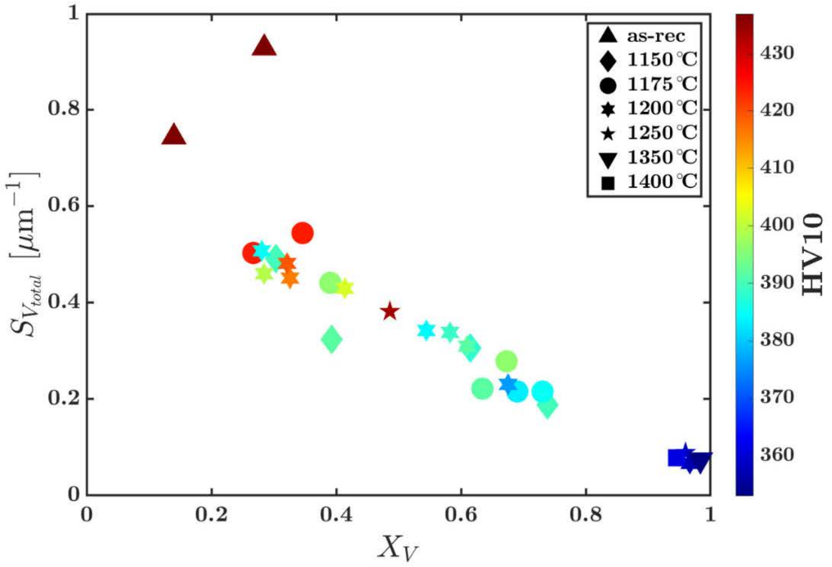

Figure 11: Microstructural path $S_{V_{total}}(X_V)$: Total surface density in the entire maps in dependence on fraction recrystallized X_V for tungsten warm-rolled to 80 % thickness reduction (W80) and annealed at different conditions. The colors of the symbols reflect the Vickers hardness according to the color bar.

In Fig. 12, the microstructural path of the contiguity ratio $C_{rxrx}(X_V)$ is presented. The dashed black line shows the theoretical evolution of the contiguity ratio for uniformly random, site-saturated nucleation[27]. The experimentally observed microstructural path follows the theoretical tightly up to a fraction recrystallized of 60 %. At recrystallized fraction between 60 % to 75 %, a slight deviation towards lower contiguity ratios is observed indicating a mild tendency towards an ordered arrangement of nuclei and recrystallized grains.

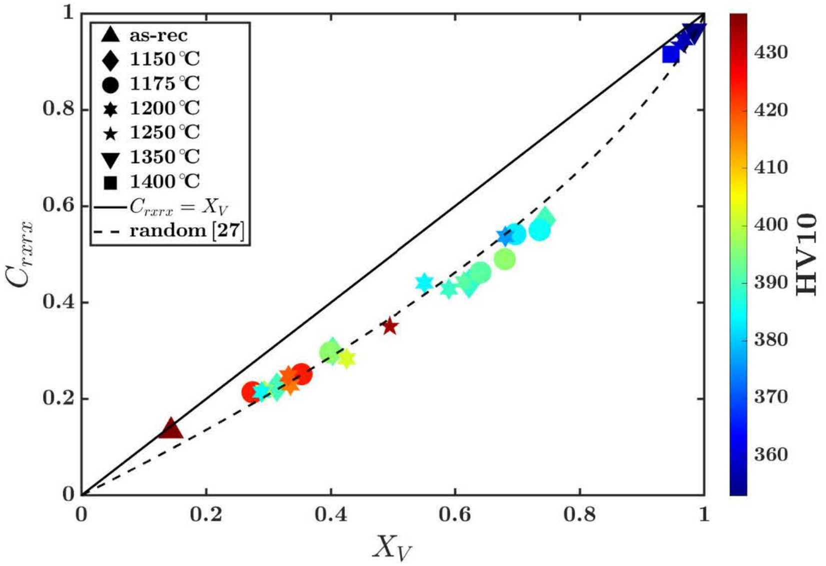

Figure 12: Microstructural path $C_{rxrx}(X_V)$: Contiguity ratio in dependence on fraction recrystallized X_V for tungsten warm-rolled to 80 % thickness reduction (W80) and annealed at different conditions. The colors of the symbols reflect the Vickers hardness according to the color bar. The black straight line shows a linear relation $C_{rxrx} = X_v$, while the dotted, black line shows the theoretical dependence of the contiguity ratio for uniformly random, site saturated nucleation[27].

The microstructural path of the average chord length $\langle\lambda_{rx}\rangle(X_V)$ of recrystallized grains in Fig. 13 reveals that the average chord length of around 16 µm increases only slightly for fractions recrystallized up to 50 %, followed by a more significant increase up to the fully recrystallized condition having an average chord length of 32 µm.

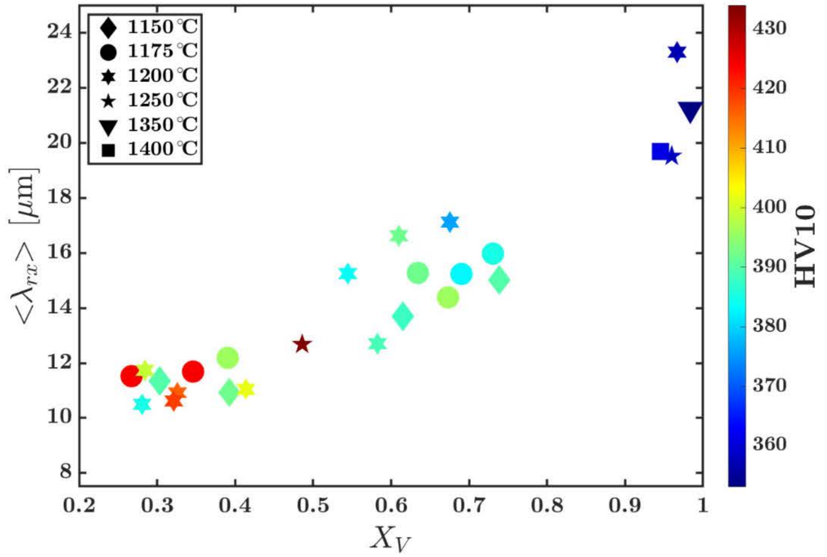

Figure 13: Microstructural path $\langle\lambda_{rx}\rangle$ (X_V): Average chord length of recrystallized grains in dependence on fraction recrystallized X_V for tungsten warm-rolled to 80 % thickness reduction (W80) and annealed at different conditions. The colors of the symbols reflect the Vickers hardness according to the color bar.

The outlined microstructural paths and the potential changes at about 60 % recrystallized fraction observed for them shall be analyzed further in terms of eqs. (3) and (5) in order to obtain additional information on the nucleation behavior. According to eq. (5) of the microstructural path modelling, the exponent p and the coefficient K_λ can be inferred when normalizing the average chord length by the cube root of the recrystallized volume fraction and plotting against the extended recrystallized volume fraction $-\ln(1-X_V)$. From the corresponding double logarithmic plot in Fig. 14, it is concluded that below a fraction recrystallized of 60 %, the normalized chord length remains approximately constant (i.e. a vanishing exponent $p = 0$), while a strong increase up to the nearly fully recrystallized samples is observed above this fraction recrystallized. Fitting of eq. (5) to the range of X_V above 60 %, leads to an exponent p of 0.15. This indicates that the kinetic change from the initial behavior to the latter at about 60 %.

A similar observation is made for the evolution of another microstructural parameter under consideration, the boundary surface density $S_{V_{rxrc}}$ of rxrc grain boundaries. A double logarithmic plot of $S_{V_{rxrc}}/(1 - X_V)$, the so-called extended boundary surface density, against the logarithm of the extended recrystallized volume fraction -ln(1-X_V) corresponding to eq. (3) is shown in Fig. 15. An initial increase of the extended boundary surface density is observed with an exponent q equal to 0.72 until a recrystallized fraction of about 60% is reached, followed by an increase with a much lower q of about 0.12 up to the fully recrystallized condition. Both parameters, $\langle \lambda_{rx} \rangle / X_V^{1/3}$ and $S_{V_{rxrc}}/(1 - X_V)$ indicate a change in the kinetics at about 60 % recrystallized fraction, i.e. when stagnation in the recrystallization behavior occurred.

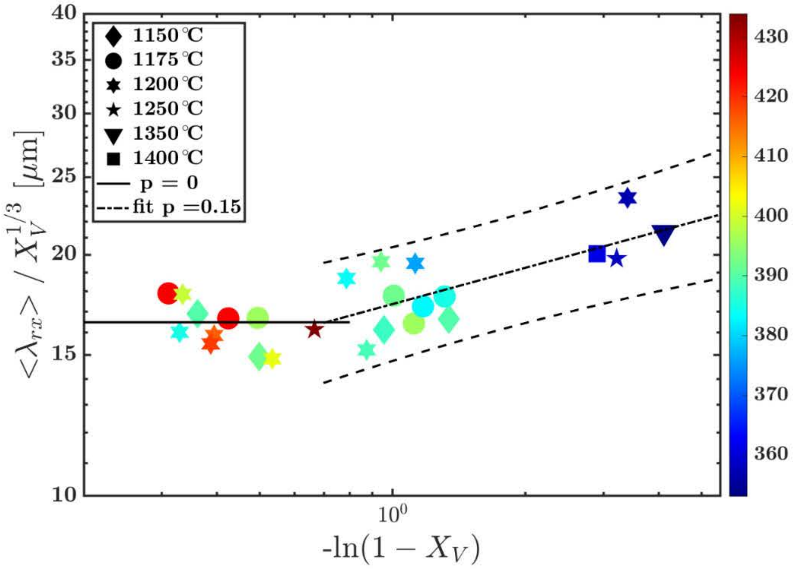

Figure 14: Microstructural path $\langle \lambda_{rx} \rangle$ (X_V) for annealed conditions only: Normalized average chord length of recrystallized grains $\langle \lambda_{rx} \rangle / X_V^{1/3}$ as a function of the extended recrystallized volume fraction $- ln(1{-}X_V)$. The solid lines represent fits of eq. (6) to the different regions below and above X_V = 60 % with different coefficients K_λ and p; for fitting the initial part p is forced to 0. The dashed lines represent confidence intervals of 95%.

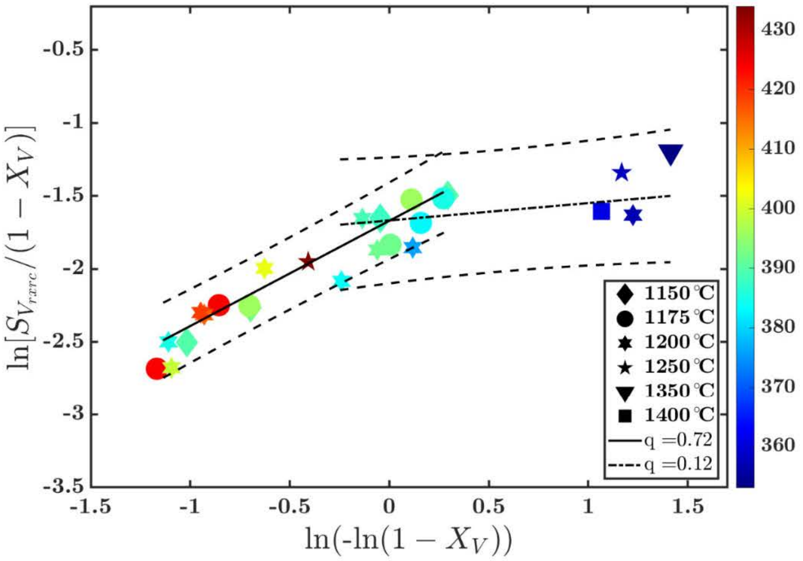

Figure 15: Microstructural path $S_{V_{rxrc}}(X_V)$ for annealed conditions only: Double logarithmic plot of the "extended" boundary surface density $S_{V_{rxrc}}/(1-X_V)$ of rxrc boundaries as a function of the extended recrystallized volume fraction $-ln(1-X_V)$. The solid lines represent fits of eq. (4) to the different regions below and above X_V = 60 % with different coefficients q. The dashed lines represent confidence intervals of 95%.

3.5 Boundary surface and stored energy densities

For the as-received and annealed conditions, the local boundary surface densities S_V^* of different type of boundaries in their respective regions are summarized in Fig. 16 (for rcrc boundaries in the recovered region, for rcloc boundaries in the rcloc region, i.e. the part of the recovered region just ahead of the recrystallization front, for rxrc and rxrx boundaries the recrystallized region). All the specific boundary densities in Fig. 16a (with respect to their respective regions) decrease with increasing fraction recrystallized. The total specific boundary surface density within the recovered region comprises all rcrc boundaries (HABs, LABs and IBs). For the rcloc region, additionally to HABs, LABs and IBs in the rcloc region also the rxrc boundaries forming the recrystallization front (HABs as well as LABs) are accounted for, but only for half of them. As seen from Fig. 16, the specific boundary surface densities of LABs are always larger than that of HABs (due to the abundance of LABs in the deformation structure induced by rolling) for the rcrc and rcloc regions. The opposite is true for the rxrc boundaries most likely because LABs residing at the recrystallization front are actually orientation pinned[35]. They are not expected to move further and get detached from the recrystallization front. While the specific boundary surface densities for LABs of the rcrc and rcloc regions decrease significantly due to recovery by dislocation annihilation and subgrain coarsening, the same cannot be stated for the HABs and IBs whose densities reduce only slightly or remain constant, respectively. The latter, however, might be an artefact of the very large step size used to map the annealed specimens implying that many deformation-induced boundaries formed on a smaller length scale are actually not resolved[32,33]. Deformation-induced boundaries enclosing a single pixel will also not appear as IBs as they become classified as rcrc boundaries instead.

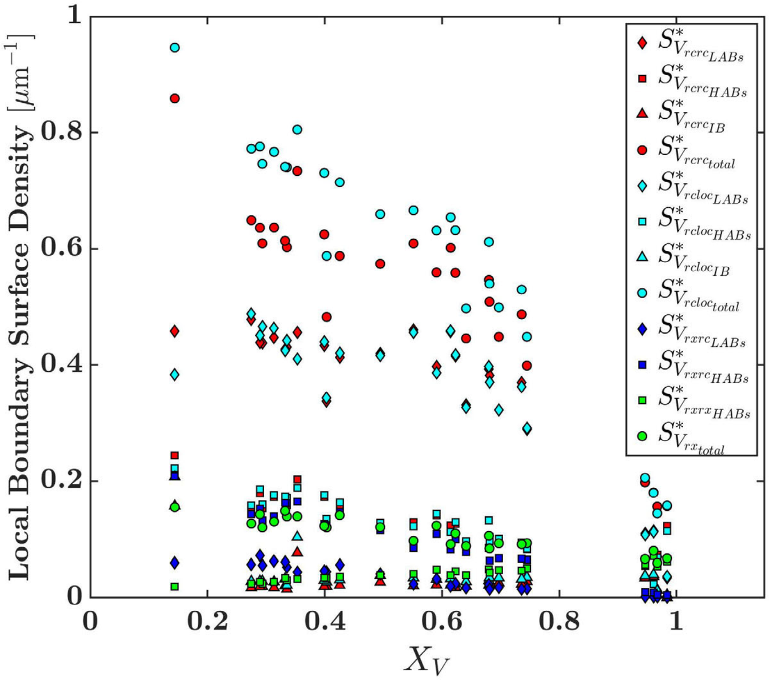

Figure 16: Local boundary surface densities in the recovered region (rcrc region), the part of the recovered region (rcloc) just ahead of the recrystallization front and the recrystallized region (rx region).

Fig. 16 summarizes also the total local boundary surface densities from all regions in the maps (marked as circles). The total boundary surface density of the recrystallized region (rx region) $S^*_{V_{rx_{total}}} = S^*_{V_{rxrx_{HABs}}} + S^*_{V_{rxrx_{LABs}}} + \frac{1}{2}S^*_{V_{rxrc_{HABs}}} + \frac{1}{2}S^*_{V_{rxrc_{LABs}}}$ consists of the rxrx boundaries together with half of the rxrc boundaries (HABs and LABs at the recrystallization front) . The local boundary surface densities in the recrystallized region are much smaller than those in the recovered regions as a consequence of recrystallization eliminating of the deformation structure. Interestingly, the local boundary surface density of rxrx HABs increases with progress of recrystallization within the material as rxrx boundaries are created first by impingement of recrystallized grains (isolated recrystallized grains have no rxrx boundaries, only rxrc boundaries), whereas the total boundary surface density within the rx region decreases slightly due to the loss of rxrc boundaries by impingement. In the fully recrystallized state, almost no rxrc boundaries are left and the total boundary surface densities approach each other.

Similar trends are revealed from the local stored energies of the different regions in Fig. 17. The stored energy densities within the rcloc regions are slightly higher than that of the rest of the recovered region (rcrc region) partially due to including the contribution of half of the rxrc boundaries in the stored energy density of the rcloc regions. Due to static recovery, the stored energy densities due to all types of boundaries decrease within the recovered regions (both rcrc and rcloc regions) from about 600 kJ/m^3 in the as-received condition to about 400 kJ/m^3 at a recrystallized fraction of 60 % at which recrystallization stagnates. Low stored energy densities of 100 kJ/m^3 are found for the small surviving recovered regions in the almost fully recrystallized condition.

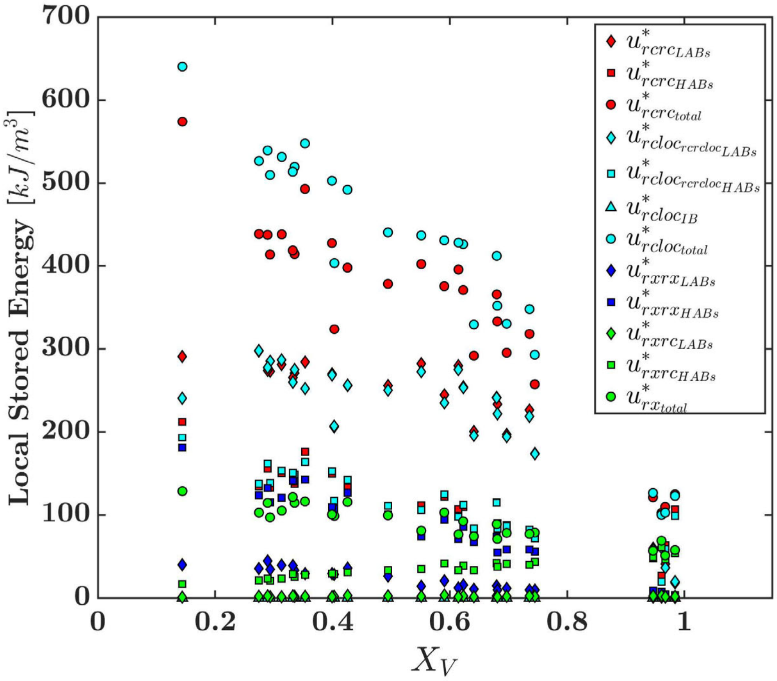

Figure 17: Local stored energy densities in the recovered region (rc region), the part of the recovered region (rcloc) just ahead of the recrystallization front and the recrystallized region (rx region) due to the different types of boundaries (HABs, LABs and IBs) and summed over all types. The stored energy densities due to rxrc boundaries at the recrystallization front are added for comparison purposes.

4. Discussion

Inspecting the as-received condition of the warm-rolled tungsten plate W80 revealed a quite weak bcc rolling texture. The maximum orientation density is less than 2 times random, well below the orientation densities of the as-received condition of two other plates warm-rolled in an analogous manner by the same supplier[12,13,36]. These two formerly analyzed plates warm-rolled to 67 % and 90 % thickness reduction showed maximum orientation densities of 3.7 and 6.4 times random, respectively. The average stored energy densities (610 kJ/m^3 and 2 MJ/m^3) in the as-received conditions of these plates were obtained from orientation maps gathered with step sizes of 0.5 µm and 0.2 µm [36]. Interestingly, in both of these plates W67 and W90, the stored energy density in the components belonging to the θ-fiber were as high as those of the γ-fiber, which is different from the observation on W80 where the energy densities stored in the θ-fiber components are slightly smaller than those in γ-fiber components. The average stored energy density of 575 kJ/m^3 revealed for W80 is lower than the vales found for the two other plates, but almost comparable to the value of the plate with 67 % thickness reduction. The similar values for the stored energy densities of W67 and W80, obtained with exactly the same step size, reveal the presence of about the same amount of deformation-induced boundaries in both plates. The lower stored energy in the deformation structure of W80 than expected compared to W67 having a lower thickness reduction can be rationalized readily by static recovery after the last rolling path, because some restauration must have occurred after the last path statically or meta-dynamically as evident from the recrystallized fraction of 15 % in the as-received condition. Based on the lower stored energy density of the as-received condition in combination with the observation of a rather weak rolling texture, one even suspects that during processing of W80 recrystallization has taken place in between different rolling passes also.

Considering the weak texture of the as-received condition, it does not come as a surprise that no major changes in the major texture components occur. The only variation in the volume fractions of the texture components was observed in the recovered regions, for which the γ-fiber texture components were depleted much faster than all the other texture components during annealing. This is understandable, recalling that the stored energy density in the γ-fiber texture components was highest (575 kJ/m^3) among all fibers. Components with higher stored energy are depleted first by the moving recrystallization front as they exert a higher driving for becoming invaded. The components belonging to the α-alpha fiber having a low energy density do not show such a fast decrease in volume fraction. This indicates that invasion of recrystallizing grains into deformed and recovered grains of the α-fiber texture component does not take place in a preferential manner as in recovered grains belonging to the γ-fiber. Components of the θ-fiber even increase their relative contribution indicating a reluctance of invading these particular texture component despite their relatively high stored energy density compared to components of the α-fiber.

No texture changes were observed for the recrystallized regions during the course of recrystallization. Hence, even the fully recrystallized condition nearly preserves the weak texture of the as-received condition, for which the three fiber components combined account for about 60 % of the volume fraction. In comparison, in the fully recrystallized condition of formerly investigates plates W67 and W90, the three fiber texture components amount only to a volume fraction of 20 % and 25 %, with almost no γ-fiber components left after recrystallization [36].

In parallel to the stagnation of the progress of recrystallization during annealing after about 60 % recrystallized fraction, a change in the microstructural paths is observed: the evolution of the normalized average grain chord length $\langle\lambda_{rx}\rangle/X_V^{1/3}$ of recrystallized grains (Fig. 14) and the "extended" boundary surface density $S_{V_{rxrc}}/(1-X_V)$ of boundaries separating the recovered from the recrystallized regions (Fig. 15) both indicate this change. Both exponents, *p* and *q,* obtained by fitting the theoretical relations of eqs. (3) and (5) to the experimental data up to recrystallized volume fractions of 60% indicate uniformly random nucleation and shape-preserving growth with uniform impingement, which is further confirmed by the microstructural path of the contiguity ratio in Fig. 12. For recrystallized fractions above 60% the obtained exponents (p=0.15 and q=0.12) indicate non-uniform impingement (linear and planar impingement, respectively). This indicates that after 60 % recrystallization the impingement does not occur uniformly any longer, but locally rather differently in certain directions. On the other hand, the contiguity ratio is particularly sensitive for any deviation from spatial uniform random distributions [24,37]. The slightly lower values of the contiguity ratio (than expected for site-saturated uniform random nucleation) at recrystallized fractions above 60 % are considered indicative for a slightly ordered arrangement of recrystallization nuclei/recrystallizing grains. The combination of both, ordered nucleation and non-uniform impingement (which might occur coupled and not independent of each other), appear to be responsible for (or at least related to) the observed stagnation in the recrystallization process.

The non-uniform impingement supposed to take place at higher recrystallized fractions than 60 % could not be traced towards full recrystallization due to the lack of annealing conditions above recrystallized fractions of 75 %. While ample evidence is gathered for random distribution of nuclei and uniform impingement for recrystallized fractions below 60 %, there are not enough annealing conditions available to determine precisely which kind of partial microstructural path function could best fit the evolution beyond. Neither the type of impingement (linear or planar), nor the ordered arrangement of nuclei can be identified precisely.

The decrease of the specific boundary surface densities in both recovered regions (rcrc and rcloc regions) are caused by persisting recovery in these regions lowering the driving force for further recrystallization. Additionally, the continuously increasing specific boundary surface density between recrystallized grains rules out any extensive grain growth during annealing of W80 in parallel with recrystallization and corroborates the occurrence of impingement.

It is suggested, that the occurrence of non-uniform impingement between recrystallized grains is caused by an alignment of the progress of recrystallization with features in the deformation structure as lamellar boundaries or orientation bands with common orientation parallel to the rolling plane. The impingement of boundaries at the recrystallization front (rxrc boundaries) of recrystallized grains may occur differently along and inclined to these features.

5. Summary

The progress of recrystallization of a tungsten plate warm-rolled to a thickness reduction of 80 % stagnated after having achieved a recrystallized volume fraction of 60 %. The microstructure of partially recrystallized samples annealed mainly at 1150 °C, 1175 °C, and 1200 °C (with recrystallized fractions spanning from 15 % to 98 %) were investigated in terms of texture, boundary misorientations, boundary surface densities and stored energy content due to the presence of boundaries to elucidate the underlying microstructural reasons for such a halt. The weak initial texture did not change significantly during the process of recrystallization and the misorientation distributions for boundaries separating recrystallized and recovered regions did not indicate any particular feature that could be ascribed to the halt in recrystallization. The recrystallization texture after complete recrystallization resembled closely the weak texture in the as-received condition with dominating components commonly observed after rolling of bcc metals. The microstructural path methodology was adopted to describe the course of recrystallization. Analysis of several microstructural parameters reveal a change in the microstructural path beyond a fraction recrystallized of 60 %: occurrence of non-uniform impingement and evidence for ordered nucleation. In combination with the retarded motion of HABs forming the recrystallization front due to the continuously reducing stored energy density in the recovered matrix, these phenomena are able to rationalize the observed stagnation of recrystallization, but a punctual description of the halting mechanism, why it occurred and how it can be achieved by purpose, have not yet been found.

Acknowledgements

This work has been carried out partially within the framework of the EUROfusion Consortium and has received funding from the Euratom research and training programme 2014-2018 and 2019-2020 under grant agreement No 633053. The views and opinions expressed herein do not necessarily reflect those of the European Commission.

Data Availability

The raw/processed data required to reproduce these findings cannot be shared at this time as the data are part of an ongoing study.

Bibliography

1 J.H. You, E. Visca, T. Barrett, B. Böswirth, F. Crescenzi, F. Domptail, M. Fursdon, F. Gallay, B.E. Ghidersa, H. Greuner, M. Li, A. V. Müller, J. Reiser, M. Richou, S. Roccella, and C. Vorpahl: *Nucl. Mater. Energy*, 2018, vol. 16, pp. 1–11.

2 T. Hirai, F. Escourbiac, S. Carpentier-Chouchana, A. Fedosov, L. Ferrand, T. Jokinen, V. Komarov, A. Kukushkin, M. Merola, R. Mitteau, R.A. Pitts, W. Shu, M. Sugihara, B. Riccardi, S. Suzuki, and R. Villari: in *Fusion Engineering and Design*, vol. 88, North-Holland, 2013, pp. 1798–801.

3 R. Neu, J. Riesch, J.W. Coenen, J. Brinkmann, A. Calvo, S. Elgeti, C. García-Rosales, H. Greuner, T. Hoeschen, G. Holzner, F. Klein, F. Koch, C. Linsmeier, A. Litnovsky, T. Wegener, S. Wurster, and J.H. You: *Fusion Eng. Des.*, 2016, vol. 109–111, pp. 1046–52.

4 M. Rieth, S.L. Dudarev, S.M. Gonzalez De Vicente, J. Aktaa, T. Ahlgren, S. Antusch, D.E.J. Armstrong, M. Balden, N. Baluc, M.F. Barthe, W.W. Basuki, M. Battabyal, C.S. Becquart, D. Blagoeva, H. Boldyryeva, J. Brinkmann, M. Celino, L. Ciupinski, J.B. Correia, A. De Backer, C. Domain, E. Gaganidze, C. García-Rosales, J. Gibson, M.R.

Gilbert, S. Giusepponi, B. Gludovatz, H. Greuner, K. Heinola, T. Höschen, A. Hoffmann, N. Holstein, F. Koch, W. Krauss, H. Li, S. Lindig, J. Linke, C. Linsmeier, P. López-Ruiz, H. Maier, J. Matejicek, T.P. Mishra, M. Muhammed, A. Muñoz, M. Muzyk, K. Nordlund, D. Nguyen-Manh, J. Opschoor, N. Ordás, T. Palacios, G. Pintsuk, R. Pippan, J. Reiser, J. Riesch, S.G. Roberts, L. Romaner, M. Rosiński, M. Sanchez, W. Schulmeyer, H. Traxler, A. Ureña, J.G. Van Der Laan, L. Veleva, S. Wahlberg, M. Walter, T. Weber, T. Weitkamp, S. Wurster, M.A. Yar, J.H. You, and A. Zivelonghi: *J. Nucl. Mater.*, 2013, 432, vol. 432.

5 J.H. You: *J. Nucl. Mater.*, 2009, vol. 386–388, pp. 817–20.

6 J. Du, T. Höschen, M. Rasinski, S. Wurster, W. Grosinger, and J.H. You: *Compos. Sci. Technol.*, 2010, vol. 70, pp. 1482–9.

7 R. Neu, J. Riesch, A. V. Müller, M. Balden, J.W. Coenen, H. Gietl, T. Höschen, M. Li, S. Wurster, and J.H. You: *Nucl. Mater. Energy*, 2017, vol. 12, pp. 1308–13.

8 M. Battabyal, R. Schäublin, P. Spätig, and N. Baluc: *Mater. Sci. Eng. A*, 2012, vol. 538, pp. 53–7.

9 A. Šestan, J. Zavašnik, M. Maček Kržmanc, M. Kocen, P. Jenuš, S. Novak, M. Čeh, and G. Dehm: *J. Nucl. Mater.*, 2019, vol. 524, pp. 135–40.

10 P. Schade, H. Ortner, and I. Smid: *Int. J. Refract. Met. Hard Mater.*, 2015, vol. 50, pp. 23–30.

11 P. Lied, C. Bonnekoh, W. Pantleon, M. Stricker, A. Hoffmann, and J. Reiser: *Int. J. Refract. Met. Hard Mater.*, DOI:10.1016/j.ijrmhm.2019.105047.

12 A. Alfonso, D. Juul Jensen, G.N. Luo, and W. Pantleon: *J. Nucl. Mater.*, 2014, vol. 455, pp. 591–4.

13 A. Alfonso, D. Juul Jensen, G.N. Luo, and W. Pantleon: *Fusion Eng. Des.*, 2015, vol. 98–99, pp. 1924–8.

14 U.M. Ciucani, A. Thum, C. Devos, and W. Pantleon: *Nucl. Mater. Energy*, 2018, vol. 15, pp. 128–34.

15 U.M. Ciucani, A. Thum, C. Devos, and W. Pantleon: *Nucl. Mater. Energy*, 2019, vol. 20, p. 100701.

16 K. Wang, H. Sun, X. Zan, U.M. Ciucani, W. Pantleon, L. Luo, and Y. Wu: *J. Nucl. Mater.*, 2020, vol. 540, p. 152412.

17 U.M. Ciucani and W. Pantleon: *Fusion Eng. Des.*, 2019, vol. 146, pp. 814–7.

18 R.A. Vandermeer and B.B. Rath: *Metall. Trans. A*, 1989, vol. 20, pp. 391–401.

19 R.A. Vandermeer, R.A. Masumura, and B.B. Rath: *Acta Metall. Mater.*, 1991, vol. 39, pp. 383–9.

20 A.N. Kolmogorov: *Izv. Akad. Nauk SSSR, Ser. Mat.*, 1937, pp. 355–9.

21 W. Johnson and R. Mehl: *Trans. Am. Inst. Min. Metall. Eng.*, 1939, vol. 135, pp. 416–42.

22 M. Avrami: *J. Chem. Phys.*, 1939, vol. 7, pp. 1103–12.

23 R.A. Vandermeer and B.B. Rath: *Proc. Riso Int. Symp. Metall. Mater. Sci.*, 1989, pp. 589–99.

24 R.A. Vandermeer: *Acta Mater.*, 2005, vol. 53, pp. 1449–57.

25 J. Cahn and W. Hagel: in *TMS-AIME Symposium on solidification (1960)*, V.F. Zackay and H.I. Aaronson, eds., Interscience (New York), Philadelphia, Pennsylvania., 1962, pp. 131–92.

26 A.M. Gokhale and R.T. Dehoff: *Metall. Trans. A*, 1985, vol. 16, pp. 559–64.

27 P.R. Rios, R.B. Godiksen, S. Schmidt, D. Juul Jensen, and R.A. Vandermeer: *Scr. Mater.*,

2006, vol. 54, pp. 1509–13.

28 F. Bachmann, R. Hielscher, and H. Schaeben: in *Solid State Phenomena*, vol. 160, Trans Tech Publications Ltd, 2010, pp. 63–8.

29 F. Bachmann, R. Hielscher, and H. Schaeben: *Ultramicroscopy*, 2011, vol. 111, pp. 1720–33.

30 W.T. Read and W. Shockley: *Phys. Rev.*, 1950, vol. 78, pp. 275–89.

31 B.C. Allen: *J. Less-Common Met.*, 1972, vol. 29, pp. 263–82.

32 W. Pantleon: *Mater. Sci. Forum*, 2005, vol. 495–497, pp. 219–24.

33 W. Pantleon: *Probl. Mater. Sci.*, 2007, vol. 52, pp. 13–23.

34 J.K. Mackenzie: *Biometrika*, 1958, vol. 45, pp. 229–40.

35 D. Juul Jensen: in *Proceedings of ReX'96*, T. R. McNelley, ed., Monterey Institute of Advanced Studies, 1997, pp. 15–29.

36 A. Alfonso, Ph.D. Thesis, DTU - Technical University of Denmark, 2015.

37 R.A. Vandermeer and D. Jensen: *Mater. Sci. Forum*, 2004, vol. 467–470, pp. 193–6.

Chapter 6. Tungsten fiber-reinforced tungsten composite (W_fW)

In order to determine the microstructural evolution of the tungsten fiber-reinforced composite tungsten materials, thorough inspection of the as-received condition was conducted. The as-received condition was characterized topographically by SE images and crystallographically by EBSD.

6.1 As-received condition

6.1.1 Topography

Secondary electrons contrast ensured a fine, magnified image of the topography of W_f/W. In Figure 48, a cross section of the as-received condition of the W_f/W is shown. Two separate regions, the wire and the CVD tungsten surrounding matrix, can be clearly seen. The shape of the cross-section of the wire is not completely circular, some inward deviations from a perfect circular shape can be seen. This is most likely due to the dies imposing grooves on the drawn wire, which on a cross-section of the drawn wire, result as inward grooves. The wire region is characterized by a very fine arrangement of needle-like grains. Visually, these grains can be recognized by their very small circular cross-sections. These cross-sections are hard to be recognized in the center but can be seen better in the outer regions of the wire.

The CVD region is characterized by grains growing radially outwards. In Figure 48 it can be seen the thickness of these grains in the vicinity of the wire is extremely small, particularly in the very first 10 μm from the interface. In Figure 49 very long radial grains spanning several hundredths of μms are visible, departing from the smaller grain size region in the vicinity of the interface. They possess a very large aspect ratio, and are characterized by an increasing thickness with increasing distance from the wire interface, i.e. they are wedges. Other features can be seen within these wedge-like grains, at distances larger than a hundred μms from the wire. Smaller grains develop, most frequently, at grain boundaries. These could be most likely wedge-like grains at other positions in the matrix, the section of which is smaller in the surface inspected. Also, they might be newly formed grains at the extending grain boundaries along the deposition process. Also, bundles of knife-like or triangular grains can be seen all over on the surface (e.g. in the red circle of Figure 49) within these radial grains, most frequently elongating perpendicularly to the radial direction. A magnified secondary electron image in Figure 50 shows these triangular grains bulging inside the radially growing grains. The growth of the radially growing grains becomes interrupted by deposition faults and a subsequent growth of such triangular grains takes place. These topographical characteristics of the as-received condition were found in all three different types of W_fW.

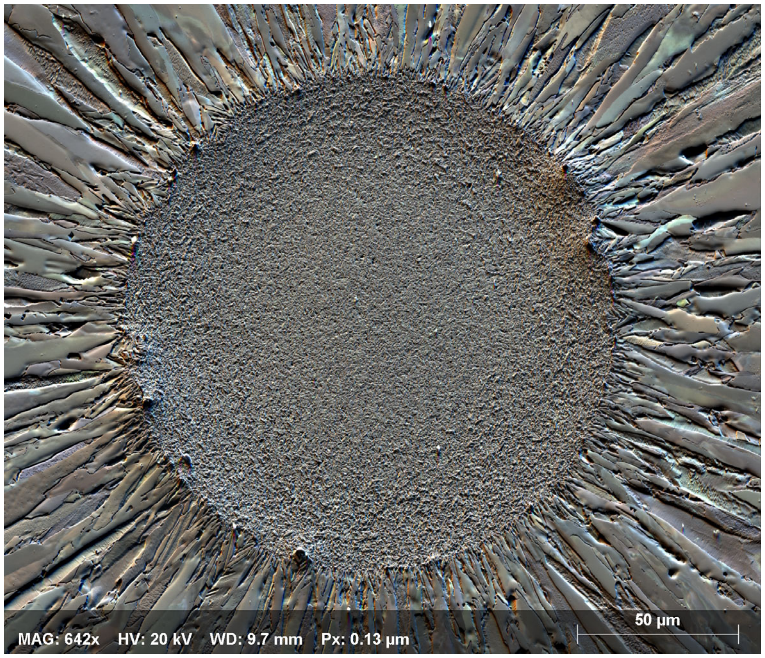

Figure 48: Cross section of W_f/W: Secondary electron image of the wire region and the CVD region in its immediate vicinity possessing a fine microstructure. The artificial colors are created by the Argus technique that can be found in the BRUKER Esprit 2.1 software.

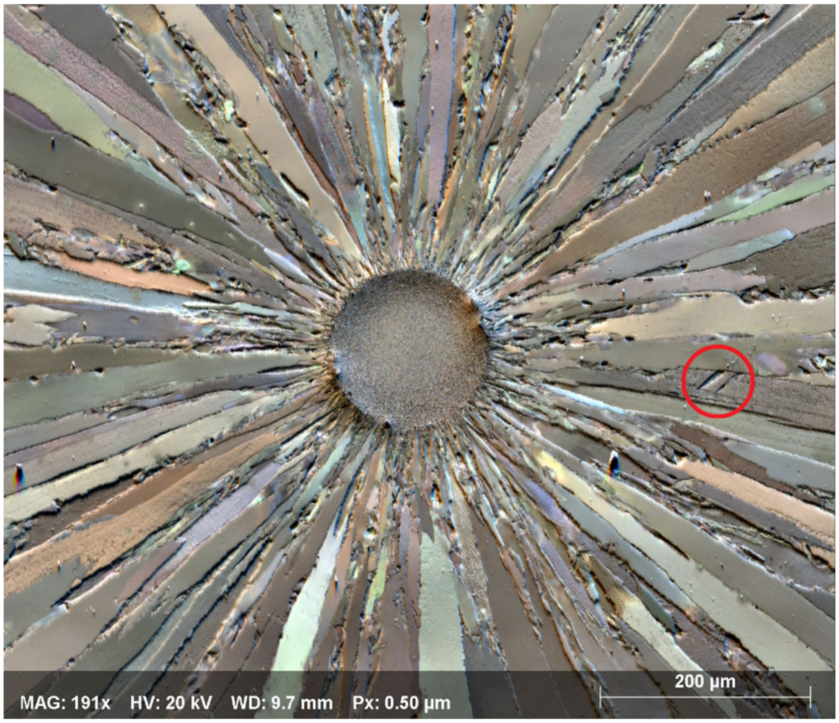
MAG: 191x HV: 20 kV WD: 9.7 mm Px: 0.50 µm
200 µm

Figure 49: Cross section of W_f/W: lower magnification secondary electron image of the wire region and the CVD region in its immediate vicinity, showing the radially growing grains whose thickness increases with increasing distance from the interface with the wire. In the red circle, knife-like grains (later referred to as triangular grains) interrupting the growth of these radially growing grains. The artificial colors are created by the Argus technique that can be found in the BRUKER Esprit 2.1 software.

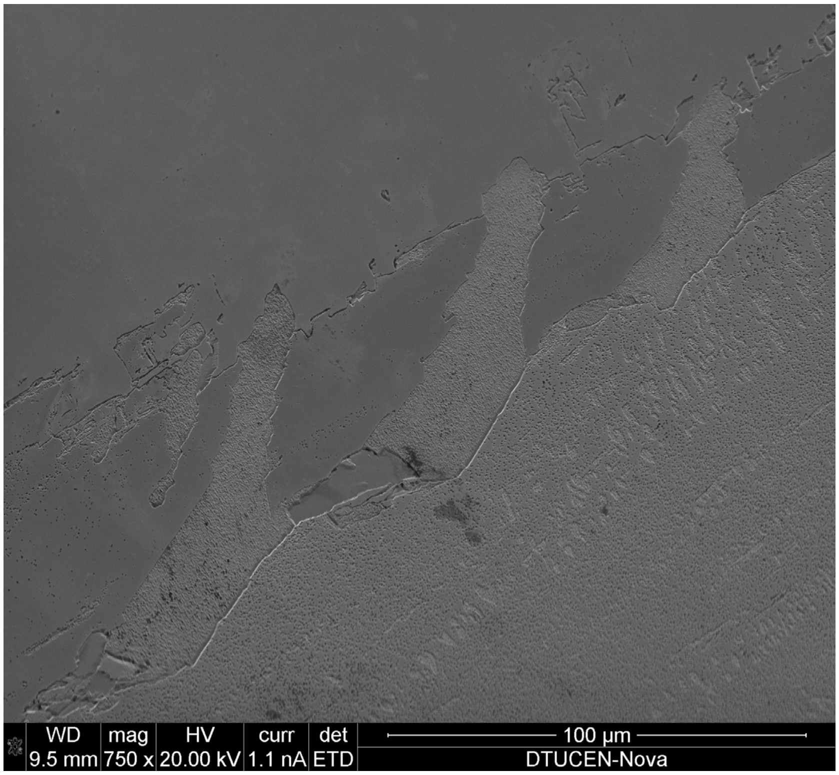
WD
9.5 mm
mag
750 x
HV
20.00 kV
curr
1.1 nA
det
ETD
100 µm
DTUCEN-Nova

Figure 50: Secondary electron image showing in detail of the triangular grains within radially growing grains.

6.1.2 Cyclic <100> ring fiber texture in CVD tungsten

The crystallographic orientations within the W_fW composites prior and after annealing were characterized by EBSD as explained in Section 3.3. The W_f/W samples will be taken as reference since the orientations of the as-received condition for both the wire and the CVD matrix are identical to all. The orientation maps of the W_f/W as in Figure 51 are showing the crystallographic orientations along the (a) the x-direction, (b) the y-direction and (c) the z-direction colored according to the inset of Figure 51b; the z-direction is normal to the surface mapped, the x- and y-direction correspond to the horizontal and vertical direction in the map; boundaries are shown in black. The shape of the indexed points of the orientation map, reveals the specimen and its shape, a cylinder. A central white circular disk circle corresponds to the cross-section of the wire for which no orientation could be revealed since the acquisition conditions for this large map were not sufficient to resolve them. The orientations within these maps belong nearly completely to the CVD region of the composite. From Figure 51a and b, a preferential orientation of the [100] directions can be determined. Also, in Figure 51c, shows colors, red to yellow to green, corresponding to the directions comprised in between the line connecting the [100] and [110] orientations.

Observation of the pole figures in Figure 52 of such orientations reveals for both the [100] and [110] directions a maxima at the azimuth, the z-direction. Also a circle of high densities can be discerned at the equator in the [100] pole figure. For the [110] pole figure, also a circle of higher density can be seen at angles of approximately 36° from the azimuth. Such an indication might indicate a fiber texture but the ring of higher densities at approximately 45° in the [111] pole figure indicates this is not the case since that ring should be located at 54° from the azimuth.

As it will be further described in the following manuscript, upon choice of an appropriate reference system exploiting the geometry of such specimens - a cylindrical coordinate system with the radial r-direction pointing radially outwards from the wire center and an azimuthal φ-direction pointing perpendicularly to the radial and axial direction – the orientation of the CVD region with respect to the radial direction can be characterized. The resulting orientation map colored according to the radial direction is depicted in Figure 53. In Figure 53 the color indicates the crystallographic direction pointing towards the radial direction: the map is completely red, indicating the complete predominance of the [100] directions pointing radially.

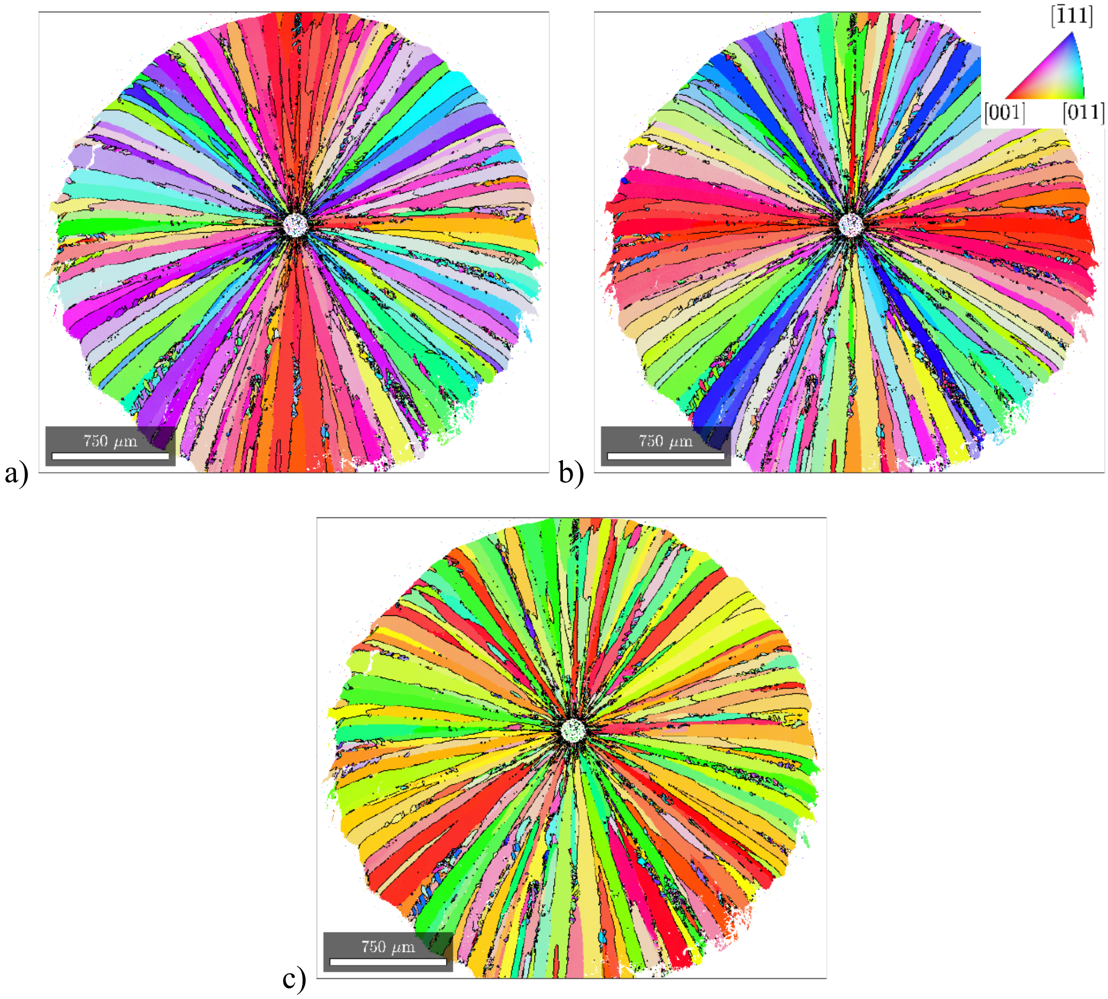

Figure 51: Orientation maps of the W_f/W as in Figure 51 are showing the crystallographic directions along the (a) the x-direction, (b) the y-direction and (c) the z-direction colored according to the inset of Figure 51b; the z-direction is normal to the surface mapped, the x- *and* y-*direction correspond to the horizontal and vertical direction in the map*

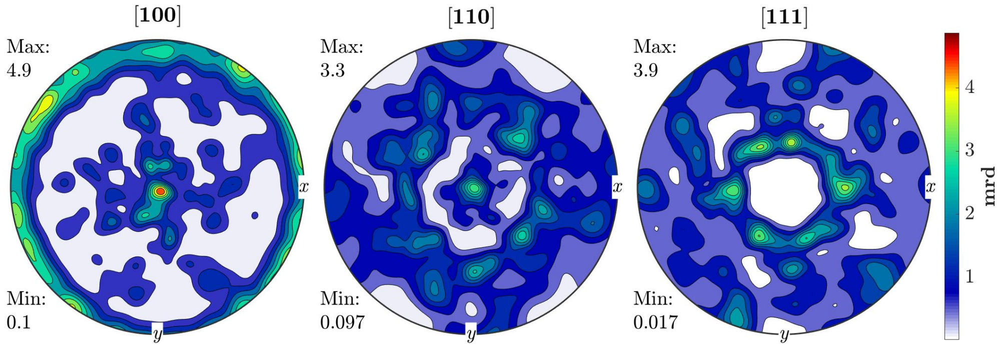

Figure 52: 100, 110 and 111 pole figures of the CVD region of the as-received condition in Figure 51, with the horizontal direction indicated by x the vertical direction by y and the transverse direction lying at the center of the pole figure. The pole densities are given in multiples of random distribution

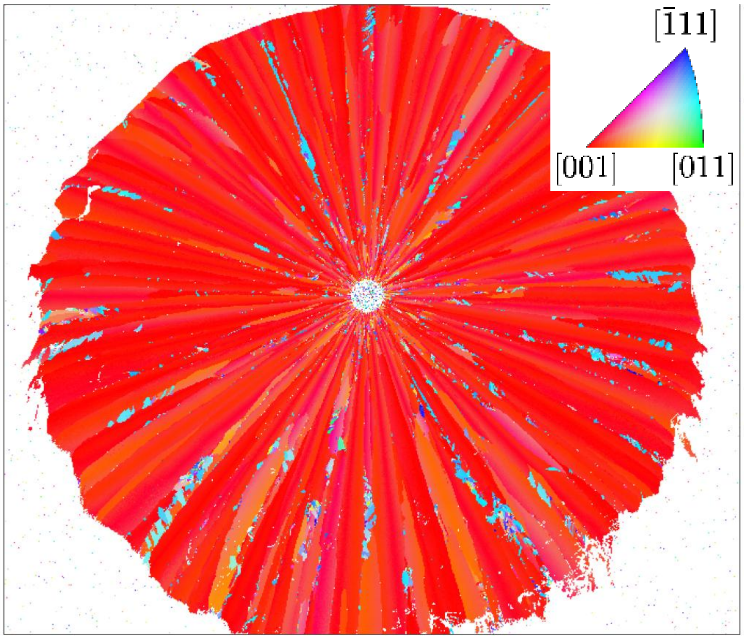

Figure 53: Orientation map of the W_f/W showing the crystallographic directions along the radial direction colored according to the inset. A complete predominance of the [100] directions is visible together with small areas characterized by a light blue to blue color.

Taking into account such an adapted specimen reference coordinate system, the pole figures can be adapted used to show the orientations according to these two new specimen directions, the radial and the azimuthal one. The pole figures according to this new specimen reference coordinate system are depicted in Figure 54.

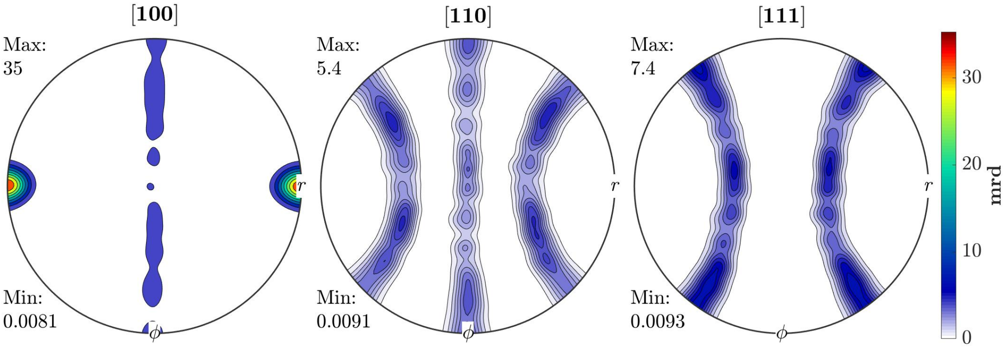

Figure 54: 100, 110 and 111 pole figures of the CVD region the W_f/W as-received condition in Figure 51, using the alternative cylindrical reference coordinate system with the radial direction indicated by r and the azimuthal direction indicated by φ. The pole densities are given in multiples of random distribution.

The 100 pole figure of Figure 54 shows a much higher pole density along the *r*-direction. In a cubic crystal, the <110> directions lie at an angle of 45° from the <100> and the <111> at an inclination of 54°. Since these are the angles at which the 110 and 111 higher densities are found with respect to the radial direction in the 110 and 111 pole figures, the radial preference of 100 directions is corroborated. Observation of the 100 pole figure in Figure 54 reveals another interesting detail, a stripe resembling a circle in the plane given by the axial and azimuthal direction. This is actually even more evident in the 110 and 111 pole figures. Together they show that the other crystallographic <100> directions of the lattice are actually pointing uniformly in all directions allowed by the rotation of the crystallographic lattice around the fixed 100 direction pointing radially. This combination of a preferential orientation of the <100> directions towards the radial direction, with the perpendicular continuous distribution of the remaining <100> directions, perpendicular to the radial direction qualifies this texture as a cyclic <100> ring fiber texture [68], [112]. Such a texture was found for all types of W_fW, as shown for the case of $W_f/Er_2O_3/W$, in the more extensive explanation and analysis of the crystallographic nature of such a CVD matrix in the manuscript attached after this section.

6.1.3 Cyclic ring fiber texture in single tungsten fiber-reinforced tungsten composite

Cyclic ring fiber textures in single tungsten fiber-reinforced tungsten composites

U M Ciucani[1], L Haus[1,2], H Gietl[3], J Riesch[3], and W Pantleon[1]

[1] Technical University of Denmark, 2800 Kongens Lyngby, Denmark.
[2] Technical University Freiberg, 09599 Freiberg, Germany.
[3] Max-Planck-Institute for Plasma Physics, 85748 Garching, Germany.

Email: pawo@dtu.dk

Abstract. Tungsten fiber-reinforced tungsten composites are considered as plasma-facing material in future fusion reactors. Such composites are obtained by chemical vapor deposition of tungsten on potassium-doped, drawn tungsten wires. In model composites containing single fibers, particular texture types develop due to the cylindrical geometry of the deposition process. The vapor-deposited tungsten layers form a cyclic <100> ring fiber texture with one of the <100> directions pointing radially along the growth direction. The procedure for revealing this non-standard texture type from orientation data obtained by electron backscatter diffraction is presented. Identification of cyclic textures requires carefully chosen acquisition regions as well as a suitable coordinate system for their analysis. It is demonstrated that quite erroneous conclusions about the texture of the layer would be drawn if this is not accounted for properly.

1. Introduction

Tungsten is considered for plasma-facing components in future fusion reactors as armor material for the first wall and the divertor. In particular, tungsten fiber-reinforced tungsten composites have achieved certain interest due to their pseudo-ductile behavior [1]. Such composites can be obtained by chemical vapor deposition of tungsten on drawn tungsten wires [2]. The microstructure of a model composite containing a single potassium-doped tungsten fiber is investigated by means of electron backscatter diffraction [3]. Focus is on revealing the particular texture caused by deposition geometry.

2. Materials and techniques

2.1. Material

A tungsten fiber-reinforced tungsten composite is produced by chemical vapor deposition of tungsten on a single tungsten fiber: A drawn tungsten wire doped with 60 ppm potassium and having a diameter of 150 µm provided by OSRAM GmbH is coated in a two-step process by reactive magnetron sputtering with a 1 µm thin interlayer of erbia. A thick layer of pure tungsten (referred to as matrix) is chemically vapor-deposited on this interlayer to a total diameter of 1.5±0.1 mm (for details see [3]). Figure 1 sketches the geometry of the cylindrical specimen. A cross section is cut perpendicular to the cylinder axis, i.e. the wire axis, and prepared for electron backscatter diffraction by mechanical grinding (on SiC-paper of grit size 2000 and 4000) and polishing (with diamond suspension with grain size 3 µm). In a final step, electro-polishing is applied using an aqueous solution containing 3 wt.% NaOH at room temperature with an applied voltage of 12 V and a current of approximately 2 A.

2.2. Microstructural investigation

Orientation data were gathered by electron backscatter diffraction on freshly prepared cross sections using a Bruker NOVA NanoSEM 600 equipped with a Bruker e-Flash HD EBSD detector applying a voltage of 20 kV. A large overview map 2000x1725 μm^2 of the entire cross section is recorded at low magnification with a step size of 5 µm. Without any filtering or removal of non-indexed points, the gathered electron backscatter diffraction data are analyzed using the MTEX toolbox Version 5.5.0 [4] and evaluated further by own purposely developed routines.

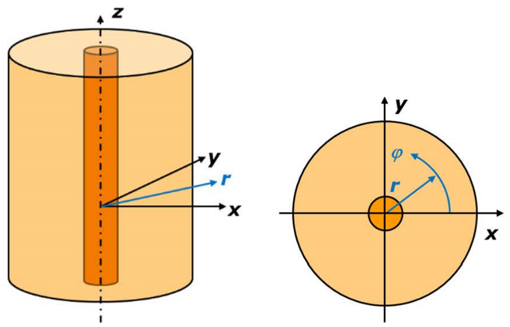

Figure 1. Sketch of the geometry of a cylindrical single tungsten fiber-reinforced tungsten composite (left) and its cross section (right). Upon a drawn, potassium-doped tungsten wire (shown in dark orange) coated with a thin erbia layer (not shown), tungsten is chemically vapor-deposited (light orange). Additional to the Cartesian coordinate system (black), a cylindrical coordinate system is introduced (blue). The radial direction *r* points in a transversal *xy*-plane outwards from the wire center, the azimuthal direction *φ* along the perimeter.

3. Results

3.1. Conventional analysis

Figure 2 presents the obtained orientation maps colored according to the crystallographic direction along the three different directions of a Cartesian coordinate system: the *z*-direction is normal to the mapped surface, the *x*- and *y*-direction correspond to the horizontal and vertical direction in the map, respectively. The cylindrical specimen can be recognized by the indexed points surrounded by a white, non-indexed region in the rectangular map. A clearly discernible central region of non-indexed points with diameter of 150 µm marks the locations of the drawn wire and the erbia interlayer. Due to defects formed by the large plastic deformation during wire drawing, orientations within the wire cannot be resolved with the chosen acquisition conditions for obtaining a large overview map. The successfully acquired orientations belong overwhelmingly to the chemically vapor-deposited tungsten matrix.

The orientation maps in figure 2 also highlight high angle boundaries which together with the orientation coloring reveal that in the vicinity of the wire a large number of small grains prevail which are not even resolved properly. In slightly larger distances from the wire, large grains are observed which stretch radially from the vicinity of the wire to the outer surface. These matrix grains grow radially and their wedge-like shape is a signature of the deposition process. The orientation map in figure 2c highlighting the crystallographic directions along the *z*-direction show dominantly colors from red over yellow to green, i.e. along the line [100]-[110], whereas bluish colors (blue, cyan or magenta) are rarely observed. This indicates the presence of preferred orientations. Further details about the texture are revealed from the corresponding pole figures in figure 3, displaying the crystallographic poles as a function of the spatial directions. The pole figures are derived based on the orientation distribution function calculated from all individual orientations in the map using a de la Valle Poussin kernel [4] with a half width of 10°.

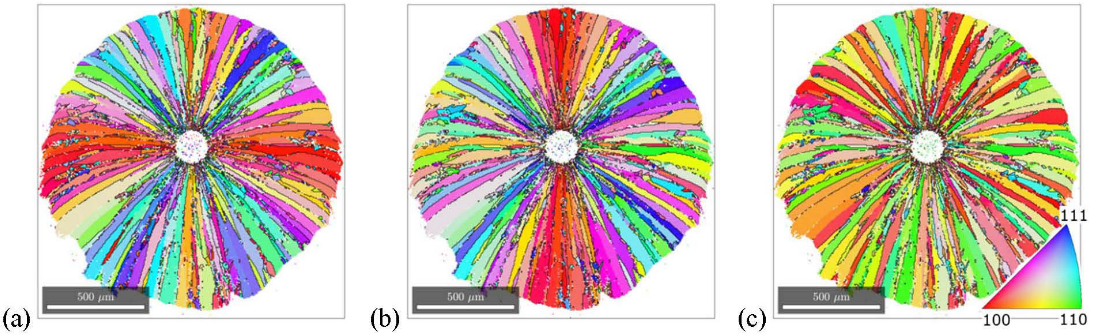

(a) (b) (c)

Figure 2. Orientation maps of the cross section of a single tungsten fiber-reinforced tungsten composite with erbia interlayer. The colors reflect the crystallographic directions along different sample directions according to the inset: (a) along *x*-, (b) along *y*- and (c) along *z*-direction, i.e. along the wire axis. High angle boundaries with disorientation angles above 15° are indicated in black.

Figure 3a presents the pole figures for the 100, 110 and 111 poles in stereographic projection onto the *xy*-plane. A maximum pole density of 2.6 compared to a random distribution of orientations is observed in the 100 pole figure where also an increased pole density along the outer perimeter is noticed. Judging solely from this 100 pole figure, the existence of a weak <100> fiber texture along the cylinder axis would be concluded. Further support for an ideal

<100> fiber texture is gained from the very weak ring at 45° in the 110 pole figure, but the apparent ring in the 111 pole figure at about 36° contradicts the idea entirely, as such a ring is expected at 54° for an ideal <100> fiber texture.

These observations are confirmed by the inverse pole figure in figure 3b along the *z*-axis which indeed shows a slight preference of [100] directions, but all directions along the symmetry line [100]-[110] are much more frequent than expected for an ideal <100> fiber texture along the *z*-direction.

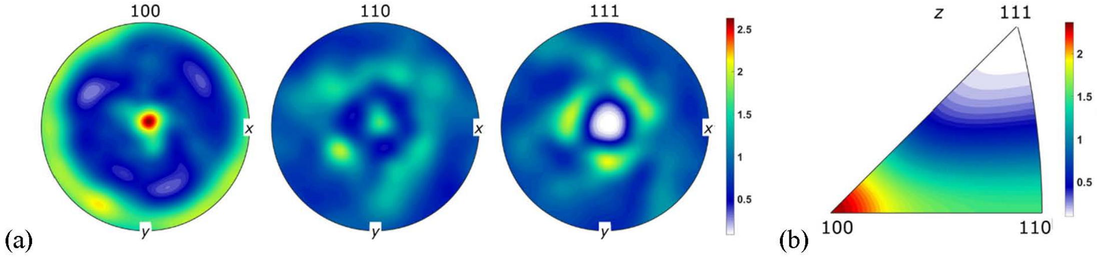

Figure 3. (a) 100, 110, and 111 pole figures and (b) inverse pole figure for *z*-direction obtained on a single tungsten fiber-reinforced tungsten composite with erbia interlayer. The data include all acquired orientations from the cross section shown in figure 2 and correspond overwhelmingly to locations in the matrix. All densities are given in multiples of random distribution according to the scale bar.

3.2. *Improved analysis*

In view of this evidence, the texture of the matrix cannot be a <100> fiber texture with a fiber axis along the wire and a more appropriate description of the texture is required. Revisiting the orientation maps in figure 2 exposes a hint: in figure 2a showing the crystallographic direction along the *x*-direction, the color red is dominating along a horizontal stripe in the center of the cross section revealing that horizontally aligned grains extend along one of their <100> directions. A similar observation can be made from figure 2b showing the crystallographic direction along the *y*-direction; here the red color of vertically aligned grains indicates that these also extend along one of their <100> directions, which in their case points along the *y*-direction, i.e. vertically instead of horizontally. Considering the cylindrical symmetry of the specimen, it seems plausible to conclude that all grains actually extend along one of their <100> directions radially outwards.

In order to exploit the observation that the grains exhibit a particular direction of extension along which one of their <100> directions is aligned, but that this direction is different from grain to grain, a special procedure for analyzing the texture is adapted. In view of the geometry of the specimen and the deposition process, a cylindrical coordinate system is introduced as shown in figure 1 where the radial *r*-direction points radially outwards from the wire center and the azimuthal φ-direction along the corresponding perimeter (the *z*-axis still coincides with the wire axis). In such a cylindrical coordinate system, the coordinate axes *r* and φ point in different directions at each position in a transversal plane.

For calculating pole figures and inverse pole figures with respect to these new coordinate axes, their local dependence must be taken into account. Such an evaluation is presently not implemented in any standard tool for evaluating orientation data. An appropriate procedure has been developed and implemented in MATLAB. The idea is basically to use standard evaluation tools for creating orientation maps, pole figures and inverse pole figures – not on the original orientations, but after a straightforward modification of the orientations in the map: Realizing that the cylindrical coordinate system is rotated by the azimuthal angle φ with respect to the Cartesian system at any position in the map, the Euler angle φ_2 of each orientation is adjusted accordingly. The resulting orientation maps, pole figures and inverse pole figures are on display on figures 4 and 5.

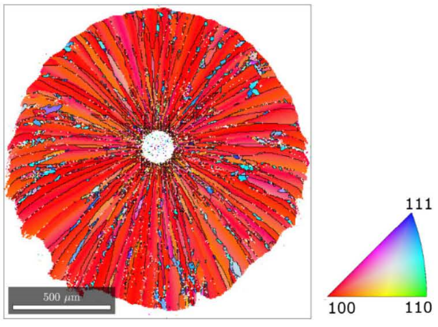

Figure 4. Orientation map of the cross section of a single tungsten fiber-reinforced tungsten composite with erbia interlayer (same data as in figure 2). The colors reflect the crystallographic directions along the radial direction of a cylindrical coordinate system according to the inset. High angle boundaries with disorientation angles above 15° are indicated in black.

In the orientation map in figure 4 colored according to the crystallographic direction along the radial direction, a dominating red color appears exposing an overwhelming dominance of <100> directions pointing radially outwards. The character of the texture is further confirmed by the pole figures in figure 5a. In the 100 pole figure, a strong alignment of crystallographic <100> directions with the radial direction is seen (with a maximum 100 pole density of 10.5), the ring in the plane comprising the azimuthal and axial direction is a direct consequence of this strong alignment and the angle of 90° between <100> directions. In a similar way, <110> directions form either an angle of 45° or 90° degrees with <100> explaining neatly the observed rings in the 110 pole figure. Finally, the angle of 54° between <111> and <100> directions rationalizes the position of the rings in the 111 pole figure. All rings in the pole figures are rather smoothly populated and no systematic variation is observed along them indicating the presence of an ideal <100> fiber texture along the radial direction.

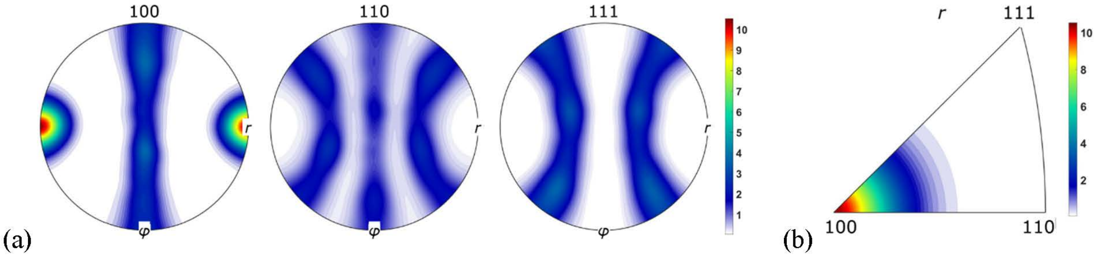

Figure 5. (a) 100, 110, and 111 pole figures with respect to cylindrical coordinates and (b) inverse pole figure along the radial *r*-direction obtained on a single tungsten fiber-reinforced tungsten composite with erbia interlayer. The data include all acquired orientations from the cross section shown in figure 2 and correspond overwhelmingly to locations in the matrix. The densities are given in multiples of random distribution according to the scale bar.

In consequence, the texture is a strong, ideal <100> fiber texture along the radial direction in the cylindrical coordinate system and not a weak <100> fiber texture along the axial direction as may have been concluded from investigating the texture in a Cartesian coordinate system. In view of these findings, the texture in the sample system must be described differently: At first, there is a preferred alignment of <100> directions in the transversal plane with free rotation around that aligned direction. Such textures are classified as ring fiber textures [5] (alternatively, the term planar texture is used [6]). Additionally to one of the <100> directions occurring in the transversal plane (and free rotations around it), this specific direction aligns with the radial direction causing a different preferred orientation at any spatial position. Textures featuring a certain crystallographic direction aligned with the radial direction are termed cyclic textures [5,7] (or cylindrical textures [8] or circular textures [9]) and usually discussed in connection with cylindrical objects (wires or tubes). In consequence, the texture of the deposited layer must be classified as cyclic <100> ring fiber texture.

4. Discussion

A cyclic <100> ring fiber texture is concluded for the deposited layer with <100> directions aligned in the transversal plane perpendicular to the wire axis and the particular feature from cylindrical symmetry, that these <100> directions point radially. The possibility of cyclic ring fiber textures has been discussed theoretically [5], but to the knowledge of the authors never been reported before.

Cyclic fiber textures and cyclic ring fiber textures might be more widespread than commonly reported, because it might be difficult to resolve spatial correlations between preferred orientations as in the present case. To illustrate the danger of underestimating the impact of spatial correlations for obtaining a proper texture description, different regions of the original map are analyzed separately. Four different subsets of orientations are obtained from four smaller quadratic or rectangular regions (each comprising about half the number of indexed points) as illustrated in the top row of figure 6.

The corresponding 100 pole figures in the bottom row of figure 6 show rather different pole distributions: From the 100 pole figure of the entire map (figure 6a), a <100> fiber texture along the *z*-axis would be concluded naively. For the square region in figure 6b, 100 poles are observed under 45° with respect to *x*- and *y*-direction implying preferred orientations belonging to a {100}<011> texture component (a cube orientation rotated by 45° around *z*); for the rotated square region (figure 6c), 100 poles along both *x*- and *y*-direction are dominating implying the presence of an ideal {100}<001> cube component; for the horizontal rectangle, 100 poles appear along the *x*-direction and an additional ring in the *yz*-plane (in figure 6d) implying a <100> fiber texture along the *x*-axis. Just the opposite is true for the vertical rectangle; the 100 pole figure in figure 6e indicates a <100> fiber texture along the *y*-direction. Hence, depending on the choice of the region from which orientations are acquired, rather different texture types are concluded based on the 100 pole figures as summarized in table 1: in some cases, fiber textures with different fiber axes (<100> fiber texture along *x*-, *y*-, or *z*-direction), in other cases, textures with orthorhombic symmetry (cube or rotated cube).

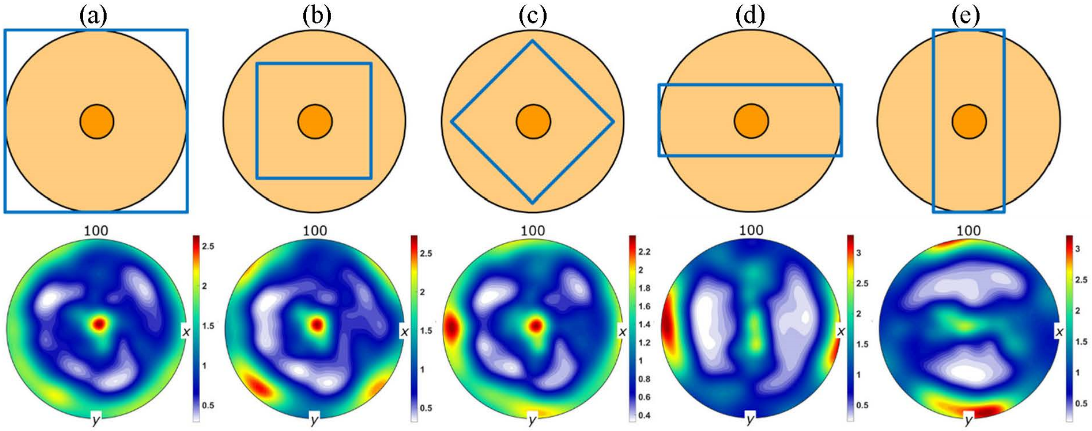

Figure 6. Schematic drawing of different acquisition regions on the cross section of a single tungsten fiber-reinforced tungsten composite with erbia interlayer (top row) and corresponding 100 pole figures (bottom row) for (a) data acquired for the entire cross section corresponding to figure 2, (b) to (e) different square and rectangular regions with about half of the number of indexed points.

Table 1. Quantitative texture analysis for different regions on the cross section (cf. figure 6)

Region	Max. 100 pole density	Texture index	Texture entropy	Texture type (as concluded from 100 pole figure)
Full map (Cartesian coord.)	2.6	1.55	-0.28	<100> fiber texture along *z*
Full map (cylindrical coord.)	*10.5*	*5.09*	*-1.16*	*Cyclic <100> ring fiber texture*
Central square	2.7	1.62	-0.29	{100}<011> *z*-rotated cube texture
Rotated square	2.4	1.51	-0.26	{100}<001> cube texture)
Horizontal rectangle	3.3	1.92	-0.39	<100> fiber texture along *x*
Vertical rectangle	3.2	1.84	-0.38	<100> fiber texture along *y*

The cyclic nature of the texture can be substantiated further by the measures of texture strength in table 1: When using a Cartesian coordinate system, independent of the chosen region rather weak textures are indicated by 100 pole densities of maximal 3.3, texture indices [10] less than 2 and texture entropies [11] above -0.4. Using an appropriate cylindrical coordinate system with spatially different coordinate axes for the description of the orientations confirms the strong preference of certain directions and orientations seen in the pole figures and inverse pole figure in figure 4. The maximal 100 pole density of 10.5 verifies that a much better texture description is achieved by realizing the presence of a cyclic texture. The existence of a strong cyclic ring fiber texture is further substantiated by the high texture index above 5 and the large negative value -1.16 of the texture entropy.

5. Conclusion

A tungsten fiber-reinforced tungsten composite has been investigated by electron backscatter diffraction. The chemically vapor-deposited tungsten matrix shows a peculiar texture identified as cyclic <100> ring fiber texture. The required thorough texture analysis is detailed and the effect of inappropriate choices for the acquisition regions outlined. This clearly demonstrates how important an adequate characterization becomes and how strongly results can be affected by spatial correlations, if sample symmetry is not respected. When using an inappropriate coordinate system, completely erroneous textures might be concluded. On the other hand, when utilizing an appropriate coordinate system even more complicated texture types can be identified as the cyclic <100> ring fiber texture.

Acknowledgments

This work has been carried out partially within the framework of the EUROfusion Consortium and has received funding from the Euratom research and training programme 2014-2018 and 2019-2020 under grant agreement No 633053. The views and opinions expressed herein do not necessarily reflect those of the European Commission.

References

[1] Riesch J, Höschen T, Linsmeier C, Wurster S, and You J H 2014 *Phys. Scr.* **2014** 014031
[2] Du J, You J H, and Höschen T 2012 *J. Mater. Sci.* **47** 4706
[3] Ciucani U M, Haus L, Gietl, H, Riesch J, and Pantleon W 2021 *J. Nucl. Mater.* **543** 152579
[4] Bachmann F, Hielscher R, and Schaeben H 2010 *Solid State Phenom.* **160** 63
[5] Wassermann G and Grewen J 1962 *Texturen metallischer Werkstoffe* 2nd edition (Berlin: Springer Verlag) pp 7-11
[6] Saraf R F 1994 *Polymer* **35** 1359
[7] Stüwe P 1961 *Z. Metallkde.* **52** 34
[8] Leber S 1961 *Trans. Amer. Soc. Metals* **52** 697
[9] Kocks U F, Tomé C N, and Wenk H.-R. 1998 *Texture and Anisotropy* (Cambridge: Cambridge University Press) p 151
[10] Bunge H.-J. 1982 *Texture Analysis in Materials Science* (Butterworth & Co) p 88
[11] Schaeben H 1988 *J. Appl. Phys.* **64** 2236

6.1.4 Twin boundaries in CVD tungsten

A closer analysis of Figure 53 reveals a smaller yet visible amount of orientations of a different kind, shown in the map by light blue/blue color. Interestingly, these orientations seem to be the only ones besides the radial [100] preferred orientations. Closer analysis of the orientation of these alternatively oriented grains - which correspond the triangular grains in Figure 50 - was performed with the help of the recorded electron backscatter patterns (EBSPs). From a more detailed, magnified map showing such triangular grains, few are selected and indicated in Figure 55 by the numbers 1,2 7/9 and 8; and the EBSPs of points in those grains across in the vicinity of boundaries, inspected.

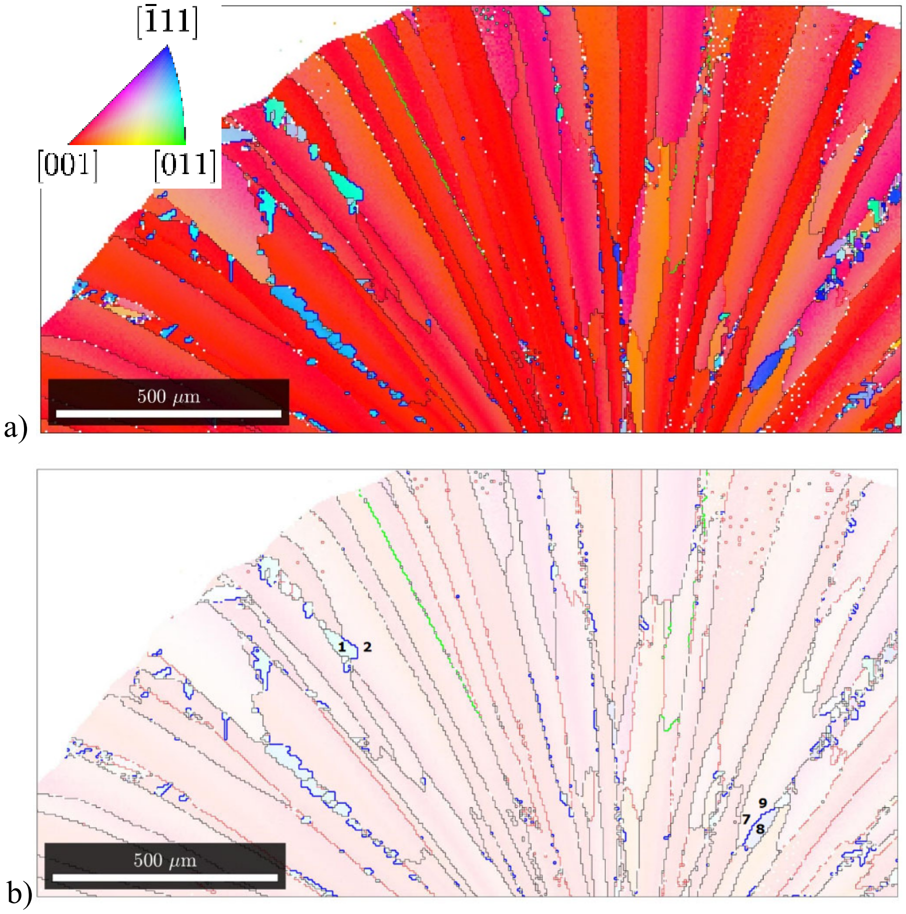

Figure 55: Magnified region of the orientation map in Figure 53 showing a region filled with many light blue colored grains consisting in grains separated from the preferential [100] radially growing grains by twin boundaries shown in blue in b) boundary map of the same region of Figure 55a with points shown as numbers indicating the points of origin of the diffraction patterns in Figure 56. In black, any other boundary in the map. The colors indicate the crystallographic direction along the radial direction colored according to the inset.

In Figure 56 the EBSPs for each point are shown. If one operates a horizontal mirroring of the pattern from point 1, it will results in the pattern from point 2, if one allows for a small mismatch of the bands of the other pattern.

This final result is best seen for the second subset of grains: point 7/9 and point 8. Point 7/9 has two numbers indicating it since two positions within that same grain are considered, so to create a path starting at position 7, passing through 8 and ending at 9, for which the boundary is crossed twice and three EBSPs can be acquired and analyzed. The actual patterns for the points 7, 8 and 9 are shown in the upper line of Figure 56b and pattern 7 can be seen to be identical to pattern 9. The red lines are the indexed Kikuchi lines for the pattern and serve as a reference in the following mirroring procedure. Mirroring of pattern 8 turns it into basically the same of patterns 7 and 9, as shown in the bottom line of Figure 56b.

Horizontal mirroring by 180° of the pattern from each point (2 and) just across the boundary returns the same pattern from the adjacent region 1 and 7/9. This is a proof of the twin character of the boundary, e.g. a Σ3 boundary. Such a mirroring operation corresponds to a 60° rotation around the [111] direction which defines a twin boundary. Hence, the analysis of the EBSPs indicates these alternatively oriented grains to be related to the wedge like grains by a twin boundary. These twin boundaries have been found for all the different types of W_fW material.

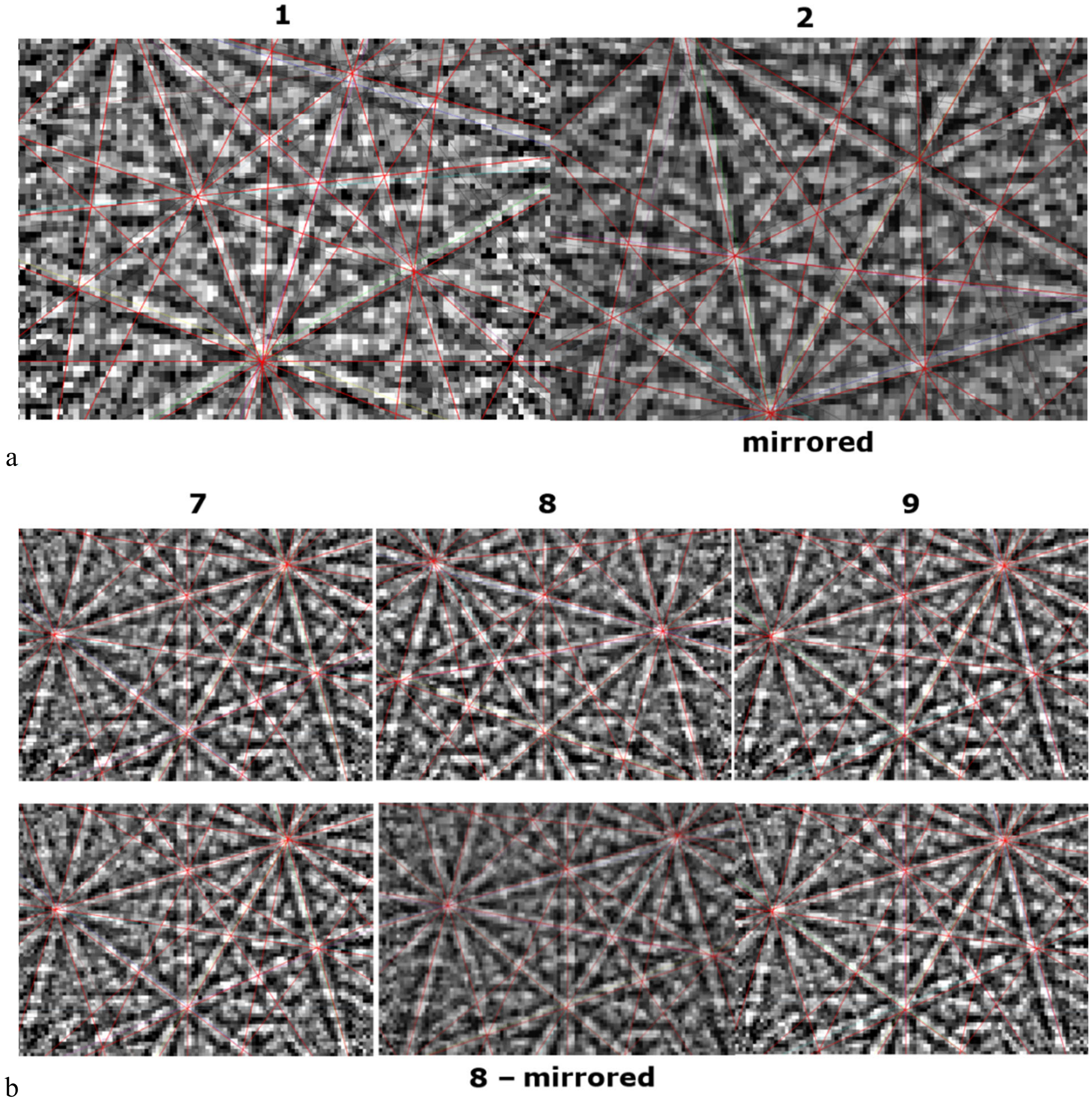

Figure 56: EBSD patterns from the points indicated in Figure 55 as a) 1, 2, and b) 7, 8 and 9. The identical pattern found upon mirroring of the patterns implies a twin boundary is dividing the triangular grains from the [100] preferential direction radially growing grains..

6.1.5 Cyclic <110> fiber texture in tungsten wires

The same method used to analyze the orientations and infer the cyclic ring fiber texture in the CVD region revealed an interesting novel detail about the texture of the wire. In Figure 57, the orientation map only from the wire cross-section as from Figure 48 is shown, colored according to the z direction, which is the wire drawing direction, to indicate the orientation along that axis according to the conventional inverse pole figure scheme as in the insert of Figure 51. The predominance of the green color is clear which is also what is expected for the texture of bcc drawn products [68]. The pole figures for this region as in Figure 58 confirm this texture: the needle-like grains within the wire are preferentially oriented with their [110] direction parallel to wire drawing direction, this texture is commonly referred to as <110> fiber texture [68]. If the pole figures are plotted to account for lower densities in the range 3.5 to 1 mrd, a ring at the equator becomes visible in the 110 pole figure; a deeper analysis is needed and performed using the cylindrical reference coordinate system as for the CVD matrix.

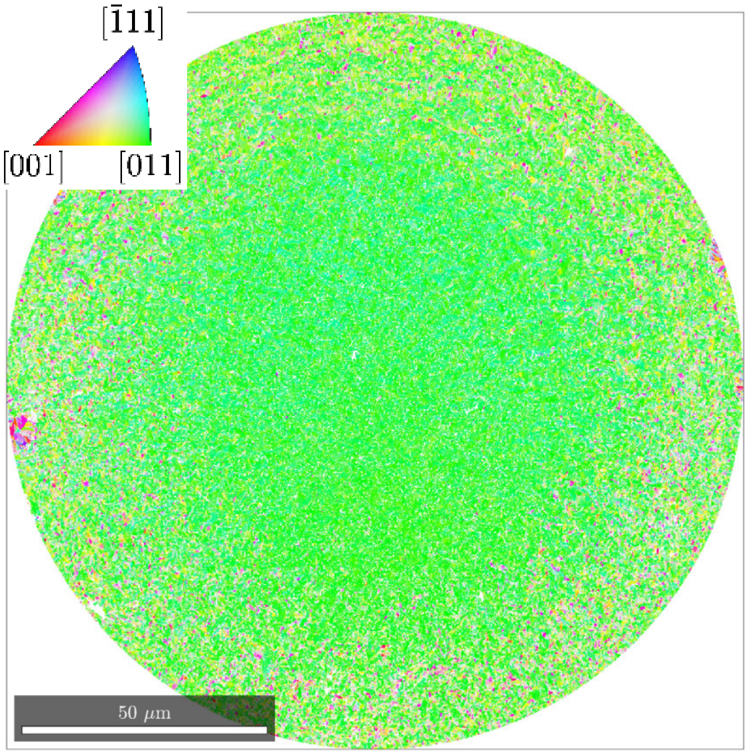

Figure 57: Orientation map of the W_f/W region of the wire only as from Figure 48, colored according to the z-direction, using the color scheme as in the inset.

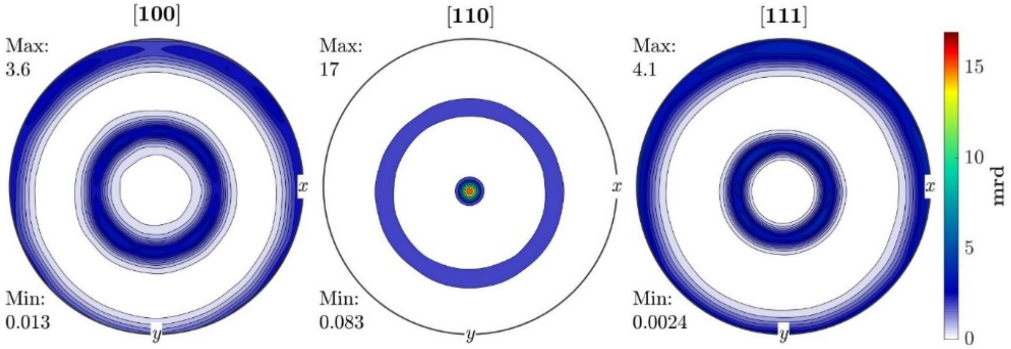

Figure 58:100, 110 and 111 pole figures from the orientations of the wire region only (from the orientation map in Figure 57) onto the specimen reference coordinate system having the horizontal direction indicated by x and the vertical direction direction indicated by y. The pole densities are given in multiples of random distribution.

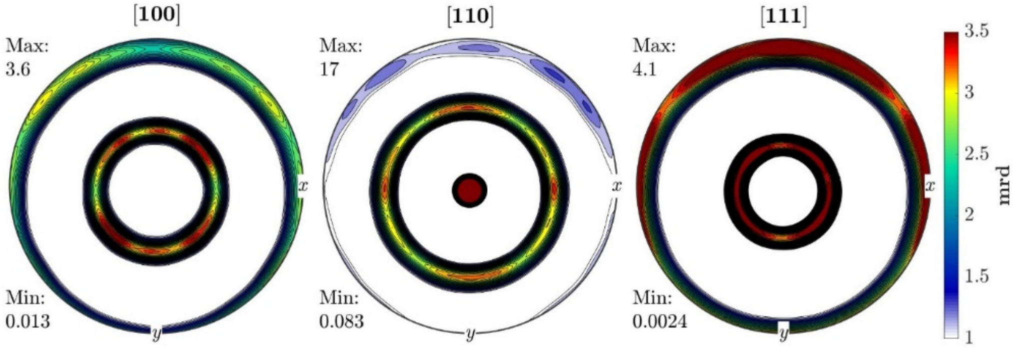

Figure 59: 100, 110 and 111 pole figures from the orientations in the wire region only (from the orientation map in Figure 57) onto the specimen reference coordinate system having the horizontal direction indicated by x and the vertical direction direction indicated by y. The pole densities are given in multiples of random distribution. The pole densities below 3.5 are highlighted

In Figure 60 the orientation map of the wire region only of Figure 48 is shown, colored according to the radial direction as for Figure 53, using the color scheme as in the inset. In this map, the region of the wire can be distinguished from that of the CVD matrix surrounding it by the very small grain size of grains in the circular area in the center of the image. These small grains are actually the cross-sections of the very long, needle shaped grains typical of drawn wires. The CVD region is characterized by the afore-mentioned radially growing grains of increasing thickness with increasing distance from the interface of the two regions. A distinction is needed with respect to the former analysis of the CVD region.

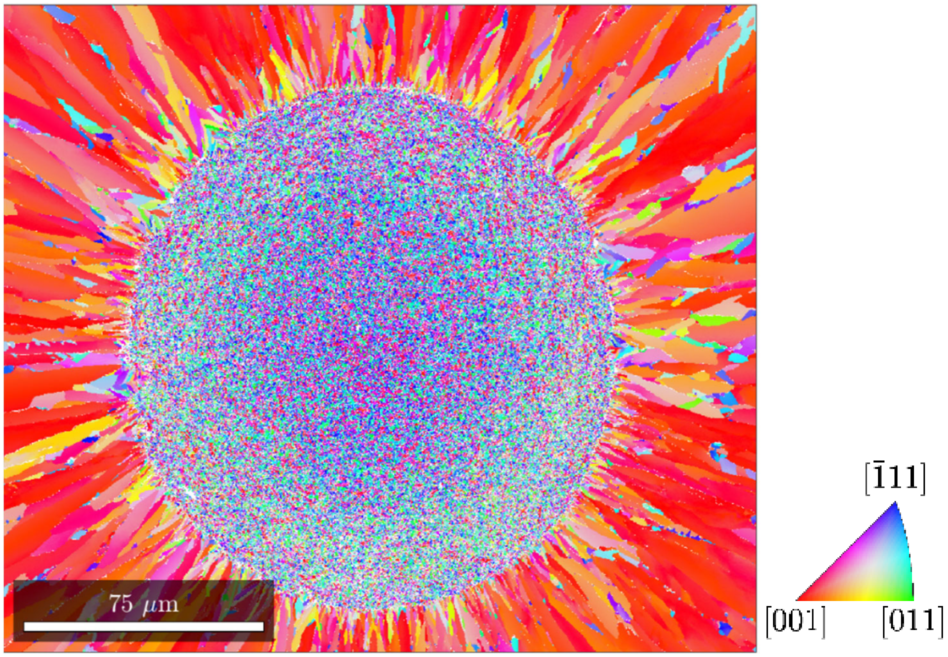

Figure 60: Orientation map of the W_f/W region of the wire and the closest regions of the CVD matrix surrounding the wire as from Figure 48, colored according to the radial direction as in Figure 53, using the color scheme as in the inset.

In this higher magnification mapping, the grains closest to the interface possess a much smaller aspect ratio compared to those at larger distances from the interface in this map. They are rather short in radial length and it was suggested growth selection favouring [100] radially oriented grain to take place in this acicular zone, in the immediate vicinity of the interface. Grains possessing an orientation with a [100] direction pointing radially grow preferentially outwards to form wedge grains. Concerning the orientations, the abundance of red color in the CVD region confirms once again the [100] radially preferred direction of grains. In the wire, a relatively large amount of orientations can be distinguished possessing a light blue / green coloring. The orientation of the grains within the wire only, according to their radial and azimuthal directions can be further analysed by the pole figures of Figure 61. The pole figures of Figure 58 seem replicated but a higher pole density in the 110 pole figure along the radial direction is visible. The weak ring found in the xy plane in the 110 pole figure of Figure 59 now merged to a higher pole density (1.8) along the radial direction as shown in Figure 62. In Figure 62, white and red stars are located at spots in the pole figures at which maximum intensities should arise in the case the wire would possess an ideal {110}<110> orientation. At these locations a higher pole density is found (in Figure 62) respect to one expected for a normal <110> fiber texture. These results indicate an additional preferential orientation of the grains is present, that of the [110] direction along the radial direction;

This result holds for every type of the W_fW analysed as they have the same wires. Such a finding implies tungsten drawn wires exhibit a texture that can not be defined by a fiber texture solely. It is finally inferred the texture of the wires is a cyclic {110}<110> fiber texture, where on top of an alignment of <110> directions along the wire axis, a second alignment of <110> directions with the radial direction occurs.

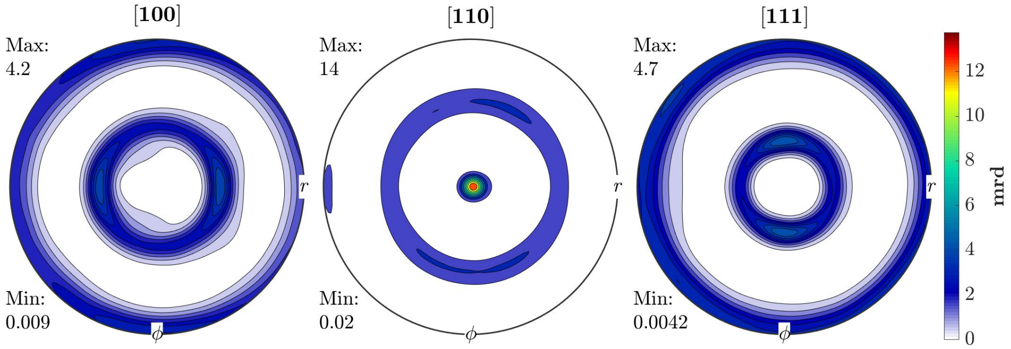

Figure 61: Pole figures for the wire region only in orientation map in Figure 60 using the alternative cylindrical reference coordinate system with the radial direction indicated by r and the azimuthal direction indicated by φ.

`

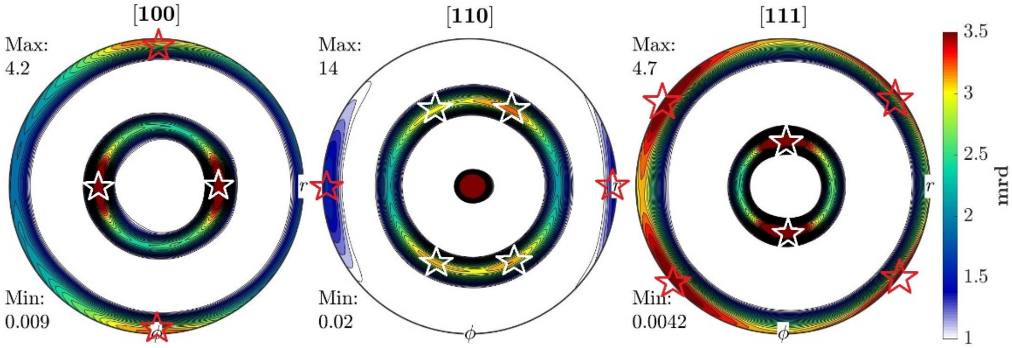

Figure 62: Pole figures for the wire region only in orientation map in Figure 60 using the cylindrical reference coordinate system with the radial direction indicated by r and the azimuthal direction indicated by φ, highlighting densities between 1 and 3.5 random. The stars indicate the points in the pole figures where the higher pole densities for an ideal {110}<110> orientation should be.

6.2 Annealed Condition

6.2.1 Microstructural evolution in single tungsten fiber-reinforced tungsten composites during annealing: recrystallization and abnormal grain growth

Journal of Nuclear Materials 543 (2021) 152579

Contents lists available at ScienceDirect

Journal of Nuclear Materials

journal homepage: www.elsevier.com/locate/jnucmat

Microstructural evolution in single tungsten fiber-reinforced tungsten composites during annealing: recrystallization and abnormal grain growth

Umberto M. Ciucani [a,†,*], Lea Haus [a], Hanns Gietl [b,c], Johann Riesch [b], Wolfgang Pantleon [a]

[a] *Section for Materials and Surface Engineering, Department of Mechanical Engineering, Technical University of Denmark, 2800 Kongens Lyngby, Denmark.*
[b] *Max-Planck-Institut für Plasmaphysik, 85748 Garching, Germany.*
[c] *Technische Universität München, 85748 Garching, Germany.*

ARTICLE INFO

Article history:
Received 28 February 2020
Revised 25 June 2020
Accepted 5 October 2020
Available online 8 October 2020

Keywords:
Tungsten fiber-reinforced tungsten
Recrystallization
Grain growth
Microstructural evolution
Thermal stability
EBSD

ABSTRACT

Tungsten is considered as plasma-facing material in future fusion reactors. Due to the high operation temperatures, the occurrence of microstructural restoration processes as recovery, recrystallization and grain growth will unavoidably alter the desired microstructure obtained after processing and impede otherwise beneficial mechanical properties. Potassium-doping proved to be efficient in hindering or at least delaying such phenomena. Tungsten fiber-reinforced tungsten composites with drawn tungsten wires embedded in a tungsten matrix show a certain pseudo-ductility. Cylindrical single fiber composites with a single potassium-doped drawn tungsten wire in a chemically vapor deposited tungsten matrix, with or without a rare-earth oxide interlayer, were investigated as model systems. Individual specimens were annealed at 1400 °C up to four weeks and changes in their microstructure tracked by electron backscatter diffraction. In the as-processed condition, the tungsten matrix showed large wedge-shaped grains stretching radially from either the interface between matrix and wire or the oxide interlayer to the outer surface with very small grains in the vicinity of the interface/interlayer. Upon heating, two zones with larger grains compared to the as-processed condition developed: in the wire regions close to its perimeter primary recrystallization led to formation of new grains with orientations deviating slightly in alignment of their crystallographic <110> directions with the wire axis compared to the drawn wire. In the matrix, abnormally grown grains consumed the as-deposited microstructure in the vicinity of the interface/interlayer. Without an interlayer, abnormally growing grains from the matrix invaded the recrystallizing wire progressively consuming the wire. Both erbia and yttria interlayers efficiently prevented abnormally growing grains from invading the wire (except at few occasions where the oxide interlayer presented imperfections). In this manner, the presence of an interlayer becomes crucial for retaining an interface essential for the pseudo-ductility of the composite.

© 2020 The Author(s). Published by Elsevier B.V. All rights reserved.

1. Introduction

Fusion is set to become one of the major means of world energy production in future. The operation of fusion reactors impose demanding working conditions [1] and strong requirements on the materials [2]. Armor material of plasma-facing components will face extreme heat and particles fluxes requiring an outstanding heat resistance in combination with a fast heat transport.

Tungsten (W) and tungsten alloys are considered the main candidate materials for plasma-facing components thanks to superior characteristics of tungsten: low-activation, high thermal conductivity, low sputtering yield, high strength and creep resistance at elevated temperatures [3–6]. Due to its body centered cubic lattice and high melting temperature, pure annealed tungsten has a high brittle-to-ductile transition temperature and behaves brittle at room temperature [4,7–10] restricting its use as plasma-facing material, whereas plastically deformed tungsten in general behaves more ductile at ambient temperatures. Large plastic deformation has been utilized for more than hundred years for fabrication of ductile tungsten wires by wire drawing [11]. Efforts are currently

---

[*] Corresponding author: Umberto M. Ciucani, Section for Materials and Surface Engineering, Department of Mechanical Engineering, Technical University of Denmark, 2800 Kongens Lyngby, Denmark, +45 45254883.

E-mail addresses: umciuc@mek.dtu.dk, umbertomariaciucani@gmail.com (U.M. Ciucani).

[†] Corresponding Author ORCID: orcid.org/0000-0003-3881-4811.

https://doi.org/10.1016/j.jnucmat.2020.152579

0022-3115/© 2020 The Author(s). Published by Elsevier B.V. All rights reserved.

undertaken to lower the brittle-to-ductile transition temperature of tungsten plates even below room temperature also by cold rolling [12].

Unfortunately, the deformation structures obtained by plastic deformation are not stable at the operation temperatures of 800 °C and above of plasma-facing components. During operation, they will undergo restoration processes altering the microstructure by recovery, recrystallization and grain growth [13,14]. In particular, recrystallization consisting of nucleation and growth of defect-free grains at the expense of the ductile matrix will reinstate the intrinsic brittleness of tungsten.

Several pure tungsten plates warm- or cold-rolled to different rolling reductions have been studied in terms of their thermal stability (see e.g. [15–21]). Moderately rolled tungsten plates (see [15–19]) are sufficiently thermally stable to withstand microstructural changes at the expected temperatures of 800 °C for the first wall, but will not be able to endure the higher expected divertor temperatures of 1100 °C and above for the required two years.

Attempts to improve the mechanical properties of tungsten focus on ductilization by means of alloying (Re, Ti, Ta and V, e.g. [22,23]) or dispersion strengthening by oxides or other particles (Y_2O_3, La_2O_3 or TiC, see e.g. [24,25]). Particle dispersions provide an additional advantage as they stabilize deformation structures by preventing boundary migration through Zener pining [26].

Similar to impeding boundary motion by particle dispersions, doping with potassium has been utilized for preventing tungsten wires from losing their beneficial mechanical properties obtained after wire drawing through undesired microstructural restoration processes [11]: During processing, insoluble potassium forms potassium bubbles which impede grain boundary motion and stabilize the microstructure of the drawn wires. In this manner, ductile wires with sufficient life time at high temperature are achieved and successfully applied in commercial light bulbs. More recently, attempts were undertaken to utilize potassium-doping also for cold-rolled tungsten plates (e.g. [21]).

As an alternative to bulk tungsten material, pseudo-ductile tungsten fiber composites are considered where tungsten (W) is chemically vapor deposited as matrix material on drawn potassium-doped tungsten wires forming reinforcing fibers (W_f) [27,28]. Such tungsten fiber-reinforced tungsten (W_f/W) composites consist of two different “phases” with rather different properties, both formed by almost pure tungsten: the chemically vapor deposited tungsten matrix behaves brittle, whereas the drawn tungsten wires are able to deform plastically under mechanical load. The plastic work required for their deformation as well as the energy dissipation at the interface between wire and matrix will prevent crack propagation and ensure a certain pseudo-ductility of the composite [29,30]. Multifilament composites with tungsten deposited on layered meshes of drawn tungsten wires are considered for plasma-facing components [31,32]. The debonding behavior between fibers and matrix during mechanical loading of multifilament composites with parallel fibers has been investigated in the as-processed state as well as in an embrittled state after annealing for 30 min at 1727 °C [30,31].

A model system containing a single tungsten fiber in a tungsten matrix can elucidate the crucial role of the interface between wire and matrix for the behavior of the composite. Different interlayers have been applied to modify the cohesive properties and to improve the mechanical behavior [27,33]. Until now, the microstructure of single fiber composites has been investigated with respect to cohesion and integrity of the interlayer only during short time annealing at a temperature of 800 °C [33].

In view of the importance of thermally stable microstructures for the performance of W_f/W composites under operation conditions in a fusion reactor, the microstructural evolution in single fiber composites with and without a rare-earth oxide interlayer is investigated here during isothermal annealing at 1400 °C for long terms up to 28 days. Future investigations at lower temperatures will establish the temperature dependence of the observed phenomena allowing extrapolation of the findings to the operation temperature of plasma-facing components.

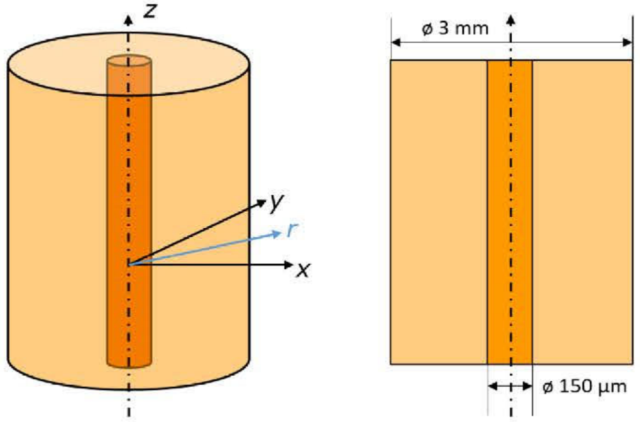

Fig. 1. Sketch of the geometry of single fiber W_f/W composites (not to scale). Upon a drawn potassium-doped tungsten wire with a diameter of 150 µm (dark orange), tungsten is chemically vapor deposited (shown in light orange) - either without interlayer (as sketched) or with an oxide interlayer physically vapor deposited on the wire before CVD of the matrix (not shown). The radial direction r in a transversal (xy) plane perpendicular to the wire axes (i.e. in a cross section) points outwards from the wire center as indicated.

2. Materials and methods

Single fiber composites containing a single tungsten wire in a chemically vapor deposited tungsten matrix are investigated as models system for tungsten fiber-reinforced tungsten composites (W_f/W). The geometry of such cylindrical single fiber composites is illustrated in Fig. 1, their production detailed in [29,30,33]. Tungsten wire doped with 60 ppm potassium and drawn to a diameter of 150 µm were provided by OSRAM GmbH. Pure tungsten is deposited by chemical vapor deposition (CVD) directly on the wire at temperatures between 580 °C and 620 °C through the chemical reaction

$$WF_6 + 3H_2 \rightarrow W + 6HF \quad (1)$$

In this manner, cylindrical specimens with larger diameter of 3.0 ± 0.1 mm are achieved. Additional to single fiber composites without any interlayer, two different single fiber composites with a thin rare-earth oxide interlayer are produced. For this, the drawn tungsten wires were coated in a two-step process by reactive magnetron sputtering with a 1 µm thin layer of either erbia (Er_2O_3) or yttria (Y_2O_3), before the tungsten matrix is grown by CVD. Cylindrical single fiber composite specimens with diameters of 1.5 ± 0.1 mm and 2.1 ± 0.1 mm are obtained for erbia and yttria coated tungsten wires, respectively.

From the produced cylindrical single fiber composites, disc-shaped samples were cut to a height of 1.35 ± 0.05 mm. In order to remove the mechanically induced deformation layer, one of the cut surfaces was mechanically grinded (with SiC-paper of subsequent grit sizes 800, 1200, 2500 and 4000) and chemo-mechanically polished (with different oxide particle suspensions) and only this surface was investigated further. For protection of the specimens against oxidation and formation of volatile WO_3 during annealing treatments, specimens were encapsulated in quartz glass ampoules (either individually or together with other specimens having different interlayers). The procedure consists of evacuating the ampoules, flushing them with Argon (with purity higher than

99.999%), and finally sealing them with a blowtorch. Isothermal annealing of encapsulated specimens at 1400 °C was performed for up to 28 days (672 h). The ampoules were put in a pre-heated ceramic tube furnace NaberTherm RHTC 80-230/15, removed after the desired annealing time and cooled to room temperature by air-cooling. For four different annealing times (7 days, 14 days, 21 days and 28 days), the microstructure of a single specimen was investigated for each of the three different types of single fiber W_f/W composites.

For microstructural investigations, one of the two surfaces of the specimens (corresponding to cross sections of the single fiber composites) were prepared using a standard metallographic route consisting of mechanical grinding (on SiC-paper of grit size 2000 and 4000), polishing (with diamond suspension with grain size 3 µm), and final electro-polishing using an aqueous solution containing 3 wt.% NaOH at room temperature with an applied voltage of 12 V and a current of approximately 2 A.

EBSD investigations on freshly prepared samples were accomplished using a Bruker NOVA NanoSEM equipped with a Bruker e-Flash HD EBSD detector applying a voltage of 20 kV to investigate either the entire cross sections or specifically the regions around the original wire and the wire itself. Maps were obtained with different magnifications and different step sizes Δx: Large overview maps of the entire cross section were recorded at lowest magnification with a step size of 5 µm. For revealing the microstructural details of the tungsten wire and the region just around it, a higher magnification and smaller step sizes of 150 nm and 500 nm were used for the as-processed state and the annealed conditions, respectively. The reason for recording maps with different step sizes is routed in the necessary compromise between sufficient resolution for the analysis of the microstructural details in the wire and a reasonably short acquisition time for the entire CVD region. Without any filtering or removal of non-indexed points, the gathered EBSD data are analyzed using the MTEX toolbox [34] and evaluated further by own purposely developed routines.

3. Results

3.1. As-processed condition

The microstructure of the single fiber W_f/W composites in their as-processed condition is presented in Fig. 2 where secondary electron images of cross sections of a specimen without any interlayer (Fig. 2(a-b)) and a specimen with an erbia interlayer (Fig. 2c) are shown. In both cases, the drawn wire and the CVD matrix can be clearly distinguished. Due to the drawing process, tungsten grains in the wire are fibrous and elongated along the wire drawing direction (e.g. [35]). Their extremely small cross sections cannot be resolved individually even with the higher magnification of Figs. 2(b-c). On the other hand, large tungsten grains can be observed in the CVD matrix in Fig. 2a. These grains are elongated radially, i.e. along their growth direction during the deposition process. Their azimuthal width (i.e. their width along a circle of constant radius) increases with increasing distance from the center. Some of the wedge-shaped grains even grow radially through the entire deposited layer from the vicinity of the wire all the way to the outer surface (cf. Fig. 2a). The geometry of these wedge-shaped grains will be explored further based on EBSD data. In matrix regions in the vicinity of the wire, very small grains are observed which are slightly elongated, but not as much as the wedge-shaped grains in the outer region. The location of the oxide interlayer can also be clearly identified from the groove caused by electro-polishing for the specimen with an erbia interlayer in Fig. 2c. From the appearance of the oxide interlayer in Fig. 2c as well as from the discernable interface between matrix and wire in Fig. 2b of the specimen without an interlayer, it becomes obvious that the wire does not

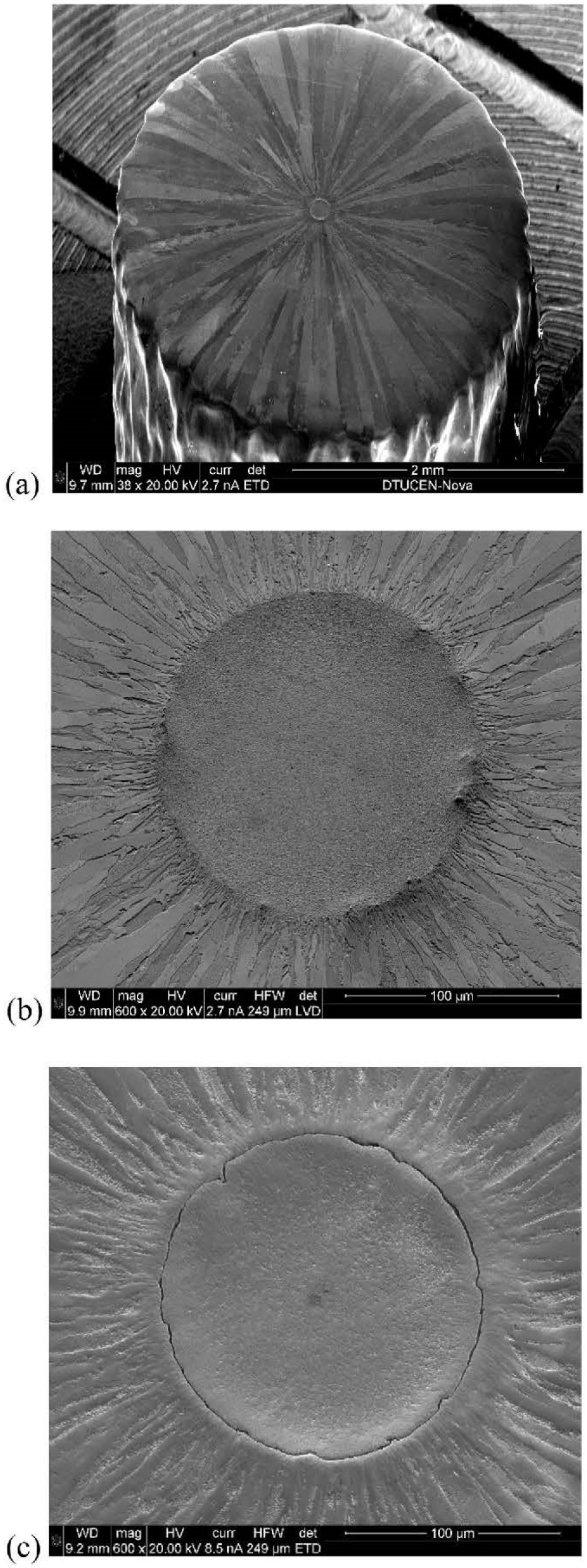
(a)
WD mag HV curr det 2 mm
9.7 mm 38 x 20.00 kV 2.7 nA ETD DTUCEN-Nova
(b)
WD mag HV curr HFW det 100 µm
9.9 mm 600 x 20.00 kV 2.7 nA 249 µm LVD
(c)
WD mag HV curr HFW det 100 µm
9.2 mm 600 x 20.00 kV 8.5 nA 249 µm ETD

Fig. 2. Secondary electron images obtained by scanning electron microscopy on cross sections of single fiber W_f/W composites in their as-processed condition: composite without interlayer (a) with smallest possible magnification and (b) with highest recorded magnification; (c) composite containing an erbia interlayer (obvious from the groove caused by electro-polishing) at highest recorded magnification.

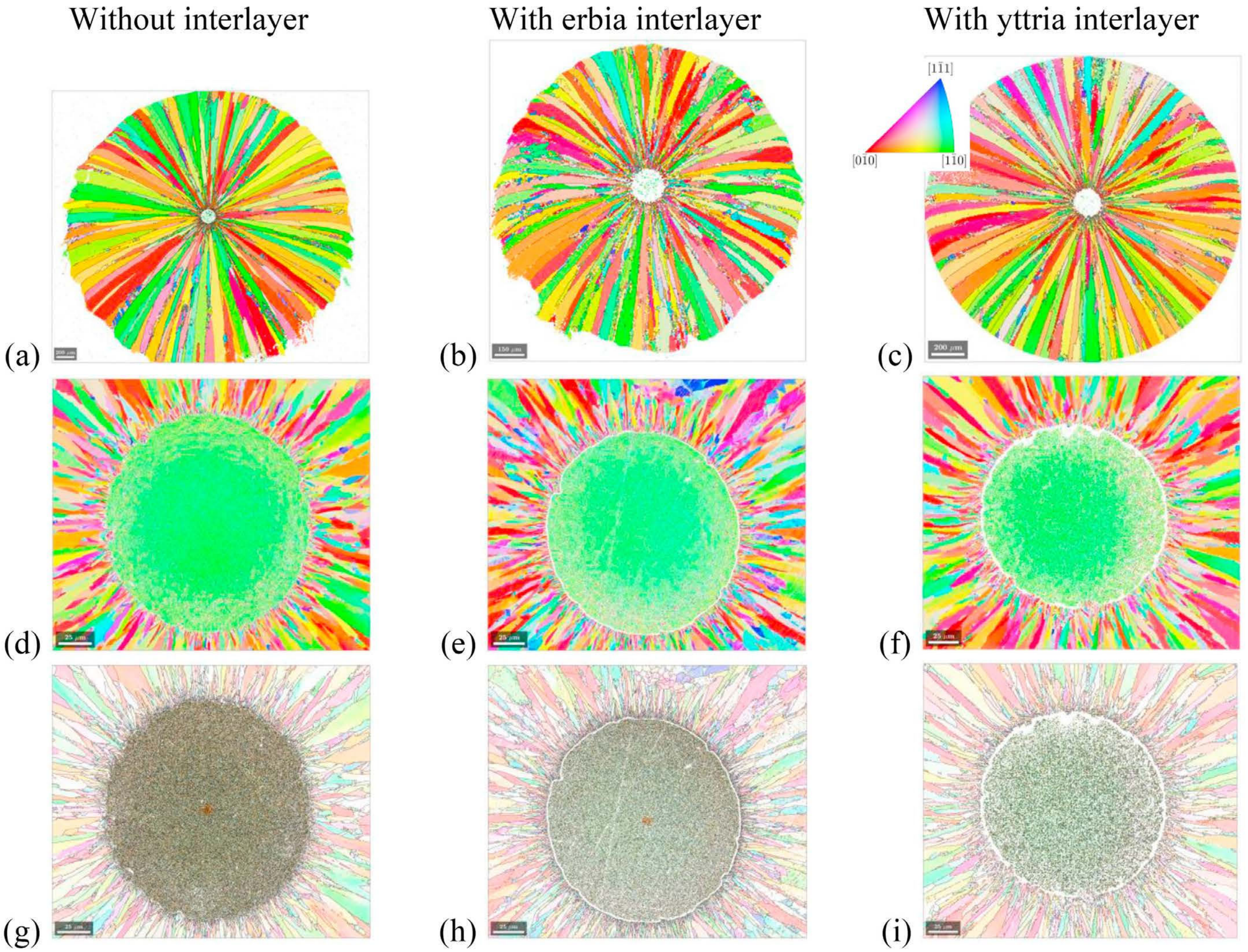

Fig. 3. Orientation maps obtained by EBSD on cross sections of single tungsten fiber-reinforced tungsten composites W_f/W with and without an oxide interlayer: left column (a,d,g) without any interlayer, center column (b,e,h) with erbia interlayer and right column (c,f,i) with yttria interlayer. (a-c) present large overview maps all obtained with a step size of 5 µm (but shown with different magnification), (d-i) smaller maps of the wire and its vicinity with a step size of 150 nm. The coloring reflects the crystallographic direction along the wire axis, corresponding to the inset in (c). Boundaries are highlighted in (a-c) and (g-i): High angle boundaries with disorientation angles above 15° in black and low angle boundaries with disorientation angles between 2° and 15° in light brown. In the boundary maps (g-i) the colors representing orientations are rendered transparent.

exhibit a perfect circular cross section. Several extrusion and intrusion can be clearly recognized.

A more detailed assessment of the as-processed microstructure is enabled by orientation mapping by means of EBSD. Fig. 3 shows orientation maps obtained on all three different types of single fiber W_f/W composite. Grains in the matrix are easily discerned. Obviously, these grains are elongated along the radial direction, i.e. the direction pointing outwards from the wire center in the cross sectional view. Their increasing width with distance from the center confirms the observation of wedge-shape grains in Fig. 2a.

All overview maps (Figs. 3a-c) reveal that with the small magnification chosen it becomes impossible to determine the orientation of tungsten grains in the wire. Almost none of the points in the wire could be properly indexed. This is different for the detailed maps obtained with higher magnification where a high indexing rate is achieved also for points in the wire. Most of the points in the wire appear green, revealing the preference for a crystallographic <110> direction along the wire axis as expected for a body centered cubic metal after wire drawing [36,37]. In the center maps of the specimens with an oxide interface (Fig. 3(e.f)), the position of the interlayer is clearly delineated by the presence of non-indexed points. (For determination of the phases and orientations present in the oxide layers, the conditions for recording ESBD patterns would have to be improved even further.) Contrarily, in the CVD matrix, different grains can be clearly distinguished from their different color (mainly red, yellow and green) revealing different crystallographic directions (from <100> to <110>, correspondingly) along the wire axis.

In order to reveal microstructural details quantitatively, disorientations between neighboring points are determined from the orientations gathered by EBSD and boundaries identified in the maps (Figs. 3(a-c) and (g-i)). For each indexed point, the upper and the left neighbors are considered, if they are indexed points as well. If the disorientation angle is above 2° the presence of a boundary is presumed. High angle boundaries (HABs) with disorientation angles above 15° are distinguished from low angle boundaries (LABs) with disorientation angles between 2° and 15°. Most of the identified boundaries in the outer regions of the matrix are aligned along the radial direction delineating clearly the wedge-shaped grains. Several of the grains, show a continuous increase in

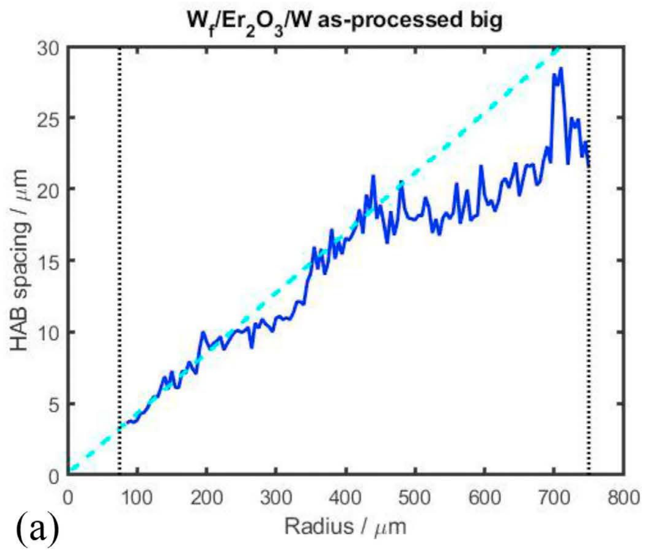

Fig. 4. High angle boundary spacing λ (according to eq. (2)) in dependence on the distance from the center of the wire for a tungsten fiber-reinforced tungsten composite with an erbia interlayer in the as-processed condition as obtained (a) from the overview map in Fig. 3b and (b) from the center map in Fig. 3h. The dotted, black lines represent the positions of the interlayer at a radius of 75 μm and the outer surface. The dashed, cyan lines are fits of a linear dependence of the HAB spacing on the radius in the CVD matrix. The dashed, black line in (b) illustrates the constant HAB spacing in the center of the wire.

width with increasing distance from the center and the boundary density decreases in the outer regions. Some of them have grown apparently through the entire deposition process of the CVD matrix. In the matrix regions in the vicinity of the wire, many smaller, not as elongated grains are observed and a radial alignment of the boundaries is not pronounced.

For characterizing the microstructure in dependence on the radial distance r from the wire center, all indexed points of a map in a ring with radius r and a width corresponding to the step size Δx are considered. Their number in an interval between r and $r + \Delta x$ are counted (N_{points}) as well as the number of high angle boundaries to their left (N_{left}) and upwards (N_{up}). The mean spacing between high angle boundaries along such a ring follows, consequently, as ratio between the perimeter length of the ring formed by indexed points (given by $N_{\text{points}}\Delta x$) and the total number of high angle boundaries

$$\lambda = \frac{N_{\text{points}}\Delta x}{N_{\text{left}} + N_{\text{up}}} \tag{2}$$

The relevance of the proposed evaluation procedure is illustrated for the as-processed condition of the tungsten fiber-reinforced tungsten composite with an erbia interlayer. For the large orientation map presented in Fig. 3b, quantitative analysis of the boundary spacing is only possible in the CVD matrix (i.e. for radii between 75 μm and 750 μm as seen in Fig. 4a) as points in the wire could not be indexed when acquiring the data with a large step size Δx of 5 μm and small magnification. On the other hand, when acquiring data with a finer step size Δx of 150 nm, the patterns could be more reliably indexed (in Fig. 3h) and orientation information in the wire, i.e. for radii below 75 μm, becomes available (cf. Fig. 4b).

Fig. 4a reveals that the HAB spacing in the CVD matrix depends almost linearly on the radius r, at least up to radii of 450 μm. In this region, the slope $\varphi = d\lambda/dr = 0.042 = 2.4^\circ$ of the curve in Fig. 4a is rather constant showing (i) that the number of HABs along a perimeter given by $2\pi/\varphi \approx 150$ is constant (confirming the earlier visual impression from the orientation maps) and (ii) that the number of grains does not increase with increasing radius. Instead, all grains grow out radially and develop a wedge shape covering in average an angle φ of 2.4° as reflected in the orientation map in Fig. 3b.

As obvious from Fig. 4a, the linear increase of the HAB spacing does not continue for radii above 450 μm. In this outer region, the emergence of additional grains can be identified by careful inspection of the orientation map in Fig. 3b. (Along the perimeter of a ring with radius 600 μm, for instance, about 200 high angle boundaries can be identified, i.e. substantially more than the constant number of 150 reported above along perimeters for radii below 450 μm.) The reason for the occurrence of further grains and the impeded azimuthal growth of the wedge-shaped grains might be either lateral growth of neighboring grains along the wire direction or local disturbances in the deposition process causing the formation of grains with new orientations.

As seen from Fig. 4b obtained from the more detailed orientation map of the center region (Fig. 3h), the linear dependence of the HAB spacing on the radius in the CVD matrix continues undisturbed to lower radii almost entirely towards the erbia interlayer. In the wire itself, the spacing between high angle boundaries with 0.42 μm is almost constant with possibly a slight decrease towards the wire edge. This is considered as an effect of heterogeneous deformation during wire drawing (from contact with the die) and not observed in all as-processed specimen. As noted earlier, the erbia interlayer is not exactly located at 75 μm around the entire perimeter, some intrusion and extrusions are seen. Due to these local deviations from cylindrical symmetry, information on the spacing between HABs gets averaged between matrix and wire in regions close to the interlayer.

Annealed condition Orientation maps from single fiber composites with an erbia interlayer after annealing for four different times up to 28 days are presented in Fig. 5. Marked differences to the as-processed condition in Fig. 3e and 3h are observed: larger grains (compared to the as-processed condition) can be identified in the orientation map after annealing on both sides of the interlayer. In particular, the very small, slightly elongated grains just outside the interlayer are replaced by larger grains which differ strongly in their morphology from both the grains they replaced and the grains further out. They are almost equiaxed and extend only slightly more along the radial direction than along the az-

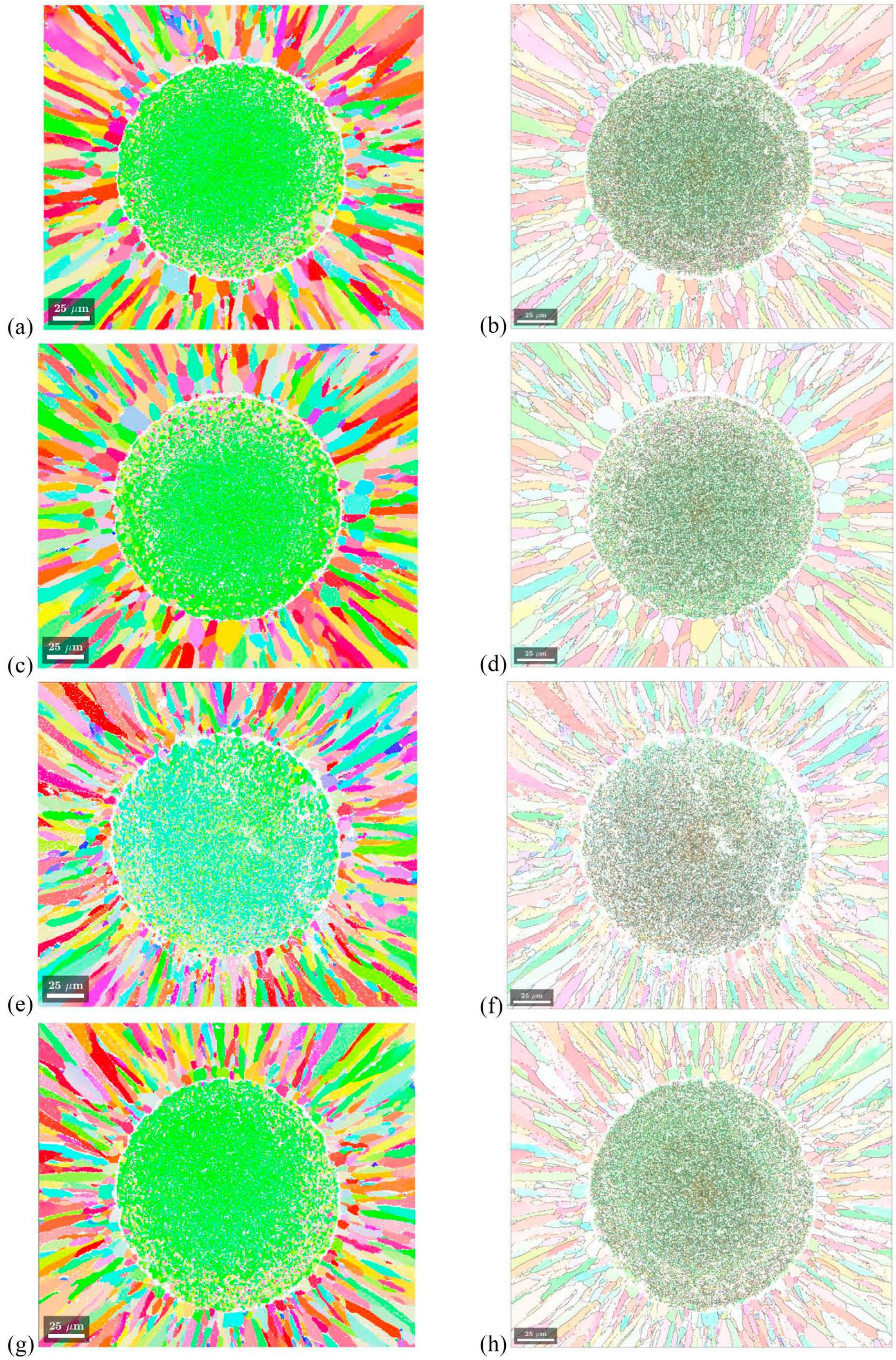

Fig. 5. Orientation maps of the wire and its vicinity obtained by EBSD with a step size of 500 nm on cross sections of single tungsten fiber-reinforced tungsten composites with an erbia interlayer after annealing at 1400 °C for different times: (a,b) 7 days, (c,d) 14 days, (e,f) 21 days and (g,h) 28 days. The coloring reflects the crystallographic direction along the wire axis, corresponding to the inset in (b). Boundaries are highlighted in the right column (b,d,f,h): High angle boundaries with disorientation angles above 15° in black and low angle boundaries with disorientation angles between 2° and 15° in light brown. In the boundary maps (b,d,f,h) the colors representing orientations are rendered transparent.

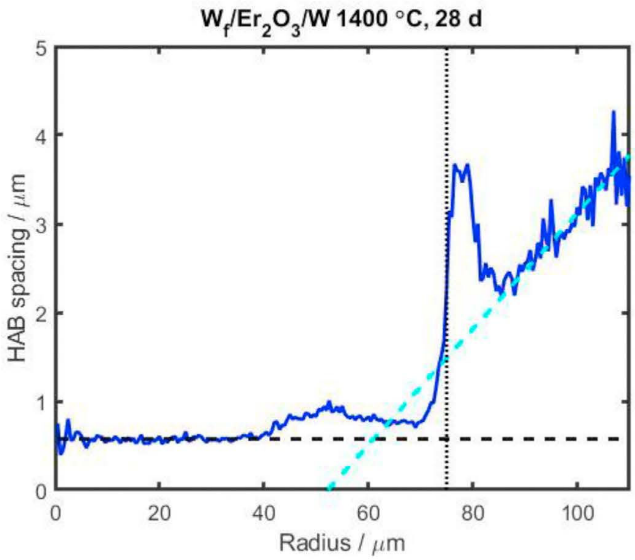

Fig. 6. High angle boundary spacing λ (according to eq. (2)) in dependence on the distance from the center of the wire for a tungsten fiber-reinforced tungsten composite with an erbia interlayer after annealing at 1400 °C for 28 days as obtained from the center map in Fig. 5h. The dashed, cyan line is a fit of a linear dependence of the HAB spacing on the radius in the outer regions of the CVD matrix. The dashed, black line illustrates the constant HAB spacing in the center of the wire. The dotted, black line represents the position of the interlayer at a radius of 75 μm.

imuthal direction. Obviously, they do neither reach the aspect ratios observed before annealing in that region close to the interlayer, nor the extreme ratios of the wedge-shaped grains still remaining in the outer regions.

Within the wire, small grains of slightly deviating orientation can be recognized by their yellow or lilac colors contrasting the dominant green color in the as-processed condition, indicating that the alignment of the crystallographic <110> direction with the wire axis is not as pronounced as before annealing. These newly emerging grains in the outer region of the wire are larger than the original fibrous grains in the as-processed condition as they are clearly revealed from the orientation map, despite its larger step size of 500 nm compared to the one (150 nm) of Fig. 2c. These emerging grains are considered to be free of defects and do not contain any deformation structures as neither LABs, nor color differences indicating disorientations within them are discerned.

These observations are further substantiated by determining the spacing between HABs in different distances from the wire center as shown for the single tungsten fiber-reinforced tungsten composites W_f/W with an erbia interlayer after annealing at 1400 °C for 28 days in Fig. 6.

From Fig. 6, the occurrence of a zone with large grains can be identified in the CVD matrix in the vicinity of the interlayer with grains much larger than in the as-processed condition, but still small compared to the wedge-shaped grains. From the HAB spacing profile obtained after annealing for 28 d at 1400 °C, a 10 μm wide large grain zone from the interlayer (at 75 μm) to a radius of about 85 μm becomes obvious. Within this zone, the HAB spacing increased from about 0.5 μm close to the interlayer in the as-processed condition to nearly 4 μm revealing the presence of much larger grains and a significant decrease in boundary density.

The observation of a second zone of larger grains within the wire is clearly supported by Fig. 6. For radii between 40 μm and 75 μm, an increased boundary spacing up to 1 μm is detected which is significantly larger than both, the one in the center of the wire (0.57 μm) and the one in the as-processed condition (0.42 μm). The slightly higher HAB spacing of 0.57 μm in the center of the wire (up to radii of 30 μm) compared to the as-processed condition (0.42 μm) is attributed to the slightly larger step size of 500 nm used which does not allow resolving boundary spacings smaller than 0.5 μm.

As seen in Fig. 5, the development of two zones (one in the matrix, the other in the wire) with larger grains than in the as-processed condition is observed – albeit to a different extent – in all single fiber composites with an erbia interlayer annealed for 7 d, 14 d, 21 d or 28 d.

The orientation maps of all three different types of single fiber composites (without any interlayer, with either an erbia or an yttria interlayer) after annealing at 1400 °C for 28 days in Fig. 7 reveal also two zones of larger grains developing in each composite. The development of these zones seems a universal behavior of all investigated single fiber composites, but the extent of the zones and their specific location depend on annealing time and the presence of an interlayer. While both single fiber composites with an oxide interlayer behave rather similar, the large grain zones appear strikingly different in the single fiber composite without any interlayer. This difference and its consequences will be discussed in more detail in Section 4.3.

4. Discussion

For an understanding of the annealing phenomena in the single tungsten fiber-reinforced tungsten composites it is essential to consider that the two different tungsten constituents are produced in a total different manner: tungsten wires are produced by large plastic deformation through wire drawing where an abundance of lattice defects becomes stored in the deformation structures. The chemically vapor deposited tungsten matrix, on the other hand, is deposited atom-by-atom so that almost perfect crystalline lattices are built containing only a small number of growth defects, mainly boundaries between differently oriented grains. In this manner, the stored energy density being the driving force for thermally activated restoration phenomena occurring during annealing is entirely different for both constituents. This essential difference forms the basis for an interpretation of the different processes occurring in these W_f/W composite during annealing.

4.1. Microstructure evolution in the wire

During plastic deformation by wire drawing, dislocations are formed in the drawn tungsten wires. They get stored in the deformation structure and form dislocation boundaries. Grains become elongated and aligned along the drawing direction; the resulting microstructure consists of fibrous grains showing a strong fiber texture. At elevated temperatures, this deformation structure will undergo restoration processes, in particular, recovery and recrystallization, to lower the energy stored in the defect content, mainly in form of dislocations and dislocation boundaries. As chemical vapor deposition of the tungsten matrix is performed at relatively low temperatures below 620 °C [30] (compared to the expected operation temperatures in fusion reactors and the annealing temperature of 1400 °C used in this study) occurrence of only slight recovery is expected during CVD and no recrystallization is observed. The microstructure of the wire in the as-processed condition resembles the expectations from the drawing process with very small grains (with a resolved boundary spacing of 0.42 μm) and a strong alignment of the <110> direction with the wire axis.

Significant changes are observed after isothermal annealing at 1400 °C: a zone of larger grains with average boundary spacing up to 1 μm develops in a certain distance from the wire center up to the wire edge. At the same time, the strong alignment of the <110> directions gets weaker. The resolved grains of slightly

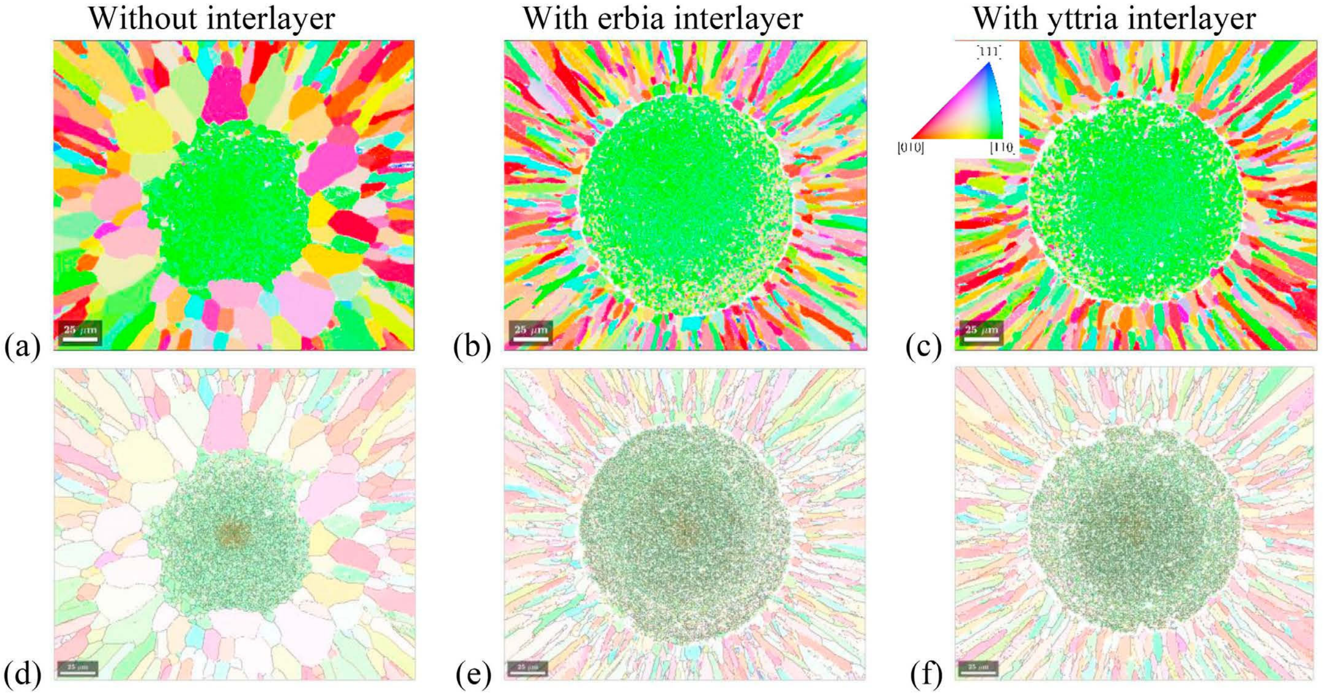

Fig. 7. Orientation maps of the wire and its vicinity obtained by EBSD with a step size of 500 nm on cross sections of single tungsten fiber-reinforced tungsten composites W_f/W with and without an oxide interlayer after annealing at 1400 °C for 28 days: left column (a,d) without any interlayer, center column (b,e) with erbia interlayer and right column (c,f) with yttria interlayer. The coloring reflects the crystallographic direction along the wire axis, corresponding to the inset in (c). Boundaries are highlighted in (d-f): High angle boundaries with disorientation angles above 15° in black and low angle boundaries with disorientation angles between 2° and 15° in light brown. In the boundary maps (d-f) the colors representing orientations are rendered transparent.

larger size might be the result of either primary recrystallization of the deformation structure by moving high angle boundaries or a process commonly referred to as *recrystallization in-situ* which is essentially extended recovery by subgrain growth [13]. Due to the strong texture with alignment of <110> directions along the wire axis in the deformation structure, deformed grains are quite often separated by low angle boundaries only, rendering a distinction between subgrains and grains somehow inapplicable. Nevertheless, occurrence of primary recrystallization by nucleation of new defect-free grains and migration of HABs (instead of *recrystallization in-situ*) seems more likely to be the occurring phenomenon due to the development of larger grains with new orientations in the wire. (The new defect-free grains with crystallographic directions along the wire axis deviating from <110> and without any internal disorientations were neatly revealed from the orientation maps.) Comparing the different microstructures after different times of annealing, it becomes obvious that the extension of the large grain zone in the wire is progressing towards the wire center. Contrarily, one gets the impression that recrystallized grains in the wire do neither prefer growing radially, nor grow much further at all during continued annealing after their initial formation. The latter observation is supported by the quantitative analysis in Fig. 6. For radii between 40 μm and the position of the interlayer, i.e. within the zone of large grains in the wire, the spacing between high angle boundaries varies only slightly between 0.75 μm and 1 μm.

This restricted growth of the recrystallized grains and absence of further grain coarsening might be a consequence of either orientation pinning within the wire or Zener pinning by potassium bubbles due to the doping of the wire: Due to the sharp texture of the drawn wire with <110> directions strongly aligned to the wire axis, a moving high angle boundary of a recrystallization nucleus may encounter a deformed grain with similar orientation, turn into low angle boundary and get pinned due its lower mobility [38]. Alternatively, the potassium bubbles purposely created during the manufacturing process by insoluble potassium restrict the motion of boundaries by Zener pining (cf. [26]) and hinder the further growth of recrystallized grains. Under the present annealing conditions, the recrystallized grains in the wire of the single fiber composites with an erbia interlayer may not have reached the critical grain size for overcoming boundary pinning by potassium bubbles [39]. Further quantitative analysis of the microstructural evolution along the outlined lines is required to clarify the details and planned for the future.

4.2. Microstructure evolution in the matrix

The microstructure of the chemically vapor deposited tungsten matrix does not contain any deformation-induced defects (as dislocation and dislocation boundaries which would cause orientation variations within the individual grains). Moreover, the as-deposited matrix consists of a grain structure with wedge-shaped grains along the radial deposition direction. In the vicinity of the erbia interlayer, the HAB spacing is small, almost comparable to the one in the wire. (The latter comparison must to be considered with caution as the chosen step size of the orientation maps may affect the quantitative result.) In the absence of a deformation structure neither recovery, nor recrystallization can occur. In case of recrystallization, not only the driving force is lacking, recrystallization nuclei cannot be formed from other lattice defects either. The only possible restoration process is grain growth driven by reduction of the energy stored in the grain boundaries themselves, i.e. grain coarsening [13,14].

After annealing at 1400 °C, the occurrence of rather large grains in the immediate vicinity of the oxide interlayer is observed. In the region between 75 μm and 85 μm, the boundary spacing increased from about 0.5 μm to 4 μm during 28 h of annealing. This exceptional increase in boundary spacing by a factor 8 outperforms clearly the observed increase in regions further out, e.g. at around a radius of 100 μm the boundary spacing increased from 1.8 μm to 2.8 μm, i.e. by a factor 1.5 only.

Further out in the matrix beyond the large grain zone, no major changes in the microstructure due to annealing at 1400 °C are seen. For instance, the HAB spacing and its dependence on the radius as described by the slope φ remains almost unaltered. This is in accordance with several investigations on the lateral growth of columnar grains in CVD tungsten where very little growth was reported for annealing at 1520 °C for 100 h [40] or at 1500 °C for 3 h [41].

The major difference in grain growth in the vicinity of the interlayer and regions further out in the matrix is caused by the peculiar microstructure after deposition. In the outer regions of the CVD matrix, the boundary density and hence the driving force for grain growth is rather low. Additionally, the wedge shaped grains separated by relatively long and straight boundary segments render curvature-driven grain growth by motion of triple junctions rather slow (due to the absence of both, curved boundaries and triple junctions), if not impossible.

On the other hand, the higher boundary densities closer to the interlayer exert a higher driving force for restoration due to the higher stored energy density. Grains in the vicinity of the interlayer are not extremely elongated as those further out and possess a growth advantage due to their morphology. Initially, some grains in that region start to grow at the expense of their neighbors and gain a slight size advantage. Due to the microstructure consisting of wedge-shaped grains even a slightly larger azimuthal size of some grains will turn into a growth advantage: the mobile growth front along a perimeter will border more radially aligned boundaries (of wedge-shaped grains) on the outside than on the inside. The growth front will continue to move outwards due to the slightly larger azimuthal grain size and slightly lower boundary density behind. In this manner, some grains can get a decisive growth advantage and will be able to undergo exceptional growth. The process does not proceed in a homogeneous manner and should not be considered as homogeneous grain coarsening or normal grain growth. Due to the growth advantage of a few grains in the microstructure, the process must rather be envisaged as abnormal grain growth (also termed secondary recrystallization) [42] with a few exceptionally growing grains. If wedge-shaped grains on the outside of the growth front are replaced by abnormally growing wedge-shaped grains an existing growth advantage will prevail during growth and abnormally growing grains are expected to continue to grow radially without limitation.

4.3. Microstructure evolution at the interlayer

Extrusion and intrusions were observed from secondary electron images and the orientation maps for oxide interlayers as well as the interface between wire and matrix in the absence on an interlayer. These deviations of the wire from a cylindrical shape are inherited from the manufacturing process. During wire drawing, geometrical imperfections of the die (or alien material deposited at the surface) result in drawing grooves on the wire surface. This commonly undesired drawing scars may actually have positive effects on the mechanical behavior of tungsten-fiber reinforced tungsten composites as grooves increase the surface area between wire and matrix and hence the energy required for relative motion between wire and matrix, if the cohesion between both is not impeded otherwise.

The presence of an interlayer plays a decisive role for the development of the two zones of large grains during annealing: For the composites with an interlayer, the wire region can be clearly distinguished from the matrix region by the presence of the non-indexed interlayer in Figs. 7(b-c). The two large grain zones are clearly separated by the erbia or yttria interlayers and in general no growth of grains from the large grain zone in the matrix into the wire is observed. Only at certain locations where the erbia or yttria interlayer seems disrupted, larger grains from the matrix have seemingly invaded the wire region. In some occasions where in-growth is observed and the interlayer seems to be still in place, it is believed that in-growth occurred through holes in the interface at a different depth in the specimen. Such imperfections in the rare-earth oxide interlayers might originate from the magnetron sputtering process occurring in two steps to coat the entire wire (such imperfections are revealed by tungsten bridges from wire to matrix through yttria interlayers [43]) or formed during annealing by disintegration of the interlayer (the latter being frequently observed for yttria interlayers and much less for erbia interlayers [43]).

The single fiber composite without an interlayer shows an entirely different behavior (cf. Figs. 7a): After annealing the original interface between matrix and wire cannot be located any longer. Two zones with large grains have developed in the wire and matrix, respectively, but extraordinarily large grains have invaded the wire. Grains growing abnormally in the tungsten matrix must have achieved such an enormous size advantage (above a critical size for effective Zener pining), that they are able to grow into outer parts of the wire at the expense of the recrystallized grains (in the large grain zone there) despite the inhibition of the boundary motion by the potassium bubbles. It becomes obvious from Fig. 7a, that these abnormally growing grains become much larger than the ones in the composites with an interlayer in Figs. 7(b-c). With further annealing time, it can expected that the abnormally growing grains will invade the tungsten wire entirely. As a consequence, the benefit of the tungsten wires on the improved mechanical properties of the fiber-reinforced composite will be lost, not only due to the removal of the deformation structure in the wire, but also due to the complete removal of any interface between wire and matrix. While embrittlement of the wire by recrystallization may not impede the pseudo-ductility significantly [30], the loss of any debonding capability due to the loss of an interface will be detrimental. A protective interlayer between wire and matrix is therefore of uttermost importance for preserving the tungsten wires in the composite – even if they undergo recrystallization.

5. Conclusions and outlook

As a model system for more complex tungsten fiber-reinforced tungsten composites, single fiber composites containing a single drawn potassium-doped tungsten wire in a chemically vapor deposited tungsten matrix are investigated. The thermal stability of three different systems with or without an erbia or yttria interlayer is characterized. During annealing at 1400 °C for up to 28 d, two rather different zones develop both showing much larger grains than in the as-processed condition. As indicated by subtle, but notable orientation changes, new defect-free grains (without any deformation structure or internal orientation variations) form in the wire by primary recrystallization through nucleation of defect-free grains and boundary migration. These emerging grains are larger than in the drawn state, but their growth seems limited to a certain size by either orientation pinning or pinning at potassium bubbles. Suppression of further growth of the recrystallized grains by Zener pinning would indicate that potassium bubbles which might have grown to larger sizes [44] are still persisting in the wire. In the CVD matrix, grains in the vicinity of the interlayer with moderate aspect ratios grow abnormally at the expense of others leading to a corona of (almost) equiaxed grains. The wedge-shaped grains in the further distant parts of the matrix are only slightly affected by the heat treatment.

The rare earth oxide interlayers provide an effective barrier for separating the restoration process occurring in both parts: primary recrystallization in the wire and abnormal grain growth (or secondary recrystallization) in the matrix. The motion of grain boundaries is blocked by the alien phase as long as the interlayer remains intact and no pathways between the two different parts exist. Without the presence of such an interlayer, the restoration processes in both regions occur coupled and grains of the matrix having achieved a major size advantage there start to grow into the recrystallized outer regions of the wire without an oxide phase preventing their growth and seemingly without effective boundary pinning by potassium bubbles due to their size. In this manner, the presence of an oxide interlayer between the wire and the CVD matrix is indispensable for the thermal stability of W_f/W composites. The potassium-doped wire can only retain its superior thermal stability if shielded from the CVD matrix by an interlayer and no intergrowth occurs.

Data availability

The raw/processed data required to reproduce these findings cannot be shared at this time as the data also forms part of an ongoing study.

Declaration of competing interest

None

CRediT authorship contribution statement

Umberto M. Ciucani: Methodology, Software, Validation, Formal analysis, Investigation, Data curation, Writing - original draft, Writing - review & editing, Visualization, Supervision. **Lea Haus:** Investigation, Formal analysis, Writing - review & editing. **Hanns Gietl:** Resources, Writing - review & editing. **Johann Riesch:** Resources, Writing - review & editing. **Wolfgang Pantleon:** Conceptualization, Methodology, Software, Formal analysis, Resources, Writing - review & editing, Visualization, Supervision, Project administration, Funding acquisition.

Acknowledgements

This work has been carried out partially within the framework of the EUROfusion Consortium and has received funding from the Euratom research and training programme 2014-2018 and 2019-2020 under grant agreement No 633053. The views and opinions expressed herein do not necessarily reflect those of the European Commission.

Supplementary materials

Supplementary material associated with this article can be found, in the online version, at doi:10.1016/j.jnucmat.2020.152579.

Reference

[1] F. Romanelli, EFDA, Fusion Electricity: a roadmap to the realisation of fusion energy, (2012) 1–75. ISBN 978-3-00-040720-8.
[2] J.H. You, E. Visca, C. Bachmann, T. Barrett, F. Crescenzi, M. Fursdon, H. Greuner, D. Guilhem, P. Languille, M. Li, S. McIntosh, A.V. M.üller, J. Reiser, M. Richou, M. Rieth, European DEMO divertor target: operational requirements and material-design interface, Nucl. Mater. Energy 9 (2016) 171–176, doi:10.1016/j.nme.2016.02.005.
[3] J.W. Davis, V.R. Barabash, A. Makhankov, L. Plöchl, K.T. Slattery, Assessment of tungsten for use in the ITER plasma facing components, J. Nucl. Mater. 258–263 (1998) 308–312, doi:10.1016/S0022-3115(98)00285-2.
[4] E. Lassner, W.-.D. Schubert, Tungsten: Properties, Chemistry, Technology of the Element, Alloys, and Chemical Compounds, 1st Ed., Springer, Boston, MA, 1999, doi:10.1007/978-1-4615-4907-9.
[5] R.G. Abernethy, Predicting the performance of tungsten in a fusion environment: a literature review, Mater. Sci. Technol 0836 (2016) 1–12, doi:10.1080/02670836.2016.1185260.
[6] E.E. Bloom, R.W. Conn, J.W. Davis, R.E. Gold, R. Little, K.R. Schultz, D.L. Smith, F.W. Wiffen, Low activation materials for fusion applications, J. Nucl. Mater. 122 (1984) 17–26, doi:10.1016/0022-3115(84)90570-1.
[7] B. Gludovatz, S. Wurster, A. Hoffmann, R. Pippan, Fracture toughness of polycrystalline tungsten alloys, Int. J. Refract. Met. Hard Mater 28 (2010) 674–678, doi:10.1016/j.ijrmhm.2010.04.007.
[8] D. Rupp, R. Mönig, P. Gruber, S.M. Weygand, Fracture toughness and microstructural characterization of polycrystalline rolled tungsten, Int. J. Refract. Met. Hard Mater 28 (2010) 669–673, doi:10.1016/j.ijrmhm.2010.05.006.
[9] D. Rupp, S.M. Weygand, Experimental investigation of the fracture toughness of polycrystalline tungsten in the brittle and semi-brittle regime, J. Nucl. Mater. 386–388 (2009) 591–593, doi:10.1016/j.jnucmat.2008.12.184.
[10] B. Gludovatz, S. Wurster, T. Weingartner, A. Hoffmann, R. Pippan, Influence of impurities on the fracture behaviour of tungsten, Philos. Mag 91 (2011) 3006–3020, doi:10.1080/14786435.2011.558861.
[11] P. Schade, 100 years of doped tungsten wire, Int. J. Refract. Met. Hard Mater (2010) 648–660, doi:10.1016/j.ijrmhm.2010.05.003.
[12] C. Bonnekoh, A. Hoffmann, J. Reiser, The brittle-to-ductile transition in cold rolled tungsten: on the decrease of the brittle-to-ductile transition by 600 K to − 65 °C, Int. J. Refract. Met. Hard Mater 71 (2018) 181–189, doi:10.1016/j.ijrmhm.2017.11.017.
[13] F. Haessner, Systematic survey and basic problems of recrystallization, in: Recryst. Met. Mater., Riederer Verlag GmbH, 1978, pp. 1–10.
[14] F.J. Humphreys, M. Hatherly, Recrystallization and Related Annealing Phenomena, Elsevier B.V., 2004, doi:10.1016/b978-0-08-044164-1.x5000-2.
[15] A. Alfonso, D. Juul Jensen, G.N. Luo, W. Pantleon, Recrystallization kinetics of warm-rolled tungsten in the temperature range 1150-1350 °C, J. Nucl. Mater. 455 (2014) 591–594, doi:10.1016/j.jnucmat.2014.08.037.
[16] A. Alfonso, D. Juul Jensen, G.N. Luo, W. Pantleon, Thermal stability of a highly-deformed warm-rolled tungsten plate in the temperature range 1100-1250 °C, Fusion Eng. Des 98–99 (2015) 1924–1928, doi:10.1016/j.fusengdes.2015.05.043.
[17] U. Ciucani, W. Pantleon, Stagnant recrystallization in warm-rolled tungsten in the temperature range from 1150 °C to 1300 °C, Fusion Eng. Des (2019), doi:10.1016/j.fusengdes.2019.01.088.
[18] U.M. Ciucani, A. Thum, C. Devos, W. Pantleon, Isothermal annealing of thin rolled tungsten plates in the temperature range from 1300 °C to 1400 °C, Nucl. Mater. Energy 15 (2018), doi:10.1016/j.nme.2018.03.009.
[19] U.M. Ciucani, A. Thum, C. Devos, W. Pantleon, Recovery and recrystallization kinetics of differently rolled, thin tungsten plates in the temperature range from 1325 °C to 1400 °C, Nucl. Mater. Energy 20 (2019) 100701, doi:10.1016/j.nme.2019.100701.
[20] C. Bonnekoh, U. Jäntsch, J. Hoffmann, H. Leiste, A. Hartmaier, D. Weygand, A. Hoffmann, J. Reiser, The brittle-to-ductile transition in cold rolled tungsten plates: impact of crystallographic texture, grain size and dislocation density on the transition temperature, Int. J. Refract. Met. Hard Mater 78 (2019) 146–163, doi:10.1016/j.ijrmhm.2018.09.010.
[21] P. Lied, C. Bonnekoh, W. Pantleon, M. Stricker, A. Hoffmann, J. Reiser, Comparison of K-doped and pure cold-rolled tungsten sheets: as-rolled condition and recrystallization behaviour after isochronal annealing at different temperatures, Int. J. Refract. Met. Hard Mater 85 (2019), doi:10.1016/j.ijrmhm.2019.105047.
[22] Y. Mutoh, K. Ichikawa, K. Nagata, M. Takeuchi, Effect of rhenium addition on fracture toughness of tungsten at elevated temperatures, J. Mater. Sci. 30 (1995) 770–775, doi:10.1007/BF00356341.
[23] S. Wurster, B. Gludovatz, A. Hoffmann, R. Pippan, Fracture behaviour of tungsten-vanadium and tungsten-tantalum alloys and composites, J. Nucl. Mater. 413 (2011) 166–176, doi:10.1016/j.jnucmat.2011.04.025.
[24] M. Battabyal, R. Schäublin, P. Spätig, N. Baluc, W-2wt.%Y 2O 3 composite: microstructure and mechanical properties, Mater. Sci. Eng. A 538 (2012) 53–57, doi:10.1016/j.msea.2012.01.011.
[25] M.V. A.guirre, A. Martín, J.Y. Pastor, J. Llorca, M.A. Monge, R. Pareja, Mechanical properties of Y2O3-doped W-Ti alloys, J. Nucl. Mater. 404 (2010) 203–209, doi:10.1016/j.jnucmat.2010.07.016.
[26] C.S. Smith, Grains, phases, and interfaces - An interpretation of microstructure, Trans. Am. Inst. Min. Metall. Eng 175 (1948) 15–51.
[27] J. Du, T. Höschen, M. Rasinski, S. Wurster, W. Grosinger, J.H. You, Feasibility study of a tungsten wire-reinforced tungsten matrix composite with ZrOx interfacial coatings, Compos. Sci. Technol 70 (2010) 1482–1489, doi:10.1016/j.compscitech.2010.04.028.
[28] J. Riesch, T. Höschen, C. Linsmeier, S. Wurster, J.H. You, Enhanced toughness and stable crack propagation in a novel tungsten fibre-reinforced tungsten composite produced by chemical vapour infiltration, Phys. Scr 2014 (2014) 014031, doi:10.1088/0031-8949/2014/T159/014031.
[29] H. Gietl, J. Riesch, J.W. Coenen, T. Höschen, C. Linsmeier, R. Neu, Tensile deformation behavior of tungsten fibre-reinforced tungsten composite specimens in as-fabricated state, Fusion Eng. Des 124 (2017) 396–400, doi:10.1016/j.fusengdes.2017.02.054.
[30] J. Riesch, J.Y. Buffiere, T. Höschen, M. Scheel, C. Linsmeier, J.-.H. You, Crack bridging in as-fabricated and embrittled tungsten single fibre-reinforced tungsten composites shown by a novel in-situ high energy synchrotron tomogra-

phy bending test, Nucl. Mater. Energy 15 (2018) 1–12, doi:10.1016/j.nme.2018.03.007.

[31] R. Neu, J. Riesch, J.W. Coenen, J. Brinkmann, A. Calvo, S. Elgeti, C. García-Rosales, H. Greuner, T. Hoeschen, G. Holzner, F. Klein, F. Koch, C. Linsmeier, A. Litnovsky, T. Wegener, S. Wurster, J.H. You, Advanced tungsten materials for plasma-facing components of DEMO and fusion power plants, Fusion Eng. Des 109–111 (2016) 1046–1052, doi:10.1016/j.fusengdes.2016.01.027.

[32] R. Neu, J.W. Coenen, C. Linsmeier, T. Höschen, M. Li, R. Neu, Chemically deposited tungsten fibre-reinforced tungsten – The way to a mock-up for divertor applications, Nucl. Mater. Energy 9 (2016) 75–83, doi:10.1016/j.nme.2016.03.005.

[33] J. Du, J.H. You, T. Höschen, Thermal stability of the engineered interfaces in W/f/W composites, J. Mater. Sci. 47 (2012) 4706–4715, doi:10.1007/s10853-012-6339-9.

[34] F. Bachmann, R. Hielscher, H. Schaeben, Texture analysis with MTEX- Free and open source software toolbox, in: Solid State Phenom., Trans Tech Publications Ltd, 2010, pp. 63–68. 10.4028/www.scientific.net/SSP.160.63.

[35] P. Zhao, J. Riesch, T. Höschen, J. Almanstötter, M. Balden, J.W. Coenen, R. Himml, W. Pantleon, U.von Toussaint, R. Neu, Microstructure, mechanical behaviour and fracture of pure tungsten wire after different heat treatments, Int. J. Refract. Met. Hard Mater 68 (2017) 29–40, doi:10.1016/j.ijrmhm.2017.06.001.

[36] E.S. Meieran, D.A. Thomas, Structure of drawn and annealed tungsten wire, Trans. Metall. Soc. Aime 233 (1965) 937.

[37] A. Barna, I. Gaal, O. Geszti-Harkner, G. Radnoczi, L. Uray, The fibre structure of K-Si-Al doped tungsten wires, High Temp. - High Press 10 (1978) 197–205.

[38] D. Juul Jensen, Effects of orientation on growth during recrystallization, in: Microstruct. Crystallogr. Asp. Recryst. (16th Risø Int. Symp., 1995, pp. 119–137.

[39] F.J. Humphreys, A unified theory of recovery, recrystallization and grain growth, based on the stability and growth of cellular microstructures. 2. The effect of second-phase particles, Acta Mater 45 (1997) 5031–5039.

[40] Y.T. Auck, J.G. Byrne, Grain growth of chemical vapour deposited tungsten-22 wt% rhenium alloy, J. Mater. Sci (1973) 559–564.

[41] Y. Lian, F. Feng, J. Wang, X. Liu, J. Song, Y. Wang, Z. Chen, J. Chen, No Effect of high temperature annealing on the microstructure and thermal shock resistance of tungsten coatings grown by chemical vapor deposition, J. Nucl. Mater. 513 (2019) 241–250, doi:10.1016/j.jnucmat.2018.11.006.

[42] K. Detert, Secondary recrystallization, in: Recryst. Met. Mater., 2nd ed., Riederer Verlag GmbH, 1978, pp. 97–109.

[43] H. Gietl, Weiterentwicklung von wolframfaserverstärktem Wolframverbundwerkstoff für den Einsatz in der Fusion, Technical Univeristy of Munich, 2018.

[44] P. Schade, Potassium bubble growth in doped tungsten, Int. J. Refract. Met. Hard Mater 16 (1998) 77–87.

6.2.2 Further analysis

Upon annealing of all W_fW, a ring of coarse, almost equiaxed grains around the drawn wire formed. The presence of these coarse grains indicates the occurrence of restoration processes during annealing; they have replaced the small, slightly elongated grains of almost random orientation observed in the acicular zone just outside the perimeter of the wire in the as-received state (Figure 60 and Figure 63). Comparison of the different annealed conditions reveals that in general the longer the annealing time, the wider the coarse grain region becomes. A detailed analysis of the annealed condition at 1400 °C, as compared to the as-received one for the W_f/W and $W_f/Er_2O_3/W$ type is described in Ref. [53] (see Section 6.2.1). The ring of nearly-equiaxed grains developed upon annealing was termed Large Grain Zone (LGZ) and its evolution tracked with respect to annealing time. In Figure 63 the orientation map in the vicinity of the drawn wire of the single W_f/W without any interlayer after annealing at 1400 °C for seven days is shown. Three circles are present, delimiting two different zones, the inner LGZ (between the cyan and the blue rings) and the outer LGZ (between the cyan and the pink circles). These circles were determined by analysis of both the HABs and LABs boundary spacings in dependence of the radius from the center of the fiber (red mark). Within individual rings of rather small width (corresponding to the step size of 500 nm) around the fiber center (shown as red mark in Figure 63), the boundary spacing between all types of boundaries (i.e. high angle boundaries (HABs) with disorientation angles above 15° as well as low angle boundaries (LABs) with disorientation angles between 2° and 15°) was evaluated [113]. The boundary spacing as a function of the distance from the centre of the wire is shown in Figure 64 and a sharp increase – to 8 µm – followed by a decrease in the boundary spacing can be seen and corresponds to the LGZ. The dashed lines represent fits in the different ranges used to determine the borders of the LGZs, e.g. between 65 µm and 85 µm. The intersection of the blue and the cyan dashed line determines the outer border of the outer LGZ (pink ring) whether the intersection between the blue and the red the inner border of the outer LGZ (cyan ring). At smaller distances from the center a positive deviation from the constant boundary spacing (green dashed line) of the first 45 µm can be seen. The whole range of this deviation up to the crossing point between the green and the red lines (the inner radius of the outer LGZ) is considered the inner LGZ. In this manner, an objective definition of the position of all borders of the large grain zones is achieved and its evolution with annealing time evaluated and shown in Figure 65.

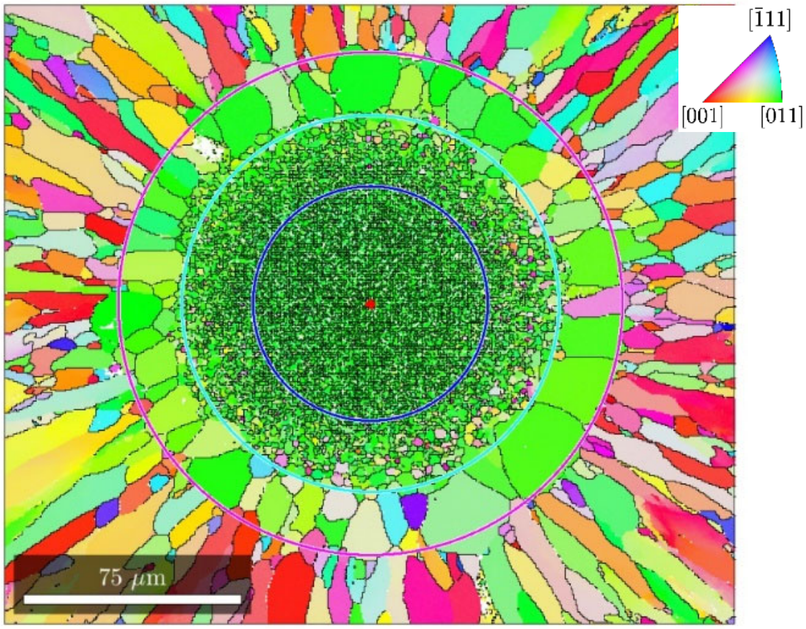

Figure 63: Orientation map in the vicinity of the drawn wire of the single W_f/W without any interlayer after annealing at 1400 °C for seven days. The blue circle highlights the inner, inner LGZ radius, in cyan the outer, inner LGZ radius and in pink the outer, outer LGZ radius. The colors are showing the crystallographic directions along the z-direction colored according to the inset.

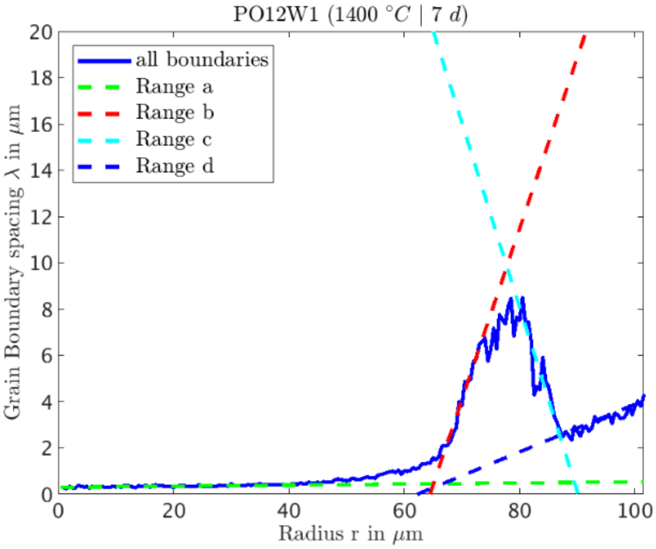

Figure 64: Dependence of the boundary spacing on the radius to determine the ranges of the inner and outer LGZs.

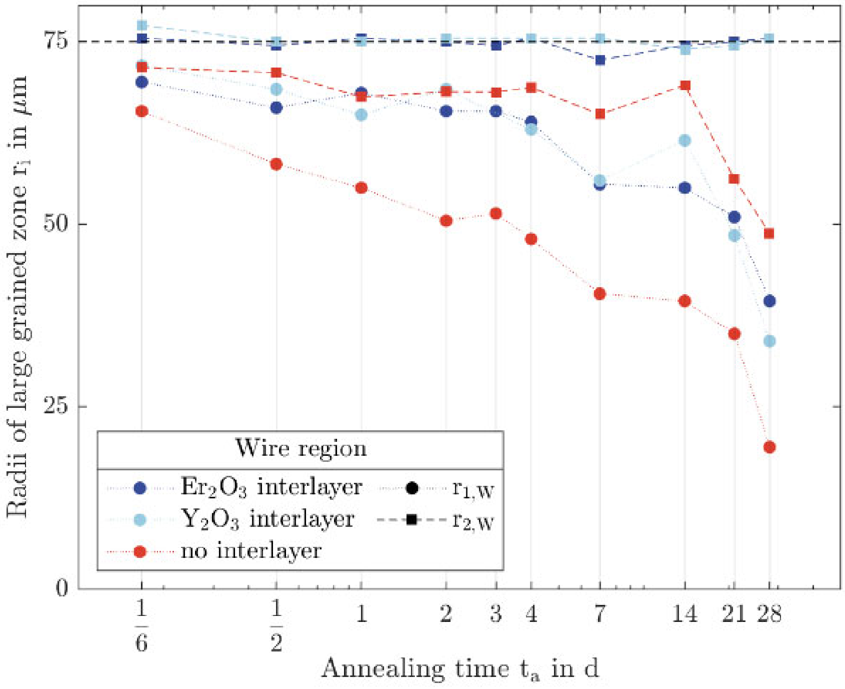
Radii of large grained zone r_i in μm
75
50
25
0
Wire region
Er_2O_3 interlayer
Y_2O_3 interlayer
no interlayer
$r_{1,W}$
$r_{2,W}$
$\frac{1}{6}$
$\frac{1}{2}$
1
2
3
4
7
14
21
28
Annealing time t_a in d

a)

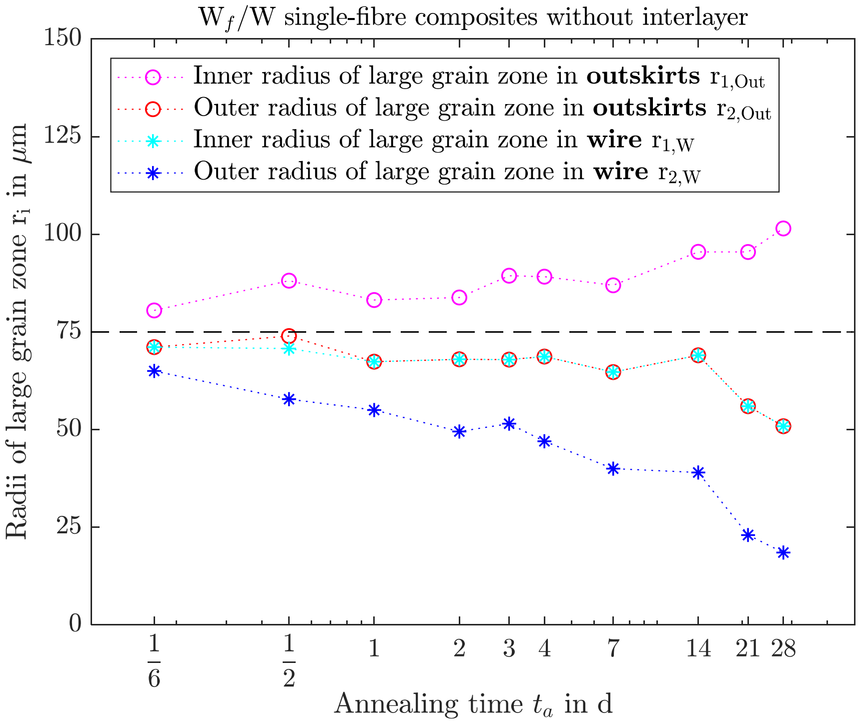
W_f/W single-fibre composites without interlayer
Inner radius of large grain zone in **outskirts** $r_{1,Out}$
Outer radius of large grain zone in **outskirts** $r_{2,Out}$
Inner radius of large grain zone in **wire** $r_{1,W}$
Outer radius of large grain zone in **wire** $r_{2,W}$
Radii of large grain zone r_i in μm
150
125
100
75
50
25
0
$\frac{1}{6}$
$\frac{1}{2}$
1
2
3
4
7
14
21
28
Annealing time t_a in d

b)

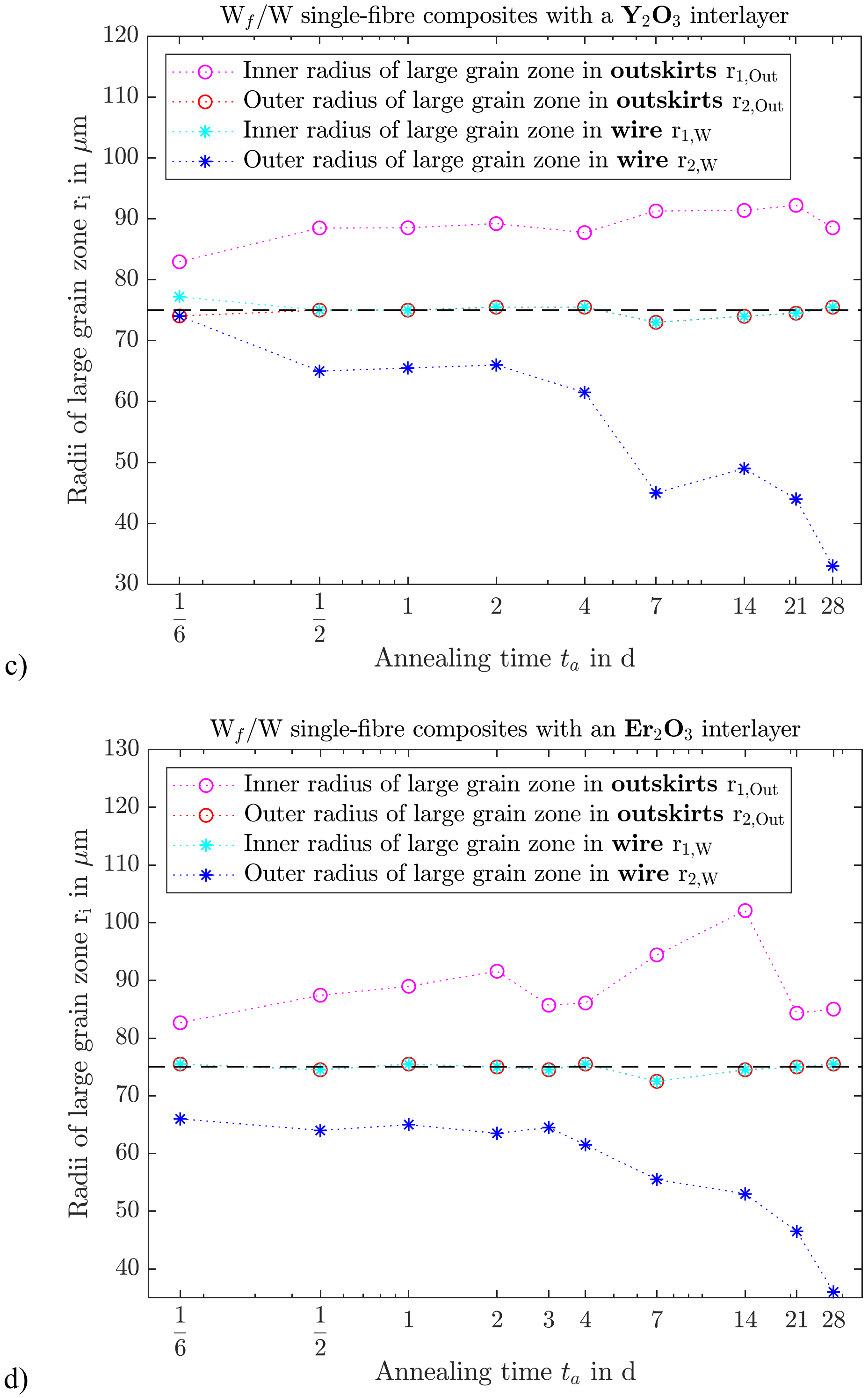

Figure 65: Positions and widths of the large grain zones for the single W_f/W upon annealing at 1400 °C from 6 hours to 28 days.

Figure 65 reports the findings for the positions and the widths of the large grain zones for the single W_f/W. In Figure 65a, as the annealing time increases, the inner border of the inner LGZ moves further and further towards the center of the wire. The deformation structure is altered most likely by recrystallizing grains that are larger compared to the one in the deformed core, but still relatively small compared to the grains in the outer LGZ. From Figure 65a is clear that the progress of the primary recrystallization front without any interlayer towards the inside is much faster, than in the presence of either an yttria or an erbia interlayer; both oxide interlayers apparently retard the recrystallization process in a similar manner.

The outer large grain zone forms dominantly in the CVD matrix where there is neither any deformation structure as in the drawn wire, nor any driving force for primary recrystallization. Consequently, formation of exceptionally large grains in that zone must occur by abnormal grain growth. The abnormal growth of the grains in this zone is associated with the growth of the zone itself. Without an interlayer, a continued outward growth of the outer LGZ is observed (in Figure 65b), whereas in the presence of an oxide interlayer no pronounced growth occurs after the initial formation of large grains. As seen in Figure 65c and Figure 65d, the outer LGZs are established already after short-term annealing and their outer border at about 85 µm does not move much further with further annealing. The border between the inner and the outer large grain zones does not move at all due to the presence of the oxide interlayer. This is significantly different from the composite without an interlayer as seen from Figure 65b. In the latter case, the border between the outer and inner large grain zone is constantly moving towards the center of the wire, replacing the relatively small grains after recrystallization by much larger, abnormally grown grains from the outer large grain zone.

For the moment being such a preliminary work proves W_fW to be very promising for application as PFM in fusion reactors. Work is still along the way to fully characterize the behavior of these composites in hot environments, given that higher temperatures are to be expected in fusion reactors, besides short plasma instabilities. At the time of writing this thesis, it is actually planned further isothermal experiments shall be performed at even higher temperatures to further characterize the material at the interface, but also to characterize the kinetics of grain growth in the acicular zone.

Chapter 7. Conclusions and Outlook

The investigation of the thermal stability of different tungsten plates and W_fW was the aim of this work, in order to assess their behavior at operational temperatures in fusion reactors as PFMs. Isochronal and isothermal annealing experiments at different temperatures were performed up to complete primary recrystallization. The microstructural evolution during annealing was tracked by both Vickers hardness testing and electron backscatter diffraction. Well-established kinetic models for recovery and recrystallization allowed a concise description of the observed hardness evolution for the TPs. The stagnation in the evolution of recrystallization which prevented an analysis via the JMAK model, called for a deeper study to understand the reasons for such a halting since inhibition or delaying of recrystallization is craved for PFMs. The microstructural path method demonstrated to be useful in providing insights about the microstructural evolution during annealing of the W80 plate, against a hardness evolution showing stagnation. Tracking of the boundary spacing at the interface between the tungsten fibres and the CVD tungsten matrix in W_fW allowed the understanding of the coupled recrystallization and grain growth therein.

The obtained kinetic parameters for the different phenomena in the TPs are consistent with the expectations from the amount of plastic deformation from processing, with exception of one plate, the TP1, deviating from these expectations for which a mistakengly lowered amount of deformation was suggested. Description of recovery using Kuhlmann's model showed a linear dependence of the recovery coefficient A on the hardness loss during recovery. Analysis of the kinetics of recrystallization via the JMAK model yielded Avrami exponents equal to 2, a nucleation and growth coefficient *b* and incubation time, dependent on the work-hardening experienced by the plates as expressed by the as-received hardness and resulted in a lower activation energy for recrystallization for the two plates which underwent larger work-hardening. Correlations between the hardness loss due to recovery and the recovery coefficient A or the nucleation and growth coefficient *b* indicate the paramount role of the microstructure and the stored energy in determining the character of the annealing behavior rather than the thickness of the plate. The obtained activation energies were comparable to the activation energy of self-diffusion in tungsten for the TP 2 and TP 1, and to the activation energy of grain boundary diffusion in tungsten for the TP 0.5 and TP 0.2. Such an analysis of the kinetics allowed the extrapolation of service temperatures for a desired time of 2 and 5 years as plasma-facing components in service as divertor and first wall respectively. The TPs are expected to sustain temperatures in the range 1000 °C – 1100 °C for a 2 years operation time before half of the volume undergoes recrystallization, ignoring neutral particle bombardment. Such a range is sufficient for application of the TPs as first wall material but is too low for use as divertor material. An analysis of the thermal stability of pure thin tungsten plates in terms of the kinetics of the restoration processes via JMAK and Kuhlmann's models was unprecedented in literature. Deepened understanding of the microstructural restauration phenomena in such tungsten materials is of utmost importance for the fusion materials community: the findings in this work will serve as additional information to further improve solutions aiming at more thermally stable rolled products.

The annealing behavior of a tungsten plate warm-rolled to 80 % thickness reduction (W80) as characterized by hardness evolution showed intervals of stagnation at a recrystallized volume fraction of 60 %. During long periods of time, no hardness changes, nor progress of recrystallization were observed. Such a halt deems the W80 plate more suitable for application as armor material than the inferred activation energy of 548 kJ/mol as extrapolated from the times to half-recrystallization suggests. The microstructure of partially recrystallized samples was investigated in terms of their texture, boundary character, boundary surface densities and stored energy content, to elucidate the underlying microstructural reasons for such a halt. The microstructural path methodology was adopted to describe the evolution of recrystallization from a stereological standpoint. The texture of the plate did not show major changes with the evolution of recrystallization while the misorientation distributions for the boundaries in between the recrystallized and recovered regions did not suggest any particular feature motivating the halt. Analysis of the partial path functions of the stereological parameters from the microstructure indicated non-uniform impingement above a fraction recrystallized of 60%. A slow motion of high angle boundaries constituting the recrystallization front due to the continuously decreasing stored energy in the recovered matrix, combined with reduced nucleation (retarded by concurrent recovery) and a non-uniform impingement can motivate stagnation of recrystallization. Though, a comprehensive description of the halting mechanism and how to achieve it by purpose have not yet been found.

Nevertheless tungsten plates, especially W80, need further examination as a material design for tungsten as PFM, since a halt in recrystallization such as that of W80 is key, if understood, for operation in fusion reactors. Use of the MP methodology was never attempted before on warm-rolled tungsten plates and this work shows how such useful this approach can be to obtain further understanding of the restoration processes that are of paramount importance for PFMs. From this work, it can be questioned if tungsten plates that undergo conventionally undesired extensive restoration processes during work-hardening could actually provide a solution to the problem of thermal stability. The two most thermally stable plates analysed here or reported from previous work are the W67 and the W80. A rolling processing, performed at temperatures high enough to allow for extensive restoration processes to take place in the first passes, as it might have happened to the W80, and to lower temperatures in the last passes, providing the dislocation density necessary for ductile behaviour is envisioned. Alternatively, intermediate annealings to achieve recrystallization in between passes are suggested. Experimental campaigns could be performed aiming at: 1) testing the ductility of the material at different temperatures to ensure the same safe structural use over the entire operational range in fusion reactors as for warm-rolled plates 2) verify the replicability of the thermal stability of W80 in these newly designed plates and 3) have a larger wealth of material that can be studied to understand the actual reason behind such an unexpected improved thermal stability as found in the W80.

Single tungsten fiber composites, with or without an erbia or yttria interlayer, containing a single drawn potassium-doped tungsten wire in a CVD tungsten matrix were investigated in terms of their thermal stability. Upon annealing at 1400 °C for up to 28 d, two different zones develop possessing much larger grains than in the as-processed condition. Small but notable orientation changes indicate new defect-free grains (larger than in the as-received condition) forming in the wire, indicating primary recrystallization. These newly formed grains seem not to grow more than a certain size and orientation pinning or Zener pinning by potassium bubbles still persisting in the wire seems to take place. Some of the very thin grains in the proximity of the interlayer in the CVD region grow abnormally at the expense of others to form a final microstructure (corona) of almost equiaxed grains. The interlayers, acting as barriers, constitute an efficient solution in separating the microstructural annealing phenomena occurring in the different regions: primary recrystallization in the wire and secondary recrystallization in the matrix.

The inward motion of grain boundaries from the CVD region is blocked by the interlayer as long as it remains intact or no pathways between the two different regions exist. Without the interlayer the grains in the CVD region possess a size advantage with respect to those in the wire and start to grow into the recrystallized outer layer of the wire. The presence of an interlayer between the two regions is paramount for the thermal stability of such a designed tungsten material. Successful implementation of these W_fW as plasma facing material requires the wires to be shielded by an interlayer so that internal growth of grains from the CVD matrix do not deplete the microstructure of the wire which is ultimately responsible for the desired extrinsic ductility of the composite. The present work suggests that the structural design of W_fW will not be influenced by microstructural restoration damage if an interface between the wire and the CVD matrix is present. Such a finding is paramount for the safe application of W_fW as PFMs and provides an additional proof of suitability of this novel design for implementation in fusion reactors. Further research shall be directed at better understanding the kinetics of grain growth in the acicular zone of the composite, as well as at characterizing the behavior at the interfacial zone at higher temperatures; which are foreseen in a fusion reactor.

Analysis of the as-received condition of the W_fW resulted in interesting novel findings on the microstructure of both the wire and the CVD tungsten surrounding the wire. For the wire, an additional preferred orientation in the as-deformed microstructure was found on top of that defining the well-known fiber texture. As a consequence, the texture of tungsten drawn wires can be now re-defined as cyclic {110}<110> fiber texture. Concerning the CVD matrix of W_fW, the texture found represent to the knowledge of the author the very first reported example of a texture that was so far only theoretically defined, that of a cyclic <100> ring fiber texture. These two finding represent a solid contribution to the knowledge of texture in materials and have potential to influence or suggest future works aiming at exploiting these characteristics.

Bibliography

[1] USSR Communist Party, “Twentieth Congress of the Communist Party”, 1956.

[2] G. McCracken and P. Stott, *Fusion*. Elsevier Inc., 2013.

[3] V. P. Smirnov, “Tokamak foundation in USSR/Russia 1950-1990”, *Nucl. Fusion*, vol. 50, p. 8, 2010, doi: 10.1088/0029-5515/50/1/014003.

[4] F. Romanelli, “EFDA, Fusion Electricity: A roadmap to the realisation of fusion energy”, pp. 1–75, 2012, doi: ISBN 978-3-00-040720-8.

[5] Nuclear Energy Agency and International Atomic Energy Agency, *Uranium 2018: Resources, Production and Demand*. OECD - Organisation for Economic Co-operation and Development, 2018.

[6] I. A. E. Agency, *ITER conceptual design*. IAEA, 1990.

[7] D. Naujoks, *Plasma-Material Interaction in Controlled Fusion*. Springer Berlin Heidelberg, 2006.

[8] H. Bolt *et al.*, “Materials for the plasma-facing components of fusion reactors”, in *Journal of Nuclear Materials*, 2004, vol. 329–333, no. 1-3 PART A, pp. 66–73, doi: 10.1016/j.jnucmat.2004.04.005.

[9] E. E. Bloom *et al.*, “Low activation materials for fusion applications”, *J. Nucl. Mater.*, vol. 122, no. 1–3, pp. 17–26, 1984, doi: 10.1016/0022-3115(84)90570-1.

[10] N. Baluc *et al.*, “Status of R&D activities on materials for fusion power reactors”, *Nucl. Fusion*, vol. 47, no. 10, pp. 696–717, Sep. 2007, doi: 10.1088/0029-5515/47/10/S18.

[11] J. Knaster, A. Moeslang, and T. Muroga, “Materials research for fusion”, *Nature Physics*, vol. 12, no. 5. Nature Publishing Group, pp. 424–434, 01-May-2016, doi: 10.1038/NPHYS3735.

[12] M. Rieth *et al.*, “Recent progress in research on tungsten materials for nuclear fusion applications in Europe”, *Journal of Nuclear Materials*, vol. 432, no. 1–3. pp. 482–500, Jan-2013, doi: 10.1016/j.jnucmat.2012.08.018.

[13] M. Rieth *et al.*, “Review on the EFDA programme on tungsten materials technology and science”, in *Journal of Nuclear Materials*, 2011, vol. 417, no. 1–3, pp. 463–467, doi: 10.1016/j.jnucmat.2011.01.075.

[14] Z. jian Zhou, S. xiang Song, J. Du, and C. chun Ge, “High heat flux testing of tungsten plasma facing materials”, *J. Nucl. Mater.*, vol. 367-370 B, no. SPEC. ISS., pp. 1468–1471, Aug. 2007, doi: 10.1016/j.jnucmat.2007.04.006.

[15] R. A. Causey and T. J. Venhaus, “The use of tungsten in fusion reactors: A review of the hydrogen retention and migration properties”, in *Physica Scripta T*, 2001, vol. 94, pp. 9–15, doi: 10.1238/physica.topical.094a00009.

[16] E. Lassner and W.-D. Schubert, *Tungsten: Properties, Chemistry, Technology of the Element, Alloys, and Chemical Compounds*, 1st Ed. Springer, Boston, MA, 1999.

[17] M. G. Randall, *Powder Metallurgy and Particulate Materials Processing*. 2005.

[18] A. V. Babak and E. I. Uskov, “High-temperature embrittlement of tungsten”, *Strength Mater.*, vol. 15, no. 5, pp. 667–672, May 1983, doi: 10.1007/BF01523215.

[19] S. N. Mathaudhu, A. J. deRosset, K. T. Hartwig, and L. J. Kecskes, “Microstructures and recrystallization behavior of severely hot-deformed tungsten”, *Mater. Sci. Eng. A*, vol. 503, no. 1–2, pp. 28–31, Mar. 2009, doi: 10.1016/j.msea.2008.03.051.

[20] M. Rieth *et al.*, “Tungsten as a Structural Divertor Material”, *Adv. Sci. Technol.*, vol. 73, pp. 11–21, 2010, doi: 10.4028/www.scientific.net/AST.73.11.

[21] A. V. Babak, “Effect of recrystallization on the fracture toughness of tungsten”, *Sov. Powder Metall. Met. Ceram. (english Transl. Poroshkovaya Metall.*, vol. 22, no. 4, pp. 316–318, 1983.

[22] K. Farrell, A. C. Schaffhauser, and J. O. Stiegler, “Recrystallization, grain growth and the ductile-brittle transition in tungsten sheet”, *J. Less-Common Met.*, vol. 13, no. 2, pp. 141–155, 1967, doi: 10.1016/0022-5088(67)90177-4.

[23] J. Reiser, M. Rieth, B. Dafferner, and A. Hoffmann, “Charpy impact properties of pure tungsten plate material in as-received and recrystallized condition (1 h at 2000 °C (2273 K))”, *J. Nucl. Mater.*, vol. 442, no. 1-3 SUPPL.1, pp. S204–S207, 2013, doi: 10.1016/j.jnucmat.2012.10.037.

[24] D. Hull and D. J. Bacon, *Introduction to Dislocations*. Elsevier Ltd, 2011.

[25] E. J. Mittemeijer, *Fundamentals of materials science: The microstructure-property relationship using metals as model systems*. Springer Berlin Heidelberg, 2011.

[26] P. Lied, C. Bonnekoh, W. Pantleon, M. Stricker, A. Hoffmann, and J. Reiser, “Comparison of K-doped and pure cold-rolled tungsten sheets: As-rolled condition and

recrystallization behaviour after isochronal annealing at different temperatures", *Int. J. Refract. Met. Hard Mater.*, vol. 85, p. 105047, Dec. 2019, doi: 10.1016/j.ijrmhm.2019.105047.

[27] M. Muzyk, D. Nguyen-Manh, K. J. Kurzydłowski, N. L. Baluc, and S. L. Dudarev, "Phase stability, point defects, and elastic properties of W-V and W-Ta alloys", *Phys. Rev. B - Condens. Matter Mater. Phys.*, vol. 84, no. 10, p. 104115, Sep. 2011, doi: 10.1103/PhysRevB.84.104115.

[28] M. Muzyk, D. Nguyen-Manh, J. Wróbel, K. J. Kurzydłowski, N. L. Baluc, and S. L. Dudarev, "First-principles model for phase stability, radiation defects and elastic properties of W-Ta and W-V alloys", *J. Nucl. Mater.*, vol. 442, no. 1-3 SUPPL.1, 2013, doi: 10.1016/j.jnucmat.2012.10.025.

[29] S. Wurster, B. Gludovatz, and R. Pippan, "High temperature fracture experiments on tungsten-rhenium alloys", in *International Journal of Refractory Metals and Hard Materials*, 2010, vol. 28, no. 6, pp. 692–697, doi: 10.1016/j.ijrmhm.2010.03.002.

[30] M. Rieth *et al.*, "A brief summary of the progress on the EFDA tungsten materials program", *J. Nucl. Mater.*, vol. 442, no. 1-3 SUPPL.1, pp. S173–S180, 2013, doi: 10.1016/j.jnucmat.2013.03.062.

[31] P. Krautwasser, H. Derz, and E. Kny, "Influence of fast neutron fluence on the ductile-brittle transition temperature of tungsten, W-10Re, and W-3.4Ni-1.6Fe", *High Temp. - High Press.*, vol. 22, no. 1, pp. 25–32, 1990.

[32] H. Li, S. Wurster, C. Motz, L. Romaner, C. Ambrosch-Draxl, and R. Pippan, "Dislocation-core symmetry and slip planes in tungsten alloys: Ab initio calculations and microcantilever bending experiments", *Acta Mater.*, vol. 60, no. 2, pp. 748–758, Jan. 2012, doi: 10.1016/j.actamat.2011.10.031.

[33] M. Rieth and B. Dafferner, "Limitations of W and W–1%La2O3 for use as structural materials", *J. Nucl. Mater.*, vol. 342, no. 1–3, pp. 20–25, Jun. 2005, doi: 10.1016/j.jnucmat.2005.03.013.

[34] M. Rieth and A. Hoffmann, "Influence of microstructure and notch fabrication on impact bending properties of tungsten materials", in *International Journal of Refractory Metals and Hard Materials*, 2010, vol. 28, no. 6, pp. 679–686, doi: 10.1016/j.ijrmhm.2010.04.010.

[35] G. M. Song, Y. J. Wang, and Y. Zhou, “Thermomechanical properties of TiC particle-reinforced tungsten composites for high temperature applications”, *Int. J. Refract. Met. Hard Mater.*, vol. 21, no. 1–2, pp. 1–12, 2003, doi: 10.1016/S0263-4368(02)00105-1.

[36] L. Veleva, “Contribution to the production and characterization ofW–Y, W–Y2O3 and W–TiC Materials for Fusion Reactors”, Ph.D. Thesis, EPFL, 2011.

[37] J. W. Davis, V. R. Barabash, A. Makhankov, L. Plöchl, and K. T. Slattery, “Assessment of tungsten for use in the ITER plasma facing components”, *J. Nucl. Mater.*, vol. 258–263, no. PART 1 A, pp. 308–312, 1998, doi: 10.1016/S0022-3115(98)00285-2.

[38] J. Du, T. Höschen, M. Rasinski, and J. H. You, “Interfacial fracture behavior of tungsten wire/tungsten matrix composites with copper-coated interfaces”, *Mater. Sci. Eng. A*, vol. 527, no. 6, pp. 1623–1629, Mar. 2010, doi: 10.1016/j.msea.2009.10.046.

[39] J. Du, J. H. You, and T. Höschen, “Thermal stability of the engineered interfaces in W/f/W composites”, *J. Mater. Sci.*, vol. 47, no. 11, pp. 4706–4715, Jun. 2012, doi: 10.1007/s10853-012-6339-9.

[40] J. Du, T. Höschen, M. Rasinski, and J. H. You, “Shear debonding behavior of a carbon-coated interface in a tungsten fiber-reinforced tungsten matrix composite”, in *Journal of Nuclear Materials*, 2011, vol. 417, no. 1–3, pp. 472–476, doi: 10.1016/j.jnucmat.2010.12.254.

[41] J. Du, T. Höschen, M. Rasinski, S. Wurster, W. Grosinger, and J. H. You, “Feasibility study of a tungsten wire-reinforced tungsten matrix composite with ZrOx interfacial coatings”, *Compos. Sci. Technol.*, vol. 70, no. 10, pp. 1482–1489, Sep. 2010, doi: 10.1016/j.compscitech.2010.04.028.

[42] J. Reiser, M. Rieth, B. Dafferner, and A. Hoffmann, “Tungsten foil laminate for structural divertor applications - Basics and outlook”, *J. Nucl. Mater.*, vol. 423, no. 1–3, pp. 1–8, Apr. 2012, doi: 10.1016/j.jnucmat.2012.01.010.

[43] J. Reiser, M. Rieth, B. Dafferner, A. Hoffmann, X. Yi, and D. E. J. Armstrong, “Tungsten foil laminate for structural divertor applications - Analyses and characterisation of tungsten foil”, *J. Nucl. Mater.*, vol. 424, no. 1–3, pp. 197–203, May 2012, doi: 10.1016/j.jnucmat.2012.02.030.

[44] K. Chawla, “Ceramic matrix composites,” 2013.

[45] R. Neu, J. W. Coenen, C. Linsmeier, T. Höschen, M. Li, and R. Neu, “Chemically

deposited tungsten fibre-reinforced tungsten – The way to a mock-up for divertor applications", *Nucl. Mater. Energy*, vol. 9, pp. 75–83, 2016, doi: 10.1016/j.nme.2016.03.005.

[46] J. Riesch, "Tungsten-fibre reinforced tungsten composites: A novel concept for improving the toughness of tungsten", *Iccm Int. Conf. Compos. Mater.*, 2011.

[47] A. Alfonso, D. Juul Jensen, G. N. Luo, and W. Pantleon, "Thermal stability of a highly-deformed warm-rolled tungsten plate in the temperature range 1100-1250 °C", *Fusion Eng. Des.*, vol. 98–99, pp. 1924–1928, 2015, doi: 10.1016/j.fusengdes.2015.05.043.

[48] A. Alfonso, D. Juul Jensen, G. N. Luo, and W. Pantleon, "Recrystallization kinetics of warm-rolled tungsten in the temperature range 1150-1350 °C", *J. Nucl. Mater.*, vol. 455, no. 1, pp. 591–594, 2014, doi: 10.1016/j.jnucmat.2014.08.037.

[49] U. M. Ciucani, A. Thum, C. Devos, and W. Pantleon, "Isothermal annealing of thin rolled tungsten plates in the temperature range from 1300 °C to 1400 °C", *Nucl. Mater. Energy*, vol. 15, pp. 128–134, 2018, doi: 10.1016/j.nme.2018.03.009.

[50] U. M. Ciucani, A. Thum, C. Devos, and W. Pantleon, "Recovery and recrystallization kinetics of differently rolled, thin tungsten plates in the temperature range from 1325 °C to 1400 °C", *Nucl. Mater. Energy*, vol. 20, p. 100701, Aug. 2019, doi: 10.1016/j.nme.2019.100701.

[51] U. M. Ciucani and W. Pantleon, "Stagnant recrystallization in warm-rolled tungsten in the temperature range from 1150 °C to 1300 °C", *Fusion Eng. Des.*, vol. 146, pp. 814–817, 2019, doi: 10.1016/j.fusengdes.2019.01.088.

[52] U. M. Ciucani and W. Pantleon, "Microstructural path investigation into the stagnation of recrystallization in warm-rolled tungsten", 2021.

[53] U. M. Ciucani, L. Haus, H. Gietl, J. Riesch, and W. Pantleon, "Microstructural evolution in single tungsten fiber-reinforced tungsten composites during annealing: recrystallization and abnormal grain growth", *J. Nucl. Mater.*, vol. 543, p. 152579, 2021, doi: 10.1016/j.jnucmat.2020.152579.

[54] P. Schade, H. Ortner, and I. Smid, "Refractory metals revolutionizing the lighting technology: A historical review", *Int. J. Refract. Met. Hard Mater.*, vol. 50, pp. 23–30, 2015, doi: 10.1016/j.ijrmhm.2014.11.002Review.

[55] P. Schade, "100 years of doped tungsten wire", in *International Journal of Refractory*

Metals and Hard Materials, 2010, vol. 28, no. 6, pp. 648–660, doi: 10.1016/j.ijrmhm.2010.05.003.

[56] C. Bonnekoh, A. Hoffmann, and J. Reiser, "The brittle-to-ductile transition in cold rolled tungsten: On the decrease of the brittle-to-ductile transition by 600 K to − 65 °C", *Int. J. Refract. Met. Hard Mater.*, vol. 71, pp. 181–189, 2018, doi: 10.1016/j.ijrmhm.2017.11.017.

[57] D. B. Snow, "The recrystallization of commercially pure and doped tungsten wire drawn to high strain", *Metall. Trans. A*, vol. 10, no. 7, pp. 815–821, Jul. 1979, doi: 10.1007/BF02658299.

[58] V. Nikolić, J. Riesch, and R. Pippan, "The effect of heat treatments on pure and potassium doped drawn tungsten wires: Part I - Microstructural characterization", *Mater. Sci. Eng. A*, vol. 737, pp. 422–433, 2018, doi: 10.1016/j.msea.2018.09.027.

[59] P. Jenuš, A. Iveković, M. Kocen, A. Šestan, and S. Novak, "WC-reinforced tungsten prepared using different precursors", *Ceram. Int.*, vol. 45, no. 6, pp. 7995–7999, Apr. 2019, doi: 10.1016/j.ceramint.2018.11.187.

[60] S. Novak *et al.*, "Beneficial effects of a WC addition in FAST-densified tungsten", *Mater. Sci. Eng. A*, vol. 772, p. 138666, Jan. 2020, doi: 10.1016/j.msea.2019.138666.

[61] M. Battabyal, R. Schäublin, P. Spätig, and N. Baluc, "W-2wt.%Y 2O 3 composite: Microstructure and mechanical properties", *Mater. Sci. Eng. A*, vol. 538, pp. 53–57, Mar. 2012, doi: 10.1016/j.msea.2012.01.011.

[62] X. Y. Tan *et al.*, "Development of tungsten as plasma-facing materials by doping tantalum carbide nanoparticles", *Powder Technol.*, vol. 269, pp. 437–442, Jan. 2015, doi: 10.1016/j.powtec.2014.09.039.

[63] H. Kurishita *et al.*, "Current status of nanostructured tungsten-based materials development", in *Physica Scripta*, 2014, vol. T159, p. 014032, doi: 10.1088/0031-8949/2014/T159/014032.

[64] A. Šestan *et al.*, "Tungsten carbide as a deoxidation agent for plasma-facing tungsten-based materials", *J. Nucl. Mater.*, vol. 524, pp. 135–140, Oct. 2019, doi: 10.1016/j.jnucmat.2019.06.030.

[65] ITER Team and K. Tomabechi, "ITER: design overview", *J. Nucl. Mater.*, vol. 179–181, no. PART 2, pp. 1173–1178, Mar. 1991, doi: 10.1016/0022-3115(91)90316-Y.

[66] J. Humphreys, G. Rohrer, and A. Rollett, *Recrystallization and related annealing phenomena*, 3rd ed. Elsevier, 2017.

[67] C. L. Briant, F. Zaverl, and E. L. Hall, “Warm rolling of sintered tungsten ingots”, *Mater. Sci. Technol.*, vol. 7, no. 10, pp. 923–936, Feb. 2012, doi: 10.1179/026708391790182827.

[68] G. Wassermann and J. Grewen, *Texturen metallischer Werkstoffe*. Springer Verlag, 1962.

[69] A. Barna, I. Gaal, O. Geszti-Harkner, G. Radnoczi, and L. Uray, “The fibre structure of K-Si-Al doped tungsten wires”, *High Temp. - High Press.*, vol. 10, no. 2, pp. 197–205, 1978.

[70] S. K. Yerra, B. Verlinden, and P. Van Houtte, “On crystallographic texture of as-drawn doped-W wires”, in *Materials Science Forum*, 2005, vol. 495–497, no. PART 2, pp. 913–918, doi: 10.4028/0-87849-975-x.913.

[71] E. S. Meieran and D. A. Thomas, “Structure of drawn and annealed tungsten wire”, *Trans. Metall. Soc. Aime*, vol. 233, no. 5, p. 937, 1965.

[72] J. Schmidt and F. Haeßner, “Stage III-recovery of cold worked high-purity aluminium determined with a low-temperature calorimeter”, *Zeitschrift für Phys. B Condens. Matter*, vol. 81, no. 2, pp. 215–222, Jun. 1990, doi: 10.1007/BF01309351.

[73] A. Cottrell and V. Aytekin, “The flow of zinc under constant stress”, *J. Inst. Met.*, vol. 77, no. 5, pp. 389–396, 1950.

[74] J. Friedel, *Dislocations*. Pergamon, 1964.

[75] D. Kuhlmann, G. Masing, and J. Raffelsiepeer, “Zur theorie der erholung”, *Zeitschrift Fur Met.*, vol. 40, no. 7, 1949.

[76] J. Michalak and H. Paxton, “Some recovery charachteristics of zone-melted Iron”, *Trans. Metall. Soc. Aime*, vol. 221, no. 4, pp. 850–857, 1961.

[77] D. Tabor, “The hardness and strength of metals”, *J. Inst. Met.*, vol. 79, no. 1, pp. 1–18, 1951.

[78] J. Cahoon, W. Broughton, and A. Kutzak, “The determination of yield strength from hardness measurements”, *Metall. Trans.*, vol. 2, no. 7, pp. 1979–1983, 1971.

[79] J. R. Cahoon, “An improved equation relating hardness to ultimate strength”, *Metall. Trans.*, vol. 3, no. 11, p. 3040, Nov. 1972, doi: 10.1007/BF02652880.

[80] J. T. Michalak and J. Hibbard, “Effect of rolling procedure on kinetics of recrystallization of cold-rolled iron”, *Am. Soc. Met.*, vol. 53, p. 331, 1961.

[81] J. T. Michalak and J. Hibbard, “Effect of rolling procedure on kinetics of recrystallization

of cold-rolled copper”, *J. Met.*, vol. 9, no. 1, pp. 101–106, 1957.

[82] E. Lindh, B. Hutchinson, and S. Ueyama, “Effect of redundant deformation on recrystallisation behaviour of copper”, *Scr. Metall. Mater.*, vol. 29, no. 3, pp. 347–352, Aug. 1993, doi: 10.1016/0956-716X(93)90511-P.

[83] J. D. Embury, W. J. Poole, and E. Koken, “Some views on the influence of strain path on recrystallization”, *Scr. Metall. Mater.*, vol. 27, no. 11, pp. 1465–1470, Dec. 1992, doi: 10.1016/0956-716X(92)90129-3.

[84] Q. Zhu and C. M. Sellars, “Recrystallization behavior in tension/tension and tension/compression hot deformation of Al-2Mg”, *Proc. Rex’ 96, Recryst. Relat. Phenom.*, p. 195, 1997.

[85] W. B. Hutchinson and L. Ryde, *16th Int. Risø Symp.*, p. 105, 1995.

[86] J. C. Blade and P. L. Morris, *Proc. 4th Int. Conf. Textures*, p. 171, 1975.

[87] A. N. Kolmogorov, “On the Statistical Theory of Crystallization of Metals”, *Izv. Akad. Nauk SSSR, Ser. Mat.*, no. 3, pp. 355–359, 1937.

[88] M. Avrami, “Kinetics of phase change. I: General theory”, *J. Chem. Phys.*, vol. 7, no. 12, pp. 1103–1112, Dec. 1939, doi: 10.1063/1.1750380.

[89] W. Johnson and R. Mehl, “Reaction Kinetics in Processes of Nucleation and Growth”, *Trans. Am. Inst. Min. Metall. Eng.*, vol. 135, pp. 416–442, 1939.

[90] P. Gordon and R. Vandermeer, “Mechanism of boundary migration in recrystallization”, *Trans. Metall. Soc. Aime*, vol. 224, no. 5, 1962.

[91] J. W. Cahn, “The kinetics of grain boundary nucleated reactions”, *Acta Metall.*, vol. 4, no. 5, pp. 449–459, Sep. 1956, doi: 10.1016/0001-6160(56)90041-4.

[92] R. A. Vandermeer and B. B. Rath, “Modeling of recrystallization”, *Proc. Riso Int. Symp. Metall. Mater. Sci.*, pp. 589–599, 1989.

[93] R. A. Vandermeer and B. B. Rath, “Modeling recystallization kinetics in a deformed iron single crystal”, *Metall. Trans. A*, vol. 20, no. 3, pp. 391–401, 1989, doi: 10.1007/BF02653918.

[94] R. A. Vandermeer, R. A. Masumura, and B. B. Rath, “Microstructural paths of shape-preserved nucleation and growth transformations”, *Acta Metall. Mater.*, vol. 39, no. 3, pp. 383–389, 1991, doi: 10.1016/0956-7151(91)90317-T.

[95] A. M. Gokhale and R. T. Dehoff, “Estimation of nucleation rate and growth rate from time

dependence of global microstructural properties during phase transformations", *Metall. Trans. A*, vol. 16, no. 4, pp. 559–564, Apr. 1985, doi: 10.1007/BF02814229.

[96] R. A. Vandermeer, "Microstructural descriptors and the effects of nuclei clustering on recrystallization path kinetics", *Acta Mater.*, vol. 53, no. 5, pp. 1449–1457, 2005, doi: 10.1016/j.actamat.2004.10.054.

[97] P. R. Rios and A. F. Padilha, "Comment on 'microstructural path and temperature dependence of recrystallization in commercial aluminum", *Scripta Materialia*, vol. 48, no. 11. Elsevier Ltd, pp. 1561–1564, 2003, doi: 10.1016/S1359-6462(03)00055-1.

[98] R. L. Fullman, "Measurement of particle sizes in opaque bodies", *Trans. Am. Inst. Mining, Metall. Pet. Eng.*, no. 197, pp. 447–52, 1953.

[99] P. R. Rios, R. B. Godiksen, S. Schmidt, D. Juul Jensen, and R. A. Vandermeer, "Analytical expression for the evolution of interfacial area density between transformed grains during nucleation and growth transformations", *Scr. Mater.*, vol. 54, no. 8, pp. 1509–1513, Apr. 2006, doi: 10.1016/j.scriptamat.2005.12.037.

[100] J. I. Goldstein, D. E. Newbury, J. R. Michael, N. W. M. Ritchie, J. H. J. Scott, and D. C. Joy, *Scanning electron microscopy and x-ray microanalysis*. Springer New York, 2017.

[101] Y. Leng, *Materials Characterization: Introduction to Microscopic and Spectroscopic Methods*. John Wiley and Sons, 2010.

[102] V. Randle and O. Engler, *Introduction to texture analysis : macrotexture, microtexture, and orientation mapping*, 2nd ed. CRC Press, 2010.

[103] A. Morawiec, *Orientations and Rotations - Computations in Crystallographic textures*. Springer-Verlag Berlin Heidelberg GmbH, 2004.

[104] H. Bunge, *Texture analysis in materials science : mathematical methods*. Butterworths, 1982.

[105] L. Euler, "Formulae generales pro translatione quacunque corporum rigidorum", *Novi Comment. Acad. Sci. Imp. petropolitanae*, vol. 20, pp. 189–207, 1775.

[106] H. Bunge, "Zur Darstellung Allgemeiner Texturen", *Zeitschrift Fur Met.*, vol. 56, no. 12, p. 872, 1965.

[107] J. Du, "Feasibility Study of Tungsten-Fiber-Reinforced Tungsten Composites with Engineered interfaces", Ph.D. Thesis, Technische Universität München, 2011.

[108] W. F. Gale and T. C. Totemeier, *Smithells Metals Reference Book*. Elsevier Ltd, 2003.

[109] F. Bachmann, R. Hielscher, and H. Schaeben, “Texture analysis with MTEX- Free and open source software toolbox”, in *Solid State Phenomena*, 2010, vol. 160, pp. 63–68, doi: 10.4028/www.scientific.net/SSP.160.63.

[110] W. T. Read and W. Shockley, “Dislocation models of crystal grain boundaries”, *Phys. Rev.*, vol. 78, no. 3, pp. 275–289, 1950, doi: 10.1103/PhysRev.78.275.

[111] B. C. Allen, “The interfacial free energies of solid chromium, molybdenum and tungsten”, *J. Less-Common Met.*, vol. 29, no. 3, pp. 263–282, 1972, doi: 10.1016/0022-5088(72)90114-2.

[112] P. Stüwe, “Texturbildung bei der primärrekristallisation”, *Zeitschrift für Met.*, vol. 52, no. 1, pp. 34–44, 1961.

[113] M. Fuhr, M.Sc. Thesis, “Thermal stability of tungsten fibre-reinforced tungsten composites”, 2019.

DTU Mechanical Engineering
Section of Materials and Surface Engineering
Technical University of Denmark

Produktionstorvet, Bld. 425
DK-2800 Kgs. Lyngby
Denmark
Tlf.: +45 4525 2205
Fax: +45 4525 1961

www.mek.dtu.dk

February 2021

ISBN: 978-87-7475-622-4